STUDY OF NANOCOMPOSITES AND NANOWIRE DEVICES FOR THZ CIRCUIT APPLICATIONS

By

Xianbo Yang

A DISSERTATION

Submitted to
Michigan State University
in partial fulfillment of the requirements
for the degree of

Electrical Engineering—Doctor of Philosophy

2014

ABSTRACT

STUDY OF NANOCOMPOSITES AND NANOWIRE DEVICES
FOR THZ CIRCUIT APPLICATIONS

By

Xianbo Yang

Interest in terahertz (**10^{11}-10^{13}Hz**) spectral region is driven by the possibility of exploiting unique interaction between electromagnetic fields and materials in this spectral regime. Potentials of THz have been examined using quasi-optical table top systems. There is significant interest to minimize the bench-top quasi-optical systems to integrated circuit level in order to realize similar functions and benefits as in the digital and RF integrated circuit areas. Integration of both passive and active devices at the wafer level is necessary to meet this challenge. Conventional integration approaches (e.g., microstrip transmission lines) do not directly lend themselves to the design and fabrication of THz circuits and new design approaches are required. This work proposes and demonstrates novel approaches to achieve both active and passive element integration at the wafer level that are compatible with large-area and low-temperature processes, and paves the path to realize highly functional, compact, low-cost THz systems.

THz waveguide and interconnects are one of the fundamental building blocks of THz passives. This research investigates the use of thin dielectric ribbons made from polymer-ceramic nanocomposite for the fabrication of planar, low-loss, and large area compatible THz waveguides. Simulations show the ribbon waveguides provide low loss THz wave propagation when a combination of high dielectric constant (high-*k*) core and low dielectric constant cladding are used. This combination provides stronger field confinement and reduces losses at waveguide bends. Two different fabrication approaches are investigated: photopatterning of tailorable nanocomposite thin films, and laser cutting of dry nanocomposite thin films. Measurements of

different waveguide samples validate the simulated results and prove that low cost, wafer-level planar THz integrated circuits can be realized with proposed waveguides.

THz active devices are the core elements required to build THz circuits. Diode is a key component that is needed to form a basic THz active circuit. Semiconducting n-type GaAs nanowires are utilized in the fabrication of THz Schottky diodes. Nanowire based devices can be used to achieve high cut-off frequency devices, but individual nanowire has high impedance that is not suitable for wide-band impedance matching. To overcome this challenge, multiple nanowires placed in parallel are integrated together to achieve desired impedance while maintaining high cut-off frequency. A novel low-cost process using photolithography is applied to fabricate sub-micron devices. Fabrication of nanowire based devices is compatible with integration on a host of large area substrates at low processing temperature. These diodes are first utilized in the design of THz detectors, calculated and measured results show strong nonlinear rectification behavior and high sensitivity over a wide frequency band (0.1 – 1 THz).

In parallel, an alternative method of fabricating THz detector was also investigated. Active devices are embedded within the dielectric layers forming the waveguides. This avoids the use of flip-chip or wire bonds to connect the devices and thus minimizes the parasitics. GaAs Schottky Barrier Diodes (SBDs) are directly integrated with broadband log-periodic antennas to design a highly sensitive broad-band THz detector. Calculated and measured sensitivity of the detector closely matches the performance of existing commercial THz detectors fabricated using elaborate micromachining techniques. A THz image sensor is fabricated and demonstrated in this work to prove the feasibility of this concept. This fabrication approach is large-area, low-cost, and low-temperature process compatible and can also be implemented in heterogeneous integration of THz devices on a host of substrates.

ACKNOWLEDGEMENTS

I am heartily thankful to my advisor Dr. Premjeet Chahal for his advice, supports, understanding and encouragement during my whole Ph.D. study, not only in research life, but also in my daily life. His idea and perspectives mentored and guided me through lots of situations. Without his help and guidance, it is impossible for me to accomplish any piece of the research work and the dissertation.

I am also grateful to my Ph.D. committee members: Dr. K. Subramanian, Dr. Donnie Reinhard and Dr. Tim Hogan for providing me advice, idea, assistance, resources and corrections for my research work and dissertation preparation.

I would like to express my heart-whole thanks to my beloved parents for their always understanding, support and thoughtful concerns during my six years of study aboard. Their love has brought me the courage to face any challenges in the past and future.

Special thanks to Jing Zhao and her family for their encouragement and support during the tough time when preparing my dissertation, without them, it is hard for me to finish the writing in such limit of time.

It is also a pleasure to thank all the faculty and student members in the EM group, especially TESLA group, and people in ECE Cleanroom and KMF Cleanroom for their supports, suggestions and assistance.

I also would like to thank all my friends for their accompanying and help in my entire Ph.D. study. They provided useful suggestions to my research work based on their expertise, and the friendship we shared also colored my life. The time with them has become the best memory in my heart.

TABLE OF CONTENTS

LIST OF TABLES

LIST OF FIGURES

Chapter 1 Introduction

1.1 Research Overview

The rapid growth and significant development in the terahertz (THz) (frequency spanning from 10^{11} to 10^{13}Hz) gap between radio frequency and infrared spectrum (shown in Figure 1.1) holds significant potential in many research fields.

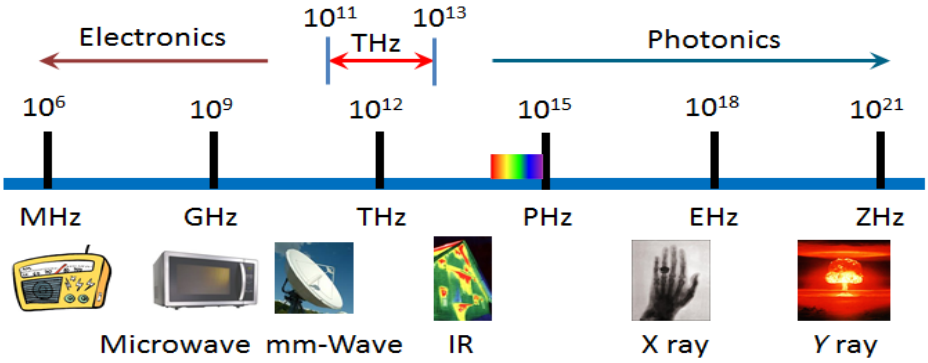

Figure 1.1 Electromagnetic spectrum showing THz gap between radio frequency and infrared radiation.

Interest in this spectral regime is driven by the possibility of exploiting unique interaction between electromagnetic fields and materials. Applications based on those fresh revealed features are being studied or have already been commercialized over the past two decades. THz has low loss transmission characteristics through thin dielectric layers such as paper, clothes, ceramics and skin (epidermis). Also, it has shorter wavelength (30μm-3mm). These two characteristics can be utilized together to realize high resolution imaging for biomedical examination and security inspection. Since THz is non-ionizing, due to its low energy, it is not harmful to live tissues [1, 2]. It also can be applied as a new technique for sensing and non-destructive evaluation [3]. Moreover, THz spectroscopy for material characterization can discover unique material properties that reside in this frequency spectrum [4, 5, 6], and it has also been utilized to identify the presence of molecules in the deep space and measure signals

that originated from the early formation of the universe. The THz spectrum also has the potential to provide sensor information in IR-blind conditions (e.g., fog, rain, dust, smoke) and THz imaging could offer clear advantages over conventional (i.e., millimeter wave, MMW) all-weather imaging approaches. Moreover, THz also has the potential to enhance communication capability between satellites and airborne platforms in space. However, the development in The THz spectrum is not matured in comparison to microwave and the optical frequency based technologies. Manufacturing and fabrication of THz systems is costly and difficult due to the equipment complexity and unavailability of necessary THz components and devices. Effective, high performance THz switches, modulators and phase-shifters are missing from the portfolios that are ubiquitous in the neighboring microwave and infrared bands. Thus, the THz frequency band remains the most immature and underutilized part of the electromagnetic spectrum. Currently there is significant ongoing research to overcome this bottleneck.

Early results using quasi-optical setups have shown the benefit and potential of THz spectrum. But, the cumbersome and complicated quasi-optical setup obstructs its extension to a wider realm [7]. To meet the application challenges, there has been a large demand to move from such quasi-optical THz setups to integrated THz circuits in order to realize similar devices functions and benefits as in the RF integrated circuits fields, and this research work is proposed to open a path and push forward to realize integrated THz circuits.

One of the fundamental passive components is THz interconnect (THz waveguide) which is required for almost all THz circuit applications. There are many challenges associated with THz integrated waveguides such as unavailability of materials, and sophisticated designation, tedious fabrication process and high interconnect losses. As the frequency goes up, suitable materials with low loss characteristics, low cost and compatibility with existing Complimentary Metal-

Oxide-Semiconductor (CMOS) technology are limited. For active devices/circuits, epitaxial grown III-V group semiconductors, are considered as good candidates, but due to the lattice mismatch between III-V group and Si, and complex epi-layer fabrication, large wafer processing is difficult to achieve, although isolated local spot fabrication can be achieved [8]. Moreover, polycrystalline and doped Si are lossy in THz frequency range, and thus CMOS devices cannot be adopted for THz circuit applications. To our knowledge, no one has yet demonstrated a **low-loss** integrated THz circuits on large area substrates. This research will demonstrate approaches to tackle this challenge.

The goal of this research work is to transform the advances in nanomaterials, micro/nanofabrication, and high-frequency designs, to achieve integrated THz circuits for the next-generation THz systems by exploring novel integration approaches that can push the boundaries of high frequency circuits and interconnects. **In particular, the research objective is to investigate design, fabrication and packaging of novel THz passive and active devices that can potentially lead to highly integrated THz systems which can be used in sensing, imaging, security, spectroscopy and host of other applications,** as depicted in Figure 1.2. The key goal is to demonstrate novel THz device designs using low-cost, large area, low temperature fabrication approaches that allows the integration of THz circuits at the wafer level. Tasks can be divided into two categories: (I) passives and (II) actives. For passives, a novel THz waveguiding approach is developed that can be used in the design of integrated THz circuits at the wafer level. For actives, device fabrication approaches are demonstrated that allows THz device integration on a host of substrates using low temperature processes. Particularly, a GaAs nanowire based Schottky diode THz detector and embedded GaAs Schottky barrier diode THz detector are

studied and fabricated to demonstrate the possibility of achieving the proposed idea. These tasks will be explained in details which are subdivided into individual chapters.

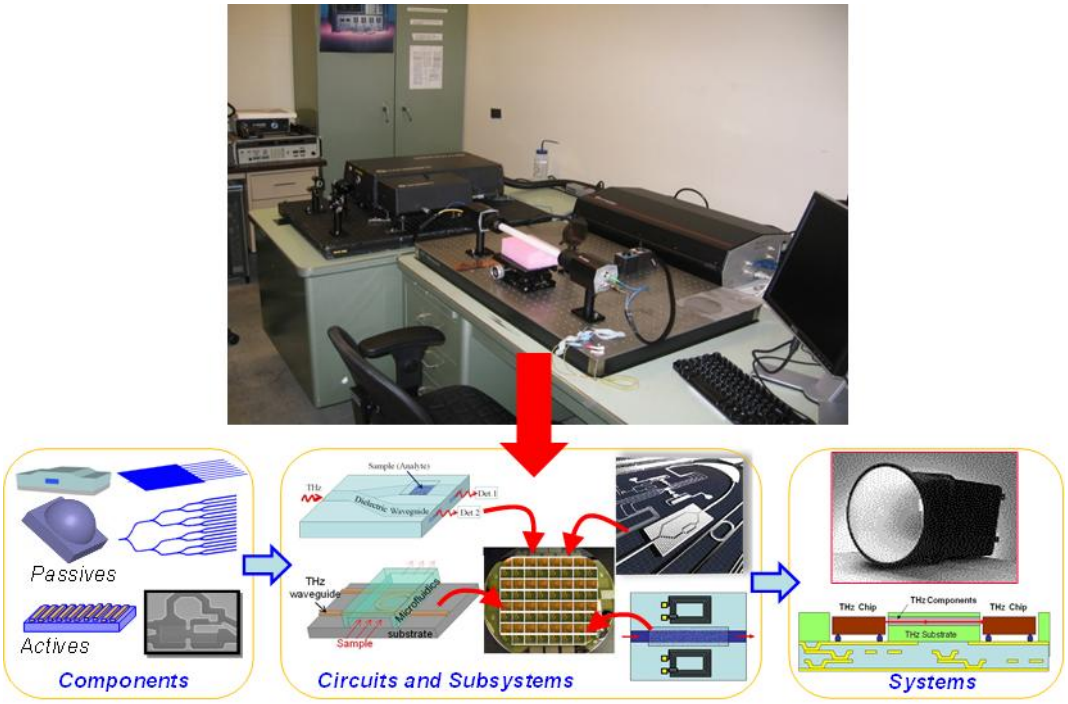

Figure 1.2 Research goal is to demonstrate fabrication of THz active and passive elements that can be integrated on a host of substrate, shrinking size from the upper sub-millimeter wave system to the lower integrated designs

Components for building THz circuits can be categorized into active and passive devices. THz source, detectors, mixers, amplifiers, multipliers and oscillators are the main active devices which exist in THz systems. Interconnects, waveguides, filters, couplers antennas and other peripheries are generally considered as passive components for THz systems. Both of these categories have received intensive research and have been made huge progress during the past two decades, and many new applications can be realized based on better and advanced THz equipment. Although progresses has been made to demonstrate minimized THz systems or circuits [9, 10], the integration level of each part of the active and passive devices is still low,

this issue keeps driving the systems miniaturization trend, and stimulates the development of novel materials with low cost and high fabrication compatibility. The following sections will first discuss different types of THz waveguides, and illustrate the benefits of proposed dielectric thin ribbon waveguide, and then different types of THz sources will be briefly discussed to demonstrate the trend and the demand of system miniaturization. The possibility of proposed embedded actives structure to be applied for THz sources will also be discussed.

1.2 THz Waveguides

In the research area of high frequency waveguides, especially for THz region, there are numerous waveguides which have been researched and developed for THz propagation, and they typically can be grouped into two categories: metallic waveguides and dielectric waveguides. Examples for each type will be discussed in detail.

1.2.1 Metallic Waveguides

Metals based waveguides and transmission lines such as striplines, microstrips and co-planar waveguides (CPW) are frequently applied for RF integrated circuits, and their conductor loss increases with respect to frequency due to the Ohmic loss. However, bare metal wire has been shown to have low attenuation ($0.03cm^{-1}$) and almost no dispersion of group velocity in THz region from 0.25THz to 0.75THz. [11] Moreover, the attenuation factor decreases as the frequency increases. This is because the surface area of the metal (0.9mm in diameter) wire interacting with the electromagnetic field is small, and most of the wave propagates in the air region. The wave guiding characteristic at bends, however, requires large curve radius to maintain low loss. Thus, it is not an effective way to achieve waveguides at integration level, though it has the simplest waveguide structure. The large group velocity dispersion at frequencies close to cutoff frequency needs to be eliminated otherwise the THz pulse width will

be stretched after propagating a large distance (tenth of centimeters). Also, the wire structures are difficult to fabricate at the wafer level. Thus, the use of wires to fabricate THz interconnects (waveguides) at the wafer level has many shortcomings.

Parallel plate waveguide is a good candidate that overcomes some of the above hurdles by carrying transverse electromagnetic (TEM) mode which has no cutoff frequency [12]. However, the attenuation factor is relatively high (~0.1cm^{-1}) above 1THz due to the higher conductor losses. Research presented in [13] later has shown some improvement by widening the separation distance between two plates from 0.5mm to 5mm and exciting TE_1 (Transverse Electric) mode in the waveguide. The cutoff frequency associated with TE_1 mode also decreases as separation is increased. However, the power confinement of the parallel plate waveguide at the bend of the waveguide becomes poor as there is no sidewall that can prevent the leakage of the wave from lateral opening sides.

Another design that is dispersion free and considerably low attenuation at THz is the metallic slit waveguide [14]. The structure has two thin metal strips (300μm x 2mm) parallel placed on the same plane with the separation of 270μm. Such structure propagates TEM mode with field along transverse direction with no cutoff frequency, and the result showed approximately 0.15cm^{-1} amplitude attenuation at 0.5 THz, which is only 3 to 5 times of the bare metal wire. However, although the power confinement is better than that of bare metal wire, (in [14] it shows the cross-section area covering 50% of the transmitted power is only approximately 2.6% in size compared to a Sommerfeld wire), the wave and power guiding at the curves still needs further improvement.

Metallic rectangular and circular hollow waveguides have been commonly used in the RF frequency spectrum for many years, and researchers have extended their operating frequency

into THz spectral region [15, 16]. However, the attenuation is large and more than one mode can be excited over broad spectrum if the dimension of the cross-section is not well engineered. Again, such structures are not compatible with on-wafer integration unlike their thin-film counterpart.

Another type of metallic waveguides that has recently drawn significant attention is the THz surface plasmonic waveguide. Metal surfaces are fabricated to be textured or corrugated, and this allows EM waves mimicking surface plasmonic (termed spoof plasmon) and propagating on the surface along the interface of corrugated metal surface and the contacting dielectric region [17]. Particularly, a stainless thin steel foil which has been etched to have periodic rectangular apertures has shown to be able to propagate broadband THz (0.2 to 0.8THz) [18]. Results also show that the propagation wave tightly bound to the perforate metal surface within 2mm, and with efficient coupling structure such as semi-circular groove, the transmission coefficient can reach close to 100% at certain frequencies. Moreover, a power divider and a coupler based on periodic metal aperture structure have been shown as well, and they showed quite promising results, but the etching and machining process increase the complex of fabricating such waveguides. In order to simplify the process, the same group used 3D printing method to create the substrate mode of the waveguide and sputtered metal layer on top of the base [19]. The 3D printed mode base has the perforate periodic structure which is same as that etched on the stainless metal foil. After calculating the skin depth of the plasmonic wave, 500nm Au which is larger than twice of the skin depths has been sputtered on the patterned polymer substrate. Y-splitter has been demonstrated with good power dividing results. However, the attenuation is about 0.17cm^{-1}, which is larger than that of stainless steel foil, this is due to the rough metal surface deposit using sputtering. This 3D printing method can be considered as one possible way

to be utilized as the waveguides for THz integrated circuits, but the power confinement at the bend and curve is not strong enough, and due to the existence of metal, the loss factor cannot be reduced to acceptable level for higher frequencies. Highly doped silicon can be also used as an alternative material to metal for fabricating the surface plasmonic waveguide using Reactive-Ion Etching (RIE) process [20]. This method can be considered as another possible solution to manufacture interconnects for high frequency ICs. However, due to the nature of the surface plasmonic, most of the wave is confined at the surface and large portion will be radiated out at sharp bends. Furthermore, the operational bandwidth of the waveguide is significantly narrow, and significant research work is required to overcome these challenges. This area of research is currently in its preliminary stage and holds significant potential in achieving efficient coupling of EM to active or sub-wavelength devices.

1.2.2 Dielectric Waveguides

Dielectric waveguides such as optical fibers are always applied for higher frequency and optical systems built for infrared and laser transmission. Metal waveguides are not suitable for these applications due to the large conductor loss at such high frequency. Optical fibers with ultra-small diameter have been used to transmit single-mode wave with low power while thicker fiber are used to carry large power but with multiple modes.. Different types of dielectric waveguides such as solid and hollow circular or rectangular dielectric waveguides [21, 22 23], have been developed and studied in detail, and novel modified structures based on these waveguides for THz transmission applications have also been investigated.

Sub-wavelength plastic fibers have been utilized to propagate THz waves with low attenuation factor [24]. A 200μm diameter solid Polyethylene (PE) wire has been successfully demonstrated to transmit 0.3THz with attenuation loss in the order of $0.01cm^{-1}$. The plastic fiber

polyethylene (PE) is lossy at higher frequencies because of the large wavelength-to-fiber-core ratio. The power confined and delivered inside the lossy core is reduced, the PE fiber only performs as guiding medium, and thus most of the wave propagates in the surrounding lossless air. Also, due to the direct coupling capability, it has the potential to be applied to current THz systems to further reduce the cost. However, its compatibility with on-wafer integration is not promising due to their circular geometry, which requires complex fabrication and having larger radiation loss at sharp bends.

A similar structure to plastic fiber is the circular hollow pipe dielectric waveguide with low index thin dielectric cladding [25, 26]. This structure is a modification of cylinder hollow dielectric waveguide with infinite cladding and the idea of hollow glass fiber for infrared transmission [27]. Since the absence of the metal film, the cladding is transparent to the resonance frequencies, and it can also leak wave at non-resonance frequency out of the waveguide. The attenuation loss is thus mainly due to the leakage of the wave. Experimental results show that the attenuation is between $0.01cm^{-1}$ and $0.02cm^{-1}$ form 0.4THz to 0.55THz. Such physical structure is easy to access since simple Teflon tube with thin wall is commercially available and inexpensive. However, it is not compatible with wafer level integration. Moreover, the frequency discontinuity due to the periodic resonance behavior limits its operational bandwidth. Although the band spectrum between two resonance frequencies can be enlarged by thinning the cladding region, this will require extra physical molding and modification, which in turn increases the design complexity.

Solid rectangular dielectric waveguides, such as dielectric thin ribbon waveguide and slab waveguide, have been investigated and presented for transmitting RF signal between 26-40GHz with low loss [28]. High frequency electromagnetic wave propagation using such dielectric

waveguide has been studied and demonstrated in [29], where THz waves are coupled into and out of a thin High Density Polyethylene (HDPE) plastic ribbon (2cm wide, 120μm and 150μm thick) by a pair of half cylinders lens. The HDPE ribbon is able to transmit dominant TM_0 mode with low attenuation factor and controllable group velocity dispersion in 0.1 to 3.5THz. Similar to the plastic fiber waveguide, the wave is mostly (~90%) propagating within the surrounding air out of the thin ribbon if the frequency is in the low THz region (below 0.5THz). However, because of this large portion of power outside the thin ribbon, sharp turns will cause most of this power to radiate out and thus increase transmission loss. At frequency higher than 1THz, the attenuation becomes high, since more power has been confined into the plastic ribbon which is lossier at higher frequency than air medium. One method to improve this is by using high-*k* material instead of low-*k* material as the thin ribbon guiding structure, such as using high resistivity Si and alumina with dielectric constant of 9.6 and 11, respectively. Simulations have shown that with increase in dielectric constant values, the power confinement becomes closer to the core region, and the radiation at the curve can be reduced greatly. Figure 1.3 shows the attenuation values for different types of waveguides. It is clear that dielectric ribbon (silicon ribbon) has the lowest attenuation compared to other waveguide types [30]. Moreover, adding low k material as the cladding on both sides of the thin ribbon can confine more power into the cladding layers from the air and increase the ability of guidance of the high-*k* core [31]. Comparing the physical geometry of such thin ribbon waveguide to the existing RF integrated circuits, one will notice that such planar structure is similar to those metallic micro-fabricated transmission lines (co-planar waveguide and microstrip), and it can support single-mode wideband transmission. Furthermore, the geometric loss factor of a ribbon waveguide is unsusceptible to small changes in cross-sectional area, especially for the dominant mode [30],

which indicates the thickness of the thin ribbon can be tuned to satisfy fabrication thickness criteria of other devices. From this point of view, it shows higher compatibility with conventional fabrication than other waveguides for THz circuits applications.

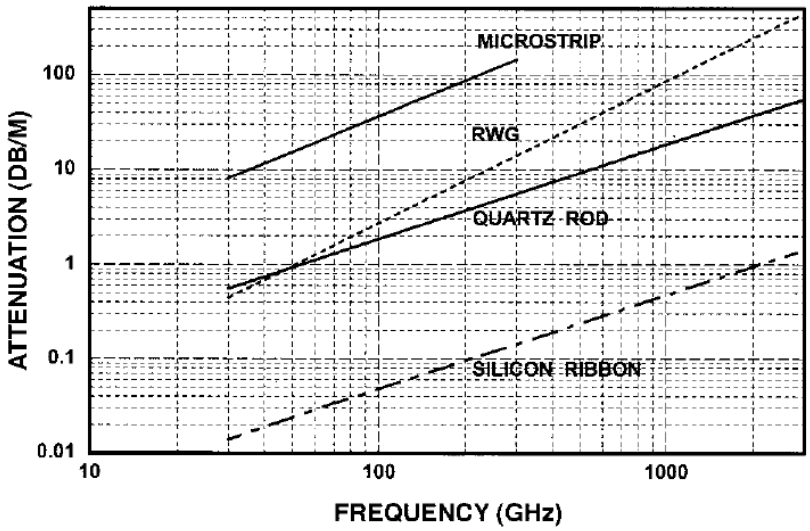

Figure 1.3 Attenuation constants of several types of conventional waveguides and silicon dielectric ribbon waveguide [30].

Those metallic and dielectric waveguides mentioned above show good mode confinement, low-loss and low-dispersion characteristics in the sub-millimeter regime. However, as demonstrated in details of each waveguides, some of these designs require delicate micro-machining of bulk materials such as metal and polymers with special equipment, and thus the fabricated waveguide structures are still incompatible with integrated circuits. Again, compatibility with wafer-level integration, such as a planar film or strip, is one of the primary interest, and this work will systematically investigate from material and fabrication point of view on how to utilize thin ribbon dielectric waveguides, which is the most compatible structure to integrate circuits, for developing micro fabrication compatible waveguides for THz circuits.

Thin dielectric ribbon waveguide can provide strong confinement and low loss to propagate THz waves, especially at waveguide bends. In the next chapter, analytical calculations for the

thin dielectric ribbon waveguide, including the basic wave functions and cutoff frequency for each propagating mode will be derived. Simulations of the thin ribbon waveguides will be carried out as well to further study the power confinement (E field pattern) characteristics. Furthermore, from the experimental point of view, material characteristics such as dielectric constant and loss tangent will be studied, and fabrication process of the waveguide will be proposed as well. It will provide a clear understanding that the thin dielectric ribbon waveguide can be a promising candidate interconnects to achieve integrated THz circuits.

1.3 THz Sources

Sources which are able to efficiently generate enough power with tunable frequency are needed in the THz spectrum. Figure 1.4 shows the applicable frequency and output power generated by different THz sources [4].

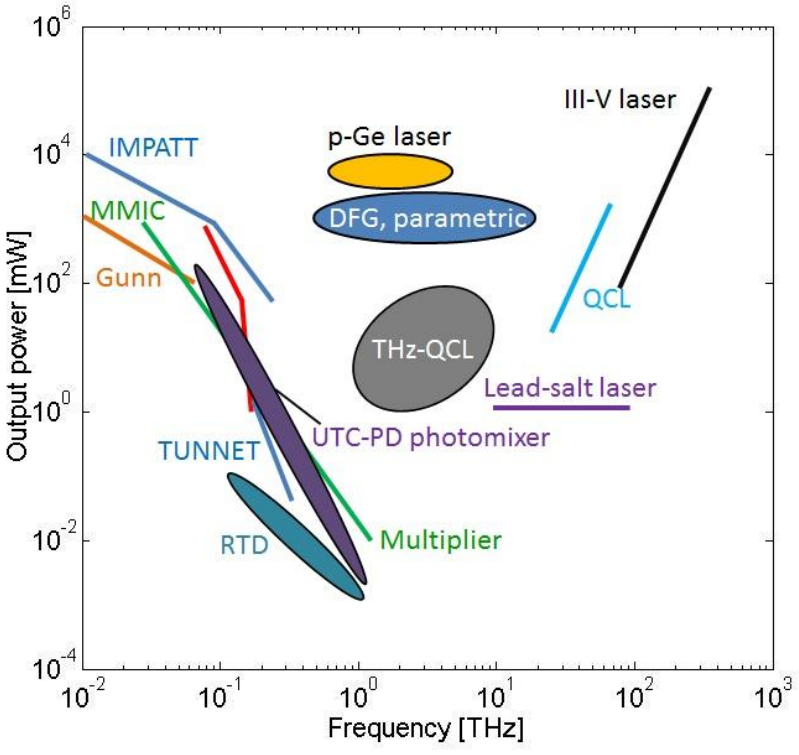

Figure 1.4 Applicable frequency and output power generated by different THz sources [4].

Conventional THz sources developed in the mid of last century based on free electron laser, such as Backward Wave Oscillators (BWO), can meet the need of such requirement. High power (1-100mW) can be generated within the frequency from 30GHz to 1.2THz [32]. However, the table-top based BWOs having electron acceleration tube and magnetic undulator restrains the capability of device shrinking and wafer level integration. Furthermore, large power supply units are required to provide high bias voltages to generate electrons and these are also difficult to integrate on a wafer.

Another common THz source is based on laser driven THz emitters. Short pulse femtosecond laser (usually Ti: Sapphire laser) illuminates on semiconductor based photoconductor, such as GaAs, to generate electron-hole pairs. The generated carriers are coupled to a broadband antenna, which then emits THz waves [33]. The power generated by such method is relatively low (hundreds of nanowatts or several microwatts), and the frequency ranges from 100GHz to 2THz. Such THz sources are typically installed in a quasi-optical based THz Time Domain System (THz-TDS); however, it is still a bench-top setup, and it is difficult to miniaturize to integrated circuit level.

There are also several other techniques which down convert the optical frequency into the THz gap, such as CO_2 laser mixing and CH_3OH optical pumped laser, are also developed [32]. Continuous wave (CW) between 0.3 to 5THz can be generated and the power can reach several tens of mW for CH_3OH optical pumped source. However, neither of these would be feasible for transforming from bulk systems to chip-scale devices due to the physical size limitations of the optical components. Apart from optical down conversion, efforts are also made in designing THz sources from solid state devices (similar to a laser diode). One example of THz source designed from electrical point of view, which has recently received intense interest, is the Quantum

Cascade Laser (QCL). Voltage is applied across the superlattice heterostrucutre active region (InGaAs/InAlAs), electrons are then injected into the structure and follow intersubband transitions, THz photons are excited and emitted when electrons tunnel through the quantum wells. The first QCL demonstrated can generate CW at 4.4 THz with average power of 2mW, and other groups can generate 50mW power, but cryogenic cooling around 100K or lower is required [34, 35]. Lots of efforts have been put to increase the operating temperature of these solid state semiconductor laser devices, and recently 3.6THz CW with output power up to 3μW operating at room temperature has been achieved. Beyond this progress, the whole system (including the waveguides) is in compact form based on micro-fabrication [36]. An example is shown in [37] where researchers have developed and fabricated THz monolithic solid state transceivers at the chip level. These huge break through creates the possibility of realizing THz integrated circuits. However, the drawbacks are also obvious: room temperature operation is still an obstacle to high power output, and such micro or nano device fabrication requires specific semiconductor material, such as InGaAs, InAlAs and GaAs, to epitaxial grow on InP substrate to form heterogeneous structure. Most importantly, large area and low cost fabrication are still missing from those designs, and a large considerable area of the substrate is wasted for periphery structures, which are not necessarily to be fabricated on costly III-V substrates.

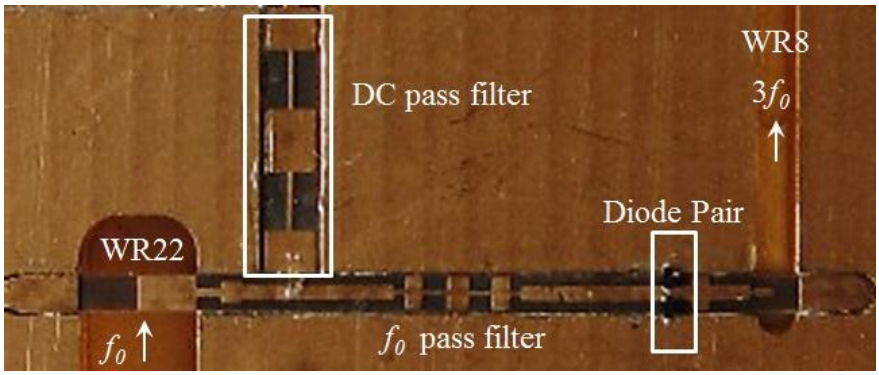

Figure 1.5 Schottky diode based frequency tripler for 114-135GHz [39] © [2010] IEEE

For THz sources operating at a lower frequency ranging from 100GHz to 400GHz, solid state sources from electronics point of view are commonly used. Multiplier chains and oscillators based on nonlinear semiconductor devices such as Schottky, Gunn, IMPATT and tunneling diodes are fabricated and assembled on microstrip line inside metallic waveguides [38, 39], as shown in Figure 1.5. Actually, diode based multiplier chains and oscillators for THz signal generation have become widely used. They are able to operate at room temperature, and the fabrication of isolated planar diodes is much more mature in comparison to semiconductor QCL sources. The output power efficiency of multiplier chain decreases as the number of stages increases. This is due to the intrinsic characteristics of the diodes in the chain. GaAs based Schottky diode are the most widely used because of the maturity of the fabrication. Research and study have shown that roughly 0.1 to 1mW power is achievable around 400GHz [32], and 1.5THz with output power around 1μW can be realized based on cascaded planar frequency doublers [40]. The development of low cost fabrication for planar Schottky diode flip-chip allows affordable frequency multiplier THz sources below 500GHz with considerable power output. In most case, microwave cavity and metallic hollow waveguides host as the mounting housing for the flip-chip diode multiplier chain due to the low loss characteristics of hollow metallic waveguide. Compared to a BWO and quasi-optical system, this compact form of source has received high attention and been well commercialized at a relatively affordable price. Clearly, applying metallic hollow waveguides to wafer level integration requires complex micromachining fabrication techniques and solutions of related material compatibility issue. Thus, to integrate the multiplier chain as well as the solid state mixer or oscillator on wafer level, novel and alternative methods need to be developed and demonstrated, and the proposed embedded active process is one of the qualified candidates.

1.4 Introduction of Embedded Actives

As discussed, it is desired that fabrication approaches allow seamless integration of different semiconductor technologies on a common substrate at low process temperatures, and have high compatibility with large-area manufacturing. An embedded active process is an attractive approach to meet this challenge. The embedded integration of electronic components for commercial CMOS integrated circuits designs have been widely studied [41 - 43]. Major benefits include reducing the manufacturing cost, decreasing the form factor for multilayer and 3D integration, increasing the packaging reliability and maintaining the electrical performances.

Embedded integration packaging technology can also offer advantages for high frequency circuits. The short interconnects enhance the electrical performances, and the homogeneous material surrounding the devices provides a uniform electrical and mechanical environment thus improving the system reliability [43]. Several monolithic microwave integrated circuits designs (MMIC) and chips such as a 77GHz SiGe Mixer [44], and high frequency power amplifier ICs [45], have been reported using embedded packaging techniques to achieve excellent performance. Also, embedded actives can be utilized in the design of novel 3D circuit structures through stacking of active devices or chips.

The aim of this research is to push the boundary of embedded actives applications into the THz frequency regime, to demonstrate integration of multiple active devices on a common substrate, and to study a host of high frequency circuits that can be designed using embedded active process. Processing at low temperatures (below 120 ℃) is preferred as this allows the use of host of low-temperature substrates, including polymer with low glass transition temperature (T_g). Key challenge to design high frequency circuits using embedded actives is to maintain the low parasitics associated with the device close to their original value at low frequency range.

One of the key elements that significantly affect the device performance is the post processed via connecting the peripheral circuits to the pads of the embedded devices, and these should be optimally designed to keep minimum disturbance to the high frequency performances. Here the process is optimized to be able to design high frequency circuits such as detector, multiplier and mixer; however, as discussed in the previous section, it also can be widely applied to other active devices. In Chapter 4, particularly, discussion will first start from the selection of the active devices to be utilized as embedded cores, and then demonstrate a THz imager circuit with imaging results.

Based on the demand of large area and low cost integrating of QCL THz sources at circuit level as well, the novel fabrication process for embedded diode THz detector developed in this research can also be one good candidate technique for QCL THz sources. It does not require bulky metallic waveguide as the housing; instead, planar but low loss material substrate serves as the supporting structure, which also allows multi-layer stacking of other different function circuits. In addition, the whole process is low temperature compatible, which opens the window of introducing other low loss plastic substrates for specific applications. It has the potential to realize low cost, large area, wafer level integration for both QCL and diode based multiplier chains.

Furthermore, this new fabrication process has the capability to integrate most of active THz devices at circuit level and enables desired functions as well. Figure 1.6 shows an example of waveguide based circuits that can potentially applying embedded active process to minimize the device physical size [10]. A 670GHz LNA front-end receivers is fabricated based on InP HEMT transistors. The lower two figures in Figure 1.6, illustrate the fabricated InP HEMT transistors forming tripler and mixer and coupling to CPW fabricated on the same substrate, and mounted in

the metallic waveguide. If using the proposed process, micromachining of bulky metallic waveguides can be avoided and all of these monolithic chips can be embedded into the dielectric layers, then connected by periphery impedance matched passive circuits (CPW for example) patterned on the top surface of the dielectric layer. The transition design of waveguide to CPW can be also eliminated, and through dielectric via is capable to transmit the signal with low parasitics. Even further, the whole InP substrate is only used to fabricate HEMT transistors and necessary pads, the on chip CPW as well as the matching network can be combined with other passives on the dielectric surface, and connect down to the pad through via. This could great reduce the expensive epitaxial substrate area that had passive CPW on top, which does not necessarily require active epi layer as the substrate. A Schematic cross section view of the proposed modified circuit using embedded active process is shown in Figure 1.7, it can largely reduce the fabrication complexity and realize planar wafer level integration.

Material characterization, structure geometry modification and circuit optimization are necessary steps while performing heterogeneously embedding different active devices. Once the design is finished, those pre-fabricated and chip-scale devices can be readily embedded into cavities opened in low loss dielectric layers, and connected to periphery passives through via to minimize the parasitics and reduce loss during high frequency operation.

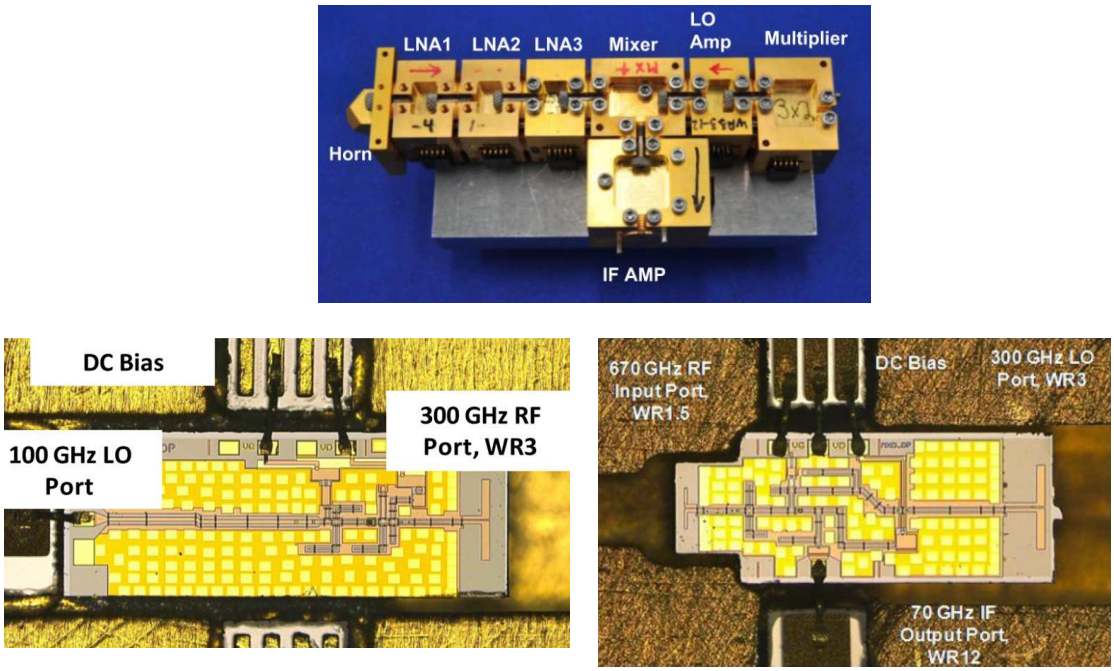

Figure 1.6 670GHz monolithic receiver with all function realized in InP HEMT (top), InP HEMT based frequency tripler chip mounted in waveguide (lower left) and InP HEMT based down converting mixer in waveguide fixure (lower right) as example components of the receiver. [10] © [2011] IEEE

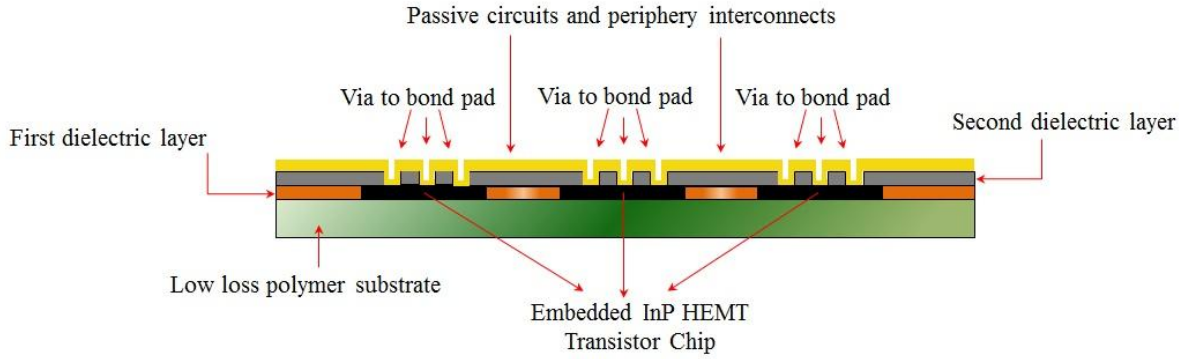

Figure 1.7 Schematic cross section view of the proposed modified circuit using embedded active process.

1.5 THz Detectors

Active devices are the core elements required in RF integrated circuits. Bringing them into THz region, the requirements for these devices to function properly are more critical, since low loss materials with high electron mobility are needed to fabricate nonlinear devices. THz detector, for example, is one of the hotspots that researchers are focusing on since majority of THz applications is based on sensing and imaging techniques. The THz waves are easy to attenuate while travelling in air and can be also easily scattered by the ambient molecules which limits its long distance propagation. Thus, high sensitivity THz detectors are under development in order to meet the need in scientific research, communications as well as public security. One of the key requirements of detectors is high sensitivity, in other words, low **Noise Equivalent Power (NEP)** values are desired. THz detectors can be divided into two types: heterodyne or indirect detector and direct detector, and the detection mechanisms are different [46], which are shown as simple schematic diagram in Figure 1.8. It can be seen that for heterodyne detector, signal W_S and background signal W_B are coupled with LO signal W_O by a diplexer, and the mixer down converts high frequency and generates the signal at the intermediate frequency to be detected using a low frequency detector element (or circuit). Here, the nonlinear mixer is the core element of the detector, and varieties of nonlinear devices can be applied here, such as superconductor-insulator-superconductor (SIS) tunnel junctions, semiconductor and super-conducting HEBs, forward biased Schottky diodes and Superlattices. The heterodyne detector can detect both amplitude and phase of the incident signal and the background noise can be override easily due to the existence of high frequency LO having high power output. However, the drawback is also obvious, high power LO sources at high frequency are not easily acquired. It requires complex techniques, and signal and the LO beam size, radius of curvature, transverse spatial mode and

polarization should match; or the detector performance would be degraded. Moreover, more substrate area will be occupied by LO devices, which increase the complexity of the imaging array, and large format detecting systems are difficult to be fabricated.

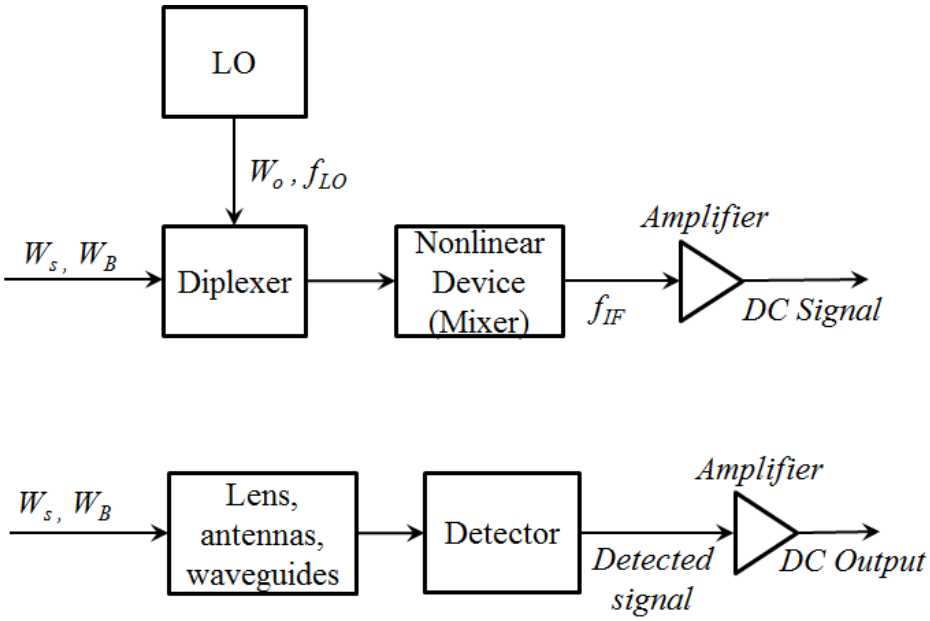

Figure 1.8 Heterodyne THz detector(upper one) and direct THz detector.(lower one).

Direct detectors do not require mixer to down convert the frequency, instead, according to the schematic, signal W_S and background signal W_B are collected and focused into the detector elements using optical lens, waveguides, or antennas, and an electrical signal is generated by the detector and amplified by the amplifier. A varied range of devices can be used as detector elements, such as Golay cells, pyroelectric detectors, field effect transistor detectors, Schottky barrier diode detectors and micro & nano bolometers. Direct detector can only sense the frequency and amplitude information of the signal, but it has advantages over heterodyne detectors. Cyro temperature bolometer can provide the lowest NEP. Also, Schottky barrier diode based THz imager can operate at room temperature, and large format THz detector arrays are simpler to fabricate. The overall power consumption is low since LO signal is not required. This

led to the Schottky diode based THz detector become one of the most popular direct detectors, and part of this research work focus on this topic. Before discussing this detector into detail, direct detectors are briefly reviewed in the following section:

1.5.1 Photoconductive THz detector

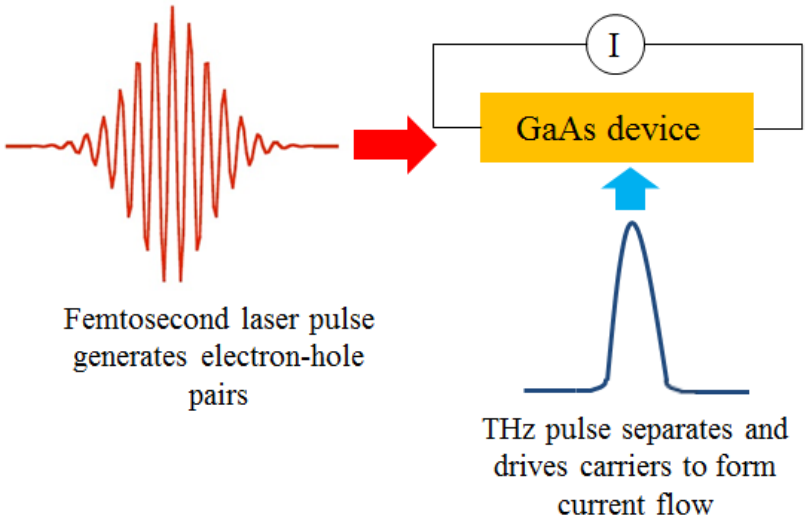

Figure 1.9 Schematic of photoconductive THz detector

As shown in Figure 1.9, a photoconductive based THz detector is the most frequently used detector in THz time domain spectroscopy [47]. There are three key steps that associated with the functioning of this detector. First a short near field infrared laser pulse directly incidence on the low temperature grown GaAs based semiconductor device. Then due to the excitation, electrons and holes pairs are created in the conduction and valence bands. Finally, the THz pulse then is illuminated on the GaAs surface, separating the charge carriers, creating the current signal whose value is proportional the power of the THz pulse. Basically, this method is the reverse way of generating THz pulse basing on the coherent THz generation. The time domain signal $I(\tau)$ can be defined by Equation 1.1[48]. $E(t)$ is the electric field of the THz pulse, $D(t)$ is the detector response, τ is the delay time.

$$I(\tau) = \frac{1}{T}\int_0^T E(t)D(t-\tau)dt \tag{1.1}$$

Although its principles are easy to understand and operate, the setup of the whole system requires relatively large space due the existence of the laser generation system as well as optical components mounting and aligning, which means large area and low cost fabrication at wafer level is impossible based on current fabrication process.

1.5.2 Thermal THz detectors

The thermal THz detector family consist a numbers of different detectors, including: bolometer, pyroelectric detector [49] and Golay cell. The basic concept of THz detecting is by changing their resistance (bolometer) or bias voltage (pyroelectric detector) due to the absorption of incidence energy which is then converted to heat. For example, a thin-film pyroelectric detector, based on ferroelectric materials such as Triglycine Sulfate (TGS) and Lithium Tantalate, exhibits large electric polarization in the active crystal respected to the changing of temperature. It generates transient bias across high impedance crystal when THz waves impinges upon the detector and increases the temperature. The changed voltage signal can be picked up by a FET and converted into digital signal. The sensitivity of such devices could vary according to the temperature of operation. In most of the cases, pyroelectric detectors are operated near 4K in order to provide lower NEP, which can be around 0.1pW/Hz$^{0.5}$. Even lower NEP ~ 10^{-13}W/Hz$^{0.5}$ can be achieved by continuing lowering the temperature to hundreds of mK. However, at room temperature it only shows low sensitivity with NEP ~ 10^{-9}W/Hz$^{0.5}$ [50]. What's more, most of these devices also require high quality materials which are expensive, thus the cost is another limitation for large area THz imaging for commercial market.

Like pyroelectric THz detectors, bolometers also respond to the change in temperature of the film due to absorption of THz radiation. The only difference is that these detectors show changes

of resistance instead of generating transient voltage due to absorption of THz radiation. The basic setup of the bolometer is explained in [50], and a simple bolometer is shown in Figure 1.10. The constant time can be calculated by

$$\tau = \frac{C}{G} \tag{1.2}$$

Where C is the heat capacity of the material, G is the thermal conductance from the material to the heat sink. The temperature difference between the absence and existence of THz can be derived from equation 1.3, where ΔP is the power delivered by the incident THz wave.

$$\Delta T = \frac{\Delta P}{G\sqrt{1+\omega^2 (C/G)^2}} \tag{1.3}$$

Equation 1.3 clearly shows that in order to obtain large temperature difference and shorter constant time, materials with small heat capacity and large thermal conductance are required. But there is a trade-off between sensitivity and response time for uncooled bolometer. In Ref. [43], for a 20ms constant time bolometer, the NEP of approximately 10^{-13}W/Hz$^{0.5}$ is achieved, while for lower NEP of 10^{-19}W/Hz$^{0.5}$, the response time increases to around 3.5×10^{4}s. For a cooled bolometer, both the response time and sensitivity can be tuned to a certain low value. However, the low temperature operation limits its applications for high sensitivity detection in environment other than that with low temperature.

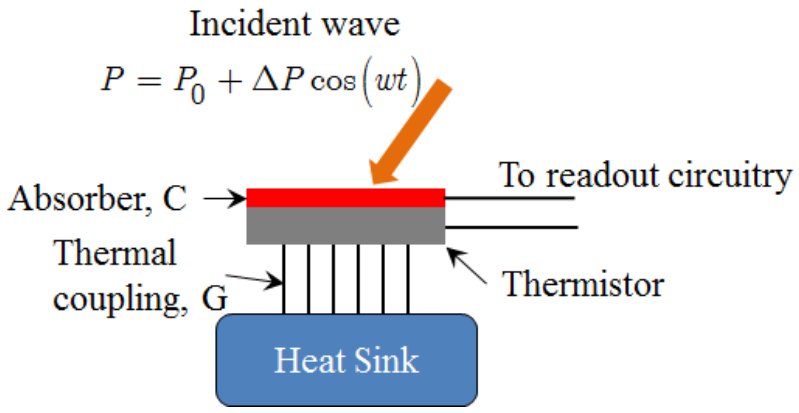

Figure 1.10 Schematic of a simple bolometer

1.5.3 Schottky Barrier Diode THz detector

The Schottky barrier diodes are one of the basic devices in THz technologies. As discussed several times earlier, they are not only used in detection and imaging, but also in some other devices/circuits such as amplifier, multiplier, mixer, due to their strong nonlinear property. The detection capability is also depend on its nonlinear I-V characteristics and the rectification behavior, and the detection principles can be explained using the equations below:

The Schottky diode I-V characteristic equation is written /given as:

$$I = I_s(\exp(\frac{V}{n\phi_t}) - 1) \tag{1.4}$$

Where I_s is the saturation current, V is the applied bias voltage, n is the ideality factor, and ϕ_t is constant which equals to kT/q, in which k is the Boltzmann constant, T is the temperature, and q is the electron charge. Suppose a small RF signal is incident on the antenna and coupled into the Schottky diode, the small signal change in voltage can be defined as:

$$dV = V_{RF} \cos \omega t \tag{1.5}$$

plug this in to Equation (2.4), and apply Taylor Expansion only to the second order:

$$
\begin{aligned}
I &= I(V_{BIAS} + dV) \\
I &= I_{BIAS} + \frac{\partial I}{\partial V}|_{V_{BIAS}}\ \partial V + \frac{1}{2}\frac{\partial^2 I}{\partial V^2}|_{V_{BIAS}}\ (\partial V)^2 + ... \\
&= I_{BIAS} + G_{RF} \cdot V_{RF}\cos\omega t + \frac{1}{2}\frac{G_{RF}}{n\phi_t}\cdot V^2{}_{RF}\cos^2(wt) \qquad (1.6) \\
&= I_{BIAS} + G_{RF} \cdot V_{RF}\cos\omega t + \frac{1}{2}\frac{G_{RF}}{n\phi_t}\cdot V^2{}_{RF}\left(\frac{1+\cos(2wt)}{2}\right) \\
V &= V_{BIAS} + V_{RF}\cos\omega t + \frac{1}{4}\frac{V_{RF}{}^2}{n\phi_t}\cos(2wt) + \frac{1}{4}\frac{V_{RF}{}^2}{n\phi_t}
\end{aligned}
$$

where the conductance of the small signal at the bias point can be represented as:

$$G_{RF} = \frac{\partial I}{\partial V}|_{V_{BIAS}} = \frac{I_{BIAS} + I_S}{n\phi_t} \qquad (1.7)$$

In Equation (1.6), besides the bias voltage V_{BIAS}, there is another DC offset voltage $\frac{1}{4}\frac{V_{RF}{}^2}{n\phi_t}$ which has been carried out, and this is the signal that the detector generates as the output rectified voltage. Finally, the incoming RF signal is rectified and this signal is readout as a DC signal. The higher the sensitivity, the higher the rectified DC output signal. Detailed calculations for the Schottky diode sensitivity will be presented in related chapter. III-V group semiconductor materials are commonly used for planar Schottky diode detectors, especially GaAs. This is because there is a satisfying balance between carrier mobility and the bandgap, which are two major criteria during the study of rectification mechanism. Moreover, GaAs has lower loss than other materials in THz region. Other III-V materials are also being studied and they also show positive results for THz applications. Schottky diodes built using Si for CMOS technology THz detector has also been published. However, the low cut-off frequencies due to the low electron mobility nature of Si comparing to GaAs, and the high loss tangent of doped Si substrate, limit

the widening of application of Si based detector, thus Si not recommended as material for detection up to THz region.

1.5.4 Novel THz detectors

Recently, novel materials like Carbon Nanotubes (CNTs) have drawn attention in many research areas, including in the development of the THz detectors. Researchers have already shown metallic CNTs between antennas performing as a bolometer device, but it still requires low operating temperature for higher sensitivity. What's more, semiconducting CNTs have also been applied for Schottky diode THz Detectors contacting with source and drain metals. The simulation results in [51] show that for 2.5THz, the NEP can reach 0.7pW/Hz$^{0.5}$ at room temperature. However, most of these devices are still based on single pixel detector due to non-uniform geometry of CNTs, which results in the large variations in electronic properties, and thus not suitable for large area array. To overcome this problem, larger diameter (50~100nm) semiconductor nanowire can be a promising replacement of CNTs since the electronic properties, such as work function, do not change respected to the varying of nanowire diameters.

Most of the semiconductor nanowires are, in general, synthesized using Vapor-Liquid-Solid (VLS) process, which requires metal nanoparticles as the catalysts [52, 53]. Gas phase semiconductor material is introduced to the heated metal catalyst (Au for example) surface, resulting in a droplet of metal/semiconductor alloy. The liquid semiconductor/metal catalyst helps to absorb semiconductor precursor and the formation of solid nanowire with aligned lattice. The diameter of the nanowire is determined by the initial size of the metal catalyst. The gas phase semiconductor of group IV can be produced by Chemical Vapor Deposition (CVD) and Molecular Beam Epitaxy (MBE), for compound III-V semiconductor, Metal-Organic CVD (MOCVD) and Laser-assisted Catalyst Growth (LCG) are applied [54]. Recently, Metal-Assist

Chemical Etching (MACE) method has been developed to synthesize high aspect ratio GaAs nanowires [55]. A very thin Au film is deposited on the epi-grown GaAs layer on Si substrate and patterned structures with nanoscale opening. Etchants including $KMnO_4$ and HF are applied to the patterned surface and etch GaAs away in the opened (or exposed) areas. By controlling the lateral etching profile, high aspect ratio GaAs can be formed under the Au region; but the diameters of the nanowires are relatively large compared to CVD based fabrication. Currently, most of the semiconductor nanowires are still synthesized using CVD-LVS method, which is well developed to control the nanowire geometry and has high production yield. In most case, semiconductor nanowires are delivered with suspension in Isopropanol (IPA), and are aligned on a desired substrate using Dielectrophoresis (DEP) force method. Because of this, CVD-VLS grown GaAs semiconductor nanowires have been commercialized for assisting nanoscale research and developing varieties of nanowire based applications [56].

Recently, InAs nanowire transistor based single pixel THz detector has been successfully fabricated and tested [57]. InAs nanowires were first synthesized on the substrate, and electrodes were then patterned on both sides of the preferred nanowire. The fabrication process is only adaptable to isolated nanowires, large area manufacturing is difficult to achieve. Also, the sensitivity is low due to weak nonlinear behavior of the transistor. These can be resolved by using nanowire based Schottky diode, where nanowires are “post-aligned” between electrodes, which results in stronger nonlinear property and lower noise. Details of the GaAs nanowire Schottky diode detector will be discussed later in Chapter 3.

Apart from semiconductor materials point of view, detectors are required to operate at THz frequencies with low parasitics (high cut-off frequency). This requires that devices have small effective area ($< 1\,\mu m \times 1\,\mu m$). Furthermore, for more practical applications such as THz imaging

and sensing, a large array (100×100 elements) of detectors coupled with antenna elements is required. In most cases, a significant area is occupied by the antenna element on the wafer, which is not being used to fabricate active devices. If using the conventional III-V semiconductor technology, the cost will be extremely high if the whole substrate is based on GaAs. Applying nanowires locally at multiple locations simultaneously on a large area low loss substrate will allow in the fabrication of large area circuits while keeping the cost low. Thus, it is highly desirable to develop a process that is large area compatible while meeting the needs for THz operation. Thus, new devices with high quality materials and compatible fabrication process are necessary, and this is not just for THz detector, it is required for most of the active devices for the building up of THz circuits.

1.6 Terahertz Integrated Circuit Examples

Previous sections discussed key THz passive components (waveguides) and active devices (sources and detectors), and potential approaches to improve these components and devices. Here, the discussion focuses on complex circuits that require integration of passive and active elements on a single wafer. Refs [58-61] can be considered as some typical examples of existing bulky circuits and devices which require such improvements. Those THz circuits include at least one of those devices, such as mixers, multipliers, amplifiers, phase shifters, oscillators, etc.

As highlighted earlier in Figure 1.2, the intent of this research is to bring together novel processes that allow design and fabrication of complex THz circuits in integrated form. As discussed earlier, there has already been ongoing research towards advancing CMOS devices for THz circuit applications. If successful, it would lead to low-cost large area THz integrated circuits. However, one of the key challenges to adopting CMOS for THz integrated circuits is substrate loss. CMOS is generally fabricated on low-resistivity silicon which leads to high

propagation losses in transmission lines fabricated on such a wafer. To date, brass based metal waveguide circuits have been useful in the design of THz circuits.

To discuss the potential of proposed process in the fabrication of THz integrated circuits, the example shown in Figure 1.5 is presented again (Reproduced in Figure 1.11, for convenience). This is a simple frequency multiplier circuit which is manually assembled. It made from brass based metal slab micromachined to achieve desired passive structures and assembly of active devices.

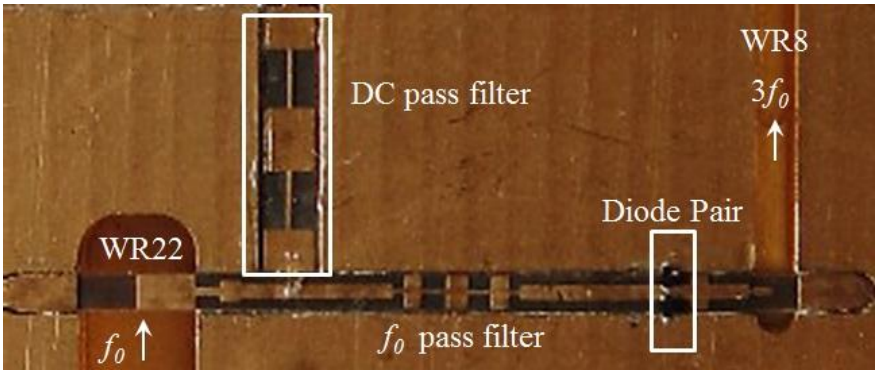

Figure 1.11 Schottky diode based frequency tripler for 114-135GHz [39] © [2010] IEEE

Frequency multiplier chain is one of the simplest and widely used approaches to achieve THz sources. Here, the frequency generated using a low frequency synthesizer (10 – 20 GHz) is multiplied to achieved output frequency reaching 1 THz. The goal of circuit in Figure 1.11, as an example design, is to realize a frequency multiplication (3X) to achieve frequency output in the range of 114-135GHz. Higher frequency is generated by cascading multiple circuits and using amplifiers in between to overcome losses. As shown in Figure 1.11, here top half the circuit block (metallic cavity) is removed, the circuit is composed of complex waveguide structures, filters banks, active devices elements, bias lines, diode elements, input and output couplers. Conventional assembly and fabrication processes are applied: micro-machined rectangular metallic waveguide is used for propagating the EM signal to the prefabricated microstrip line.

The microstip line having certain functional structures (filter, matching stubs, and bias line) is mounted and suspended in the micro-milled cavity. Nonlinear devices: Schottky diodes (DBES105a from UMS), are then glued with one pad on the microstrip line and the other to the metallic housing cavity as the ground point. Waveguide transitions are also designed in order to efficiently couple the EM signal from metallic waveguide to the microstrip line. Low pass filter and high pass filter are designed on the microstrip to suppress the unwanted frequency at the front and back end of the circuit. DC line is designed with RF choke to provide bias voltage to the diode. Input frequency f_0 goes into the WR22 waveguide, and $3f_0$ is generated and delivered out from WR8 waveguide. Measured results showed acceptable efficiency as well as low conversion loss. This 3D metallic structure is difficult to integrate at the wafer level, the micro-machining as well as milling of the metallic waveguide prevent it conducting a simple large area fabrication, the suspending microstrip line films are prone to be damaged, and the large parasitics at the pad to waveguide interface due to conductive glue can degrade the performance at high frequency. Because of such complexity and specialized labor intensive approach, such circuits can cost several thousand US dollars. To overcome these challenges and eliminate the drawbacks, the proposed thin dielectric ribbon waveguide can substitute for the metallic waveguides, and the embedded diode process can replace the “glue on” method to reduce the loss and improve power conversion efficiency.

From system point of view, the multiplier circuit can be fabricated at the wafer level using the proposed approach. Thin dielectric ribbon waveguide, made with nano-composite material and low loss cladding layers (presented in Chapter 2) can be fabricated on top of a low loss plastic substrate. Lamination or photo-patterned process can be applied depending on the material selections. One of the benefits for such ribbon waveguides is that high temperature and

machining process can be avoided. The waveguides are low-loss and planar in nature and thus compatible with wafer level integration. Diode cavities can also fabricated during the composite material patterning. Diodes are then embedded into the cavities and the top cladding layers are fabricated to form a circuit. Note that via to the diode pads are also created through the cladding. CPW with DC bias line can be patterned on the top cladding layer and connect down to the diode through via to realize the impedance matching as well as DC biasing the nonlinear devices. Conventional metal based planar waveguides (e.g., CPW or microstrip) can be fabricated directly on the dielectric ribbon waveguide layers. These may be needed for low-frequency operation (< 100 GHz). A schematic cross section of this circuit is shown in Figure 1.12. Note that certain transition designs are required at the interfaces between thin ribbon waveguide and CPW or microstrips. Another benefit of this novel circuit is the bottom substrate cladding can also be used as an isolation layer, and this approach could be used to realize multi –level circuits. In place of the embedded flip-chip Schottky diodes, GaAs nanowire Schottky diode can also be utilized. Both of these processes avoid the use of expensive GaAs substrate and epitaxial layers. In general, the embedded diode or nanowire device based processes allows a host of substrates that can be used and thus opening design flexibility.

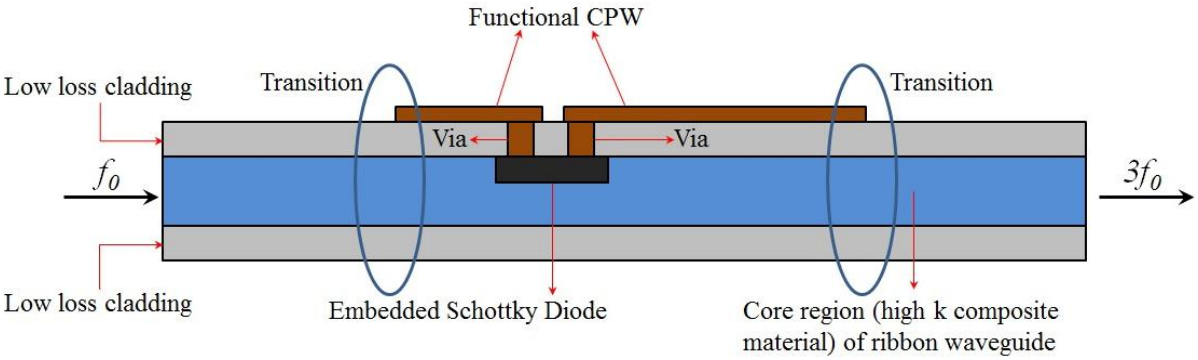

Figure 1.12 A possible method based on proposed research to realize bulky circuit in Figure 1.5 at wafer level integration.

Based on the example and analysis above, proposed ribbon waveguides and embedded process holds significant potential in the design and fabrication of THz integrated circuits (THz planar circuits). Of course, certain designs and modifications are inevitable, and they will be carried out under future work. This thesis largely focuses on the key elements that allows in the design of such a circuit. The key elements include: (i) dielectric ribbon waveguides, (ii) nano-wire Schottky diodes and (iii) embedded active devices.

1.7 Thesis Overview

A flow chart is shown in Figure 1.13 highlighting the flow of the proposed research work. Overview of integrated THz circuit is discussed at the beginning, which has been presented in the introduction section. Then the research is conducted in two parallel paths: active and passive devices. For passive devices, thin dielectric ribbon waveguide is studied in detail, including the waveguide theory, simulation, and fabrication as well as material characterization. All of these studies will flow to the fabricated waveguide measurements, in order to prove the proposed method can be used in practical applications. Another path for active devices is divided again into two parts, nanowire based THz detector and embedded diode detector. Each of these also breaks down into three parts: theory, fabrication and measurements. Then based on those

detailed study, an image sensor is then fabricated and measured to show the embedded diode process can be applied to fabricate low cost large area THz image sensor, which further shows the possibility to realize THz active device using the embedded diode process. The structure of this thesis also follows this flow chart:

Chapter 2 presents research work on THz thin ribbon waveguides;

Chapter 3 focuses on one active device based on GaAs nanowire. Devices are characterized by fabricating THz detector elements;

Chapter 4 focuses on active devices based on embedded diode process. An imaging array is designed and demonstrated using this process;

Chapter 5 summarizes the work based on the investigations of the overall research.

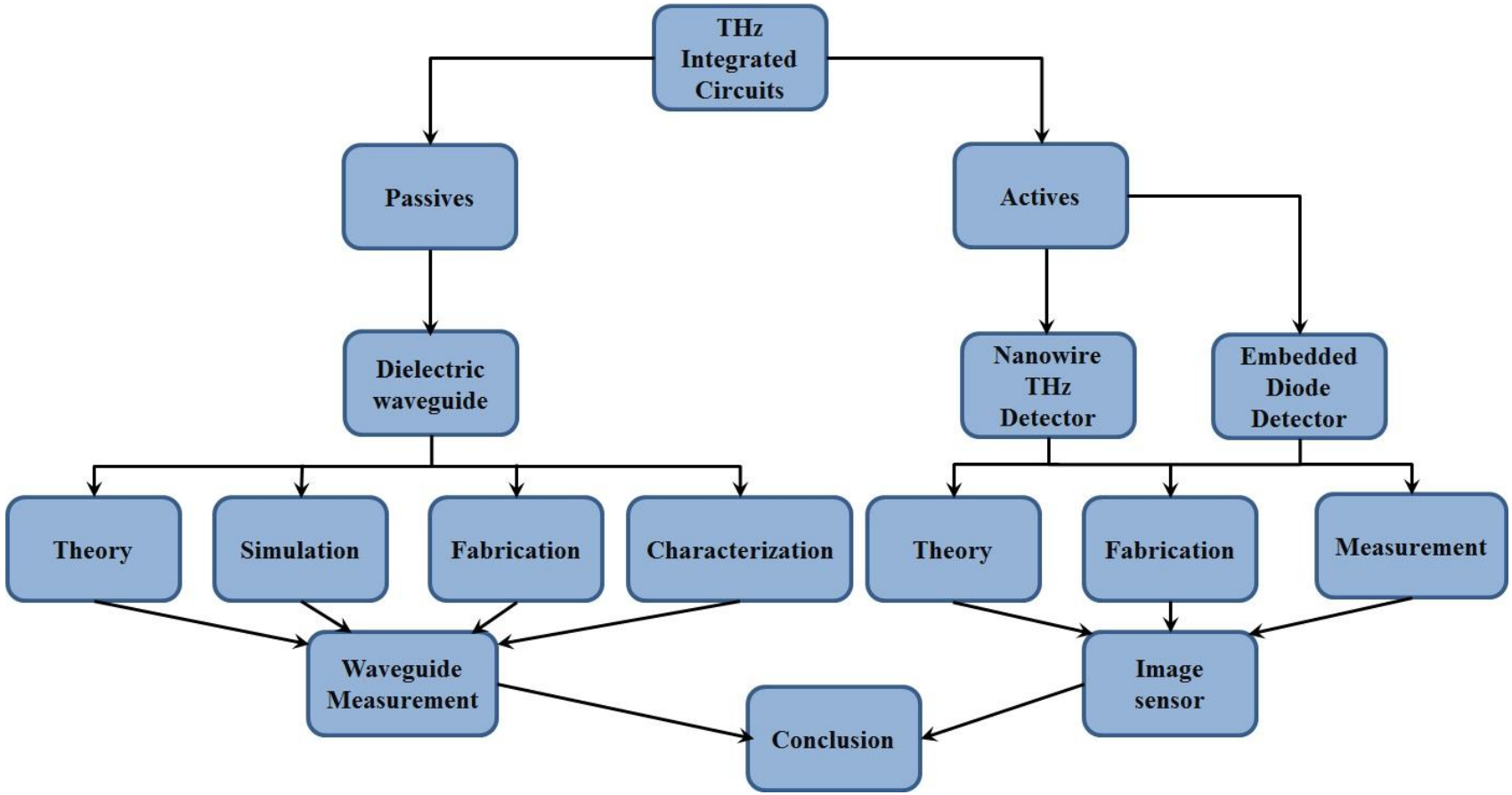

Figure 1.13 Flow chart for proposed research and thesis structure

Chapter 2 On-wafer Terahertz Ribbon Waveguides Using Polymer-Ceramic Nanocomposites

After systematic review of several types of THz waveguides in Chapter 1, the low-loss, wide-band and simple structure thin dielectric ribbon waveguide is a promising candidate that deserves further research. It can provide strong confinement and low loss to propagating THz waves, especially at waveguide bends. In this chapter, analytical calculations for the thin dielectric ribbon waveguide, including the basic wave functions and cutoff frequency for each propagating mode will be derived. Simulations of the thin ribbon waveguides will also be carried out, to further study the waveguiding properties in different folds such as the power confinement (E field pattern) and loss characteristics. From the experimental point of view, the material preparation and characterization such as dielectric constant will be also studied, and measurement results of the waveguides using different fabrication processes will also be presented and discussed.

Furthermore, low loss polymer substrates will be proposed as well in this research for fabricating high frequency devices, so the waveguide fabrication process must be studied and developed carefully to satisfy the polymer physical properties, such as low glass transition temperature and high thermal expansion coefficient. Thus, high temperature process, however, is not allowed, which indicates that high-*k* materials such as Si or alumina cannot be used as the core region. Thus, one of the key challenges is to make thin dielectric ribbon waveguide be compatible with wafer level integration. New high-*k* material must be developed to replace high temperature process material. The second challenge is to make the process low-temperature compatible so that it can be integrated on a host of substrates (organic and inorganic). To resolve these issues, polymer-ceramic nanocomposite material with tunable dielectric constant has been developed and studied, which will be shown in detail later.

2.1 Theoretical Study of Thin Ribbon Dielectric Waveguides

A thin dielectric ribbon waveguide can be treated as a dielectric slab waveguide, which has been studied and analyzed in [62, 63]. As mentioned earlier, using high-*k* core plus low-*k* cladding layers, most of the power of propagation waves will be confined in the low-*k* cladding instead of the surrounding air region. The analysis here will first focus on a thin ribbon with dielectric constant ε_2 surrounded by infinite thick cladding layers with dielectric constant ε_1. Cladding layers with finite thickness is analyzed and discussed in the next session.

2.1.1 Thin ribbon dielectric waveguides with infinite cladding layers

The waveguide structure with infinite cladding thickness is shown in Figure 2.1a, thin ribbon having dielectric constant ε_2 is surrounded by infinite cladding layers with dielectric constant ε_1 on both top and bottom faces. In order to support surface wave propagation, $\varepsilon_2 > \varepsilon_1$ must be satisfied, and the wave is propagating along the +z direction. To simplify this problem, the variation of the wave is set to be zero in y direction. Then the 3D structure can be reduced to a 2D structure, showing in Figure 2.1b.

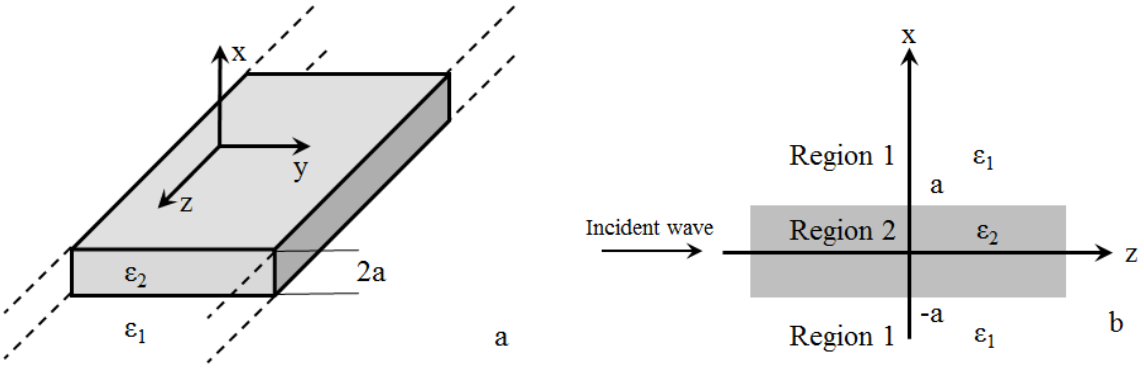

Figure 2.1 (a) 3D schematic of Thin ribbon waveguide with infinite thick cladding layers. (b) 2D schematic diagram of the structure in (a).

2.1.1.1 Transverse-Magnetic (TM) Mode

The analysis will first calculate the wave functions of the waveguide in TM mode, which gives H_z=0 and E_z≠0 along the propagation direction. The general wave functions for E and H can be represented by [64]

$$\bar{E}(x,y,z) = [\bar{e}(x,y) + \hat{z}e_z(x,y)]e^{-j\beta z}e^{-j\omega t}, \tag{2.1a}$$

$$\bar{H}(x,y,z) = [\bar{h}(x,y) + \hat{z}h_z(x,y)]e^{-j\beta z}e^{-j\omega t}, \tag{2.1b}$$

Where, $\bar{e}(x,y)$ and $\bar{h}(x,y)$ are the components for transverse electric and magnetic field, the longitudinal field components are $e_z(x,y)$ and $h_z(x,y)$, and β is the propagation constant for lossless material. $e^{-j\omega t}$ is the time-harmonic component for fields, which will be suppressed later for a simpler equation form.

Starting from the Helmholtz Equation for E_z in each region in Figure 2.1b,

$$(\nabla^2 + k_2^2)E_z = 0, \text{ for } -a \le x \le a \tag{2.2a}$$

$$(\nabla^2 + k_1^2)E_z = 0, \text{ for } x \ge a \text{ and } x \le -a \tag{2.2b}$$

in which

$$k_1^2 = \beta^2 - \varepsilon_1 k_0^2 \tag{2.2c}$$

$$k_2^2 = \varepsilon_2 k_0^2 - \beta^2 \tag{2.2d}$$

are the wave numbers for 2.2a and 2.2b. Since the field in y direction is not changing, that is $\frac{\partial}{\partial y} = 0$, and $E_z(x,y,z) = e_z(x,y)e^{-j\beta z}$, equation 2.2a and 2.2b can be rewritten as

$$(\frac{\partial^2}{\partial x^2} + k_2^2)e_z(x,y) = 0\,, \text{ for } -a \le x \le a \tag{2.3a}$$

$$(\frac{\partial^2}{\partial x^2} + k_1^2)e_z(x,y) = 0\,, \text{ for } x \ge a \text{ and } x \le -a \tag{2.3b}$$

The general solutions for 2.3a and 2.3b are:

$$e_z(x,y) = A\sin k_2 x + B\cos k_2 x\,, \text{ for } -a \le x \le a \tag{2.4a}$$

$$e_z(x,y) = Ce^{k_1 x} + De^{-k_1 x}\,, \text{ for } x \ge a \text{ and } x \le -a \tag{2.4b}$$

Where, *A* is the constant related to the incident wave, *B*, *C* and *D* are the unknown constants. Note that in 2.4b, two exponentials cannot exist together since the wave attenuates to zero when $x=\pm\infty$, but both of them are kept here for further calculating the even and odd modes. In order to solve them, certain boundary conditions must be satisfied at each interface, which gives

$$e_z^1(x,y) = e_z^2(x,y)\,, \; x = \pm a \tag{2.5a}$$

$$h_y^1(x,y) = h_y^2(x,y)\,, \; x = \pm a \tag{2.5b}$$

$$e_z^1(x,y) = 0\,, \; x \to +\infty \tag{2.5c}$$

$$e_z^1(x,y) = 0\,, \; x \to -\infty \tag{2.5d}$$

the superscription represents the number of each region, and the $h_y(x,y)$ component can be found by solving the Maxwell's Equations and represented only by E_z and H_z, as follows

$$H_x = \frac{j}{k_c^2}(\omega\varepsilon\frac{\partial E_z}{\partial y} - \beta\frac{\partial H_z}{\partial x}), \tag{2.6a}$$

$$H_y = \frac{-j}{k_c^2}(\omega\varepsilon\frac{\partial E_z}{\partial x} + \beta\frac{\partial H_z}{\partial y})\,, \tag{2.6b}$$

$$E_x = \frac{-j}{k_c^2}(\beta \frac{\partial E_z}{\partial x} + \omega\mu \frac{\partial H_z}{\partial y}), \tag{2.6c}$$

$$E_y = \frac{j}{k_c^2}(-\beta \frac{\partial E_z}{\partial y} + \omega\mu \frac{\partial H_z}{\partial x}), \tag{2.6d}$$

The wave functions are then solved separately in even and odd mode, and even mode is solved first as follows.

At *x*=*a*,

$$B\cos k_2 a = De^{-k_1 a}, \tag{2.7a}$$

$$\frac{B\varepsilon_2}{k_2}\sin k_2 a = -\frac{D\varepsilon_1}{k_1}e^{-k_1 a}, \tag{2.7b}$$

At *x*=-*a*,

$$B\cos k_2(-a) = Ce^{-k_1 a}, \tag{2.7c}$$

$$\frac{B\varepsilon_2}{k_2}\sin k_2(-a) = \frac{C\varepsilon_1}{k_1}e^{-k_1 a}, \tag{2.7d}$$

which gives *C*=*D* and

$$\frac{\varepsilon_2}{k_2}\tan k_2 a = -\frac{\varepsilon_1}{k_1}, \tag{2.8}$$

If $k_1 = \sqrt{\beta^2 - \varepsilon_1 k_0^2}$ has an imaginary part, the wave in Region 1 cannot decay down to zero at infinity, which indicates the minimum value for k_1 is zero, then $\beta = \sqrt{\varepsilon_1 k_0^2}$, and equation 2.8 becomes infinity, thus

$$k_2 a = \frac{m\pi}{2}, \; m=1, 3, 5\ldots \tag{2.9}$$

which determines the cutoff frequency f_c of the waveguide for even mode:

$$f_c = \frac{m}{4a\sqrt{\mu_0\varepsilon_0}\sqrt{\varepsilon_2 - \varepsilon_1}}, \; m=1, 3, 5\ldots \tag{2.10}$$

Similar calculations can be done for odd mode, and the cutoff frequency can be written as:

$$f_c = \frac{m}{4a\sqrt{\mu_0\varepsilon_0}\sqrt{\varepsilon_2 - \varepsilon_1}}, \; m=0, 2, 4\ldots \tag{2.11}$$

Solving the equations 2.4a and 2.4b using the boundary conditions of 2.5, unknown constants can be derived as:

$$B = A\tan k_2 a e^{-2k_1 a}, \tag{2.12}$$

$$C = \frac{A\sin k_2 a}{e^{k_1 a}}, \tag{2.13}$$

Then the wave functions for *E* and *H* in each direction can be found as:

In region 2, $-a \le x \le a$:

$$E_z(x,y,z) = A(\sin k_2 x + \tan k_2 a e^{-2k_1 a}\cos k_2 x)e^{-j\beta z}, \tag{2.14a}$$

$$E_x(x,y,z) = -\frac{Aj\beta}{k_2}(\cos k_2 x - \tan k_2 a e^{-2k_1 a}\sin k_2 x)e^{-j\beta z}, \tag{2.14b}$$

$$H_y(x,y,z) = -\frac{Aj\omega\varepsilon_2}{k_2}(\cos k_2 x - \tan k_2 a e^{-2k_1 a}\sin k_2 x)e^{-j\beta z}, \tag{2.14c}$$

In the upper region 1, $x \ge a$,

$$E_z(x,y,z) = A\sin k_2 a e^{-k_1(x+a)}e^{-j\beta z}, \tag{2.15a}$$

$$E_x(x,y,z) = -\frac{Aj\beta}{k_1}\sin k_2 a e^{-k_1(x+a)}e^{-j\beta z}, \tag{2.15b}$$

$$H_y(x,y,z) = -\frac{Aj\omega\varepsilon_1}{k_1}\sin k_2 a e^{-k_1(x+a)}e^{-j\beta z}, \tag{2.15c}$$

In the lower region 1, $x \leq -a$,

$$E_z(x,y,z) = A\sin k_2 a e^{k_1(x-a)}e^{-j\beta z}, \tag{2.16a}$$

$$E_x(x,y,z) = \frac{Aj\beta}{k_1}\sin k_2 a e^{k_1(x-a)}e^{-j\beta z}, \tag{2.16b}$$

$$H_y(x,y,z) = \frac{Aj\omega\varepsilon_1}{k_1}\sin k_2 a e^{k_1(x-a)}e^{-j\beta z}, \tag{2.16c}$$

And the surface wave impedance is:

$$Z_w = -\frac{E_z^{1+}}{H_y^{1+}} = \frac{E_z^{1-}}{H_y^{1-}} = j\frac{k_1}{\omega\varepsilon_1}, \tag{2.17}$$

2.1.1.2 Transverse-Electric (TE) Mode

The TE mode must satisfy the condition that E_z=0 but $H_z \neq 0$. The calculation procedure is similar to that of TM mode, but the boundary conditions are slightly different, which are:

$$h_z^1(x,y) = h_z^2(x,y),\ x = \pm a \tag{2.18a}$$

$$e_y^1(x,y) = e_y^2(x,y),\ x = \pm a \tag{2.18b}$$

$$h_z^1(x,y) = 0,\ x \to +\infty \tag{2.18c}$$

$$h_z^1(x,y) = 0,\ x \to -\infty \tag{2.18d}$$

Following the same procedure for calculating the TM mode, the cutoff frequency for both even and odd TE modes is calculated as:

$$f_c = \frac{m}{4a\sqrt{\mu_0\varepsilon_0}\sqrt{\varepsilon_2 - \varepsilon_1}},$$

m=1, 3, 5…for even mode, m=0, 2, 4… for odd mode (2.19d)

And the wave functions can be derived for each region easily using the boundary conditions, which are not shown here for simplicity.

2.1.2 Thin ribbon waveguides with finite cladding layers

The previous calculations are based on the conditions that the cladding layers are infinitely thick; however, thin ribbon waveguides need to be fabricated on finite claddings such as polymer dielectric layers and substrates with certain thickness in order to form the circuit level integration. In this situation, the wave propagation properties are different from the condition of infinite cladding layers, thus it is worth to look into details.

The schematic 3D structure of thin ribbon waveguide with finite thickness cladding layers is shown in Figure 2.2a, with assumption that there is no variation of the wave in the y-direction, which simplifies the calculation but still gives sufficiently accurate results. Figure 2.2b shows the 2D schematic of the waveguide, region 2 is the high-*k* core with thickness of 2a and dielectric constant ε_2, region 1 in the positive and negative x-directions is the low-*k* cladding layers with finite thickness b and dielectric constant ε_1, outside the waveguide is region 0, i.e., vacuum, which is also in the positive and negative x directions. In order to support surface wave propagation with no leaky wave, $\varepsilon_2 > \varepsilon_1 > \varepsilon_0$ must be satisfied. Again, transverse-magnetic (TM) mode will be solved first and similar calculations can be applied to TE mode.

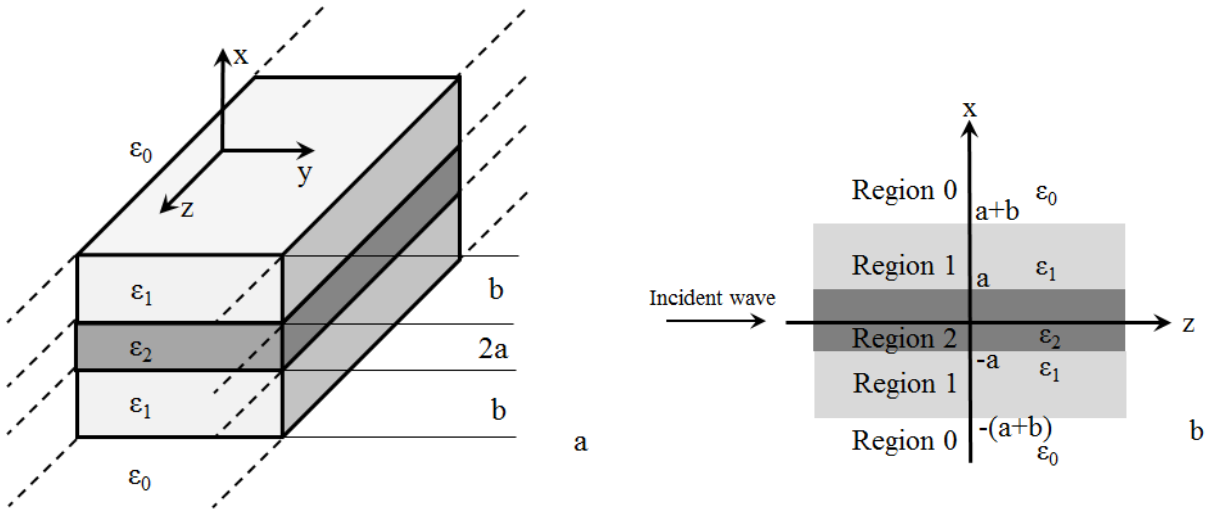

Figure 2.2 3D schematic structures for thin ribbon waveguide with finite cladding layers (a), (b) shows the 2D schematic diagram for the waveguide structure in (a).

2.1.2.1 TM Mode

Following the same procedures of calculating the infinite cladding ribbon waveguide, Helmholtz equations for finite cladding layers waveguide for each region can be written as:

$$(\nabla^2 + k_2^2)E_z = 0 \text{ ,-}a \le x \le a \text{ (region 2)} \tag{2.20a}$$

$$(\nabla^2 + k_1^2)E_z = 0 \text{ , -}(a+b) \le x \le -a \text{ (region 1-) and } a \le x \le a+b \text{ (region 1+)} \tag{2.20b}$$

$$(\nabla^2 + h^2)E_z = 0 \text{ , } x \ge a+b \text{ (region 0+) and } x \le -(a+b) \text{ (region 0-)} \tag{2.20c}$$

where, the wave numbers of the wave in each regions are:

$$k_2^2 = \varepsilon_2 k_0^2 - \beta^2 \text{, region 2} \tag{2.21a}$$

$$k_1^2 = \varepsilon_1 k_0^2 - \beta^2 \text{, region 1} \tag{2.21b}$$

$$h^2 = \beta^2 - k_0^2 \text{, region 0} \tag{2.21c}$$

Again, since the propagation wave has no y dependence, that is $\frac{\partial}{\partial y} = 0$, and $E_z(x,y,z) = e_z(x,y)e^{-j\beta z}$, the Helmholtz equations can be rewritten as:

$$(\frac{\partial^2}{\partial x^2} + k_2^2)e_z(x,y) = 0\,, \text{ region 2} \tag{2.22a}$$

$$(\frac{\partial^2}{\partial x^2} + k_1^2)e_z(x,y) = 0\,, \text{ region 1+ and region 1-} \tag{2.22b}$$

$$(\frac{\partial^2}{\partial x^2} + h^2)e_z(x,y) = 0\,, \text{ region 0+ and region 0-} \tag{2.22c}$$

The solution for each of the differential equation has the following form:

$$e_z(x,y) = A\sin k_2 x + B\cos k_2 x\,, \text{ region 2} \tag{2.23a}$$

$$e_z(x,y) = C\sin k_1 x + D\cos k_1 x\,, \text{ region 1+} \tag{2.23b}$$

$$e_z(x,y) = E\sin k_1 x + F\cos k_1 x\,, \text{ region 1-} \tag{2.23c}$$

$$e_z(x,y) = Ge^{hx} + He^{-hx}\,, \text{ region 0+} \tag{2.23d}$$

$$e_z(x,y) = Je^{hx} + Le^{-hx}\,, \text{ region 0-} \tag{2.23e}$$

Note that in region 0, E fields will decay to zero at x=±∞, which means that in equation 2.23d and 2.23e, G and L must be zero, but here they are still kept in the complete equation form for further calculating the even and odd modes. The boundary conditions must be satisfied that the tangential fields of E and H must be continuous at each interface, which gives:

at *x=a*,

$$e_z^2(x,y) = e_z^{1+}(x,y)\,, \tag{2.24a}$$

$$h_y^2(x,y) = h_y^{1+}(x,y), \tag{2.24b}$$

at *x=-a*,

$$e_z^2(x,y) = e_z^{1-}(x,y), \tag{2.25a}$$

$$h_y^2(x,y) = h_y^{1-}(x,y), \tag{2.25b}$$

at *x=a+b*,

$$e_z^{1+}(x,y) = e_z^{0+}(x,y), \tag{2.26a}$$

$$h_y^{1+}(x,y) = h_y^{0+}(x,y), \tag{2.26b}$$

at *x=-(a+b)*,

$$e_z^{1-}(x,y) = e_z^{0-}(x,y), \tag{2.27a}$$

$$h_y^{1-}(x,y) = h_y^{0-}(x,y), \tag{2.27b}$$

The guided wave can be divided into even mode and odd mode, and the entire wave is the superposition of these two modes, consider even mode first,

x=a,

$$B\cos k_2 a = D\cos k_1 a, \tag{2.28a}$$

$$\frac{B\varepsilon_2}{k_2}\sin k_2 a = \frac{D\varepsilon_1}{k_1}\sin k_1 a, \tag{2.28b}$$

x=-a,

$$B\cos k_2 a = F\cos k_1 a, \tag{2.29a}$$

$$\frac{B\varepsilon_2}{k_2}\sin k_2 a = \frac{F\varepsilon_1}{k_1}\sin k_1 a, \tag{2.29b}$$

x=a+b,

$$D\cos k_1(a+b) = He^{-h(a+b)}, \tag{2.30a}$$

$$-\frac{D\varepsilon_1}{k_1}\sin k_1(a+b) = \frac{1}{h}He^{-h(a+b)}, \tag{2.30b}$$

x=-(a+b),

$$F\cos k_1(a+b) = Je^{-h(a+b)}, \tag{2.31a}$$

$$\frac{F\varepsilon_1}{k_1}\sin k_1(a+b) = -\frac{1}{h}Je^{-h(a+b)}, \tag{2.31b}$$

equation 2.28a and 2.29a indicate that *D=F*, and equation 1.30a and 1.31a show that *H=J*. Using equation 2.28b divided by 2.28a, 2.30a divided by 2.30b, one will get:

$$\frac{\varepsilon_2}{k_2}\tan k_2 a = \frac{\varepsilon_1}{k_1}\tan k_1 a, \tag{2.32a}$$

$$-\frac{\varepsilon_1}{k_1}\tan k_1(a+b) = \frac{1}{h}, \tag{2.32b}$$

Equation 2.32a can be used to find the relation of wave numbers in the high-*k* core and the low-*k* claddings. It also can be found that 2.32b has similar form as equation 2.8 in infinite cladding case. Thus same analysis can be applied to find the cutoff frequency of thin ribbon waveguide with finite claddings. since $h = \sqrt{\beta^2 - k_0^2}$, for the nature that wave in the vacuum decays to zero at infinite, h must be a real number, and the minimum value for h is zero, which gives $\beta = k_0$, and

$$k_1(a+b) = \frac{m\pi}{2}, \; m=1, 3, 5\ldots \tag{2.33}$$

then put equation 2.33 and into 2.21b, suppress β, the cutoff frequency can be finally derived as:

$$f_c = \frac{m}{4(a+b)\sqrt{\mu_0\varepsilon_0}\sqrt{\varepsilon_1 - 1}}, \; m=1, 3, 5\ldots \tag{2.34}$$

which shows it is only related to the thickness of the high-*k* core and low-*k* cladding layers and the dielectric constant of the cladding layer. Further calculations for the odd mode provides the same cutoff frequency equation, thus it satisfies the entire TM mode.

Applying the boundary conditions to the entire wave function, the unknown constants can be solved in the form of amplitude of A, and they are shown as below:

$$B = A\left(\frac{k_1\varepsilon_2 \cos k_2 a - k_2\varepsilon_1 \sin k_2 a \cot k_1 a}{k_2\varepsilon_1 \cos k_2 a \tan k_1 a - k_1\varepsilon_2 \sin k_2 a}\right), \tag{2.35a}$$

$$C = E = A\frac{\sin k_2 a}{\sin k_1 a}, \tag{2.35b}$$

$$D = F = B\frac{\cos k_2 a}{\cos k_1 a}, \tag{2.35c}$$

$$H = J = B\frac{\cos k_2 (a+b)\cos k_2 a}{e^{-h(a+b)}\cos k_1 a}, \tag{2.35d}$$

$$G = L = 0, \tag{2.35e}$$

inserting equation 2.35 into equation 2.23, and using the solution of Maxwell equation in equation 1.6, the complete wave functions for the finite cladding layer thin ribbon waveguide in TM mode can be achieved.

2.1.2.2 TE Mode

The calculations for the wave functions in TE mode can follow the same procedure of deriving those in TM mode. The only difference is that the boundary conditions must satisfy H_z

and E_y are continuous at each boundary and interface. The cutoff frequency for TE mode has the same form as that of TM mode,

$$f_c = \frac{m}{4(a+b)\sqrt{\mu_0\varepsilon_0}\sqrt{\varepsilon_1 - 1}}, \; m=0, 1, 2, 3\ldots \tag{2.36}$$

which is also related to the thickness of the waveguide and the dielectric constant of low-*k* cladding layers. Note that if the thickness of the high-*k* core a→0, equation 2.36 will only have b, which is the same form as that in the infinite cladding case, and representing the vacuum are the cladding layers on both sides. It has been found that TM_0 and TE_0 are the two dominant modes with no cutoff frequency for both cases analyzed above [63], but this is valid only at the condition that the waveguide is symmetric, i.e., the top and bottom claddings have the same dielectric constant, otherwise there is no nonzero cutoff frequency for any TM or TE mode. In ref [65], it also shows that increasing the dielectric constant of the core region, the power will be confined more into the core, so in order to reduce the attenuation, it is necessary to find materials which have high dielectric constant but low tangent loss. The power distribution properties of thin ribbon waveguide with certain cladding thickness will be shown in details in the waveguide simulation section.

2.2 Simulation Model and Results

The theoretical calculations shown above provide the basic understanding about the modes and behavior of the wave propagating in the thin ribbon dielectric waveguides. Models and pre-simulations of the waveguide structures have been setup in order to get a more practical and intuitive view about how the wave propagates in a concrete waveguide structure. The rest of this section will focus on the simulations of thin dielectric ribbon waveguide with finite cladding

layers. The propagation properties of the thin ribbon waveguide with cladding layers are studied using commercially available simulation tools (Ansoft HFSS).

2.2.1 Thin Ribbon Waveguide vs. Microstrip Lines

In order to compare the propagation losses between ribbon waveguides and conventional microstrips, waveguides with two different lengths (5 and 9mm) but constant width (2mm) were simulated at 0.2 THz operating frequency. These results are summarized in Table 2.1. Measuring the differences in transmitted signal ($\Delta S_{21}=S_{21(short)}-S_{21(long)}$) subtracts possible coupling losses at the port that is inherently different between these two types of waveguides. ΔS_{21}/mm here represents the signal loss per unit length. Simulated results show that dielectric ribbon waveguides have lower loss compared to microstrip transmission lines. This is largely due to the fact that skin effect losses dominate at high frequencies in microstrip transmission lines.

Table 2.1 Simulated S_{21} for microstrips and thin dielectric ribbon waveguides

	S_{21} (Mag) Long (9mm)	S_{21} (Mag) Short (5mm)	ΔS_{21}(Mag) /mm
Microstrip Transmission Line	0.9170	0.9422	0.0063
Thin Dielectric Ribbon Waveguide	0.75949	0.76349	0.001

2.2.2 Ribbon Waveguides with Varying Core Thickness

The propagation properties of the ribbon waveguide with cladding layers are studied. Figure 2.3 shows the modeling structure as well as the E-field observing planes. These planes are references onto which the E-field is plotted. Low-*k* layers are cladded on top and bottom of the high-*k* ribbon core. Table 2.2 lists the geometrical values for the waveguides used in the simulations.

E-field observing planes in the model structure are used to study the E-field patterns confined within the radiation region, which helps to visualize the wave propagation properties of the ribbon waveguides. Quantitative analyses have been carried out by changing the thickness of the high-*k* core as well as that of the low-*k* cladding layers. The geometries for the E-field observing planes are also shown in Figure 2.3. Figure 2.4 shows the E-field pattern in the cross-section along the waveguide. Both Figures 2.3 and 2.4 are simulated at a solution frequency of 0.2 THz. In these simulations, the cladding thickness is fixed at 250μm, while the core thickness is varied.

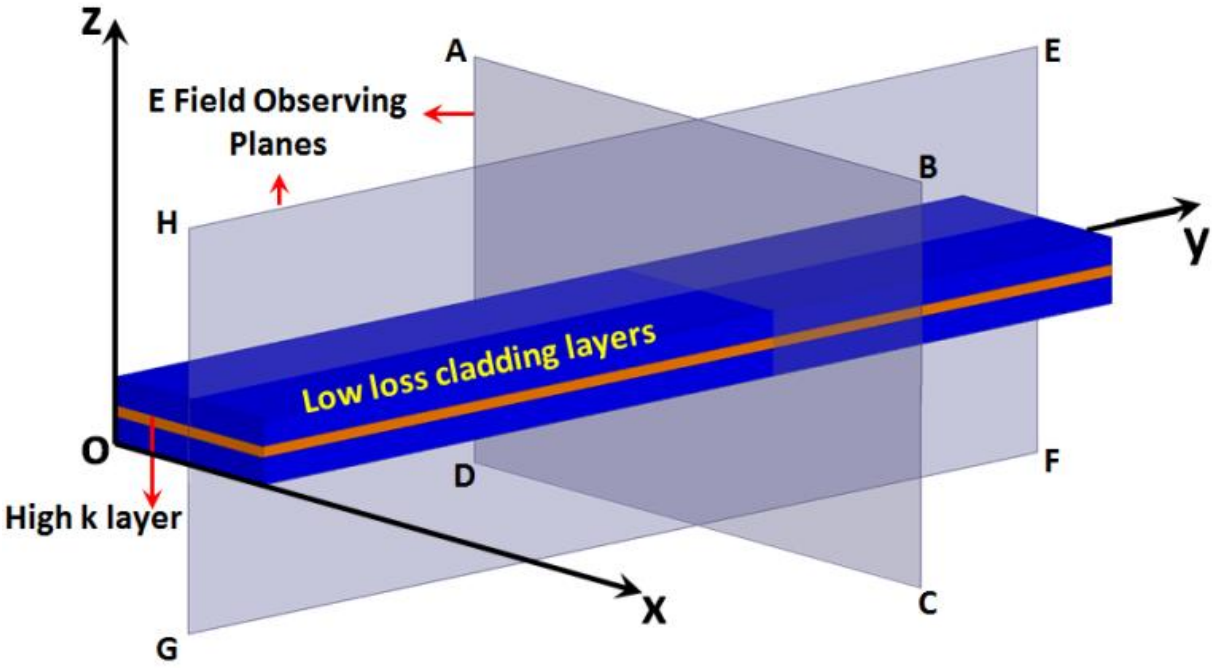

Figure 2.3 Modeling structure of cladded dielectric thin ribbon waveguide. The field polarization direction is perpendicular to the waveguide surface, which is along the z-axis. Observing plane sizes are: 6mm×3.7mm for ABCD, 10mm×3.7mm for EFGH, respectively.

Table 2.2. Parameters for the modeled structure.

Width of Ribbon Waveguide (W)	2mm
Length of the Ribbon Waveguide (L)	10mm
Thickness of High-*k* Core (t)	Swept from 0 to 150μm
Thickness of the Low-*k* Cladding (H)	Swept from 0 to 500μm
Dielectric Constant of Core Layer ε_r	10.2
Dielectric Constant of Cladding Layer ε_r	2.355
Loss Tangent of Core Layer	0.0035
Loss Tangent of Cladding Layer	0.0005

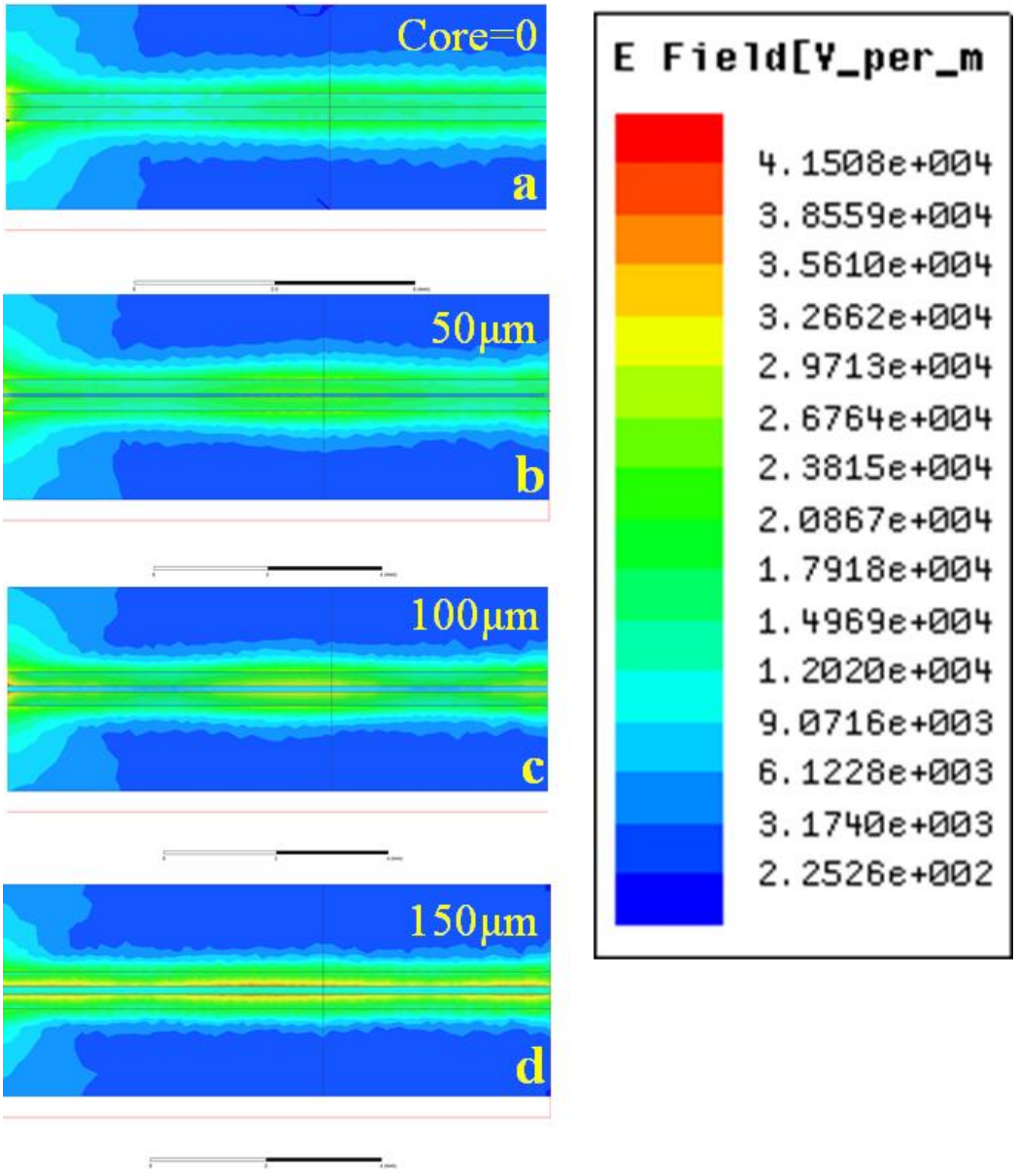

Figure 2.4 E-field pattern along the dielectric waveguide. Wave is launched from the left side, with a core thickness of (a) 0 μm, (b) 50 μm, (c) 100 μm, and (d) 150 μm.

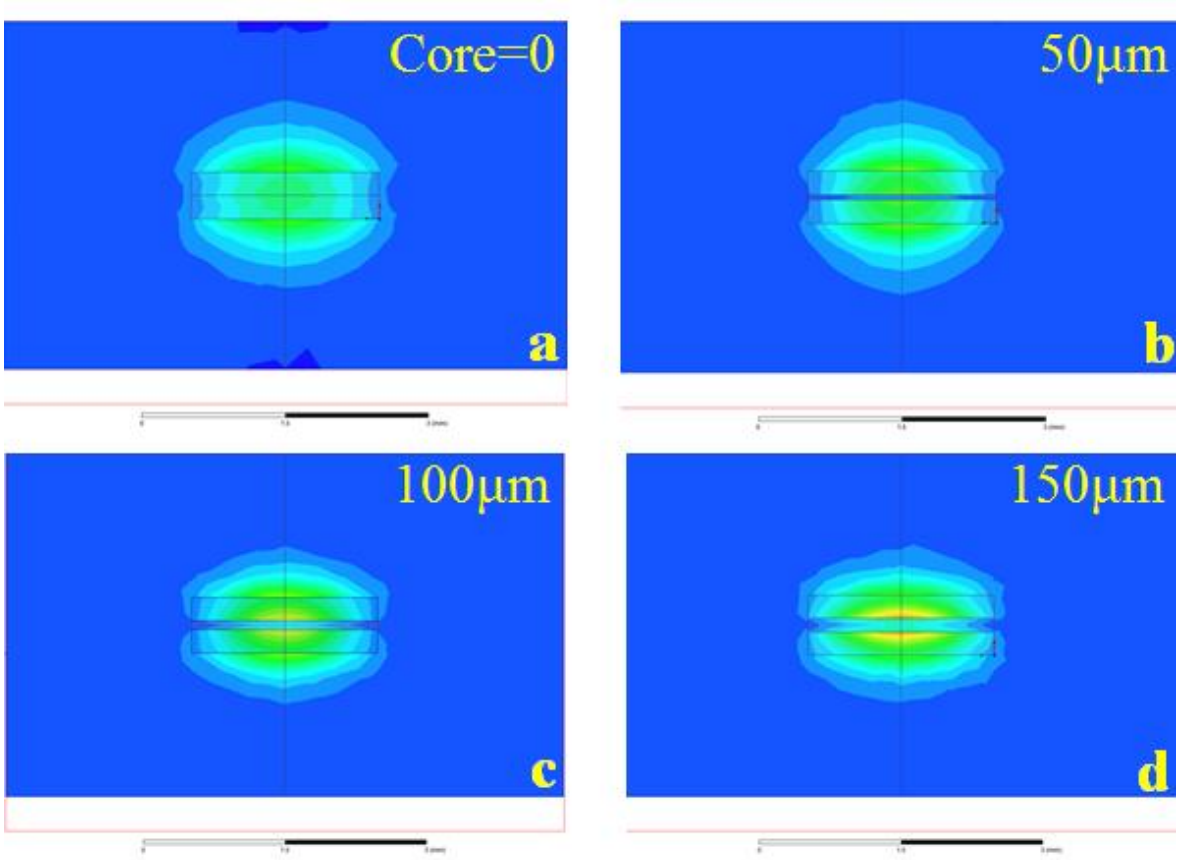

Figure 2. 5 E-field pattern on the cross section plane (6mm from the wave launching port) of the dielectric waveguide, with a core thickness of (a) 0 μm, (b) 50 μm, (c) 100 μm, and (d) 150 μm. See color legend in Figure 2.4.

Figure 2.4 illustrates that as the thickness of the high-*k* region increases, the field confinement within the waveguide also increases. Similarly, Figure 2.5 shows the E-field pattern of fields being confined transverse to the waveguides. However, higher dielectric loss (loss tangent) of the core region will lead to higher losses. This is confirmed in Table 2.3, which gives numerical values of transmitted power through different cross section areas at same position (6mm from wave launching port) on the waveguides. The total power in the transverse cross sectional area *ABCD* (entire area of each picture in Figure 2.5) increases when thicker core

region is used. The percentage of confined power in the waveguide and core region also increases. An optimized design is considered, as the thickness of the core-region should be chosen to give negligible field in the surrounding air (outside of cladding region), and relatively lower power in the high-*k* core. For the case presented here, an optimal thickness for the thin ribbon waveguide is approximately 100 μm.

2.2.3 Ribbon Waveguides with Varying Cladding Thickness

The influence of the cladding thickness on the wave propagation is also studied. Figures 2.6 and 2.7 show the E-field pattern results for a fixed core thickness of 100 μm while the cladding thickness is varied between 0 to 500 μm. The simulation frequency is also fixed at 0.2 THz. Table 2.4 shows the power confinement values within different areas of cross section planes for different cladding thicknesses. All the measurements are at the same position (6mm from the wave launching port) of the waveguides. By increasing the cladding thickness, a higher portion of power is confined in the dielectric layers. However, for cladding thickness greater than 500μm, power confinement per cross-sectional area begins to drop. Thick cladding layers are also not practical for interconnects as the thick layers limit the stacking of the waveguide for multilayer fabrication. Simulation results show that a cladding thickness of approximately 250μm is sufficient to confine the field within the dielectric layers.

Table 2.3 Power confinement of different high-*k* core thickness

Cladding 250μm (Fixed)	Total Cross Section ABCD (W)	Ribbon Waveguide Cross Section (W) (% of Total)	Core Region Cross Section (W) (% of Total)
Core=0	0.5121	0.2900 (56.63%)	--------
Core=50μm	0.5764	0.3820 (66.27%)	0.0137 (2.38%)
Core=100μm	0.6085	0.4949 (81.33%)	0.0514 (8.45%)
Core=150μm	0.7083	0.6168 (87.08%)	0.1400 (19.77%)

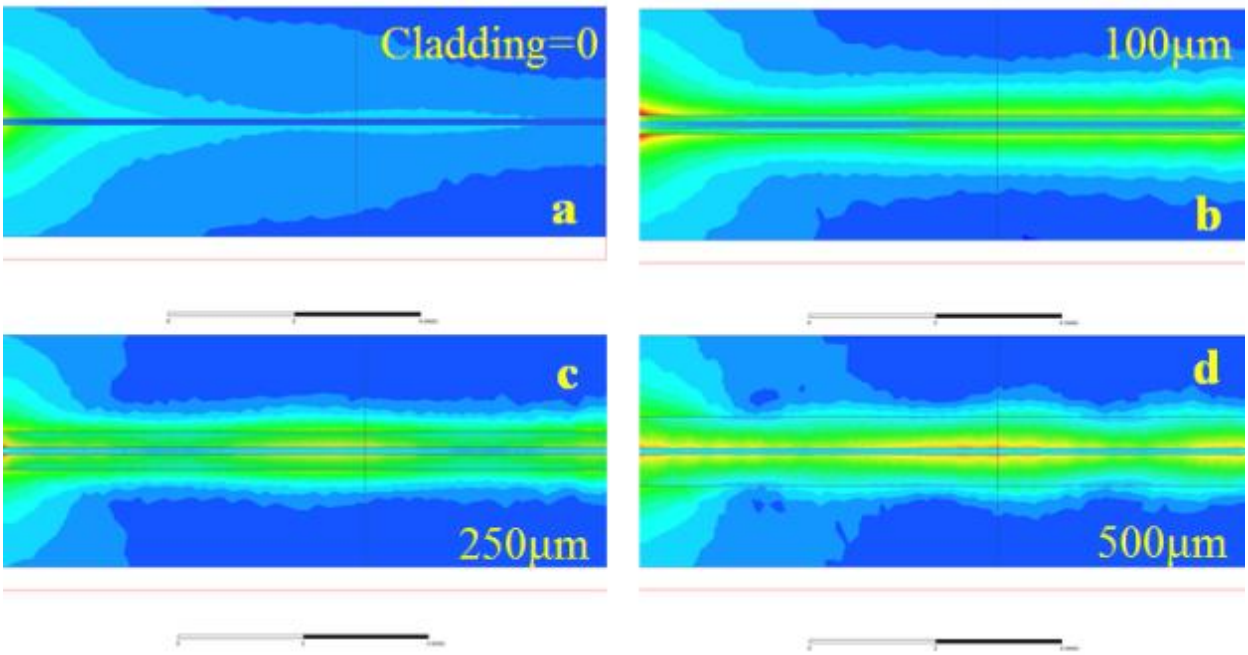

Figure 2.6 E-field pattern along the waveguide for a fixed core thickness (100 μm) and varied cladding thickness (See color legend in Figure 3). Thickness of the cladding layers are: (a) 0 μm, (b) 100 μm, (c) 250μm and (d) 500 μm.

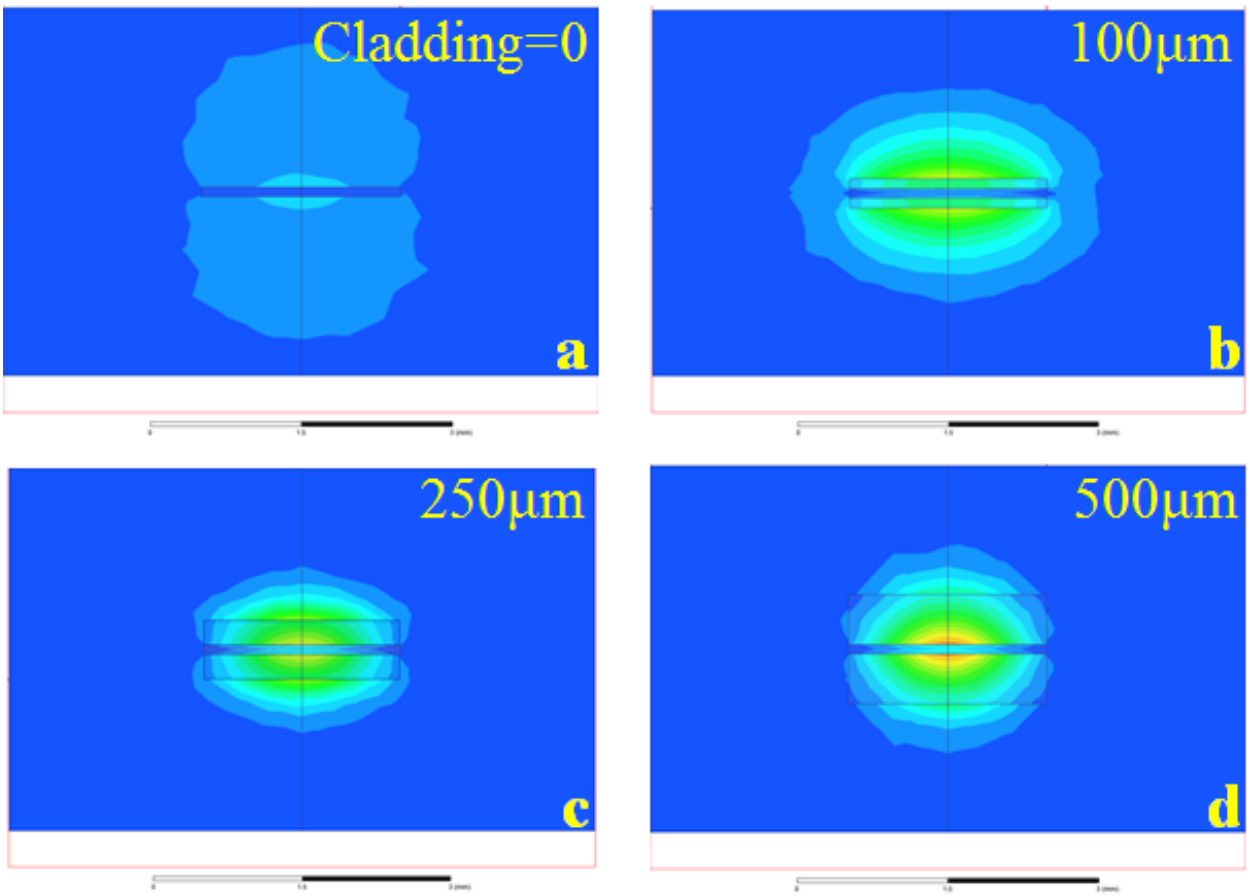

Figure 2.7 E-field pattern on the cross sectional plane (6mm from the wave launching port) of the waveguide for a fixed core thickness (100 µm) and varied cladding thickness. Thickness of the cladding layers are: (a) 0 µm, (b) 100 µm, (c) 250µm and (d) 500 µm. See color legend in Figure 2.4.

Table 2.4 Power confinement of different cladding thickness

High-*k* Core 100μm (Fixed)	Total Cross Section *ABCD* (W)	Ribbon Waveguide Cross Section (W) (% of Total)	Core Region Cross Section (W) (% of Total)
Cladding=0	0.2585	-------	0.0011 (0.42%)
Cladding=100μm	0.4276	0.0942 (22.03%)	0.0155 (3.62%)
Cladding=250μm	0.6085	0.4949 (81.33%)	0.0514 (8.45%)
Cladding=500μm	0.6013	0.5567 (92.58%)	0.0384 (6.39%)

2.2.4 Ribbon Waveguides Analysis at Different Frequencies

Here the core and cladding layers are fixed at 100μm and 250μm, which are the optimal values based on previous studies. Frequencies are varied from 0.15THz to 0.35THz in 50GHz increments. Figure 2.8 shows the E-field confinement on the transverse cross section planes 6mm away from the wave launching port. While the frequency is increased, the power is confined more into the cladding layer of the waveguide rather than the surrounding air. For a certain power confinement level at a desired frequency, it is necessary to manipulate the thickness of the core and cladding layers in order to satisfy the need for field confinement based on surrounding circuits and mutual coupling.

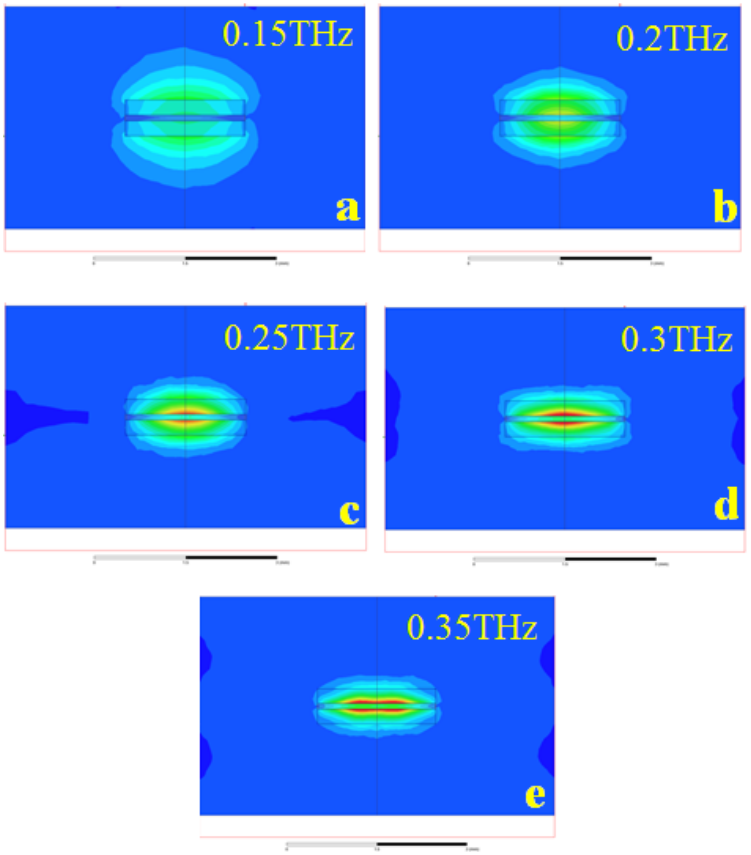

Figure 2.8 E-field pattern on the cross section planes of the waveguides (See color legend in Figure 3). From (a) to (e), frequencies are from 0.15THz to 0.35THz with 50GHz increment. The thickness of the core and cladding layers are 100μm and 250μm, respectively.

2.2.5 Ribbon Waveguides with Varying Dielectric Constant of the Core Region

To further analyze the effect of dielectric properties of high-*k* core region on wave propagation, FEM simulations are further carried out by varying dielectric constant of the high-*k* core region. Figure 2.9 shows the E-field patterns on the cross section planes of waveguides at 0.2THz. The dielectric constant is varied from 5 to 14. Thicknesses of core and cladding layers are chosen as 100μm and 250μm, which are the optimal values at 0.2THz. Here, larger value provides tighter power confinement into the cladding layer. Thus, field confinement can be

tailored by choosing an appropriate dielectric constant of the high-*k* core region. Also, this suggests that the ribbon waveguide can be further thinned by using higher dielectric constant material in core region.

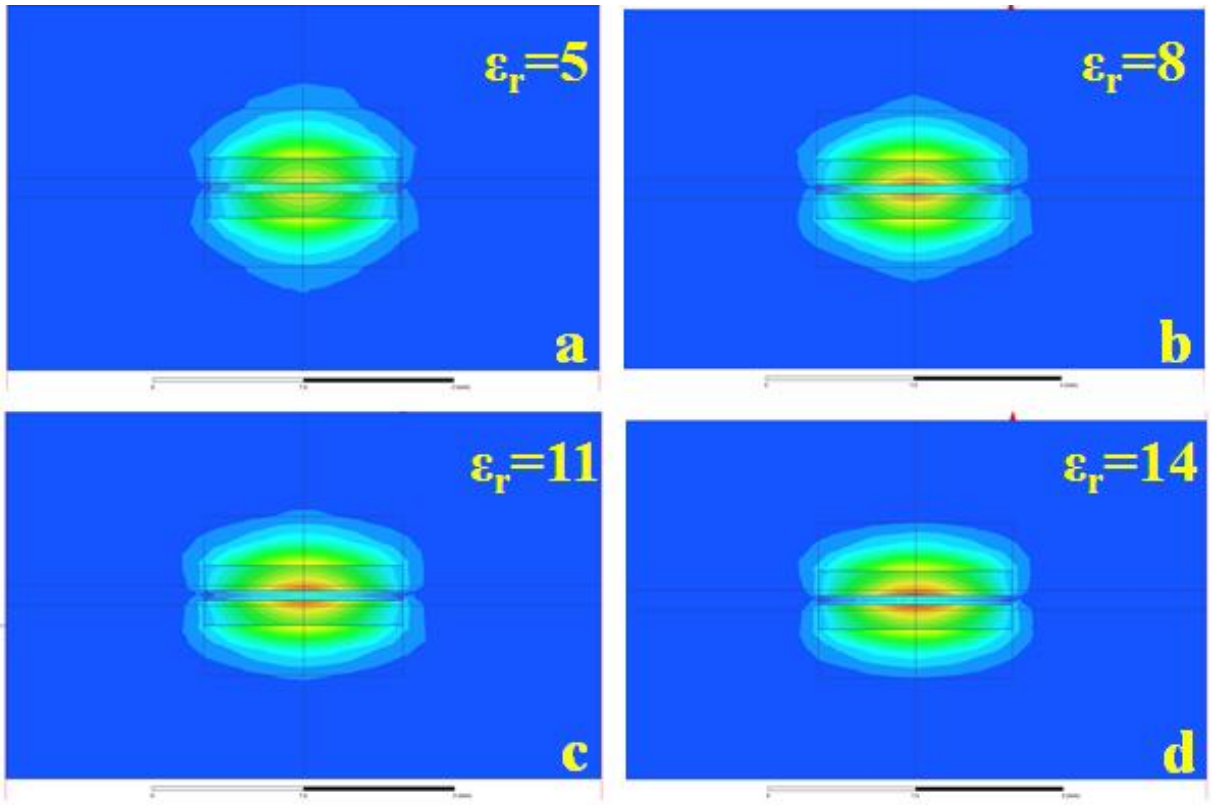

Figure 2.9 E-field pattern on the cross section planes (6mm away from wave launching port) of the waveguides with different dielectric constants at 0.2THz (See color legend in Figure 2.4). From a to d, the dielectric constants are 5, 8, 11, 14, respectively. Cladding and core layers thickness are 250μm and 100μm, respectively.

Figure 2.10 show a clear trend of such a behavior. Again, one would be able to select certain dielectric constant value during fabrication in order to meet the requirement of different power confinement.

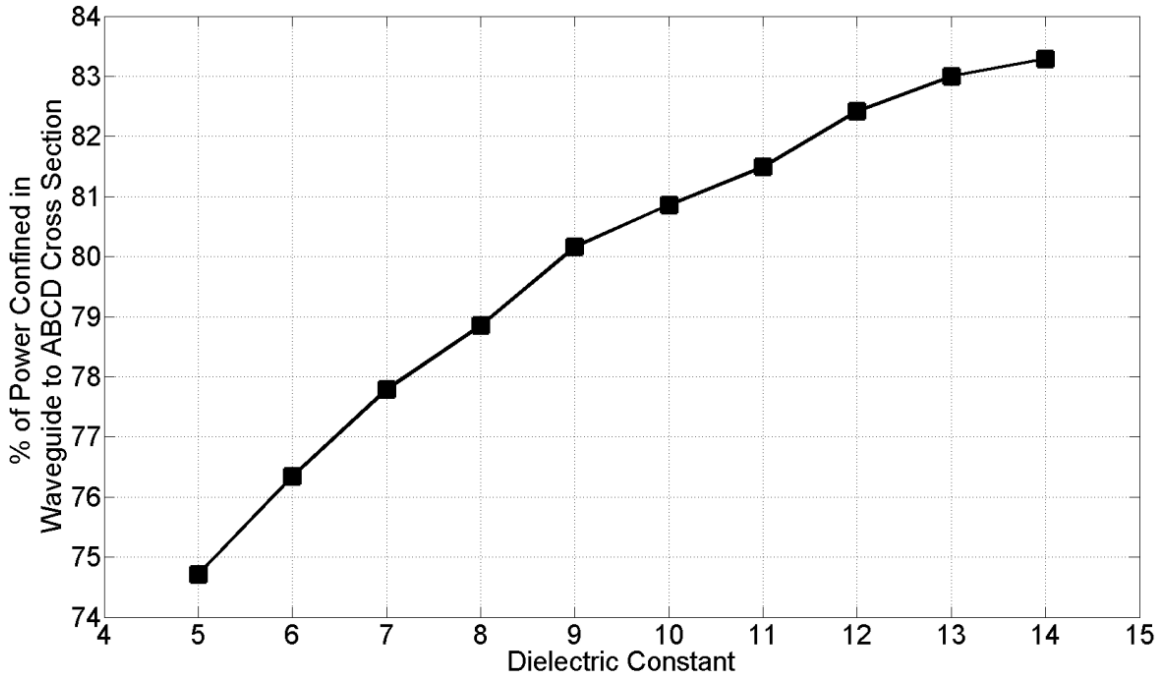

Figure 2.10 Change in percentage of power confined in waveguides as a function of change in dielectric constant of the core region.

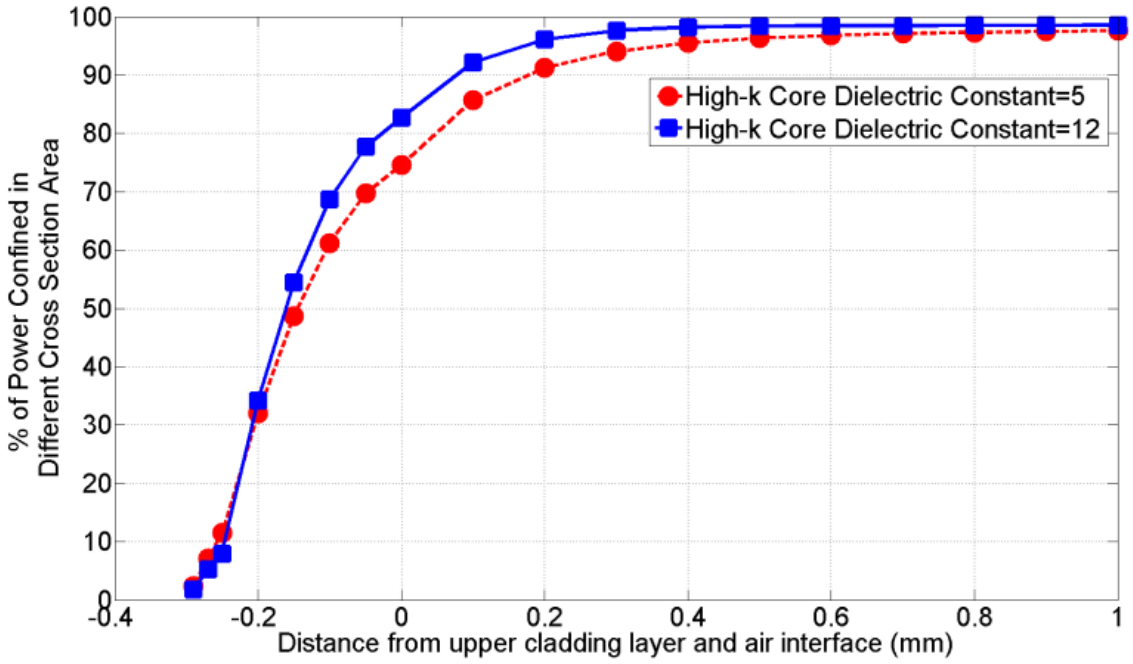

Figure 2.11 Power confinement percentage profiles for different size cross section areas of the waveguides and surrounding air.

2.2.6 Power Concentration on Ribbon Waveguides

Further simulations are carried out to examine the power confinement profile inside and outside of the waveguide structure. Figure 2.11 shows the power confinement percentage profile by changing the size of the measured rectangular cross section area on the ABCD plane. Here, the reference power value is defined as power which transmits through the total cross section area ABCD. The horizontal axis (X-axis) of Figure 2.11 stands for the Z-direction (thickness) of the waveguide geometry shown in Figure 2.3. The zero point of the X-axis represents the long edge of rectangular at the interface of upper cladding and air, positive and negative values on the X-axis mean that this edge moves out of and into the waveguides, respectively. As the waveguide is symmetrical to the X-Y plane (Figure 2.3), only half the size of the structure is studied, where the interval between -0.30mm and -0.25mm represents half of the core region. The width of the rectangular cross section area is equal to that of the waveguide. Figure 2.11 demonstrates that higher dielectric constant (ε_r=12) provides a better and tighter power confinement close to the core region than the lower dielectric constant (ε_r=5). It is also shown that up to 80% of the power is within the low dielectric constant cladding layers, while the high-*k* core region only carries a small amount of overall power. Further away from the waveguide, power carried by the surrounding air is comparatively small for this geometry.

The average transmitted power density (Poynting's vector) at certain position through the cross section area is shown in Figure 2.12. For both low and high dielectric constants, the cladding layers preserve the highest power density, and with increasing dielectric constant, power density increases in the cladding layer. Power densities in the surrounding air are similar for both low-*k* and high-*k* cores, but drops faster with a higher-*k* core. The core region has a lower power density than that of cladding. As the dielectric constant increases the power loss in

the core region increases. The electrical displacement vectors are continuous at the interface of different layers. However, because of the large difference in dielectric constants at each side of the interface, the E-field vector has large discontinuity which results in a large discontinuity of average Poynting's vector.

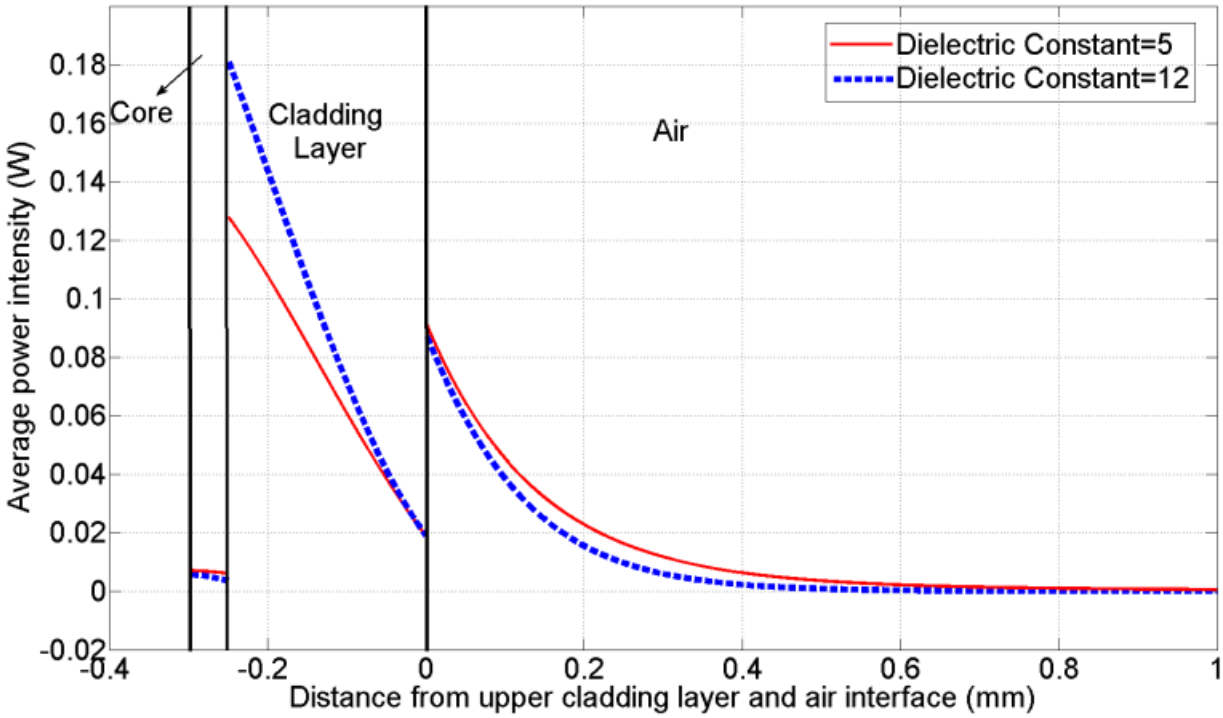

Figure 2.12 Average power intensity at different positions of the waveguides transverse cross section. Only half of the waveguide structure is shown here, the other side is symmetrical to the X-Y plane. Black lines are the interfaces between the core region and cladding, cladding and air, respectively.

2.2.7 Effect of Dielectric Loss of the Core Region

The simulations above are based on high-*k* core material with low loss tangent (0.0035). This satisfies the properties of waveguides made using commercially available Rogers 3010 thin film. However, higher loss tangent may exist for different high-*k* core region materials. Although power transmitting in the core region is significantly small (less than 10%) fraction of the total power, as shown in Figures 2.11 and 2.12, it is worth further analysis. Higher loss tangent of 0.08 for core region with different dielectric constant are investigated in direct comparison with low loss cores (Figure 2.13). The loss factors for both cases are calculated based on the differences between transmitted powers through two different cross section planes transverse to the waveguides. Planes at 5mm and 10mm away from the wave launching port having the same size (plane ABCD in Figure 2.3) are selected. The power difference between these two planes is then converted to power loss per millimeter. For low loss cores, the propagation loss is small and remains constant for high-*k* values ranging from 5 to 14. The loss factor increases by approximately 4 times as the loss tangent is increased by 22 times (from 0.0035 to 0.08). Although the propagation loss is not proportional to loss tangent of the material, it is necessary to use low-loss dielectrics in the fabrication of THz ribbon waveguides.

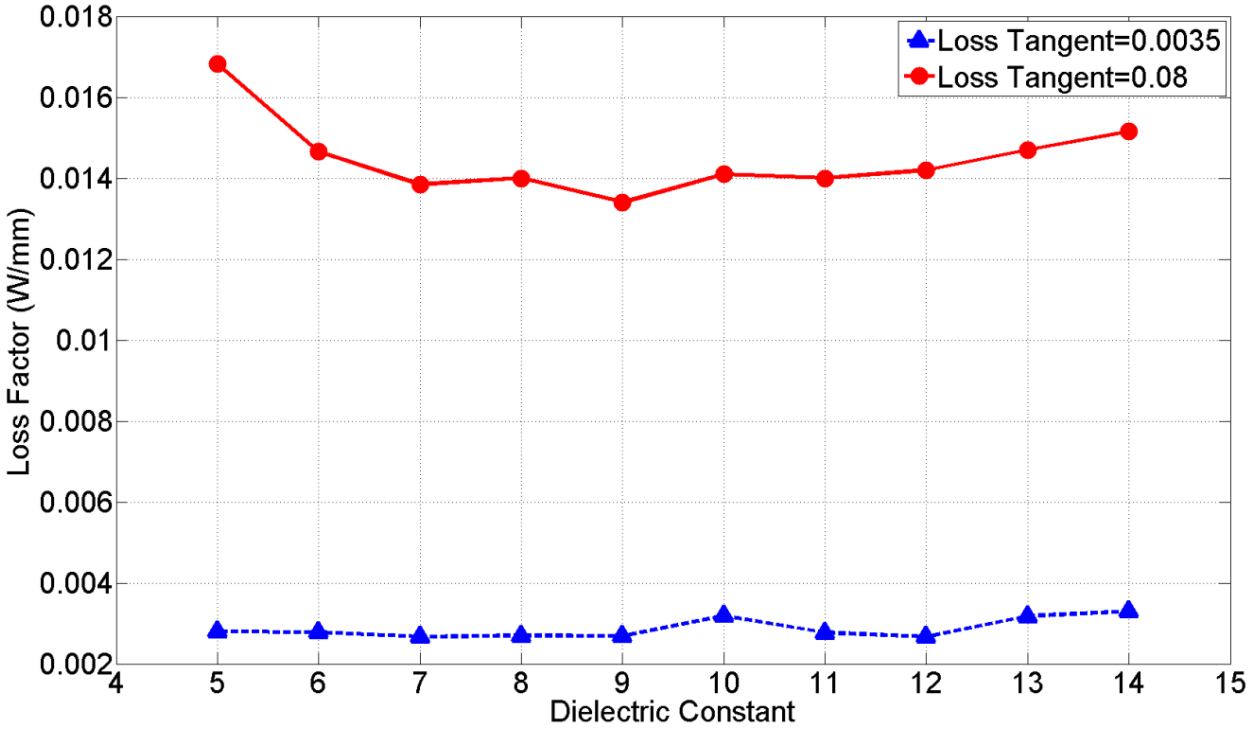

Figure 2.13 Propagation loss for waveguides with core regions having loss tangent of 0.08(Solid line) and 0.0035(dotted line).

2.2.8 Power Loss at Dielectric Waveguide Bends

Simulations for straight dielectric thin ribbon waveguides indicate that higher dielectric constant will provide a better confinement of the transmitted waves, and with a lower dielectric loss of the core region, the losses can be reduced. In addition to straight waveguides, it is necessary to analyze correlations between dielectric constant of the core region to power losses associated with bends in the waveguides.

Slowly varying 90^{o} waveguide bends were simulated to demonstrate the benefit of the high-*k* core region. Figure 2.14 shows the simulated results of waveguide structures with and without a high-*k* core region. The simulation frequency is fixed at 0.2THz, and the field is observed in the cladding region. The field in the waveguide with a high-*k* core region strongly confines the

power in the cladding layers and in turn reduces loss by minimizing the evanescent wave in the air at the bend.

A further study of the curved waveguides with high-*k* cores, including varying the radius as well as the dielectric constant is carried out. Figure 2.15 shows the E-field pattern in the cladding layers by changing the outer radius of the 90^{o} bend. There is more power loss from the waveguide for smaller outer radius (3mm) as compared to larger radius bends. However, the use of high-*k* core region significantly helps in reducing power loss at the bends.

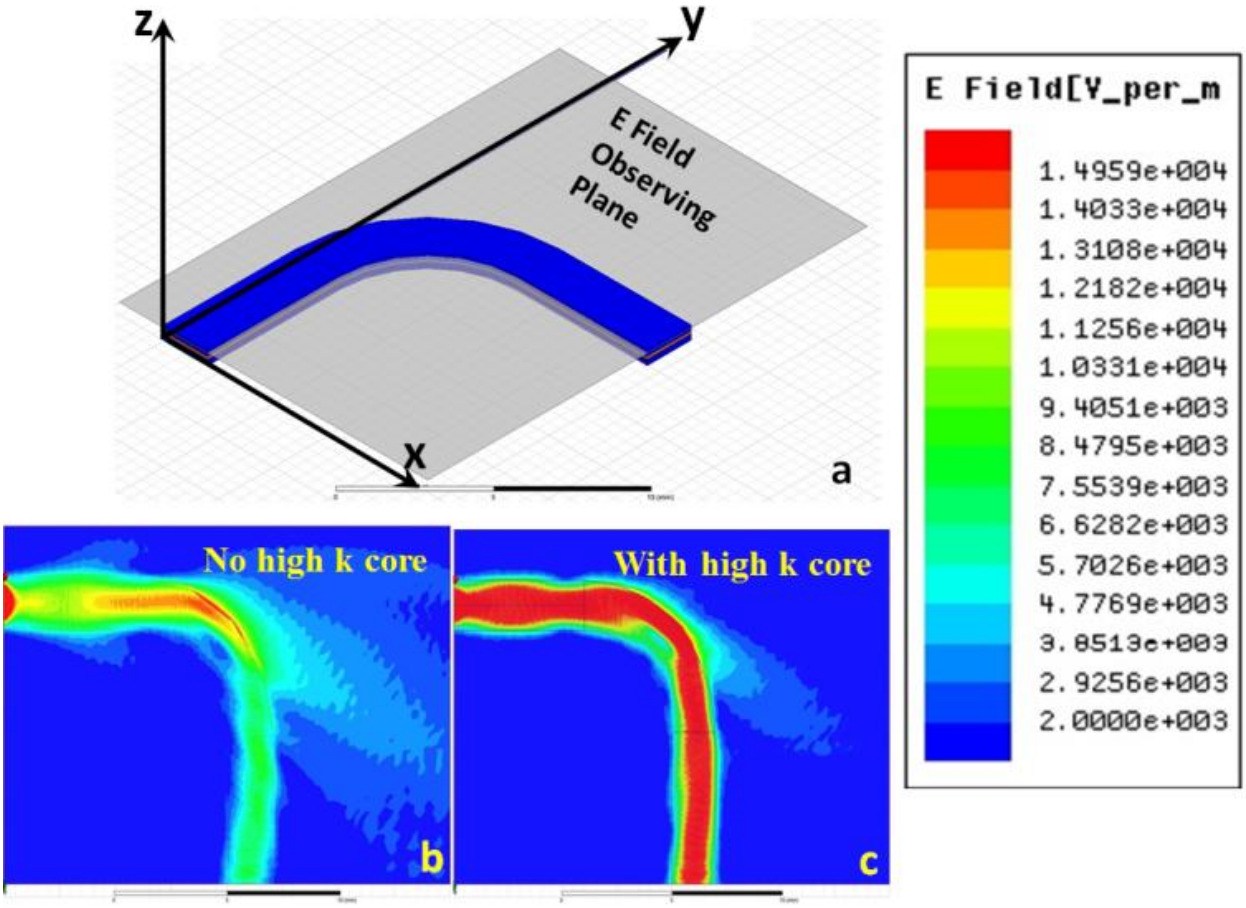

Figure 2.14 (a) A 90^{o} bend ribbon waveguide with cladding, (b) simulated field pattern of this bend having no core region, (c) simulated field pattern of this bend having a core region.

Through simulations it has been shown that an increase in dielectric constant of the core region helps tightly confine the fields to the surface of the core region of the waveguide. Moreover, it also reduces radiation losses at waveguide bends, see Figure 2.16. This figure shows the E-field overlays on the waveguide structure and decrease in radiation loss with increase in dielectric constant of the core region.

Numerical values for power loss and loss factor for each of the curved waveguides have been extracted from the simulations, and plotted in Figure 2.17 and 2.18, respectively. In Figure 2.17, the power loss is the differences between transmitted power through two cross section planes (ABCD) transverse to the waveguide before (0.4mm) and after (3.6mm) the 90^{o} bends. Smallest radius of 3mm has the highest loss. Power loss can be significantly reduced when the outer radius is equal to 6mm or higher, and reaches a minimum for 9mm radius. However, a larger radius, for example, 12mm, has higher power loss, this is due to the longer curve path that wave has travelled and the propagation loss begins to dominate over bent loss. The loss factors shown in Figure 2.18 for the bent part follow a similar trend: larger radius or higher dielectric constant has lower loss factor. Radius of 9mm has loss factor very close to that of 12mm. Based on the dielectric properties and geometry of the core and cladding regions, an optimal bend radius is 9mm.

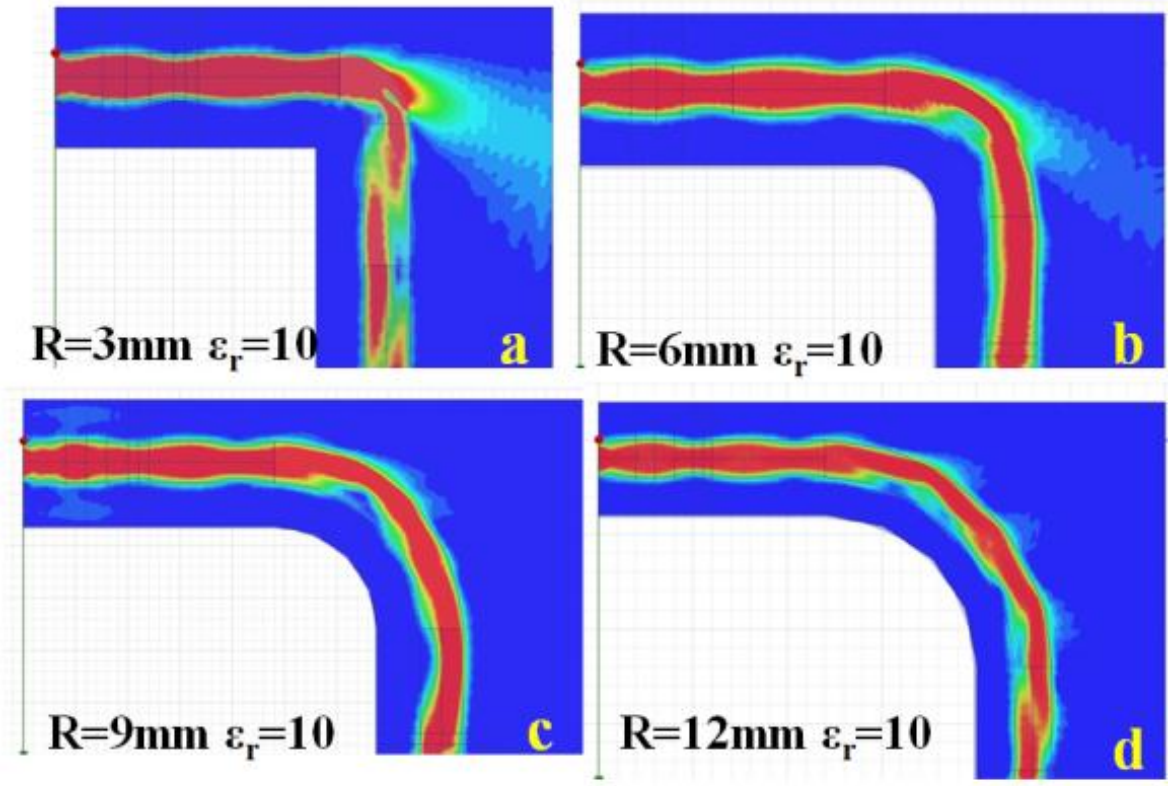

Figure 2.15 E-field patterns for curved waveguides with different bending radius, from (a) to (d), outer radiuses are changing from 3mm to 12mm. See color legend in Figure 13.

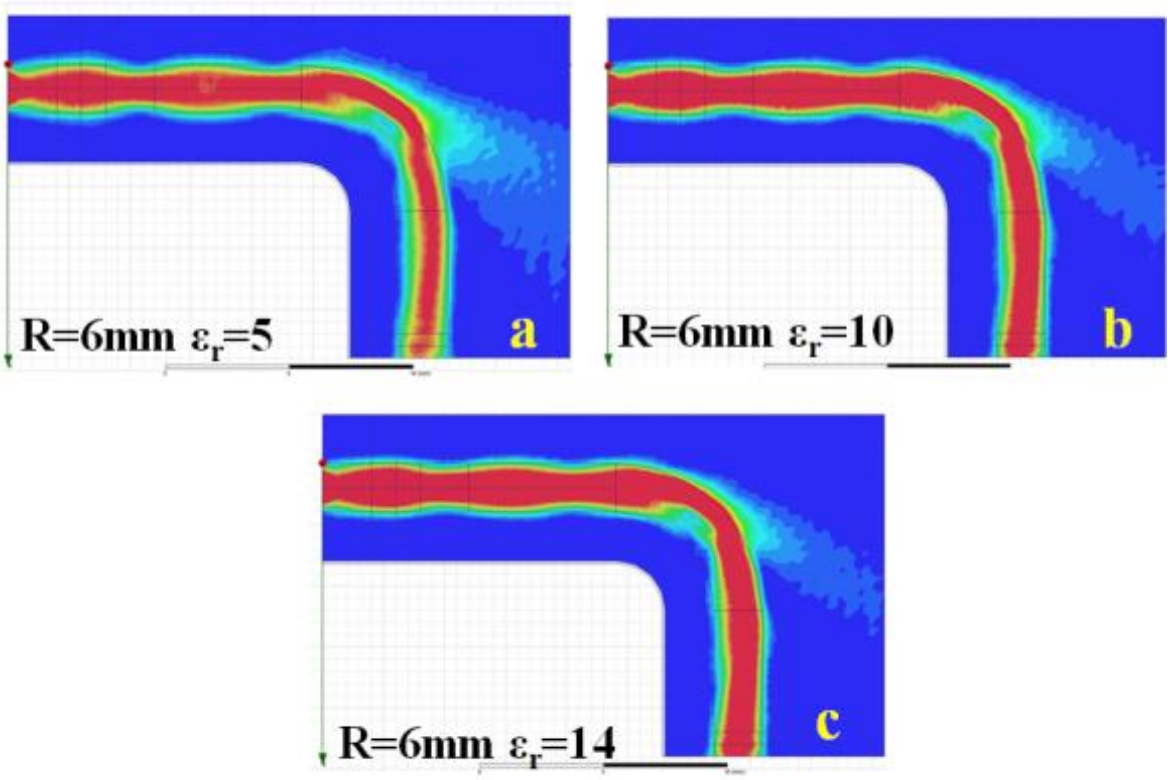

Figure 2.16 E-field patterns for curved waveguides with different dielectric constant core regions, from (a) to (c), ε_r values are 5, 10 and 14, respectively. See color legend in Figure 13.

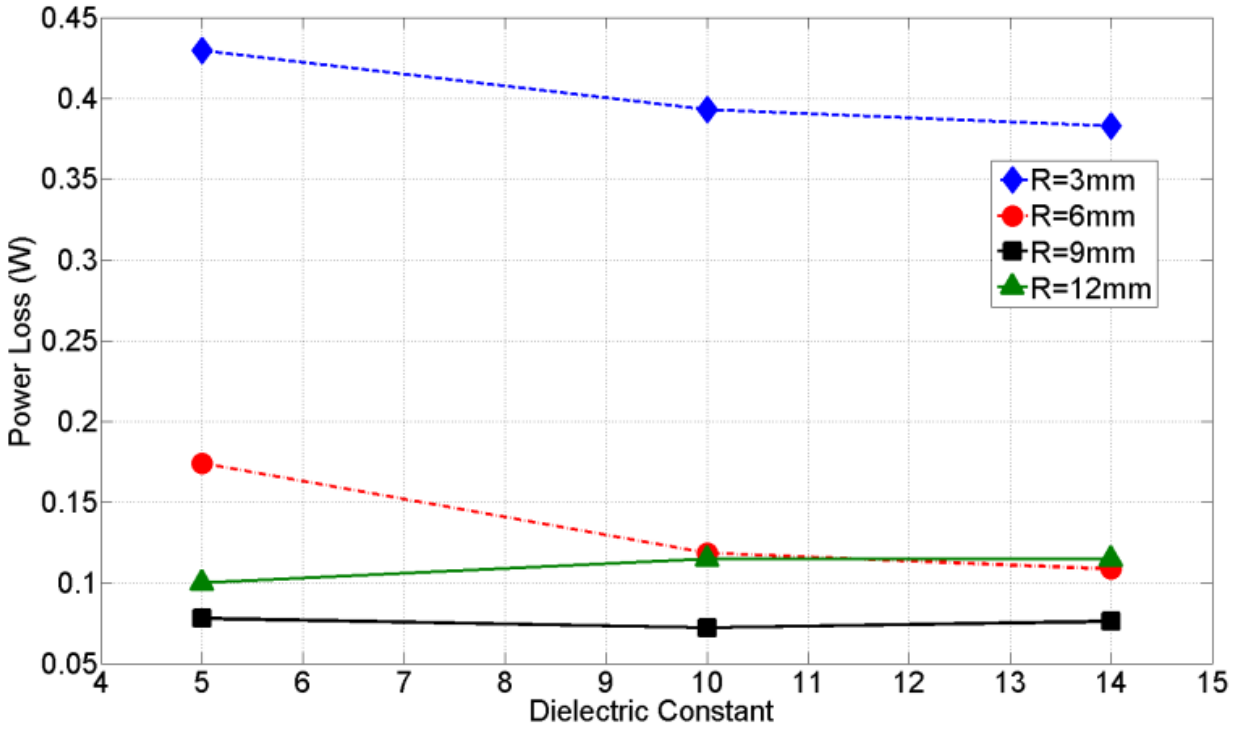

Figure 2.17 Power loss at 90^{o} bends for different dielectric constants of the core region as well as different bend radiuses.

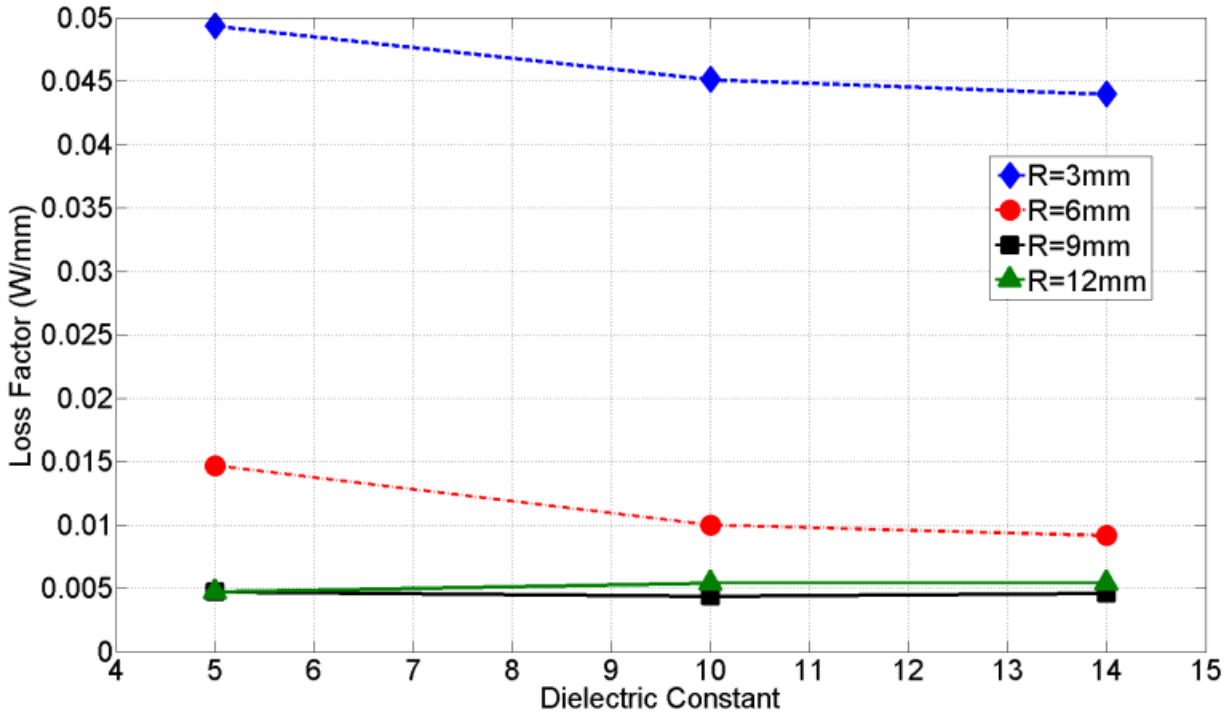

Figure 2.18 Loss factors at the bends of the curved waveguides, with different dielectric constants as well as different bending path radius. The center line of the curve is considered as the effective path that the wave travels.

The above simulation results prove the idea that thin dielectric ribbon structure with cladding layers can be used as planar waveguides or interconnects for THz circuit applications. The high-*k* core is required for both straight and curved structures to help tightly confine the wave to the waveguides. The degree of confinement can be tailored by the thicknesses of the core and the cladding regions as well as their dielectric constant values. Tightly confinement of the propagating signal allows in the design of sharper bends with reduced loss and it also helps in minimizing cross-talk between the neighboring waveguides (adjacent and top-down). The distances between neighbor waveguides required in the THz circuits can be small, and tightly confinement of the the wave helps increase the waveguide density. The key advantage of this waveguide structure is that it provides a possible route to realize low-loss THz waveguides which can be fabricated on planar substrates.

2.3 Material Characterization and Waveguide Fabrication

Materials with high dielectric constant and low loss characteristics are necessary to realize thin ribbon waveguides. There are several candidates which can meet these requirements, for example, alumina (ε_r=9.6), sapphire (ε_r=10), undoped Si (ε_r =11.9) and GaAs (ε_r =12.9). However, challenges still exist in fabricating ribbon waveguides from these materials, as they are expensive and difficult to deposit and pattern with simple micro-fabrication techniques. Therefore, it is necessary to develop materials which are low cost, large area wafer-level compatible, and require and can be processed at low temperatures. This will satisfy the need for the integration of THz waveguides on a host of substrates (organic and inorganic). Furthermore, it is desirable to be able to locally tailor the dielectric constant of the waveguide for designing complex THz circuits (e.g., filters).

A suitable material that meets the above requirements for THz dielectric thin ribbon waveguides is polymer-ceramic nanocomposites. These materials allow tailoring of their electrical and mechanical properties. Polymer nancomposites are made with nano-size fillers dispersed in a polymer host (thermoplastics, thermosets or elastomers). Nanocomposites are low cost and can be deposited on a host of substrates at a low temperature using large area compatible processes such as spin coating, molding, extrusion and inkjet [66]. These materials have been applied in a wide range of applications including manufacturing electronic components such as capacitors, the addition high-*k* nanoparticles in low-*k* polymer matrix allows tailoring the dielectric constant between that of the polymer and the nanoparticles. In general, the nanoparticles provide the electrical characteristics while the host polymer material provides mechanical integrity and low-temperature processing. The combination of dielectric and mechanical properties is hard to achieve in a one component material. The tailoring of dielectric constant allows in the design of novel components of high-*k* and low-*k* materials [67].

Two different fabrication approaches are investigated for thin ribbon waveguides. The first approach uses photopatternable nanocomposites for direct patterning using UV-lithography. The second investigates the use of nanocomposite dry films that can be patterned using laser ablation. Photopatternable nanocomposites can be designed using photosensitive polymer matrix and can be used in the fabrication of thin-film structures on large area substrates [68, 69]. SU-8 100 (Microchem) is used as the photo sensitive epoxy matrix material (binder material). Barium Titanate ($BaTiO_3$) nano-particle powder is mixed in the polymer material to achieve the desired dielectric constants by controlling volume loading. Commercial Rogers 3010 thin film (~100μm) was also used after etching away the copper claddings from both sides.

2.3.1 Material Preparation

Photopatternable epoxy resin (SU-8 100 having low molecular weight) is mixed with nano particles $BaTiO_3$ powder (nominal diameter of 700nm from Inframat Advanced Material) to form high-*k* photopatternable nanocomposite material, as shown in Figure 2.19. To reduce the viscosity, solvents (SU-8 thinner) were also added to the epoxy resin. This helps improve the dispersion of $BaTiO_3$ particle in the polymer matrix. The volume of the solvent was also optimized to achieve desired film thickness during spin coating. To achieve good particle dispersion in the polymer matrix, ball milling of > 100hrs was also carried out. Poorly dispersed particles in the polymer matrix can lead to high losses due to scattering by the particle agglomerates. Furthermore, smaller size particles ($<<\lambda$) are utilized to minimize scattering losses.

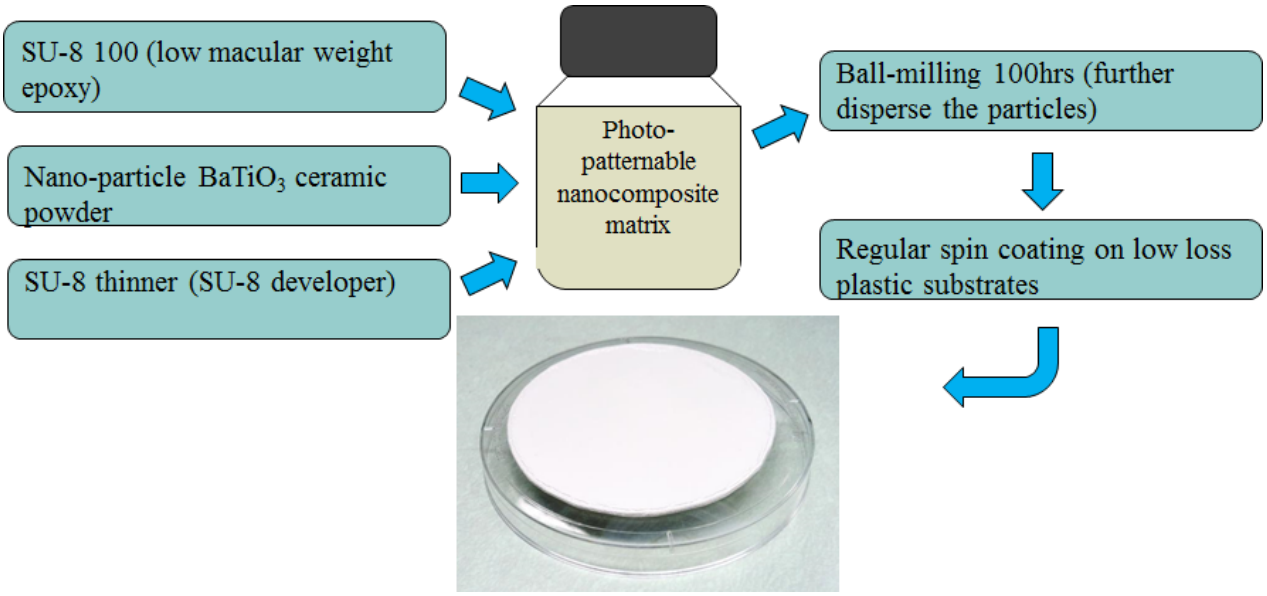

Figure 2.19 Material preparation flow chart of photopatternable nanocomposites.

2.3.2 Material Characterization

Photopatternable nanocomposite material was mixed following different volume ratios of $BaTiO_3$ nanocomposites, and their dielectric properties were measured over a wide frequency range. The matrix was spin coated on Zeonor ZF-188 (Cyclic olefin copolymer, Zeon Corporation) thin film flex substrates. This substrate material has low-loss characteristics in the THz spectral region [70], and was characterized to be chemically inert and compatible with materials in the mixed matrix. Blanket UV exposure was then applied to the spin coated sample for complete cross-linking and curing. Films were then characterized using a THz time-domain measurement system (THz-TDS). A collimated beam impinges on the sample normal to its flat surface and transmitted signal through the sample is measured.

The modified form of Lichtenecker's equation is used to carry out the theoretical calculations for the effective dielectric constants of the polymer-nanocomposite [71]:

$$\log \varepsilon_{eff} = \log \varepsilon_p + v_c(1-k)\log(\frac{\varepsilon_c}{\varepsilon_p}) \tag{2.37}$$

Where ε_{eff} is the effective dielectric constant, ε_p is the dielectric constant of polymer; ε_c is the dielectric constant of the ceramic; v_c is the volume loading ratio of the nanocompsite ceramic; and k is the fitting factor which indicates the dispersion level and air voids in the mixture. The k value between 0.2 and 0.3 usually stands for a well-dispersed mixture. The k value for spin coated polymer nanocomposite is also determined by particle size and shape, moisture and solvent content in the film.

Epoxy resin, SU-8, has an effective dielectric constant ranging between 2.8 to 3 over a frequency range of 0.1 to 1.6THz [72]. The difference can be attributed to molecular weight, curing, air voids and film uniformity. The dielectric constant is approximately 500 for $BaTiO_3$ at frequencies above 0.1THz with particle size around 0.7μm in diameter [73]. Figure 2.20 plots the

averaged dielectric constant values for different volume loadings. The error bars cover the varying range of the measured data for each volume loading, and data is fitted with Lichtenecker's Equation. $BaTiO_3$ ceramic is considered to have an unknown dielectric constant value in order to get an optimized fitting. According to the best fitting results, $BaTiO_3$ has the dielectric constant of 575 and the *k* value is equal to 0.589. Here, the larger *k* value is largely due to large porosity in the films. One of the key advantages of using nanocomposites is that the desired dielectric constant can be achieved by controlling the volume ratios of the polymer and the ceramic. This gives the possibility for tailoring the dielectric properties of the high-*k* core in the design of dielectric thin ribbon waveguides.

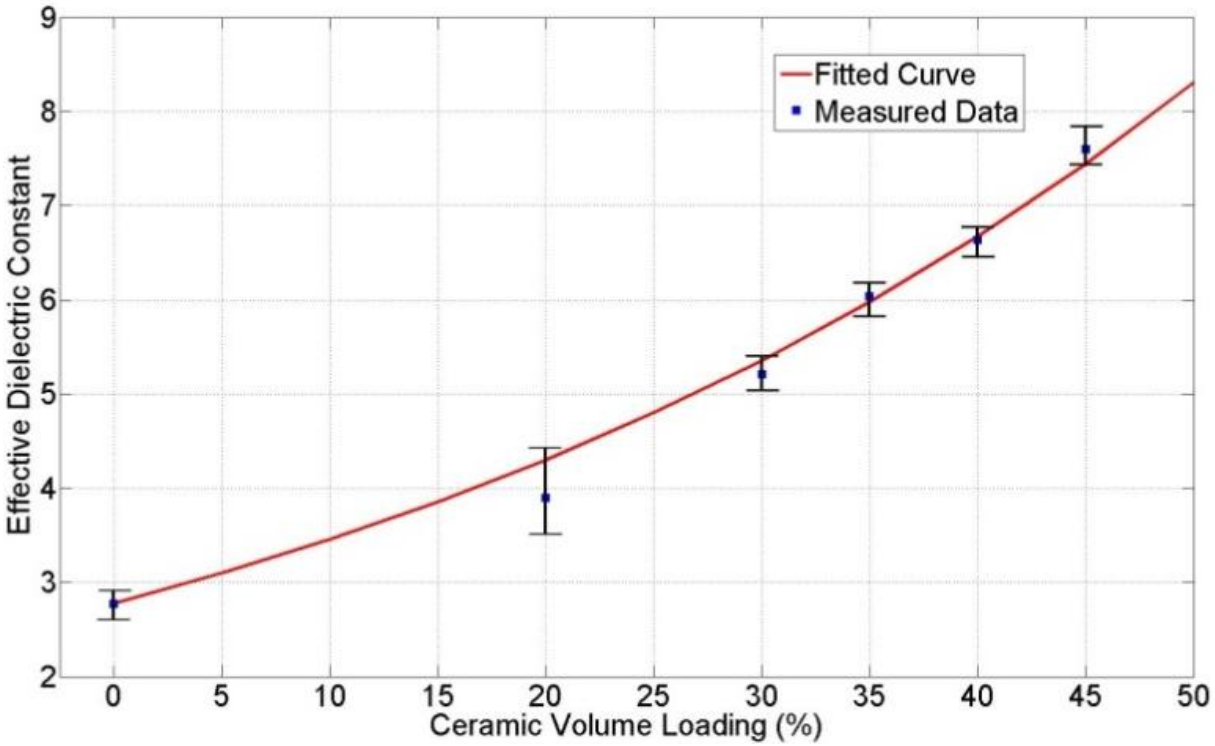

Figure 2.20 Measured dielectric constant as a function of volume loading at 0.2THz. Data fitted using Lichtenecker's equation.

2.3.3 Fabrication of Photopatternable Polymer-Ceramic Thin Film Circuits

The photopatternable thin film circuits were fabricated using the approach described in [74]. A 35% volume loaded mixture was selected and an approximately 100μm thick layer was spin coated on flex Zeonor ZF-250 ($\varepsilon_r \approx 2.35$, 250μm) substrate. However, Long UV exposure time is required due to strong scattering and absorption by the ceramic particles within the film. Figure 2.21 shows the fabricated structures based on photopatternable polymer-ceramic nanocomposite. One more Zeonor cladding substrate layer is then applied on top of the fabricated circuits to form a sandwich structure.

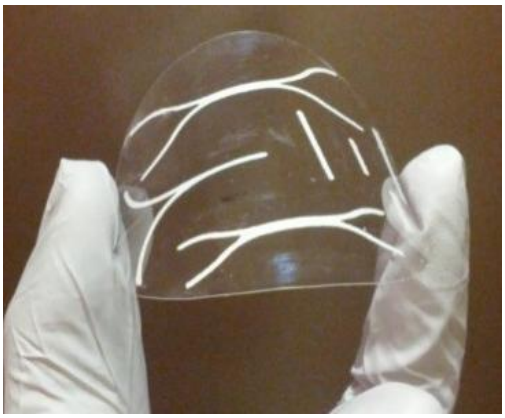

Figure 2.21 Example photopatterned planar THz ribbon waveguide circuits using polymer-ceramic nanocomposite (white) on Zeonor ZF-250 flex 250μm thick substrate (transparent).

2.3.4 Fabrication of Commercial Rogers 3010 Based Thin Film Circuits.

Rogers 3010 thin film was also applied and fabricated as an alternative material for the high-*k* core of the ribbon waveguides. This material is in dry film form which is also made from polymer-ceramic composites. It has a dielectric constant close to 10 and lower tangent loss compared to SU-8 based photopatternable nanocomposite thin films in THz spectral region.

A carbon dioxide (CO_2) laser engraving machine is used for patterning the desired circuit geometries on Rogers 3010 planar dry thin films. The laser has a peak power of 40W and resolution of 50 μm. This setup can realize smooth edges and a high resolution structure on the

nanocomposite dry thin films. An example fabricated THz circuit (power divider) is shown in Figure 2.22. This structure was designed to achieve a power division ratio of 1:2 at the output branches.

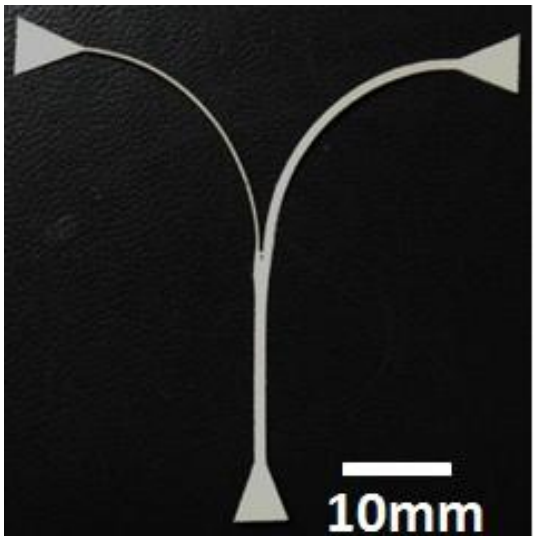

Figure 2.22 Fabricated THz uneven power splitter structure from polymer nanocoposite thin films using CO_2 laser.

2.4 Measurements and Results

Fabricated samples are tested using a THz time domain system (THz-TDS) (Picometrics 2000). Figure 2.23 shows the measurement setup. Two low loss HDPE THz probes (edge coupled) were used in order to focus and couple the THz collimated beam onto the fabricated waveguides from the transmitter and the receiver heads [75].

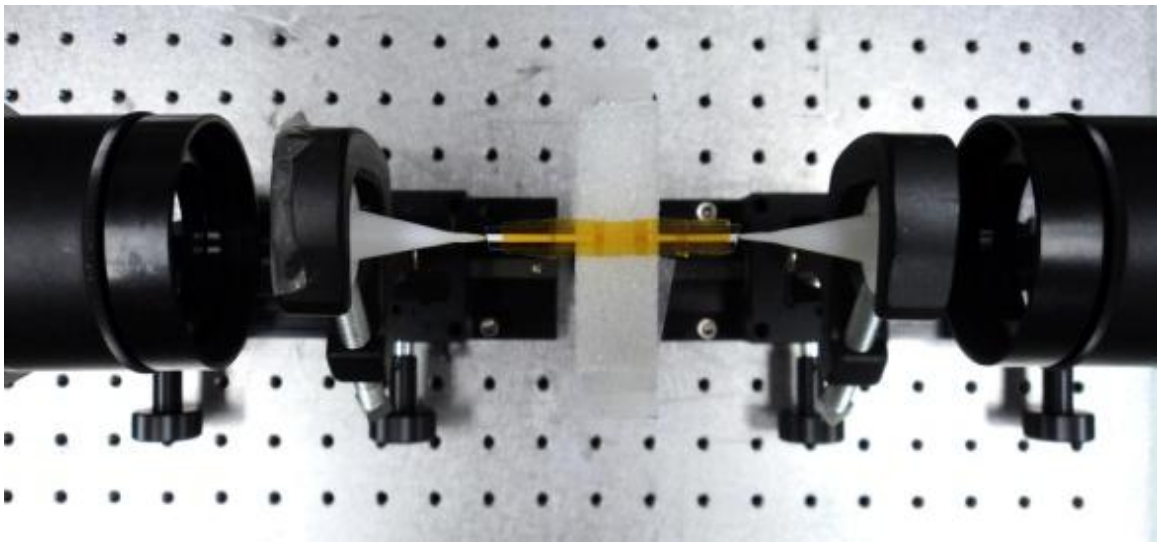

Figure 2.23 Measurement setup for straight line ribbon waveguide with cladding layers placed between the dielectric probes. Also visible are the THz transmitter and receiver heads.

Straight line structures were fabricated and the example structures are shown in Figure 2.24. The photopatternable thin film circuit was fabricated on the bottom Zeonor substrates, and the top Zeonor cladding layer was attached using a tape. Straight line samples with two different lengths are presented in order to acquire the characteristics of signal transmission, as shown in Figure 2.24. For the purpose of examining the benefits of high-*k* core region in the circuits, bare Zeonor waveguides with only the two cladding layers are made and measured. Note that Zeonor waveguides have the same lengths as that with high-*k* core. To reduce the wave reflection at the probe and waveguide interface during the measurements, all of the samples ends are cut out at an angle.

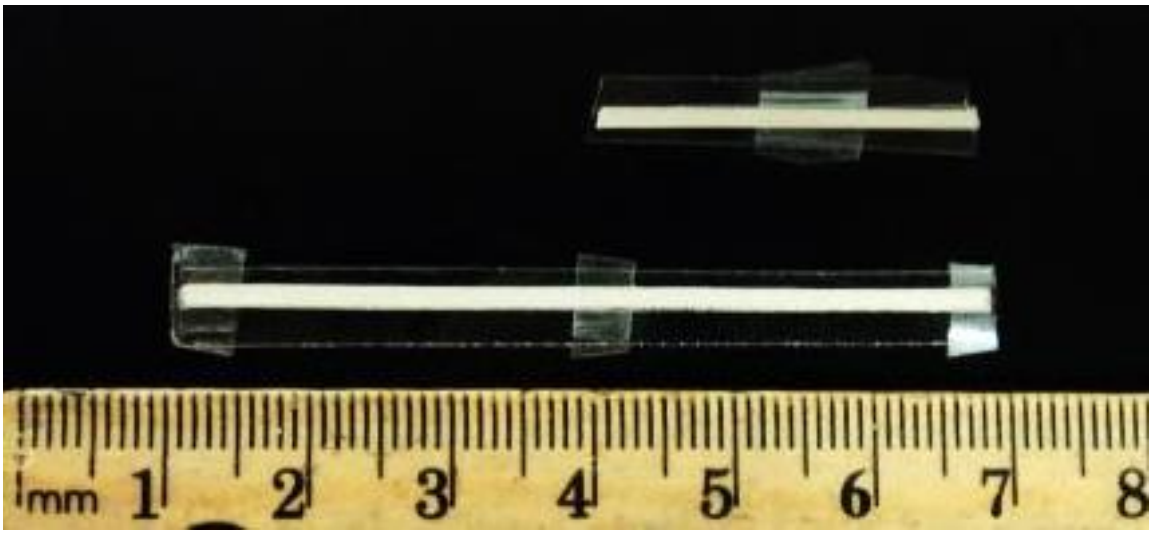

Figure 2.24 Fabricated straight ribbon waveguides with attached cladding layers. Ends are cut at an angle to minimize reflections during measurements.

Waveguides with different high-*k* cores as well as bare Zeonor cladding are measured and the results are shown in Figure 2.25, 2.26 and 2.27. Each figure shows the transmitted signal for both short and long waveguides. Rogers 3010 thin film based samples are shown in Figure 2.25. Photopatternable nanocomposite based samples are shown in Figure 2.26. The differences in the transmitted signal between two lengths indicate the effective transmission loss associated with the waveguides. The transmitted signal in all of the figures decays at higher frequencies. This is an artifact from the generated THz power as well as the dielectric probes which are not optimized for higher frequency bandwidth.

Transmitted signals in bare Zeonor cladding with different lengths are similar (Figure 2.27). According to the simulation results above, wave propagates in both the cladding and the surrounding air; this indicates the low loss characteristic of the Zeonor and air combination. Waveguides with high-*k* core have higher effective losses compared to bare Zeonor, which means that high-*k* materials have higher loss characteristics. A High-*k* core helps to confine the fields in the waveguides, but on the other hand increases the total signal loss if the dielectric loss is high and the surface is rough. The higher confinement of propagating waves is very important to achieve high density integration of THz interconnects.

Comparing Figures 2.25 and 2.26, one may find that photopatternable nanocomposite based waveguides have higher loss than Rogers 3010. This can be attributed to lossy SU-8 (epoxy dielectric), and very likely due to poor dispersion of ceramic particles in the polymer matrix, and film surface roughness. To minimize losses, polymer matrix with lower loss should be selected. Losses can also be reduced by improving the dispersion of particles in the matrix material through the use of surfactants during the milling process and also by minimizing porosity by using bimodal particle distribution [10].

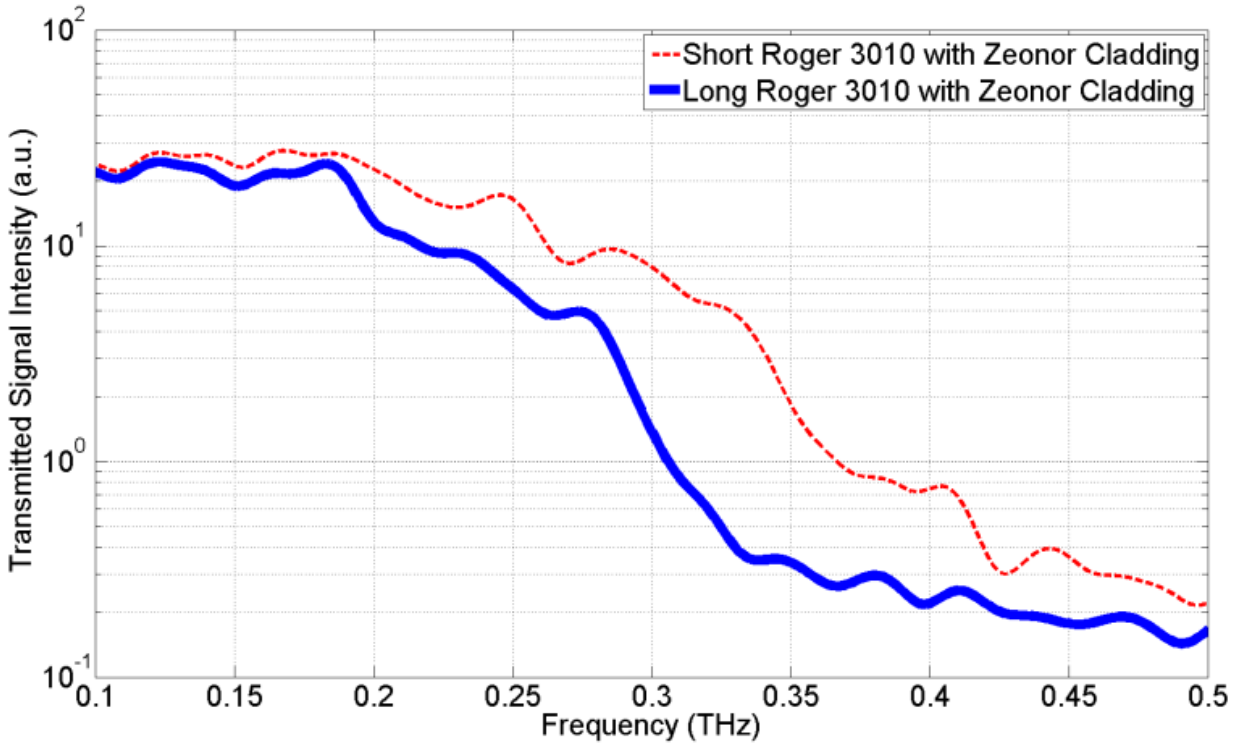

Figure 2.25 Transmitted signal intensity through short (28.5mm) and long (57mm) waveguide made using Rogers 3010 as the core region.

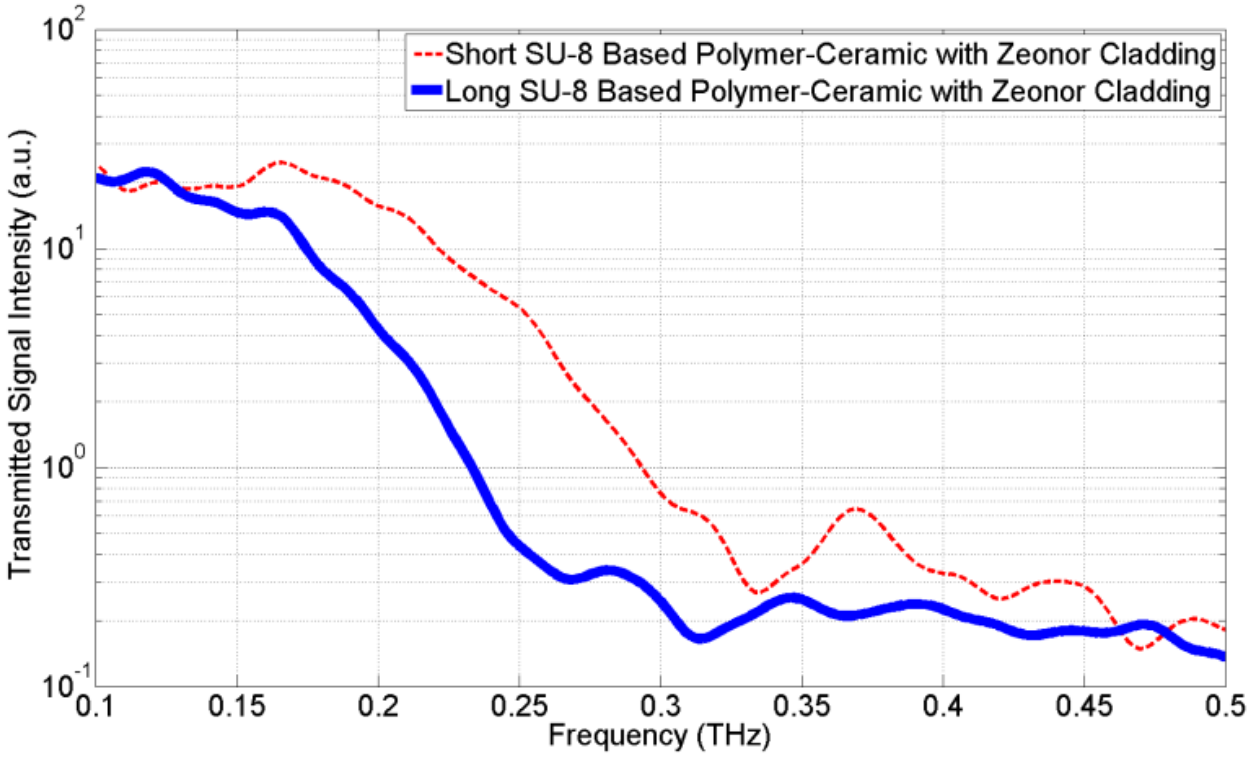

Figure 2.26 Transmitted signal intensity through short (23 mm) and long (60 mm) waveguides made photopatternable nanocomposite as the core region.

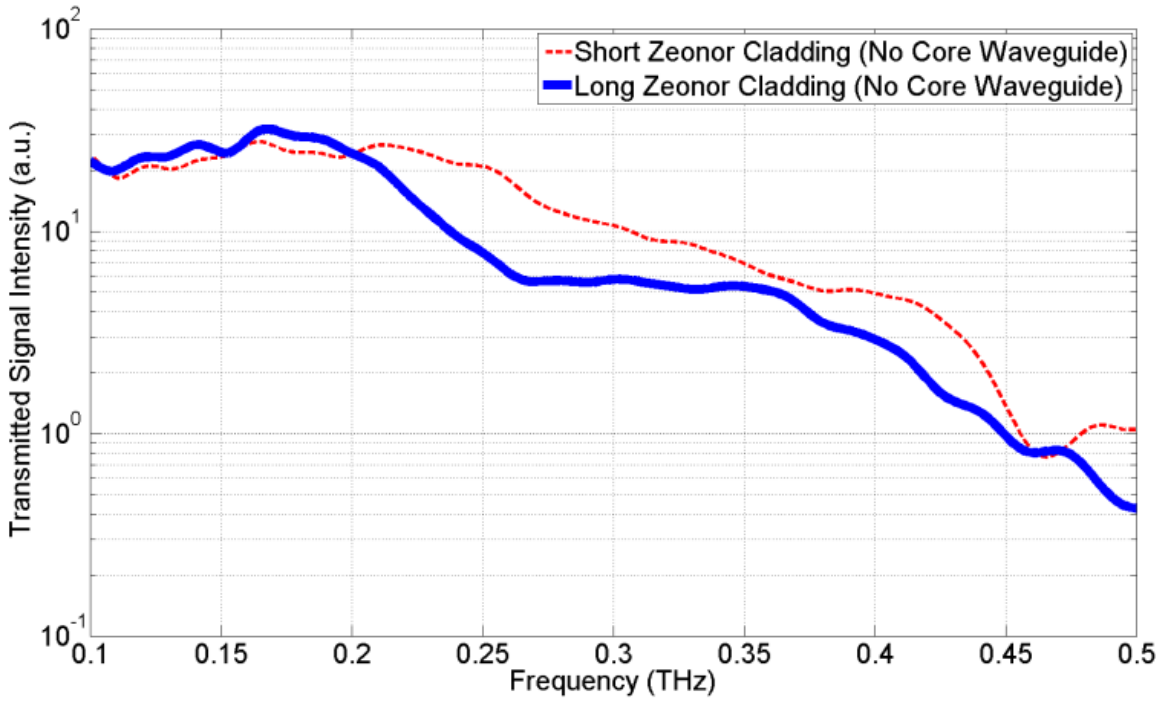

Figure 2.27 Transmitted signal intensity through a short (27 mm) and long (61 mm) waveguides made using bare Zeonor cladding layers.

Figure 2.28 shows a waveguide with a bend placed in a test setup. Bare Zeonor cladding with and without Rogers 3010 film as the core region were also tested. The outer radius of the curve is 10mm. Measured transmitted signal through the two samples is shown in Figure 2.29. Clearly, the waveguide with a Rogers 3010 core has a higher transmitted signal than the bare Zeonor sample. This result further validates the simulations showing that the waveguides with high-*k* core regions increase the field confinement along the waveguide and reduce radiation loss along the curved path. Low-transmitted signal at higher frequencies is an artifact due to poor coupling of THz radiation onto the waveguides from the THz transmitter and receiver. Also, at higher frequencies the material loss begins to dominate.

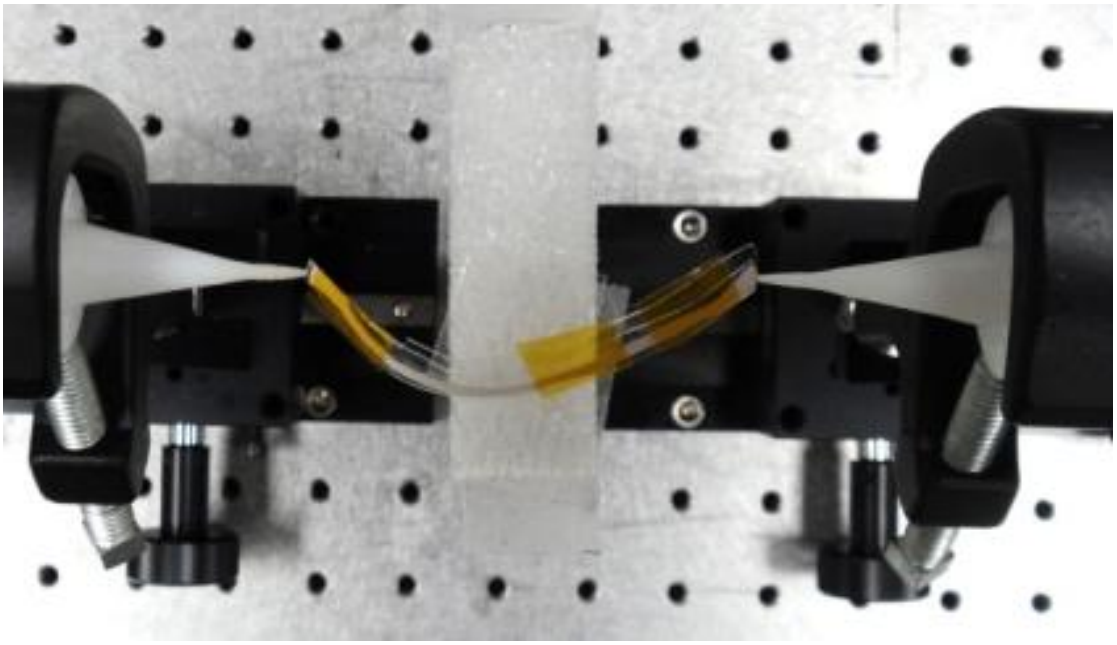

Figure 2.28 Measurement Setup for curved Rogers 3010 ribbon waveguide with attached Zeonor cladding layers

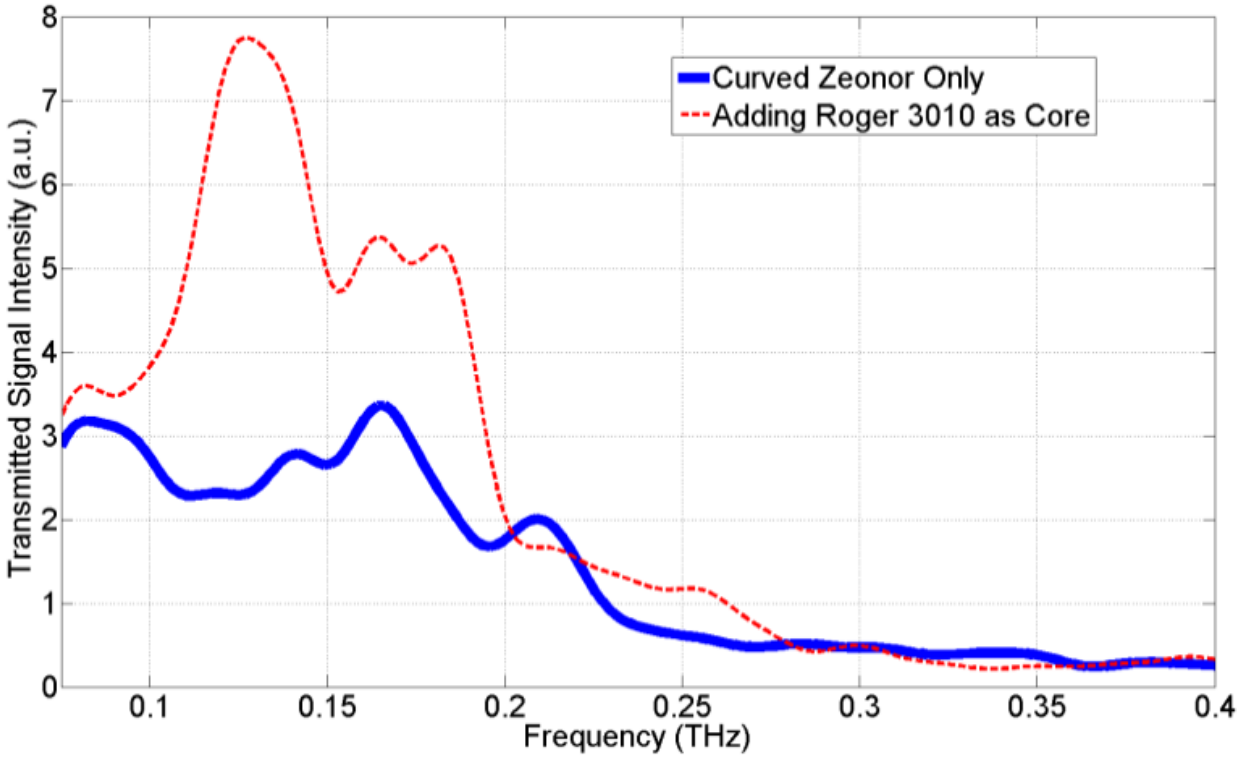

Figure 2.29 Transmitted signal intensity for curved structures made from bare Zeonor cladding and a structure having Rogers 3010 as the core region.

2.5 Modified Thin Dielectric Ribbon Waveguides

Previous sections discussed the theoretical calculations, simulation and measurement results of thin dielectric ribbon waveguides with cladding regions. It was shown that they were good candidates and suitable interconnects for THz integrated circuits. Those results are based on the condition that there is no surrounding on top and bottom of the cladding layers. However, in the practical circumstances, the waveguides might be fabricated and packaged at the wafer level and may be in contact with different layers stacking on each other to build up the integrated circuits. As mentioned above, cladding layers can serve as isolation layers between different circuit levels. For high frequency applications, low loss dielectric materials are very likely to be the adjacent layers on top and below the cladding layers, however, in some instances there may be metal ground plane surrounding the waveguides. The waveguiding properties of the thin dielectric

ribbon waveguide must be reconsidered and analyzed. According to the simulation results shown above, a significant amount of wave still propagates in the area outside the claddings and then radiate out. Adding metal plates on both sides could possibly "squeeze" the wave back into the waveguides and help reduce propagation losses, but the conductor loss also need to be accounted for. The following section will again use FEM simulation method (Ansoft HFSS) to study the case that conductive layers are placed on top of and below the thin dielectric ribbon waveguides.

2.5.1 Parallel plates assisted double cladding layers thin dielectric waveguide

The schematic geometry of thin dielectric ribbon waveguides with claddings inserted between two parallel metallic plates is shown in Figure 2.30. Two metal plates are separated by the total thickness of the dielectric ribbon waveguide. In this drawing, the wave propagates toward the direction into the paper. The widths of the parallel plates are much larger than that of the ribbon waveguide. This assumption is practical since usually the size of the waveguide on the circuits is much smaller comparing to the conductive substrates (ground planes).

Figure 2.30 Schematic geometry of thin ribbon waveguide inserted between two metal parallel plates

The waveguide parameters for simulation in HFSS are same as those in Table 2.2, and two conductor layers are added on top and bottom of the original waveguide that was shown in Figure 2.31. The simulation frequency is set as 200GHz and the E-field pattern along the waveguide after simulation is shown in Figure 2.31b. In comparison to Figure 2.31a which is the E-field pattern without the metallic parallel plates, it is clear that the power which was radiating

out of the cladding has been completely confined within the region between the parallel plates. Also, similar to the waveguide without the plate, the wave is more likely to propagate closer to the high-*k* core. From this point of view, it is necessary to examine the confinement of the power using different dielectric constants for the core region. Figure 2.32 shows the E-field patterns of transverse cross section of waveguide with difference dielectric constants used for core region.

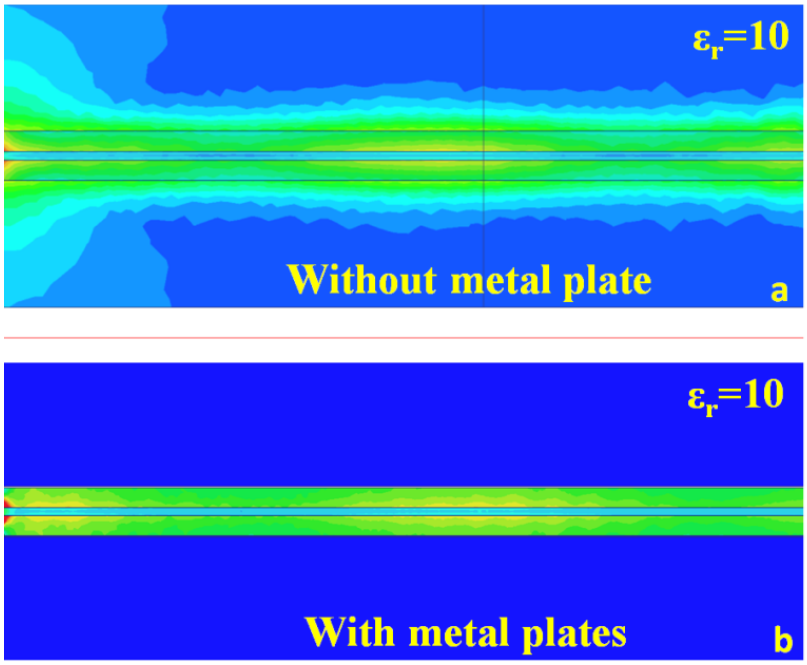

Figure 2.31 E-field patterns along the waveguide without parallel plates (a) and (b) with parallel plates

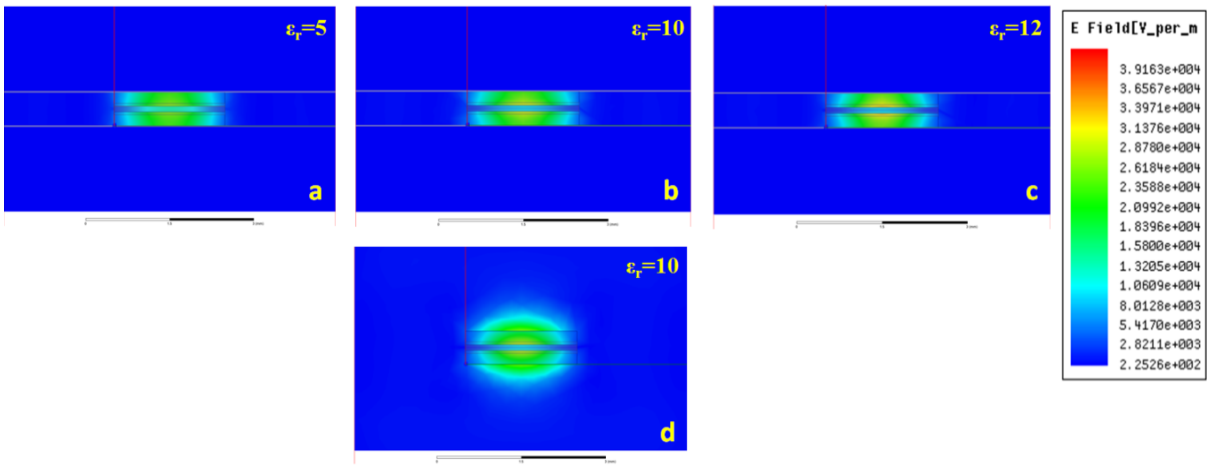

Figure 2.32 E-field patterns transverse to the waveguide having different core dielectric constants with metal parallel plates, a): ε_r=5, (b) : ε_r=10 and (c): ε_r=12. (d) shows the E field pattern of the waveguide without the metallic parallel plates

Similar to the waveguides without the parallel plates, the power confinement is stronger when the dielectric constant of the core region is larger. As predicted, metallic parallel plates can "squeeze" the wave into the waveguide region, this can be further proved by comparing Figure 2.32(b) and (d), the power radiating out of the waveguide (2.32 (d)), has been restricted into the cladding layers by the "pressing" of the metallic parallel plates on both sides.

Table 2.5. Numerical values for power confinement and loss factor of thin ribbon waveguide with metallic parallel plates

	Position from launching port	Power (W) through ABCD plane ***without*** parallel plates	Power (W) through ABCD plane ***with*** parallel plates
ε_r=5	5mm	0.5828	0.6936
	10mm	0.5695	0.6801
	Loss factor (mW/mm)	**2.7**	**2.7**
ε_r=10	5mm	0.6031	0.6896
	10mm	0.5878	0.6769
	Loss factor (mW/mm)	**3.1**	**2.5**
ε_r=12	5mm	0.6251	0.7238
	10mm	0.6091	0.7086
	Loss factor (mW/mm)	**3.2**	**3.1**

The power confinement as well as the loss factor for the thin ribbon waveguide with parallel plates can be investigated numerically by extracting the power flowing through each transverse surface of the waveguides, which is shown in Table 2.5. Here, ABCD plane represents the same plane as shown in Figure 2.3. At the same position from the launching port, power confinement is stronger in the waveguide with metal plates. It can due to a better coupling between the waveports and the waveguides, which can be seen from Figure 2.31. For each dielectric constant, the difference of the loss factors is not large between with and without the parallel plates structures. This contradicts the general understanding that conductor loss can be large at high frequency. This could possibly due to the reason that the power radiation outside the original

waveguide is equivalent to the conductor loss associated with the metallic plates. A structure with parallel metal plates will be of significant importance for future studies.

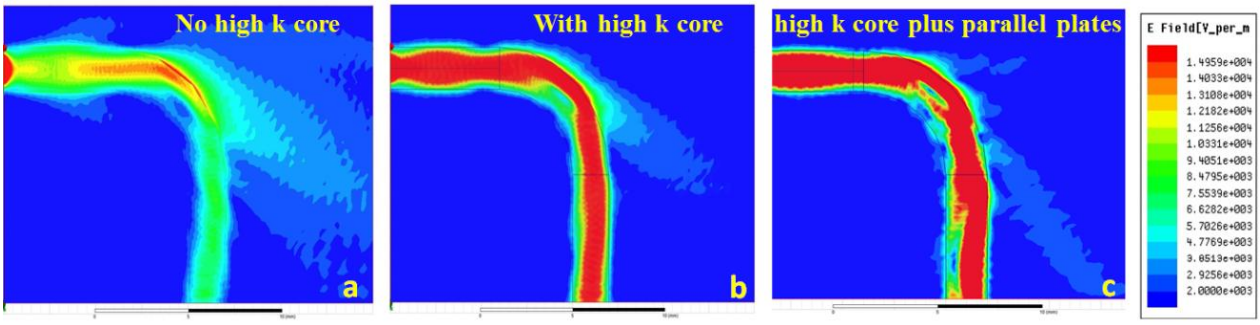

Figure 2.33 Comparison between thin dielectric waveguides. (a) no high-*k* core, (b) with high-*k* core, and (c) high-*k* core plus metallic parallel plates.

Since the wave confinement of the thin ribbon waveguide with parallel plates is better, it is necessary to study how the wave propagates at sharp curves/bends. The simulations have been setup up based on the model shown in Figure 2.14a, additionally, two metallic parallel plates are mounted on top and bottom of the curved waveguides. The simulation results is shown in Figure 2.32c, which is compared with b and c in Figure 2.14, and shown again here as Figure 2.33a and b. The radius for all of these are set at 6mm and ε_r=10 for the high-*k* dielectric constant. Comparing with Figure 2.33a and b, less power is radiated out for the ribbon waveguide with parallel plates, it help guides more power through the bent region. This indicates that parallel metal plates are beneficial at the waveguide bends, it helps reduce radiation losses.

Metallic parallel plates itself can be considered as a waveguide which is able to operate in THz region, as already discussed in chapter 1. But, it has drawbacks such as high conductor loss at high frequency and low capability to preserve power at bends. According to [64], both TM and TE modes can be excited and propagate between two metallic plates. The cutoff frequency for both TM and TE modes, which is also given in [64], can be written as:

$$f_c = \frac{n}{2d\sqrt{\varepsilon_1}\sqrt{\mu_0\varepsilon_0}}, \text{ n=0, 1, 2, 3…} \quad (2.38)$$

Where d is the distance between two plates, ε_1 is the dielectric constant of the filling material, μ_0 and ε_0 are the permeability and permittivity of vacuum. Note that the TM_0 and TE_0 are allowed, which are reduced to TEM mode. Comparing equation 2.38 to equation 2.36, in which m can also be zero and allow TM_0 and TE_0 to propagate, TM_0 (TEM for parallel plates) mode with zero cutoff frequency is allowed to propagate as two types of waveguides are combined together. Based on the structure parameters in the simulation model, d=100μm +250μm × 2=600μm, the cutoff frequency of TM_1 and TE_1 modes for metallic parallel plates is approximately 163GHz, but for thin dielectric ribbon waveguide, the TM_1 cutoff frequency is around 214GHz, which indicates TM_1 of metallic parallel plates can be excited and propagated but TE_1 mode is not possible when the simulation frequency is at 200GHz. Above all, TEM, TM_1 from metallic parallel plates and TM_0 from thin dielectric ribbon waveguide are only allowed to propagate in this waveguide thickness configuration.

2.5.2 Parallel plates assisted single cladding thin dielectric ribbon waveguide.

The waveguide structure introduced above shows great performances to confine the power closer to the high-*k* core and guide the wave through a curved path. The fabrication process is simple to make such a structure, but it requires some extra steps to keep the space between the metallic parallel plates open with vacuum or air. In addition, double cladding layers stacking on each other require good alignment to create high quality waveguide. To address this problem and simplify the process, another waveguide combined with metallic parallel plates is proposed and studied through simulations, which is shown in Figure 2.34. Here, the high-*k* material directly contacts to the bottom metal plate, while avoiding the use of cladding layer below the high-*k*

core. The whole region between the metallic plates is filled with low-*k* material. The idea of this structure originates from the waveguide introduced in last section, which can be further modified by parallel placing a perfect electric plane in the middle position between two metallic plates. The simulation results will not change since the E-field (quasi-TEM) is almost perpendicular to this perfect E plane and the structure is also symmetrical regarding to the plane. To mimic a practical case, a copper plate is used instead of the perfect electric plane. This waveguide structure is easier to fabricate than that with double claddings. It only requires patterning high-*k* strip on a planar substrate deposited with metal layer and fill the open space with low-*k* material before depositing the second metal layer. Such simple process is worthy to be studied, and the simulations results are shown below.

Figure 2.34 Schematic of waveguide with high-*k* core surrounded by low-*k* material in metallic parallel plates.

The model setup for the simulations has two metallic parallel plates having width of 5mm and separated by 150μm, a high-*k* strip with the thickness of 50μm and width of 1mm is placed on the bottom plate. The large difference between the widths of metal plates and high-*k* core can help to eliminate strong reflection from the edge of the waveguide in simulations. The rest of the region is homogeneously filled with low-*k* cladding having ε_1=3. This waveguide structure can be fabricated by laminating a low-*k* material (e.g. Liquid Crystal Polymer (LCP), Rogers 3003) on the high-*k* material ($BaTiO_3$ or Rogers 3010) pre-patterned metal surface. Figure 2.35 shows the E field patterns transverse to the propagation direction of the waveguides with different dielectric constants for the high-*k* core. The white slots are the copper plates on top and bottom

of the dielectric waveguide. It is shown that higher dielectric constant core can confine more power at the interface of different materials, and this is the same as the results of both double claddings thin ribbon waveguides with and without metal parallel plates.

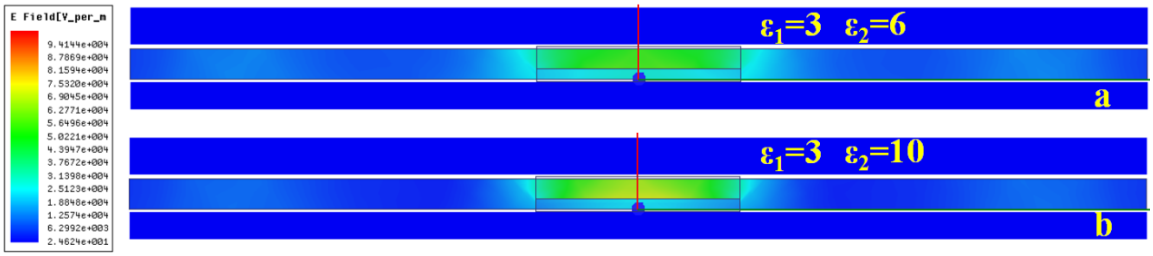

Figure 2.35 E-field patterns transverse to the propagation direction of the waveguides having dielectric constants of (a) ε_2=6 and (b) ε_2=10.

Like other waveguide structures studied in this work, the curved structure of this waveguide is also simulated, and the results of E field patterns for different curving radius are shown in Figure 2.36. The metal plates are covering the entire blue area. It is clearly showing here that with the high-*k* core, power can be confined along straight line, and the waveguide still can guide the wave through a curved path. The larger turning radius provides more power to be re-directed, which is same as those for previously studied waveguides.

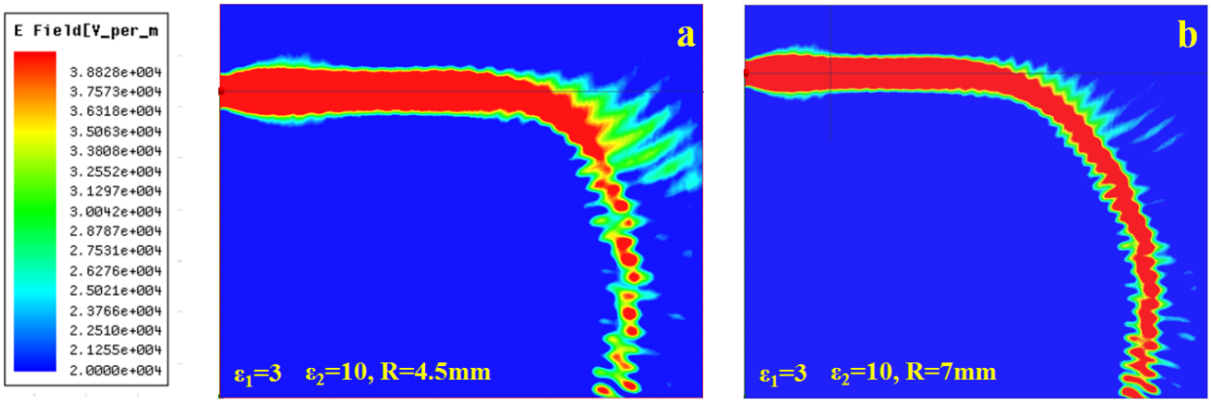

Figure 2.36 E field patterns for curved waveguide structure of high-*k* core surrounded by low-*k* material with different turning radius (a): 4.5mm, and (b) 7mm

The loss factor for a straight waveguide of this type is also studied, and the extracted numerical values are shown in Table 2.6. It has proved that dielectric constant of 10 could provide more power confinement than that of 6 at the same position along the waveguide, and shows smaller loss factor. However, the power loss factor for both 6 and 10 in Table 2.6 are approximately 10 times larger than the waveguide studied above. This is possibly because the effective conductor loss from metallic plates is dominant in this waveguide configuration. Lower dielectric constant means less power confinement to the interface of two dielectric materials, and the wave propagates closer to the upper metal plate, which results high power loss.

Table 2.6 Numerical values for power confinement and loss factors for waveguides with different high-*k* dielectric constants (150μm plate separation)

Position	ε_r=6	ε_r=10
5mm	0.8969	0.9445
10mm	0.8191	0.8888
Loss factor (mW/mm)	**31.12**	**22.28**

The problematic high loss factor of this type of waveguide needs to be solved first before applying to real circuit applications. This can be done by thickening the low-*k* layer on top of the high-*k* core, which keeps the confined power far from the conducting metal plate and reduces the conductor loss. Table 2.7 shows the results for the simulation with an increase in the thickness of top layer from 100μm to 250μm. This is exactly the half size of the thin dielectric ribbon waveguide mentioned in the last section. It can be seen that the loss factor is reduced.

Table 2.7 Numerical values for power confinement and loss factors for waveguides with different high-*k* dielectric constants (300μm for plate separation)

Position	ε_r=6	ε_r=10
5mm	0.7136	0.7247
10mm	0.6690	0.6858
Loss factor (mW/mm)	**8.92**	**7.78**

As mentioned earlier, acceptable propagation modes are determined by the thickness of the waveguide between the metallic parallel plates, which is also the separation between the two plates. In the first case, which has higher power loss, the cutoff frequency is about 577GHz. Thus, only TEM mode for parallel plates and TM_0 for dielectric ribbon are allowed to propagate since the simulation frequency is 200GHz. In the second case that has low propagation loss as mentioned above, the cutoff frequency for TM_1 for parallel plates is approximately 289GHz. For the simulation frequency of 200GHz, only TEM mode for parallel plate and TM_0 mode for ribbon waveguide are allowed to propagate.

In this chapter, THz thin dielectric ribbon waveguides were systematically studied. Basic theoretical calculations show that the cutoff frequency for each propagation mode is related to the total thickness of the high-*k* core and cladding layers. Simulations results especially numerical values have shown that such a waveguide is able to confine the power along a straight line. With the assist of high-*k* core, THz waves can be tightly confined within the low loss cladding layers of the waveguides and thus reduce the radiation loss along curved paths (waveguide bends). In order to prove this and make such a waveguide practical, two alternate fabrication methods: photopatternable nanocomposites with tailorable dielectric constant, and

laser cut Rogers dry thin films process have been developed. Several straight and curve waveguides have been fabricated and tested. Results show the possibility of such waveguides for applications in the design of planar THz integrated circuits at wafer level. These waveguides are compatible with a host of substrates (including flex substrates) because of low temperature processing requirements. In addition, to simplify the fabrication process of manufacturing such waveguide for a real circuit or device, two other modified waveguide structures were studied through detailed simulations. It is shown that thin dielectric ribbon waveguide with cladding layers inserted into a metallic parallel plate can further confine the power into the cladding layers and reduce the loss for both straight and curved waveguides. The second modified structure has been designed to further reduce the manufacturing complexity, and it also shows good power confinement for straight and curved paths albeit with increase in propagation losses. These structures show great potential to realize more complex THz integrated circuits on large area substrates.

Chapter 3 THz Active Device: Nanowire THz detector Element

As discussed in Chapter 1, semiconducting nanowires have drawn attention in the recent years and considered as another nanoscale building block for 1-D electronic devices. Like Carbon nanotubes (CNTs), they can easily be transferred from native substrates onto a vast number of substrates using dielectrophoresis (DEP) allowing heterogeneous integration. The growth mechanism of nanowires has been well studied and large amount of high quality semiconducting nanowires can be synthesized with controllable length and doping levels [76]. This provides the possibility of manufacturing more reliable nanoelectronic devices with close to uniform characteristics across the wafer than CNT based devices. CNTs differ from each other significantly with respect to length, defects, and thus difficult to achieve uniform properties, and formation of integrated circuits using CNT is still a major challenge.

Like its bulky counterpart, semiconducting nanowires can be used to create nanoscale p-n junctions and form Schottky and Ohmic contact with proper metals under controlled conditions [77-80]. Instead of fabricating small devices to achieve high cut-off frequency, use of nanowires for high frequency device fabrication readily provides an alternate method to realize THz devices where high cut off frequency is required. Here, III-V compound GaAs nanowires are used in the fabrication of THz Schottky diode detectors. Furthermore, a novel self-alignment fabrication process, which has been successfully used to create nanoscale features for CNTs based Schottky diode detectors [81], is adopted here and further refined to achieve small devices using simple photolithography process.

Strong nonlinearity in the I-V characteristics of a diode is required to achieve efficient rectification. Electromagnetic waves are rectified and converted to DC signal which is read out by a low frequency CMOS backend circuit (Figure 3.1). For high frequency designs, in the THz

range, apart from small device size, high electron mobility is also very important to achieve high cutoff frequency. GaAs nanowire has shown electron mobility well above 4000cm^2/V·s [82], and is considered as a good candidate in the design of high frequency diodes. For coupling of EM waves from free space to the diodes, an antenna is integrated with the diode element. Good impedance matching between the diode and the antenna is necessary for efficient power transfer. For imaging applications, wide band impedance matching is desired. However, this is challenging when small pixels are required in the design as in the case of a THz focal plane array (FPA). Impedance matching circuit can occupy significant surface area. In order to improve impedance matching between the diode and the antenna, a novel process is utilized as discussed below.

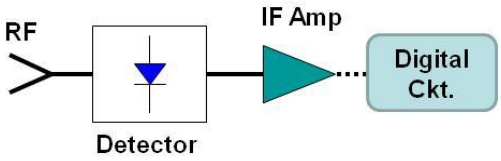

Figure 3.1 A THz detector element consists of an antenna, a detector diode, low-frequency amplifier and digital circuits.

3.1 Equivalent Small Signal Circuit and Sensitivity

The equivalent circuit of a Schottky diode detector is well established and has been studied by many research groups [81, 83, 84]. A simplified model of a diode is shown in Figure 3.2, where R_s represents the series resistance of the diode. This includes the Ohmic contact resistance between nanowires and metal, the intrinsic resistance of the nanowire as well as the intrinsic resistance of the coupled antenna electrodes. Since there are defects that exist on the nanowire surface, they will influence the electron transport and meanwhile introduce an additional series resistance. R_d is the junction resistance of the Schottky contact, which depends on applied bias voltages. C_j is the junction capacitance of the Schottky contact, and it is also bias dependent.

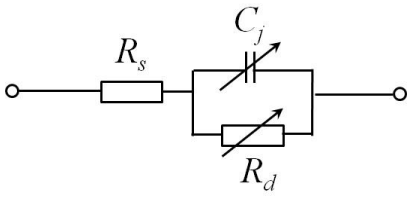

Figure 3.2 Equivalent small signal circuit of a Schottky diode.

The device sensitivity, i.e. noise equivalent power (NEP) is strongly related to the parameters above and a detailed study of NEP calculations is given in [81], for convenience, the equations are reproduced here:

$$NEP = \frac{V_n + V_{1/F}}{\beta_V} \tag{3.1}$$

$$\beta_V = \frac{\gamma}{2} \frac{R_d\left(1-|\Gamma|^2\right)}{\left(1+R_s/R_d\right)^2\left(1+\left(f/f_{ci}\right)^2\right)} \tag{3.2}$$

$$f_{ci} \equiv \frac{\left(1+R_s/R_d\right)^{1/2}}{2\pi C_j\left(R_s R_d\right)^{1/2}} \tag{3.3}$$

$$V_n = \left(4k_b T_B\left(R_s + R_d\right)\right)^{1/2} \tag{3.4}$$

$$V_{1/F} = \left(\frac{\gamma_H {V_{ds}}^2}{N \cdot F}\right)^{1/2} \tag{3.5}$$

Equations 3.1 to 3.5 can be used to find the sensitivity characteristics of a detector element. To achieve low NEP value (high sensitivity), according to Equation 3.1, diode noise (thermal noise V_n and flicker noise $V_{1/F}$) should be minimized. Meanwhile, voltage sensitivity β_V should be made as high as possible. This is tailored by device design, i.e., its non-linear characteristics. Equation 3.4 shows strong relationship between noise voltage and device resistance elements. To minimize V_n, series resistance should be made as small as possible and the junction resistance should be tailored for good impedance matching and noise minimization. Also, impedance

should be optimized for maximum signal transfer to the CMOS circuit. Flicker noise $V_{1/F}$ in Equation 3.5 is determined by the empirical Hooge's constant γ_H, which has been demonstrated to be around $2\sim4\times10^{-3}$ [85-87], and N, which is the total numbers of carriers in the device. Flicker noise is characterized at or below 1 kHz, which is the typical frequency range of the CMOS readout circuitry placed behind the THz detector element. The value of $V_{1/F}$ can range from 10^{-8} to10^{-10} V/Hz$^{0.5}$, which is smaller than thermal noise V_n. R_s and R_d also appear in equation 3.3 which affects the cut-off frequency f_{ci}. A smaller junction capacitance C_j leads to high cut-off frequency f_{ci}. Usually this junction capacitance for CNTs has the value in the order of 10^{-18}F, but for a larger diameter and lower carrier concentration nanowires, this value can range from 10^{-16} to 10^{-15}F [88]. In Equation 3.2 the value of voltage sensitivity β_V is controlled by four parameters: the curvature coefficient γ, frequency, device resistance, and the matching condition. For an ideal Schottky diode γ can be close to 40 at room temperature. The mismatch loss $(1-|\Gamma|^2)$, which is represented by the term of reflection coefficient Γ, determines the matching of Schottky diode to the antenna element. The intrinsic impedance of broadband log-periodic antenna usually varies between 50 to 200Ω over a wide frequency range. The antenna used in this detector here can be used up to 1 THz. Wide band impedance matching between the antenna and the diode is possible when the impedance of the antenna is made larger and the diode's effective impedance is made smaller (approx. 1kΩ). Smaller than 1kΩ impedance of the Schottky diode is not desirable as it also needs to be matched to the read out circuitry which typically have higher input impedance. The effective impedance of the Schottky diode can be tailored by the doping concentration, diameter of the nanowires and also by utilizing multiple nanowires in parallel within a single Schottky diode.

3.2 Material Preparation and Detector Fabrication

The n-type GaAs semiconducting nanowires were in suspension form purchased from *Cytodiagnostics*. The nanowires were suspended in Isopropanol alcohol (IPA) solution with the concentration of 1×10^6NWs/ml. The diameter of the GaAs NW's is in the range of 50-100nm, semiconductor properties such as bandgap and Fermi energy level are close to its bulk counterpart and this simplifies the Schottky contact model and reduces the strong quantum effects which smaller diameter nanowires (below 20nm) could have. Properties of this n-type GaAs semiconducting nanowires are highlighted in Table 3.1.The Fermi energy is calculated here using the carrier concentration provided by the nanowire manufacturer.

Table 3.1 Semiconducting properties of n-type GaAs nanowire

Length (μm)	Diameter (nm)	Carrier Concentration (cm^{-3})	Bandgap (eV)	Fermi Energy Level (eV)
1-4	50-100	$4\sim6\times10^{16}$	1.43	4.16-4.17

The formation of a Schottky contact can be achieved by connecting semiconductors and metals with appropriate work functions. For the case of n-type GaAs nanowire, work function of the metal (φ_m) needs to be larger than that of nanowire's Fermi energy (E_F=4.17eV). Both energy levels align at the junction part and Schottky barrier height appears at the interface. Because of Fermi level pinning can occur at the junction due to interface states, and the decreasing of barrier height occurs due to Image-force lowering, metals with much higher work function difference are desired to maintain sufficient barrier height to achieve strong nonlinear I-V characteristics. In this work, Palladium (Pd) with a work function of 5.4eV was selected as a Schottky contact. In order to form the Ohmic or weak Schottky contact on the other side of the nanowire, metal with work function slightly larger, equal to or smaller than NW's (4.17eV) is necessary. Al (4.06eV)

and Ti (4.33eV) are both candidates for this purpose. Here Ti was used in the fabrication of the device.

Fabrication steps implemented here were adopted from [81], which utilizes metal-etching undercut method to create nanoscale gap between two asymmetrical metal electrodes. This method avoids the use of e-beam lithography, which is time consuming, costly and inefficient for large area fabrication. A simplified schematic process flow is shown in Figure 3.3. A low-cost, low-loss polymer substrate PEEK (Polyether Ether Ketone) with thickness of 100μm was used as the substrate material. This polymer material has been shown to have low-loss tangent in the THz region. During the process, this flexible material is temporarily bonded onto a rigid substrate such as silicon and alumina wafer (not shown in Figure 3.3). First a 50nm of Ti is deposited by e-beam deposition and patterned to create the nanowire alignment electrodes using conventional photolithography and lift-off process, Figure 3.4(a). The alignment electrodes have the same pattern as the designed log-periodic antenna, and this Ti layer can assist the adhesion between final Pd layer antenna and the substrate. Then GaAs nanowires are aligned in the gap between the electrodes by applying dielectrophoresis (DEP): a droplet of IPA with nanowires suspending in the solution is introduced at the gap. Nanowires in the liquid tend to align in the gap between the electrodes due to the DEP force generated by the AC electric field at approximately 2 kHz. Once nanowires are aligned parallel to the electric field in the gap, they will retain their position and attach to the substrate when the solvent IPA dries. Note that the DEP force and directions applied on different dielectric materials is different since it depends on the dielectric properties of the material to be aligned in the AC electric field. Moreover, the AC frequency also influences the DEP force and its direction. Thus, the AC voltage and frequency are carefully tuned and optimized for the alignment of GaAs nanowires. Figure 3.4(b) shows an

example of aligned nanowires between the electrodes under Field Emission Scanning Electron Microscopy (FESEM). Note that multiple numbers of nanowires are aligned in parallel which is by design to achieve low-impedance devices for improving impedance matching between antenna and the connecting nanowires. The characteristic impedance of broad antennas for THz detection are usually 50 to 200Ω [89], and the impedance of semiconducting nanowires are from hundreds of Ω to several kΩ, which depends on the doping profile as well as the nanowire geometry, similar to the bulk material. The number of nanowires that gets aligned is largely dictated by the concentration of the nanowires in the IPA suspension and also on the amplitude and frequency of the signal used in DEP. Exact number is difficult to achieve especially when the concentration of nanowires in the solution is low. In this work the concentration of wire was low and thus this step was repeated multiple times to achieve desired number of NW's between the electrodes. Sometimes aligned nanowires can also connect the electrodes and the resistance can be measured using the multi-meter. The structure and the shape of the alignment electrodes are also critical factors that influence the DEP yield and efficiency. A long, but small and sharp tip will be more efficient to align large size particles such as graphene since strong E field can be achieved at the tip. In addition, better results will be seen if the tip is made to have dented pattern, however, long tips are not feasible in this work since high E field will attract too many nanowires, and this could result in agglomerate of the nanowires and degrade the performance of the detector, thus only dented tip is applied here. Following DEP, another layer of Ti (200nm) is deposited to fabricate the other side of the contact. This layer is etched using a Ti etchant (H_2O:H_2O_2: HF=200:1:1) and selected areas are protected using a photoresist layer. The Ti layer is over etched to form a nanoscale undercut beneath the photoresist. Undercut depth is determined by the thickness of this Ti layer. Eventually, the sidewall of the undercut is round

curved rather than vertical to the substrate, this is due to the isotropic property of the wet etching, and a very short extra time is added for this etching step in order to create enough gap size. Photoresist then forms a shadow mask for the next metal. A third layer of metal Pd (200nm) is then deposited to create Schottky contact with GaAs nanowires. The gap between the two contact metals is dictated by the undercut of the Ti layer. The Pd layer is also selectively patterned to form a log-periodic antenna structure, which is similar to the alignment electrodes, but smaller gap. Final step is lifting-off the interlayer photoresist which used to pattern the second metal layer undercut, and the device is completed. A photograph of an array of fabricated detectors is shown in Figure 3.5. Through the whole process, PEEK substrate is inert to all of the etchants used, which increase the reliability and compatibility of the novel fabrication process.

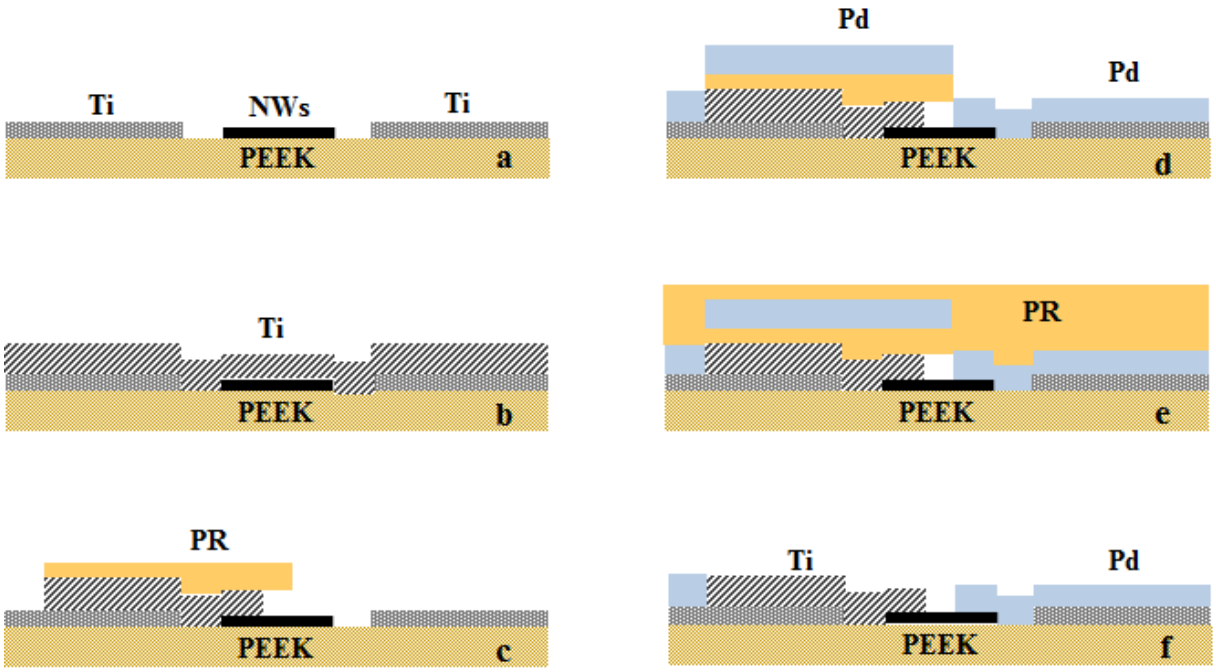

Figure 3.3 Fabrication steps. (a) Metal lift-off and alignment of nanowires using DEP; (b) and (c): depositing Ti and patterning to create weak Schottky contact and undercut. (d): deposition Pd to form Schottky contact. (e): Patterning of Pd to form the antenna structure. (f) Lift-off of the photoresist

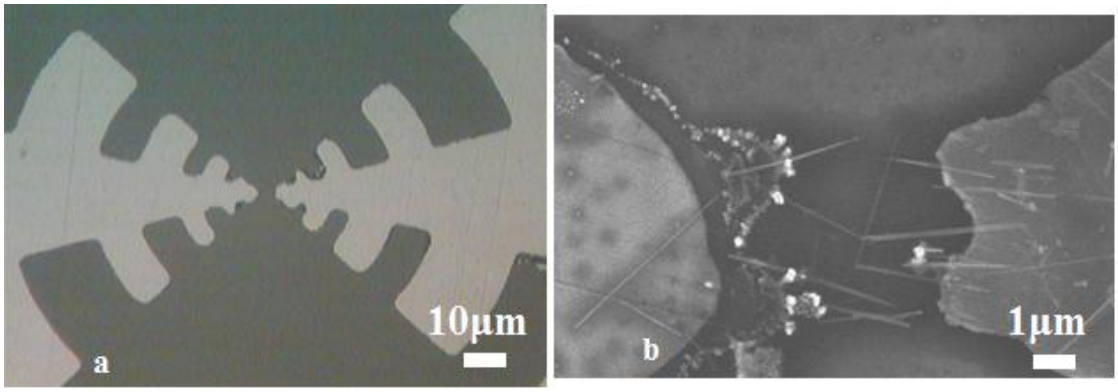

Figure 3.4 (a) Electrodes for GaAs nanowire DEP alignment and (b) close up view of aligned GaAs nanowires across the electrode gap under FESEM.

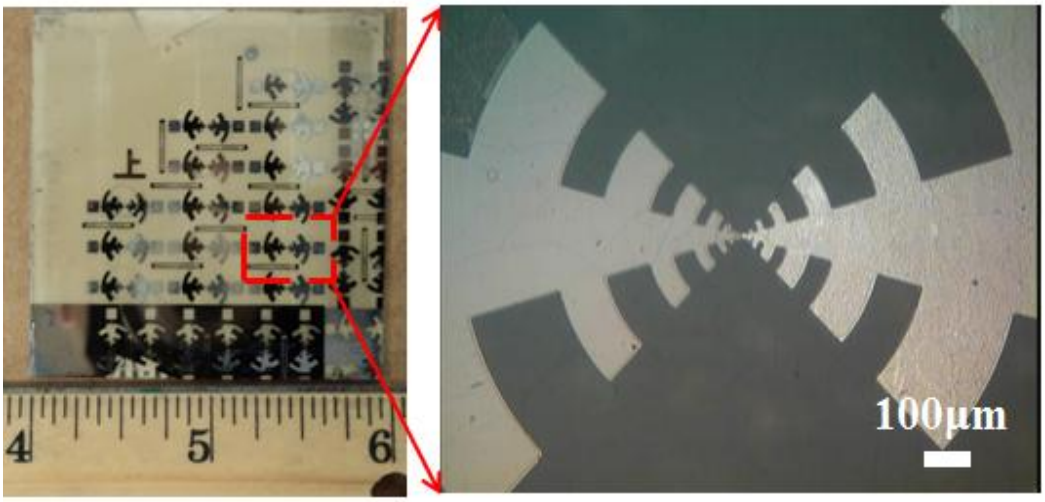

Figure 3.5 Fabricated detector array on PEEK substrate and magnified picture of a single device with asymmetric metal electrode antenna.

The selected polymer substrates for this process should meet regular micro-fabrication conditions such as soft and hard baking temperature and surface roughness. Thermal expansion coefficient (CTE) is one of the critical parameters which determine the quality of the device. It directly influences the accuracy of pattern and masks alignment for different layers. Large expansion during baking of resist will warp the substrate and lead to poor or even impossible alignment between the layers. Several temperatures related parameters are shown in Table 3.2 for some commonly used polymers. PEEK has the smallest CTE value and satisfies the processing temperature of regular photoresist. Furthermore, rapid heat up or cooling down is also avoid during the process in order to release the thermal stress and eliminate the crack on the metal surface.

Table 3.2 Temperature related parameters for several polymer substrates [81]

	Melting Point (℃)	Glass Transition Temperature (℃)	Thermal Expansion Coefficient (K^{-1}) (Linear)	Thermal Conductivity ($Wm^{-1}K^{-1}$)
PET	>250	75	3.9 E-5	0.15-0.24
PEEK	~343	143	2.6 E-5	0.25
Polyimide	---	>400	5.5 E-5	0.52

3.3 Measurements and Results

The I-V characteristic of a fabricated device was measured using Agilent 4145B semiconductor parameter analyzer (SPA). Figure 3.6 shows the measured I-V curve of a device. It shows that large series resistance exists along the channel of the device. The plot also shows the I-V relation after the effect of series resistance, R_s=9kΩ, has been subtracted from the measured results. The calculated resistance (slope of the I-V cure) profile in forward bias is shown in Figure 3.7, which indicates the total resistance is in the order of 10^4Ω. This proves the fact that multiple numbers of nanowires are required to improve the impedance matching with the antenna. This measurement also clearly shows that Schottky diodes using GaAs nanowires can be fabricated on a plastic substrate at low-temperature.

Preliminary measurements on the detector were carried out at low frequency using a ground-signal (GS) coplanar probe (40 GHz) probe. Measurements were first carried out at 5GHz and 26GHz with different input powers. Detector sensitivity at these frequencies at zero bias is shown in Figure 3.8. The rectified output voltage increases as a function of input power. This clearly shows that fabricated devices have strong non-linearity at measured frequencies and they can also be used as direct detectors. Figure 3.9 shows the measured rectified voltage as a

function of DC bias across the diode at 26 GHz. The input power of the 26GHz signal was fixed at -5dBm. In order to avoid damaging the device due to DC biasing, voltage above 1V was not applied. Strong sensitivity is achieved near 1V, which is the measured strongest non-linear part of the device.

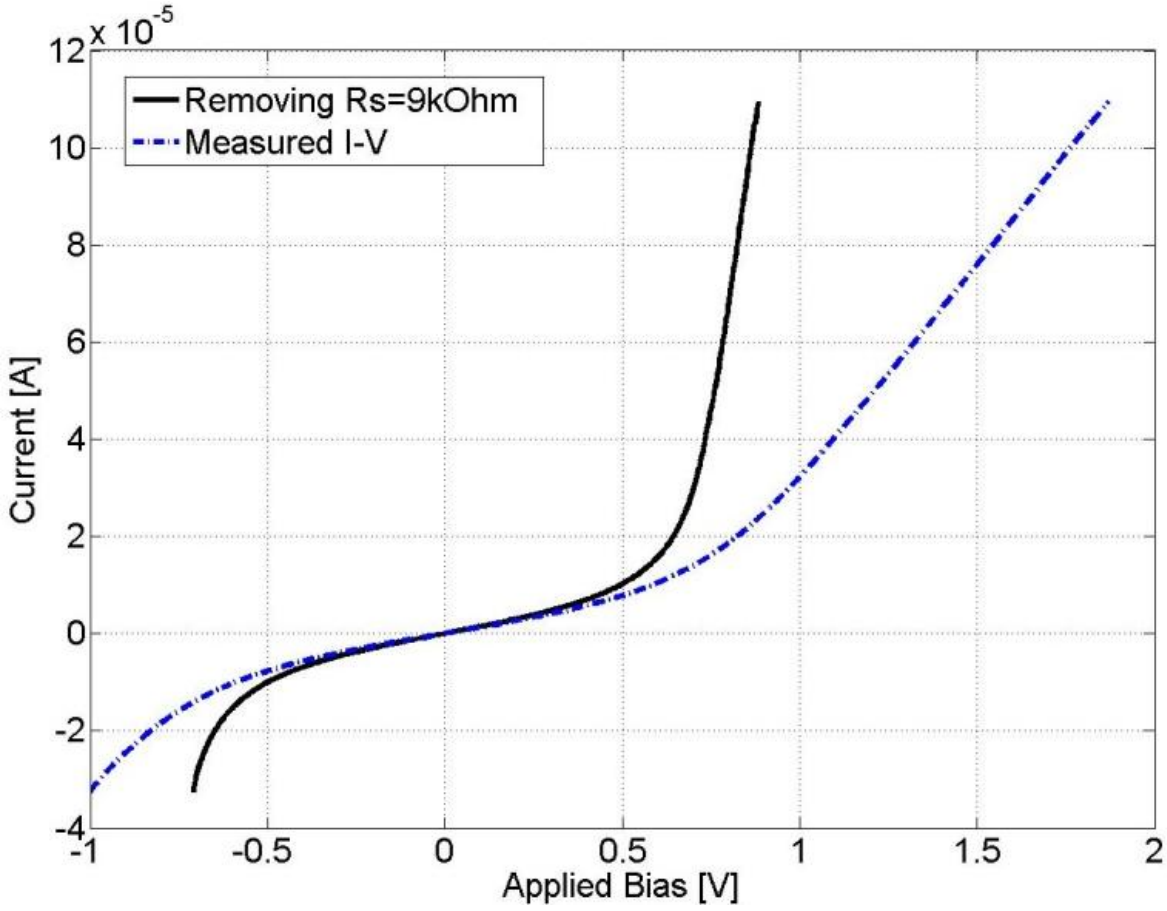

Figure 3.6 I-V characteristics of measured device before and after removing effect of series resistance (R_s=9kΩ).

The noise equivalent power (NEP) of the device was also calculated from the measured results. The lowest NEP is close to a bias voltage of 1V due to the strong nonlinear characteristics in the I-V characteristics of the device near this bias point.

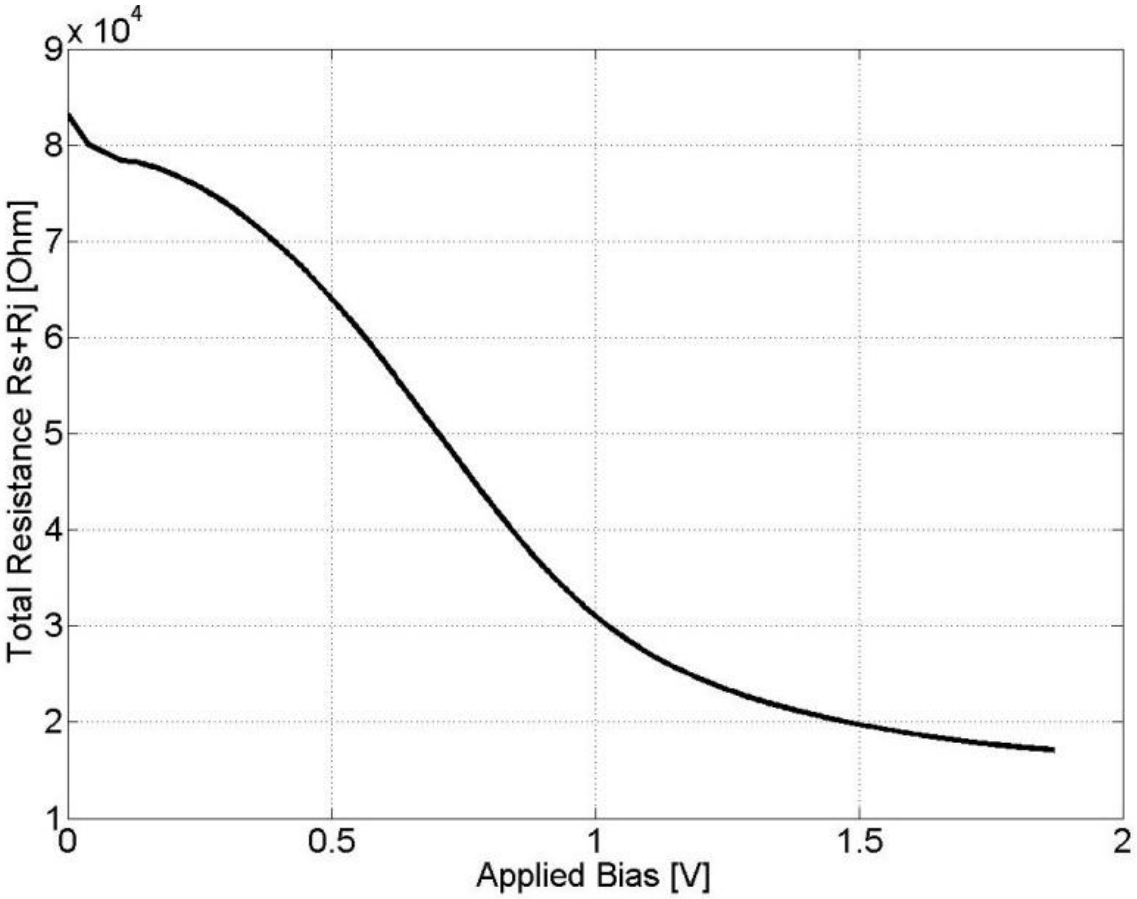

Figure 3.7 Total resistances (R_s+R_j) of a single device in the forward bias region.

The NEP value in mismatched condition at 26GHz is plotted in Figure 3.10. It demonstrates that the lowest NEP value of 11pw/Hz$^{0.5}$ occurs at about 0.8V, and then increases at higher bias voltages.

For higher frequency NEP values, calculations based on the previous equations are carried out and are plotted in Figure 3.11. It shows that at 0.5THz the lowest NEP is approximately 1000pW/Hz$^{0.5}$. Although this value is relatively high, it is comparable to some commercialized bolometer THz detectors, and is close to the value of InAs nanowire based THz detectors [90]. This large value is due to the impedance mismatch between the antenna and the Schottky diode (junction and series resistance). A large amount of power is reflected from the diode due to the high impedance mismatch. Further calculation, assuming perfect impedance match conditions,

reveals that that NEP of 44pW/Hz$^{0.5}$at 0.5THz and 170pW/Hz$^{0.5}$ at 1THz can be achieved using this device. Broadband impedance matching can be achieved by incorporating more nanowires within the device and also by reducing contact resistance through improved Ohmic contact. However, with an increase in the number of nanowires within the device, the junction capacitance also increases, which in turn reduces sensitivity (increase in NEP). Thus, aligning an optimum number of nanowires within a device is critical to achieving high sensitivity. Approach to aligning a set number of nanowires by design is undergoing. This would require tight control of nanowire concentration in the solution and also optimizing DEP aligning conditions.

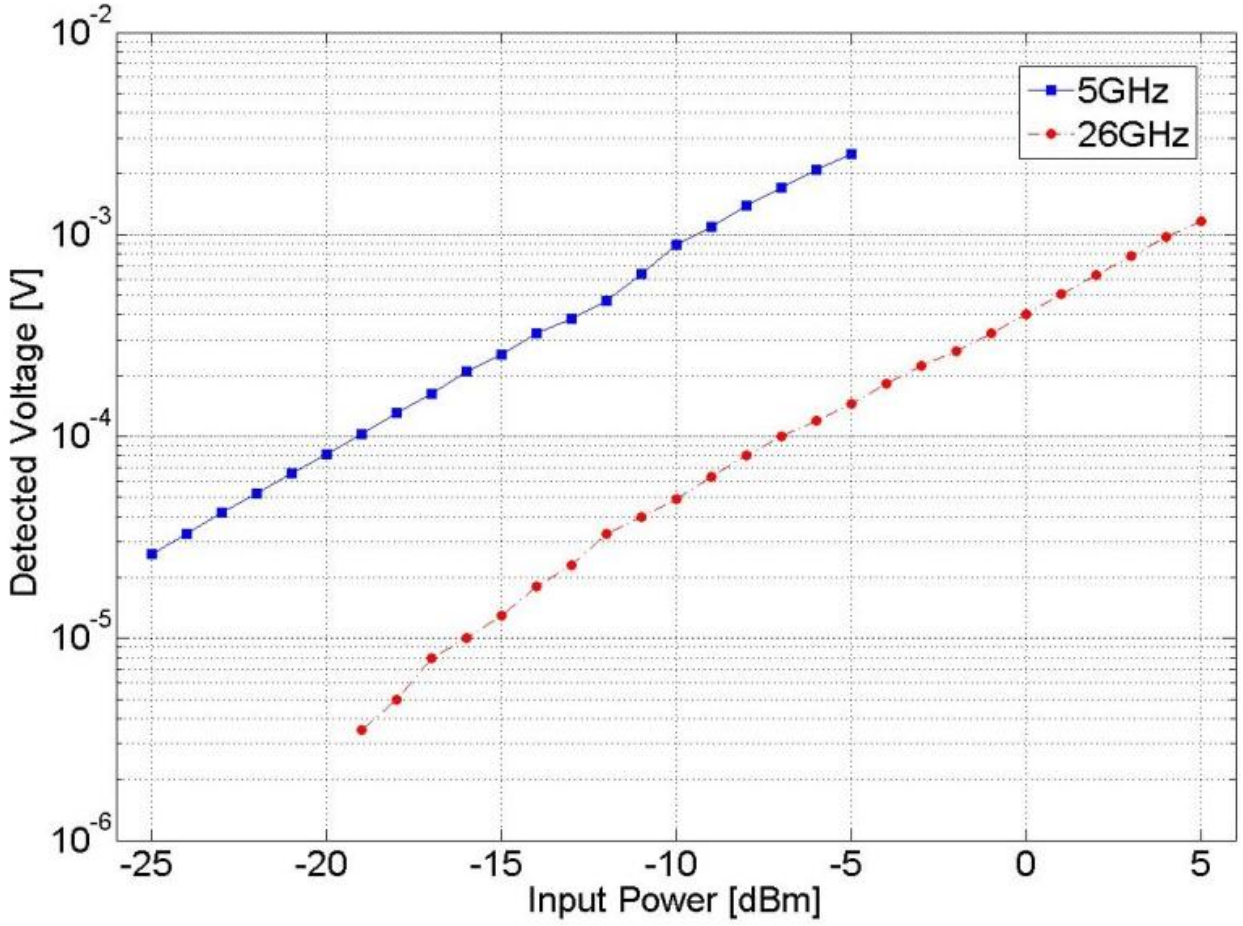

Figure 3.8 Rectified output voltage as a function of input power at 5 and 26 GHz.

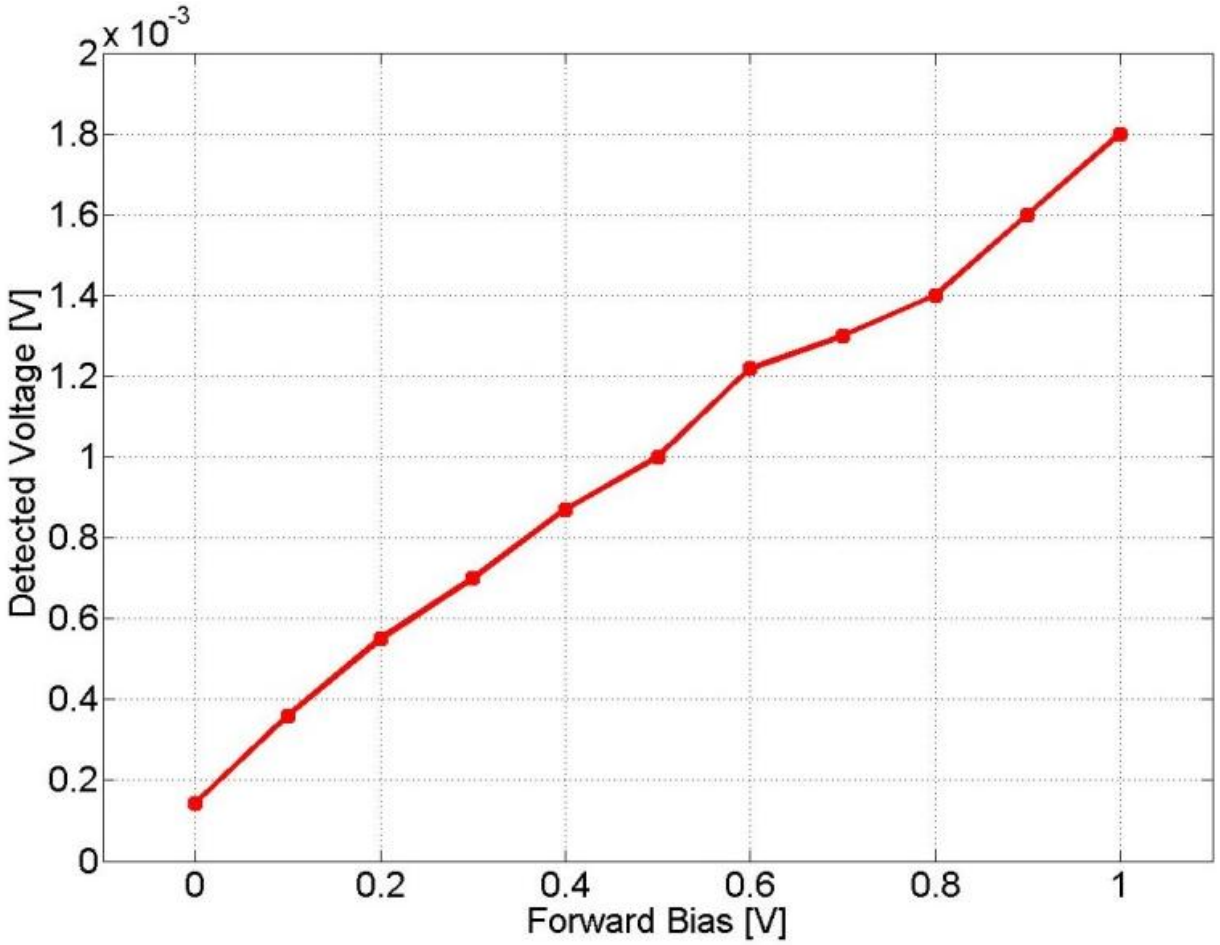

Figure 3.9 Output rectified voltage as a function of DC bias across the diode at fixed frequency (26 GHz) and power (-5 dBm).

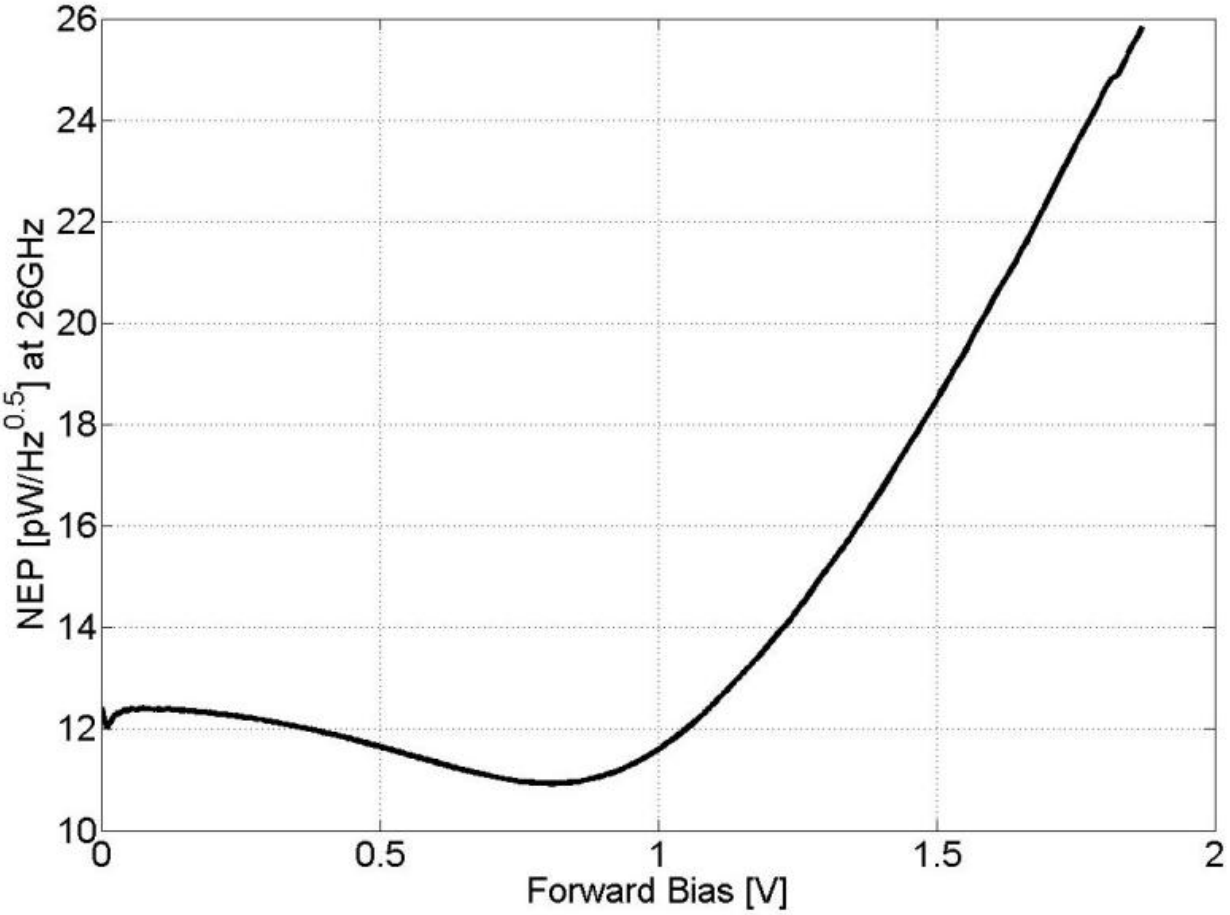

Figure 3.10 Mismatched condition NEP value at 26GHz in the forward bias region

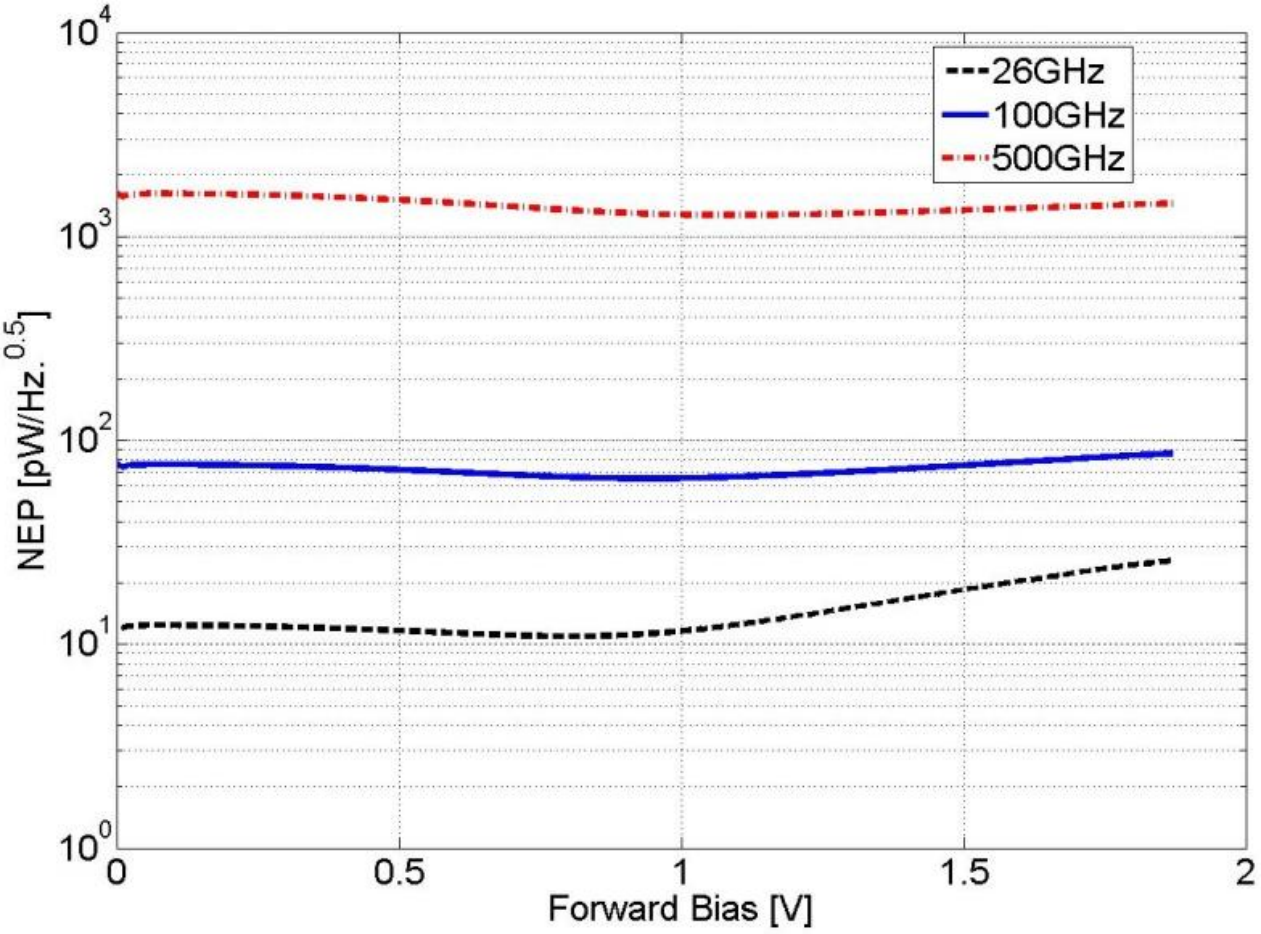

Figure 3.11 Mismatched condition NEP values at different frequencies.

In summary, GaAs nanowire based Schottky diode on flexible substrates has been fabricated and demonstrated. The device has been utilized as a direct detector. By using a novel undercut self-alignment process, nanoscale gap between the contact electrodes is achieved, leading to fabrication of small devices using conventional lithography. Strong nonlinear I-V characteristic of the fabricated device indicates the reliability of this process. Multiple numbers of GaAs nanowires are aligned in parallel, between the contact electrodes, to reduce the series and junction resistance, and further to improve impedance matching with the broadband antenna. The preliminary RF response was carried on a coplanar structure and an NEP value of $11pW/Hz^{0.5}$ at 26GHz at room temperature is achieved. Calculations of NEP at higher frequencies show that this device can perform as a THz detector. With good impedance matching, NEP of $44pW/Hz^{0.5}$ at 0.5THz and $170pW/Hz^{0.5}$ at 1THz are achievable.

Chapter 4 THz Active Device: Embedded Diode based Detector Elements

As mentioned earlier, there are many challenges that need to be overcome in order to achieve an integrated system for THz circuits. The wavelength at THz is significantly smaller than RF frequencies, translating into more stringent requirements with assembly and integration of devices. Particularly, parasitics begin to dominate with increased frequency, and significantly degrade circuit performance. In comparison to lower frequency counterparts, THz systems face a significant hurdle in reducing their sizes. However, the proposed embedded actives process developed in this work leads to a reduction of parasitics at THz frequencies, providing a vital solution to one of the most limiting factors in THz packaging.

Simulations using commercial finite element software (Ansoft HFSS) have been carried out to show the benefits of the proposed embedded fabrication process in comparison with traditional wire bonding techniques. Figure 4.1 shows the schematic cross-section view of structures used in the simulation: 50Ω microstrip is applied here as the transmission lines. The layers above the ground plane are Rogers 3003 and SU-8 respectively. SU-8 has high loss tangent (δ=0.04-0.08) in high frequency region, but for simulations here it is assigned as low loss material, this can help to eliminate the influence of loss factor from SU-8 but show the influence of different structures only. Assuming the diode has two pads, and embedded structure has via connecting to both pads, while the wire bonding structure has via on one pad but wire bonding on the other pad. Figure 4.2 (a) and (b) show the S-parameters of microstrip connecting to a diode using embedded and conventional bonding wires. It is shown here that the diode in the wire bonding structure is also embedded in the substrate, but wires are applied as interconnects to eliminate other factors influencing the results.

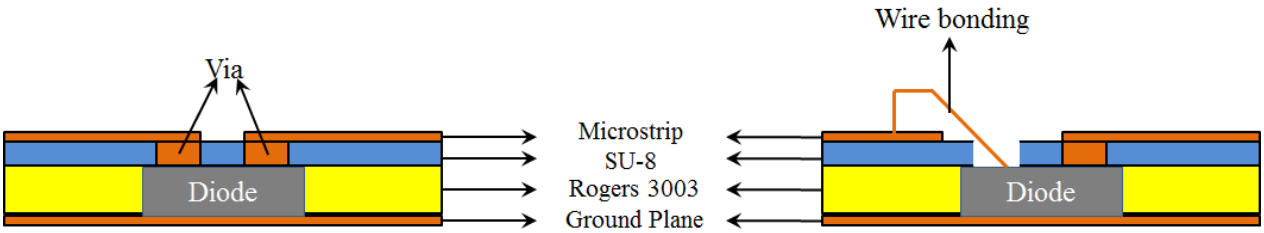

Figure 4.1 Schematic of cross-section view of embedded diode structure (left) and wire bonding structure (right).

Both structures in Figure 4.2 (a) and (b) show acceptable S_{21} at low frequencies, however, starting from 80GHz, the S_{21} of the wire bonding structure decreases dramatically while for embedded active structure it still maintains an acceptable S_{21}. The difference in S_{21} between the two approaches indicates the associated parasitic elements in the wire bonding method cannot be neglected at high frequencies. Clearly, the embedded structure has considerably low-parasitics (R, L, C), and could lead to a realization of high frequency circuits and devices.

The advantages of embedded actives can be demonstrated through a wide band focal plane array (FPA) for THz imaging. The FPA architecture relies on the availability of low-loss wide band antennas, wide band efficient diode rectifiers (high cut-off frequency, ~1THz), low-frequency IF amplifiers, and CMOS readout circuitry [91]. In a typical FPA design, a large number of detector (pixel) elements exist on one common substrate (100×100 pixels). In a THz FPA, most of the area on the wafer is occupied by passive devices such as antennas and interconnects. The core element, rectifier diodes, typically occupies less than 1% of the area within a pixel element. Thus, it is desirable to integrate the active devices with passive elements on a low-cost substrate (e.g., Si) while meeting stringent alignment tolerances.

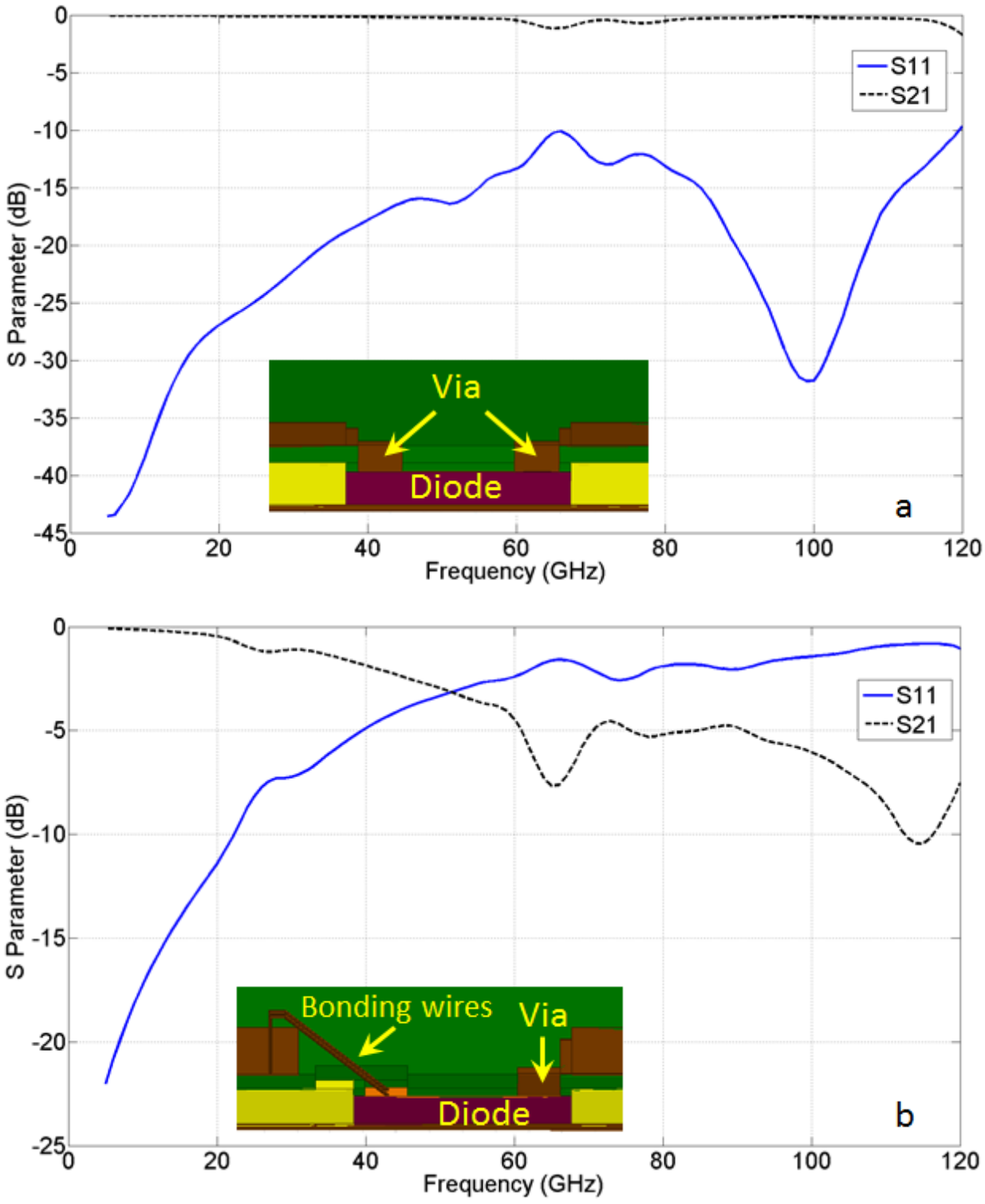

Figure 4.2 S-parameters for (a) embedded active structure and (b) wire bonding structure. Insets are schematics for the two physical structures in Ansoft HFSS.

Over the last few decades, researchers have successfully demonstrated various types of THz rectifiers (detectors) operating at room temperature with high sensitivity and broadband detection [92-95]. The basic principle of THz Schottky barrier detector (SBD) relies on strong I-V nonlinear characteristics as introduced earlier, [96], and is also shown in Figure 4.3. Here, the incoming THz signal is rectified and converted to a DC signal that can easily be detected using CMOS circuits. Different types of semiconducting materials such as III-V materials [95,97], Si, and nano-material based THz Schottky diode detectors have also been proposed [93, 94]. Ultimately, the goal is to realize a detector with low NEP. Among the many different detector choices, III-V group semiconductors, such as GaAs, are attractive as they meet the all of the above criteria. The goal is to demonstrate THz imaging array on a low-cost, low-temperature substrate utilizing embedded III-V semiconductor diodes coupled with wide band antenna elements. If successful, the process will be compatible with a large number of substrates, including silicon. This will also allow in the design and fabrication of a large number of THz circuits using a low-cost process.

Commercially available GaAs Schottky diodes were selected based on NEP analysis done using the available equivalent diode models which will be discussed later in this chapter. The diode elements are to be embedded in a dielectric layer immediately beneath the antenna element, as shown in Figure 4.4. Thus, diode chips with small form factor are selected. As discussed earlier, this approach reduces the parasitic between the antenna and the diode element and thus allowing operation in the THz region.

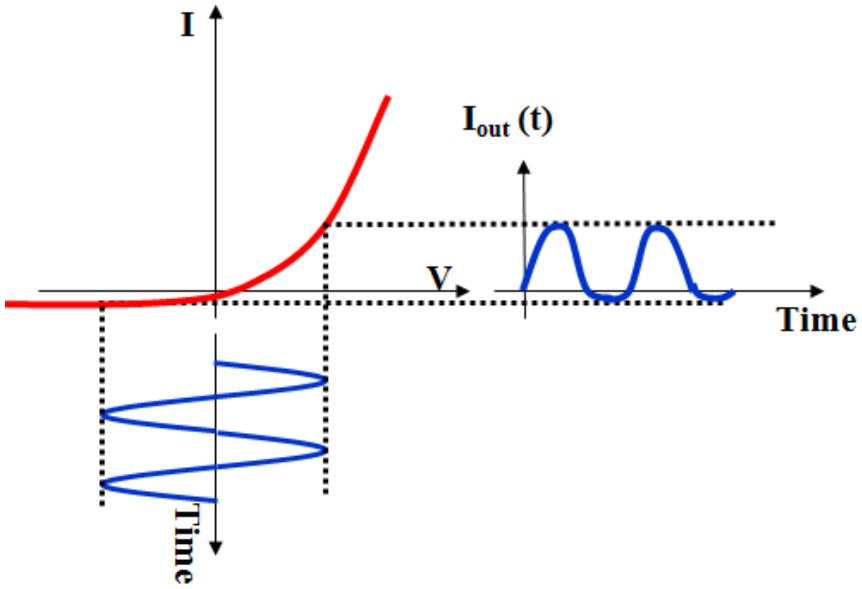

Figure 4.3 Rectification of incoming RF signals using a diode element.

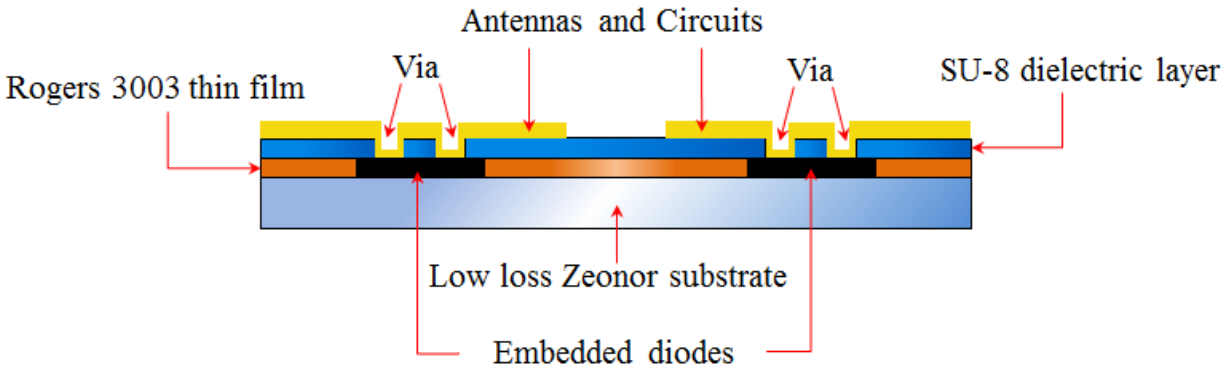

Figure 4.4 Schematic cross-section view of a finished sample with two diodes embedded.

Before stepping into the design and fabrication of THz image sensor, it is necessary to demonstrate the possibility of fabricating simple millimeter wave circuits using the embedded fabrication process. What's more, the performances of the embedded diodes structure require further study, which will also be discussed as below.

4.1 Simple Millimeter Wave Circuit based on Embedded Structure

4.1.1 Active Device Selection

For many applications such as frequency multiplication, mixing and even rectification (detection), strong nonlinear devices are indispensable components. Diodes and transistors are the most commonly used active devices to realize such functions [95, 96, 98]. Furthermore, diodes have only two terminals and are easy to operate, which simplifies the design work and fabrication procedure. Again, GaAs Schottky diodes are selected to embed for designing and fabricating varieties of microwave, MMW and THz circuits, which also reduce the complexity of the embedded active fabrication process.

One of the criteria is that the Schottky diode should be able to operate well into the microwave or even THz region in order to efficiently realize the circuit function. This requires the junction as well as parasitic capacitance of the diode to be small enough to obtain high cut-off frequencies. In brief, the parasitic of a diode are critical in the design of high frequency circuits. Thus, the intrinsic cutoff frequency of the diodes should be high and it should not degrade after the diode has been embedded in a dielectric layer and interconnected with other elements.

Based on the simple analysis above, a low-cost commercial flip-chip GaAs Schottky diode DBES105a, from United Monolithic Semiconductor (UMS), is chosen for the design of circuits. The equivalent circuit of this diode is shown in Figure 4.5. The parameters of the equivalent circuit model for single diode at zero bias are shown in Table 4.1. The chip has dual Schottky diodes connected in series. This Schottky diode flip-chip has been used in many applications, such as frequency multiplication and mixing above 200GHz [99-101].

Table 4.3 Specs of the DBES105a dual Schottky diode flip-chip

R_s (Series resistance)	C_{j0} (Junction capacitance)	C_{par} (Parasitic capacitance)	f_{co} (Cut-off frequency)
4.4Ω	9.5fF	5.8fF	2.4THz

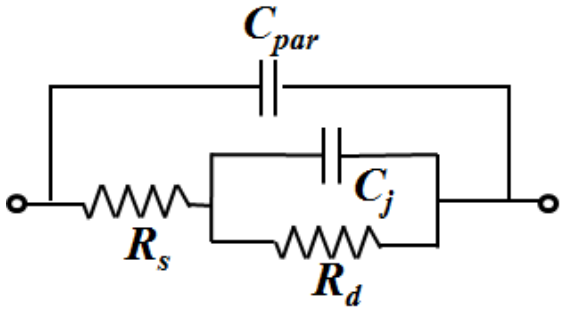

Figure 4.5 Small signal circuits of a single diode on DBES105a Schottky diode flip-chip

4.1.2 Material and Fabrication Process for Embedded Diode Structure

The concept of the fabrication process applied here was first reported in [102]. The fabrication for an embedded diode is demonstrated in the process flowchart of Figure 4.6. This process starts with a commercialized Rogers 3003 composite material with thickness of approximate 100 μm. This thin sheet comes with copper claddings on both sides, as shown in Figure 4.6a, and the flexible substrate material is made with polymer-ceramic composites, which will serve as the "housing" layer for the diode. It has a dielectric constant of approximately 3 with low dielectric loss in the THz frequency region [103]. This material is a thermoset polymer, as use of thermoplastics was avoided as it easily melts during the following laser cutting process. The bottom side of the copper cladding layer is etched and bonded temporality to a rigid supporting substrate for handling through the upcoming process, shown in Figure 4.6b. The top copper layer is then patterned through regular lithography to form the cavity outline, which acts as a hard mask for opening the diode cavities by using a CO_2 laser, as shown in Figure 4.6c. The laser

system from Full Spectrum Laser is shown in Figure 4.7. Then the laser ablation treats the whole sample surface and burns away the exposed polymer-ceramic material not being masked by copper, which is showing in Figure 4.6d. This copper etching mask provides the benefit of creating a fine structure. The CO_2 laser system has a beam diameter of approximately 50μm with a maximum peak power of 40W, which is adequate for laser ablating the substrate material. In order to minimize the residue generated by the laser ablation on the edges of and inside the cavities, the rastering speed and power are carefully controlled and optimized. Raster scanning of laser is applied several times to completely open the cavities. The copper mask is then removed by wet etching process and the "blank" Rogers 3003 thin sheet with cavities is ultrasonic cleaned to remove the material residue particles generated by the laser raster scan. Then the substrate is laminated to a 1mm Zeonor substrate, which has been mentioned to have low loss in GHz to THz regions. A thin layer (4-5μm) of diluted SU-8 photo epoxy resist is spin coated to act as the adhesive for this lamination. The GaAs Schottky diodes are then placed into the opened cavity, which is shown in Figure.6h and Figure 4.8. The sample is then placed on a hotplate to re-flow the adhesive and to tightly attach the diode as well as the Rogers 3003 thin film to the Zeonor substrate. Since the Zeonor substrate is transparent to UV, the SU-8 adhesive is planar UV exposed from the back side of the sample and cured, this further bonds the Rogers thin film to the Zeonor and secures the diode inside the cavity. In replacing of photosensitive adhesives, other adhesives can also be used to avoid the use of UV light. To demonstrate the possibility of mounting multiple diodes into the cavity, Figure 4.9 shows 4 diodes have been placed in the cavity array. Figure 4.6i shows that a thick SU-8 layer is spin coated and then patterned in order to open via to the contact pads of the diode. A short O_2 plasma etching is required here, which is shown in Figure 4.6j, to further remove the SU-8 residue from cavities on top of the contact pads.

In order to realize functional systems or circuits, a thin layer of Cu/Ti (1μm/10nm) was sputtered on top of the SU-8 layer, so that the various passive elements such as transmission lines and antennas can be patterned, and this is shown in Figure 4.6k.

There are several problems raised during this embedded diode fabrication, which are even more critical for multiple diodes embedding process. During the patterning of the outline of the cavity on the copper, the non-uniformity of the copper wet etching causes the sizes of the outlines not to be identical. This results in different size of cavities across the substrate, and leads to a significant gap between the diode and cavity side walls, and the diodes are misaligned relative to each other. This also leads to further misalignment of via with respect to the pad structures. To solve this, the wet etching procedure was improved by fine controlling the bath temperature and the incorporating periodic agitation of the liquid to achieve uniform temperature distribution as well as to uniformly replenish the etchant, respectively. This improves the cavity tolerance from 20μm to 2μm. The fine-tuned etching improves the alignment of via in the follow on process steps. Achieving uniform coating of SU-8 layer is critical to create fine-line patterns. Uniform filling of spacing between the diode and the pocket walls is also critical. This was attained by multiple coating of thin SU-8 layers and also longer pre-bake time on a leveled hot plate to allow SU-8 reflow and planarization. Overall thickness of this SU-8 layer is reduced (approx. 10–40μm) so that the via connecting top metal to the diode pads have low parasitics. The spacing between the cavity wall and the diode wall is less than 15 μm on each side providing a tight fit. In this work, a 3 by 3 cavity array is designed on a single substrate. As mentioned, four diodes are placed into the cavities next to each other to form a 2 by 2 array. Figure 4.10(a) shows the image of a fabricated wafer and Figure 4.10 (b) shows close up view of

an antenna element coupled to an embedded diode. The antenna design will be discussed later in the following sections.

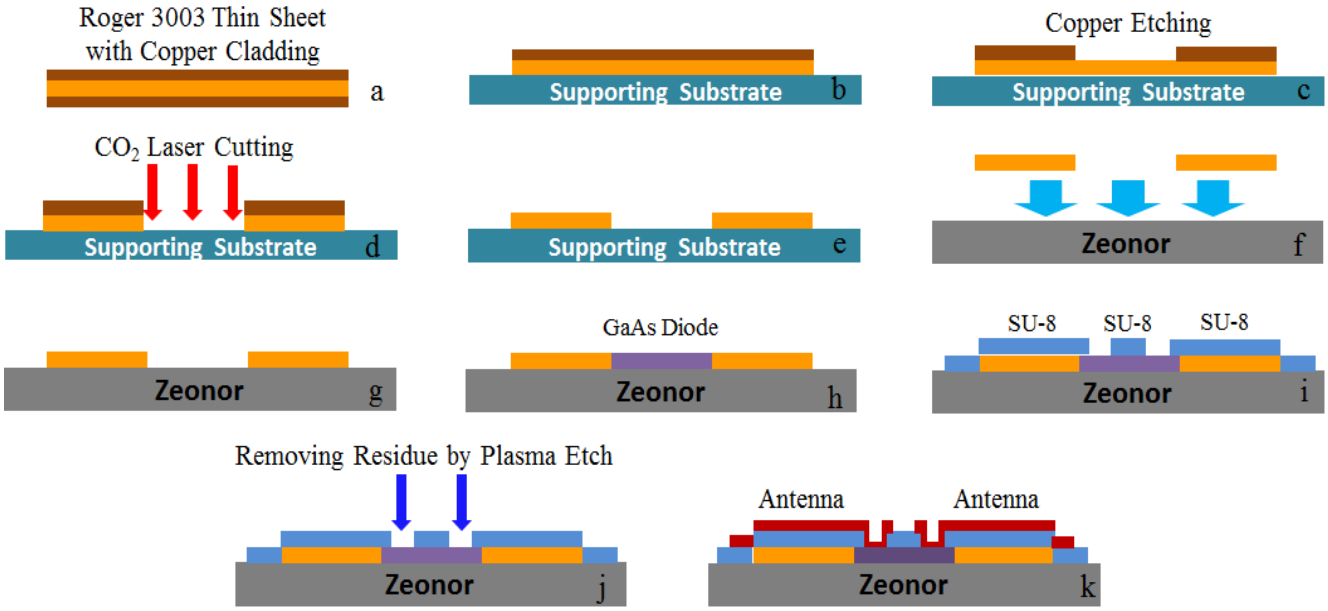

Figure 4.6 Fabrication Process of GaAs Schottky Diode THz Detector based on Heterogeneous Integration.

Figure 4.7 40W CO_2 laser engraving machine from Full Spectrum Laser

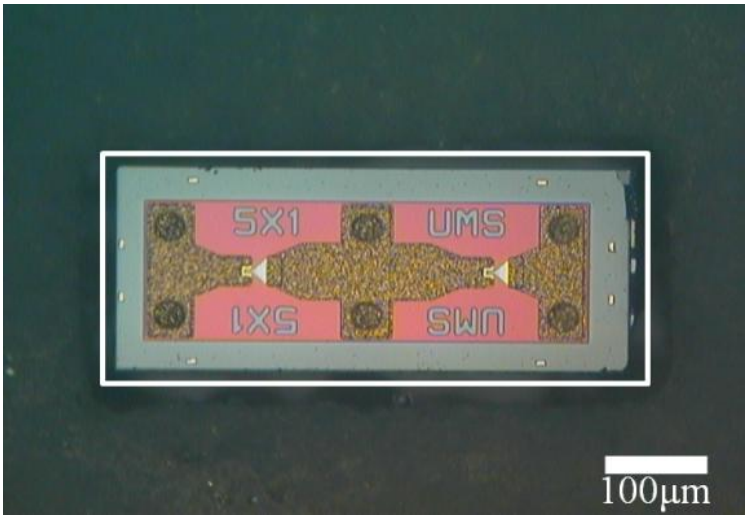

Figure 4.8 Photomicrograph of one diode placed into the cavity on Rogers 3003 thin film. Here, white line represents the outline of the cavity.

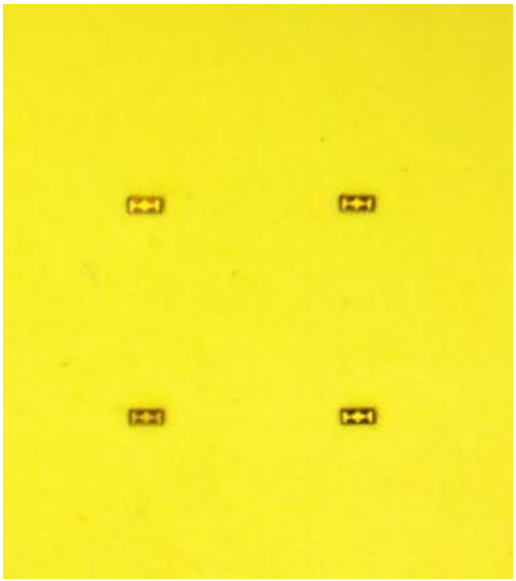

Figure 4.9 GaAs Schottky diodes that have been placed in a 3x3 cavity array.

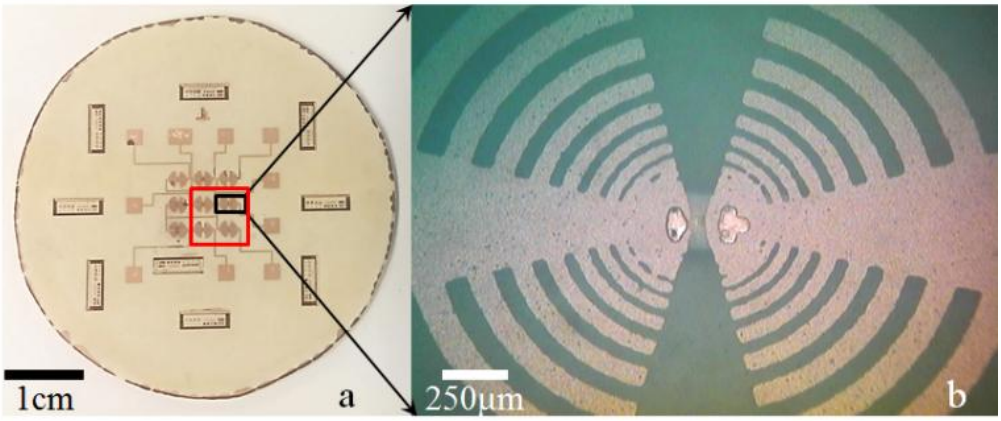

Figure 4.10 Fabricated sample with four diodes embedded to form 2x2 array highlighted by a red square box (a), and zoom in on one single device (b).

4.1.3 Measured Results for Simple Millimeter Wave Circuits

4.1.3.1 DC Characteristics

Measurements were first carried out using a semiconductor parameter analyzer (SPA) to acquire the I-V characteristics of the four embedded diodes after fabrication. Figure 4.11 shows the I-V characteristics of an embedded diode. A Fitted curve for the I-V measurement indicates that the saturation current is equal to 3.5×10^{-14}A, and the ideality factor is approximately 1.2, which matches well with the values in the diode datasheet provided by the manufacturer. Figure 4.12 shows the measured I-V curves of the four diodes from 0.65-0.75V, at which bias the diodes start to turn on. Overlapped curves show that the diodes in one fabrication batch have close I-V characteristics, indicating diodes' nonlinear performances will be very similar. This shows that this embedded fabrication process is also suitable for heterogeneous integration of multi-functional high frequency integrated circuits. However, the series resistance R_s is approximately 27Ω, which is larger than the 4.4Ω stated on the datasheet. This may be due to the polymer

residue from the SU-8 layer present on the diode pads, and it can be further cleaned in RIE prior to the deposition of the top metal layer.

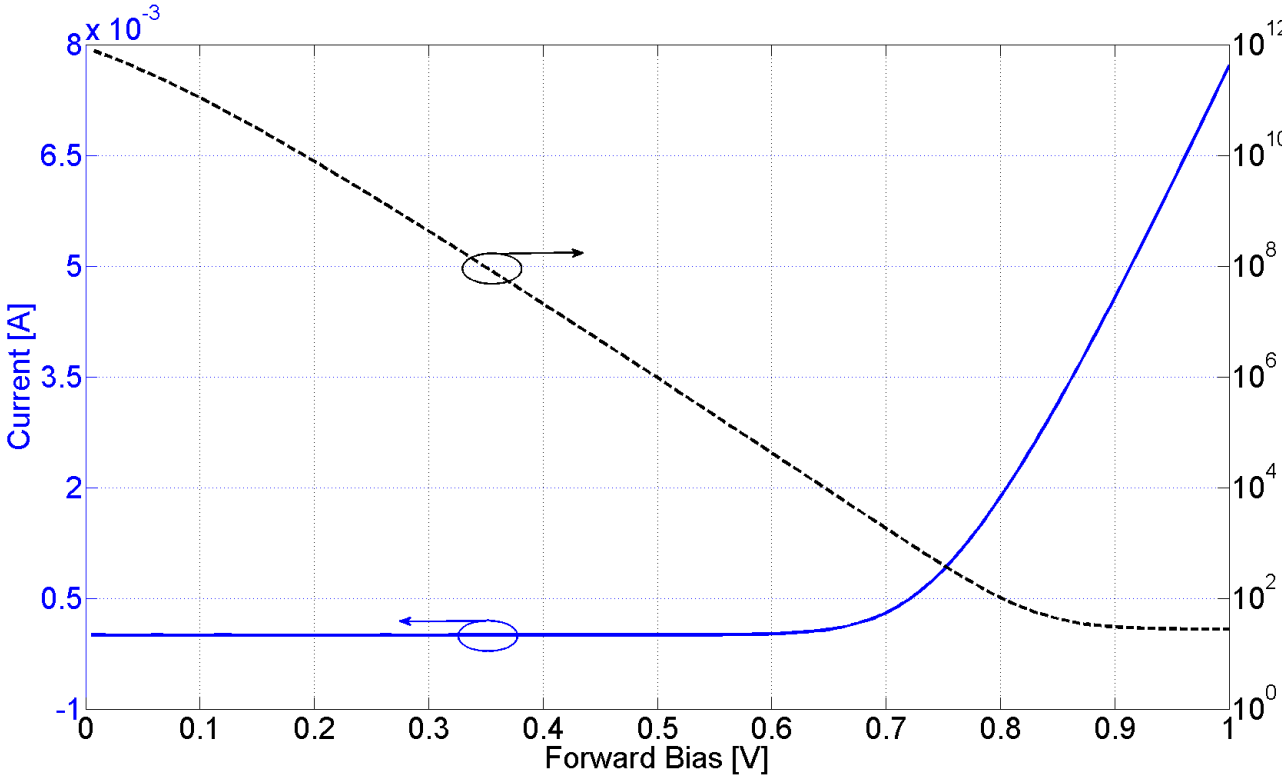

Figure 4.11 Example I-V characteristics and total resistance (R_s+R_d) of one of the embedded diodes.

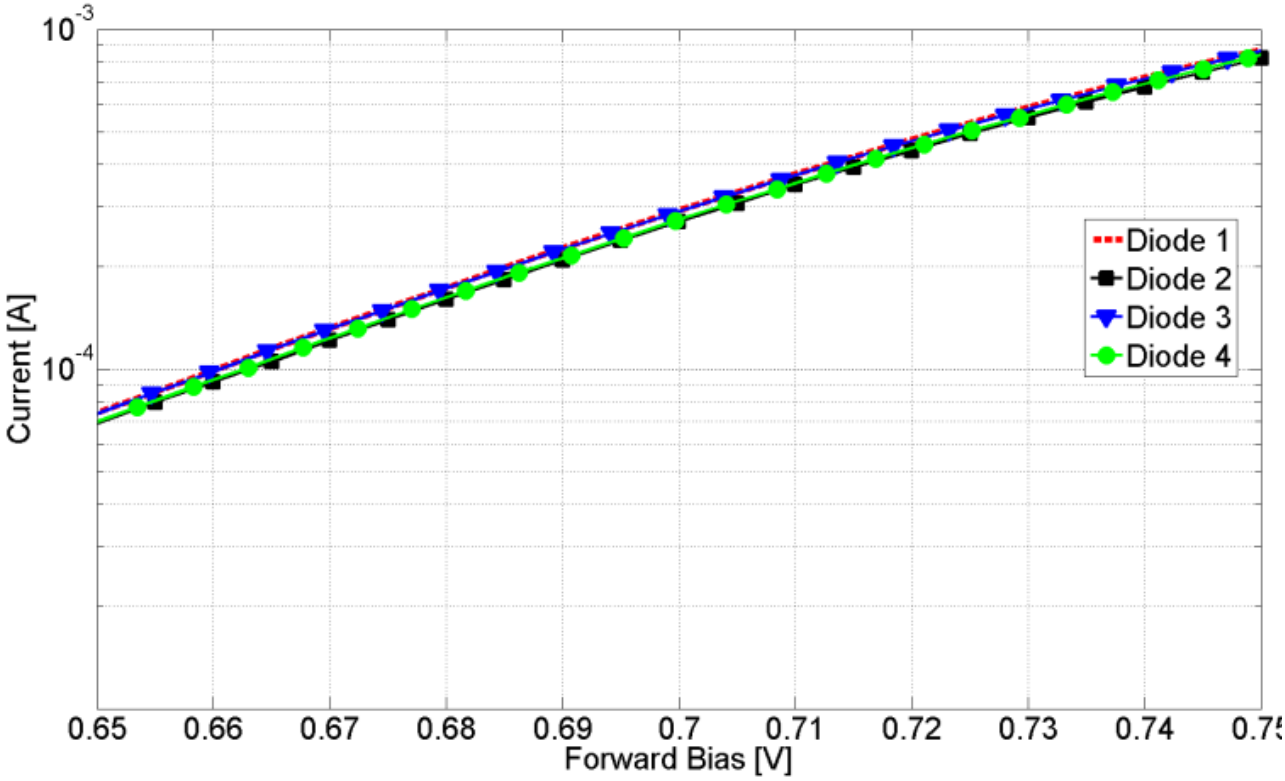

Figure 4.12 I-V characteristics within 0.65-0.75V forward bias for 4 embedded diodes on the same fabricated substrate.

4.1.3.2 S-Parameter Measurement and Equivalent Circuit

In order to acquire the equivalent circuit model for the embedded diode structure, same process was used to fabricate another sample with embedded diodes which were coupled to coplanar measurement structures. Figure 4.13 shows a schematic of a coplanar waveguide (CPW) structure, the signal line is located in the center and the ground lines are located on the top and bottom then connecting at the left side. The embedded diode being measured is buried underneath the SU-8, signal and ground lines are connected to the diode pads. The S-parameters between 10 and 20GHz of the sample were measured by probing the device using a 40GHz ground-signal-ground (GSG) probe. For comparison, a bare diode was also measured. The measured S-parameters were used to derive the equivalent circuit model of the diodes (bare and embedded), which is shown in Figure 4.5. Fitting was carried out using Agilent ADS simulator. Table 4.2 outlines the equivalent circuit values for each of the diode elements at a bias of 0.7V. This voltage provides the strongest non-linearity in the I-V characteristics of the diodes, and it will be applied to all of the circuit applications presented later. Figure 4.14 shows the measured and modeled S-parameters of bare and embedded diodes on the Smith chart.

The derived cutoff frequency for the embedded diode is similar to that of bare diode, which indicates the diode's high frequency responses have not been compromised. There is an increase in the series inductance which is largely due to the line length of the CPW structure used in the characterization. Also, the diode total resistance (R_s+R_d) is different and this may be attributed to inherent difference in diode resistance across the wafer. Overall, this embedded fabrication process is reliable and can be used in the design and fabrication of MMW and THz circuits. Note that RIE process has been applied to this sample to remove the polymer residue from the vias

prior to post processing, which results in smaller series resistance, and is comparable to that of pristine bare diode value.

Table 4.4 Values for each element of the equivalent circuit for bare and embedded diodes

	R_s	R_d	C_{par}	C_j	L_s	f_{co}
Bare diode	6Ω	42.5Ω	3fF	21fF	130pH	0.44 THz
Embedded diode	5Ω	35.7Ω	3fF	21fF	400pH	0.48 THz

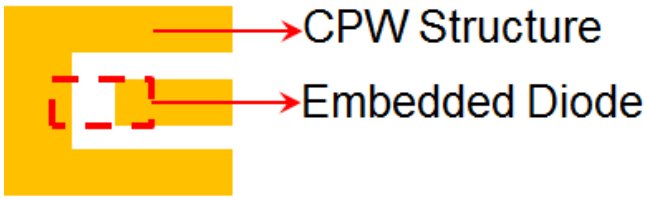

Figure 4.13 Schematic view of a CPW structure for S-parameter measurement

4.1.3.3 Rectification Measurement

For the RF measurements, a 40 GHz ground-signal (GS) probe is used to probe the devices and carry out preliminary measurements in the low frequency range. For some of the circuits, the probe is brought into contact to one of the antenna arrays connecting the diodes. Several circuit functions were tested including rectification, multiplication and mixing.

For rectification tests, 18GHz excitation with a power of -6.33dBm from the RF source is fed in through the probe to the embedded diode. Figure 4.15 shows the output rectified voltage as a function of forwards bias applied to the diode. The applied bias is maintained below 0.8V to prevent any damage to the device. The diode has the strongest nonlinearity around 0.7V, where the measured output rectified voltage is 4.56mV. This matches the I-V characteristic where around 0.7V is the turn-on voltage. Note that due to the impedance mismatch between the probe

and the diode, RF power provided by the source was not completely absorbed by the device. Further measurement shows that at 0.7V, only about -23.33dBm had been fed in through the probe to the diode element.

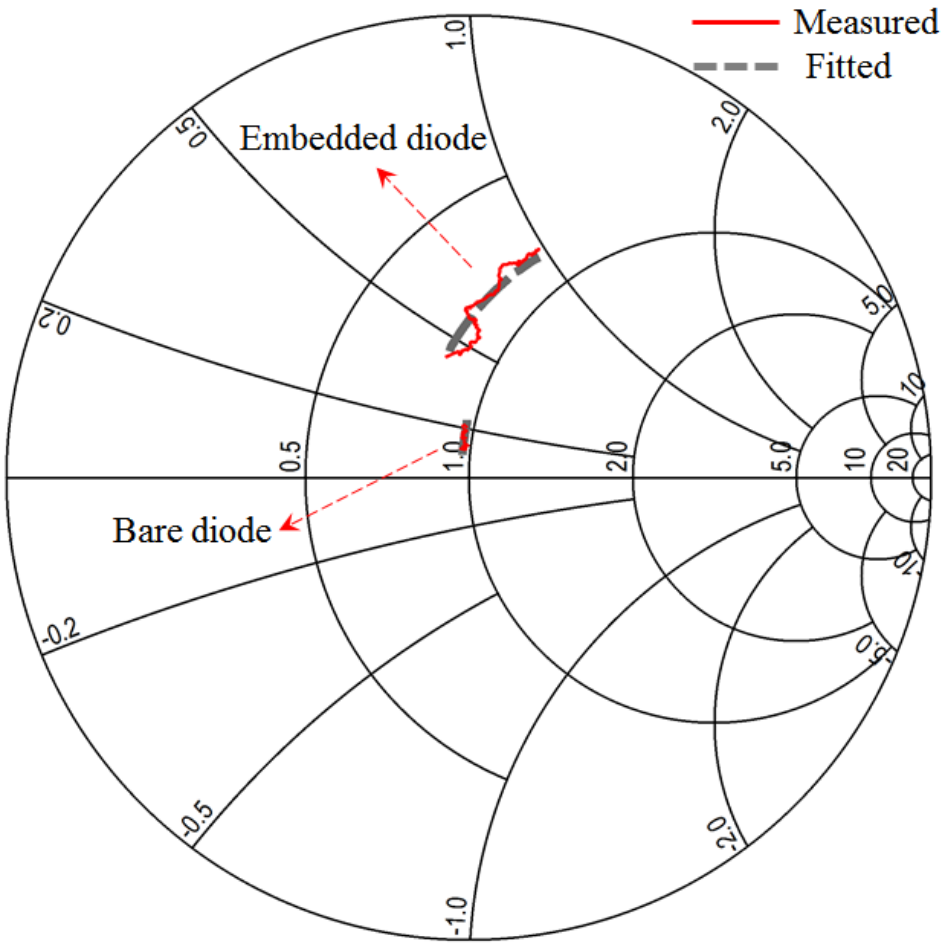

Figure 4.14 Measured and model fitted S-parameters for embedded and bare diodes at 0.7V.

The rectified voltage was also measured as a function of input RF power and the measured results are shown in Figure 4.16. Here, the applied bias is fixed at 0.7V, where the diode has the strongest nonlinear behavior.

The voltage sensitivity β and the NEP at 18GHz can be derived based on the diode equivalent circuit as well as the measured equivalent model parameters of the embedded diode. Equations for calculating NEP as well as β from Chapter 3 are used, which are reproduced here for convenience. The only difference is the equation for flicker noise, which is shown in Equation 4.5.

$$NEP = \frac{V_n + V_{1/F}}{\beta_V} \tag{4.1}$$

$$\beta_V = \frac{\gamma}{2} \frac{R_d \left(1 - |\Gamma|^2\right)}{\left(1 + R_s / R_d\right)^2 \left(1 + \left(f / f_{ci}\right)^2\right)} \tag{4.2}$$

$$f_{ci} \equiv \frac{\left(1 + R_s / R_d\right)^{1/2}}{2\pi C_j \left(R_s R_d\right)^{1/2}} \tag{4.3}$$

$$V_n = \left(4k_b T_B \left(R_s + R_d\right)\right)^{1/2} \tag{4.4}$$

$$V_{1/F} = \left(S_I \times R_d\right)^{1/2} \tag{4.5}$$

Equations here are explained again: (1) indicates that the NEP is determined by two factors: the voltage noise $(V_n+V_{1/f})$ and the voltage sensitivity β_v. Decreasing the voltage noise and increasing the voltage sensitivity help in lowering the NEP value. A lower NEP value means the detector has higher sensitivity. The total voltage noise is dominated by the sum of thermal noise V_n (Eq. (4)) and the flicker noise $V_{1/f}$, (Eq. (5)) both are strongly related to the series resistance R_s and junction resistance R_d of the SBD. S_I here represents the current form of *1/f* noise power spectrum density, and varies according to the modulation frequency and bias applied on the detector. Moreover, R_s and R_d also determine the cut-off frequency f_{ci} as well as the voltage sensitivity β_v. From this point of view, reducing the value of R_s and R_d can help in decreasing the NEP. However, the R_d should be maintained near 1kΩ to achieve better impedance matching to an IF amplifier typically used behind the detector element. Equation (2) indicates that the

voltage sensitivity depends on γ, which is called the curvature coefficient. This comes from the ratio of the 2nd derivative of the diode I–V characteristics to its 1st derivative. For a typical SBD, the highest γ value is close to 40 at room temperature. Note that the mismatch loss ($1-|\Gamma|^2$) between the antenna and the Schottky diode has to be considered in while calculating the voltage sensitivity and NEP. In order to operate at high frequencies, the junction capacitance C_j of the diode should be low to achieve a higher cutoff frequency.

The calculated β as well as NEP values is plotted as a function of applied voltage in Figure 4.17. The voltage sensitivity at 0.7V is approximately 0.9mV/μW, which matches close to the measurement results. The lowest NEP in Figure 4.17 is around 4.5pW/Hz$^{0.5}$, which can be further improved by impedance matching as shown in Figure 4.18. Both optical and electrical NEPs (under matched condition) are shown in Figure 4.18 for comparison. With good impedance matching NEP as low as 2pW/Hz$^{0.5}$ can be achieved.

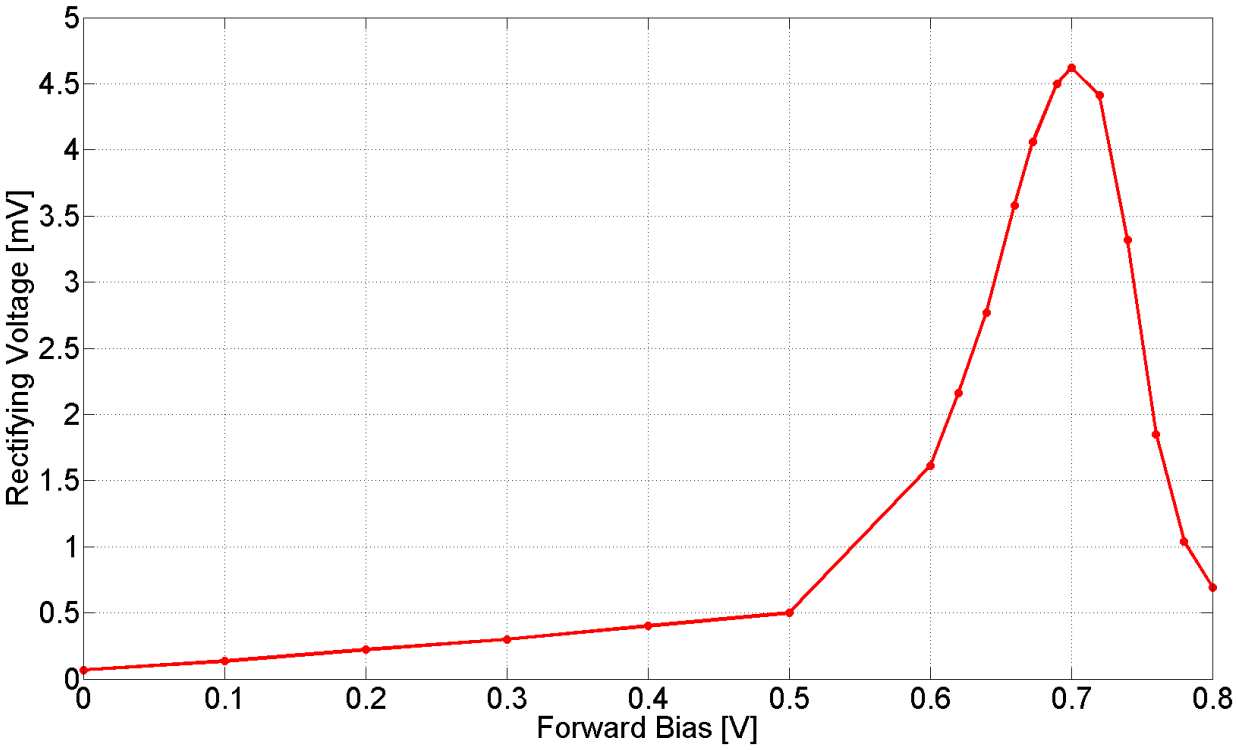

Figure 4.15 Rectifying voltage changing respected to sweeping forward bias.

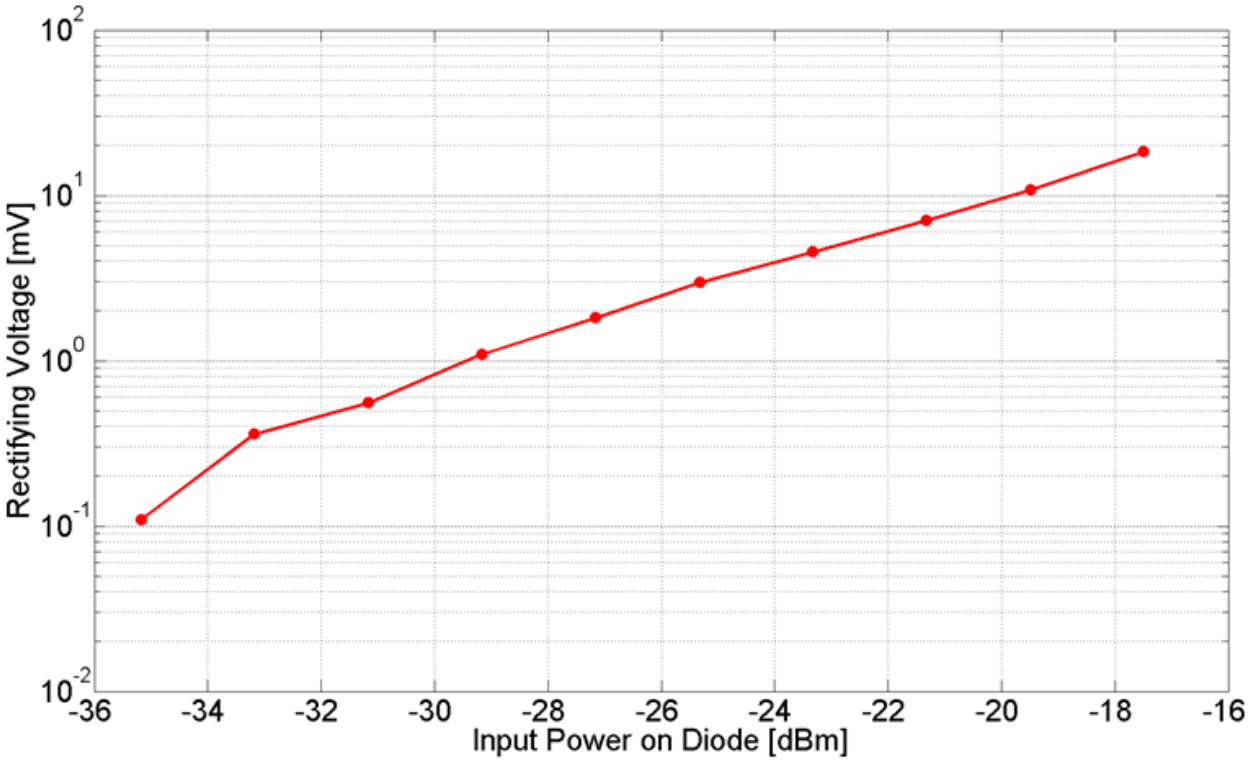

Figure 4.16 Output rectified voltage as a function of input RF power.

NEP and voltage sensitivity are also characterized for frequencies higher than 18GHz. Assuming the designed antenna is used instead of the GS probe, Figure 4.19 shows the NEP and voltage sensitivity β spanning within 10GHz to 1THz frequency range. As the frequency increases above 100GHz, the voltage sensitivity degrades and the NEP increases dramatically. At 1THz, the sensitivity is about 0.04mV/μW, and NEP is around 150pW/Hz$^{0.5}$, this is due to the strong impedance mismatch between the antenna and the embedded diode. This needs to be improved for applications in the design of THz imagers and detectors. As discussed earlier, to overcome this, small series resistance and capacitance diodes with smaller parasitics are desired. Further simulations indicate that under matched condition, the NEP can be as low as 15pW/Hz$^{0.5}$

at 1THz, and the sensitivity can be maintained around 0.4mV/μW at the same frequency, which is 10 times better than those under the mismatched condition.

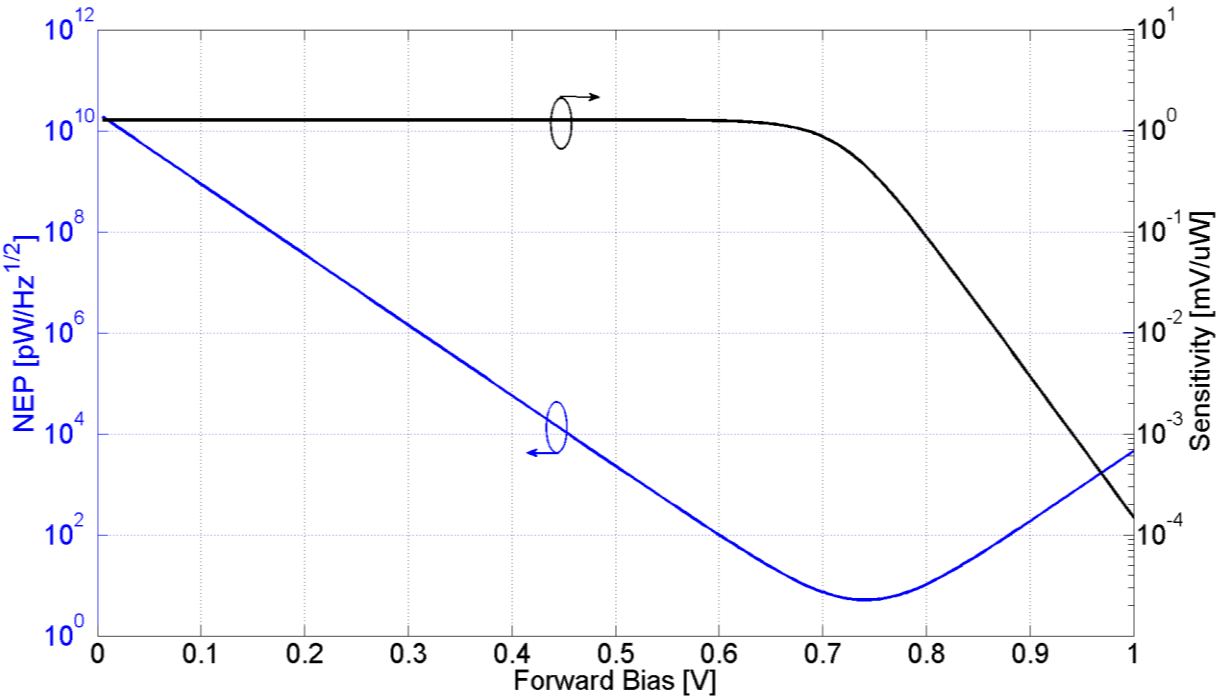

Figure 4.17 Voltage sensitivity β and the optical NEP at 18GHz under impedance mismatch condition.

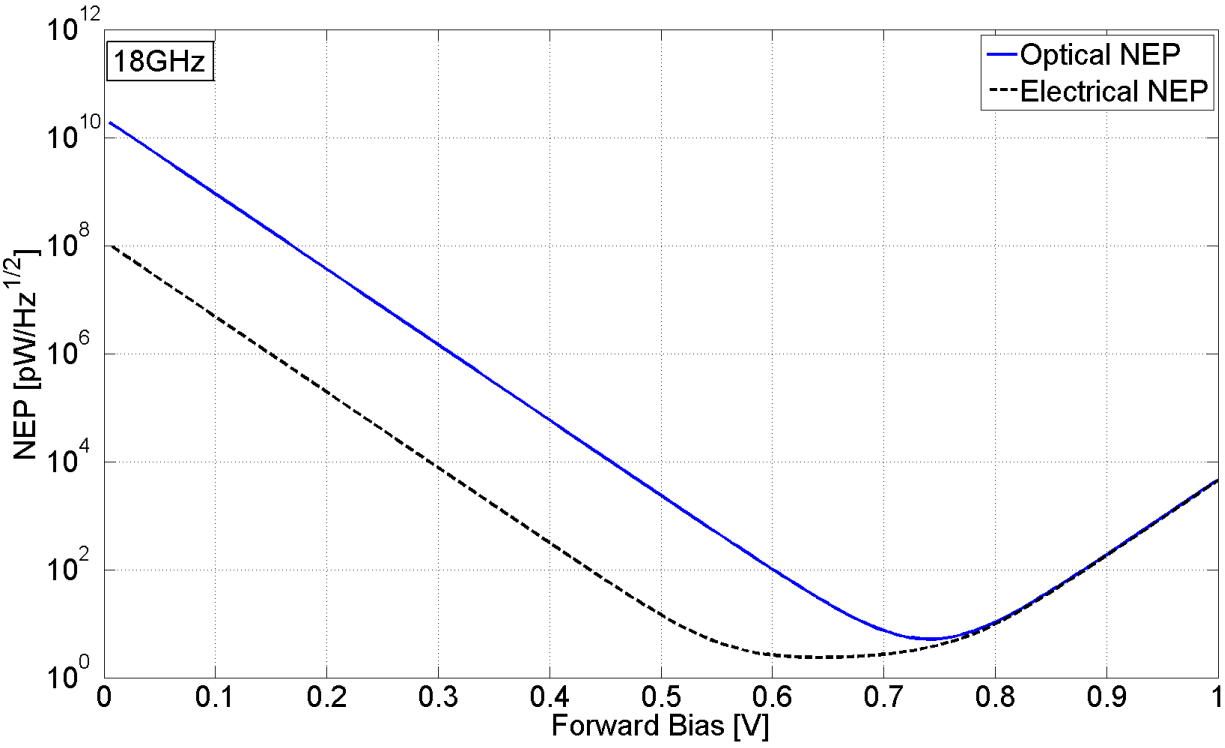

Figure 4.18 Optical (mismatched) and Electrical (matched) NEP at 18GHz under different bias conditions.

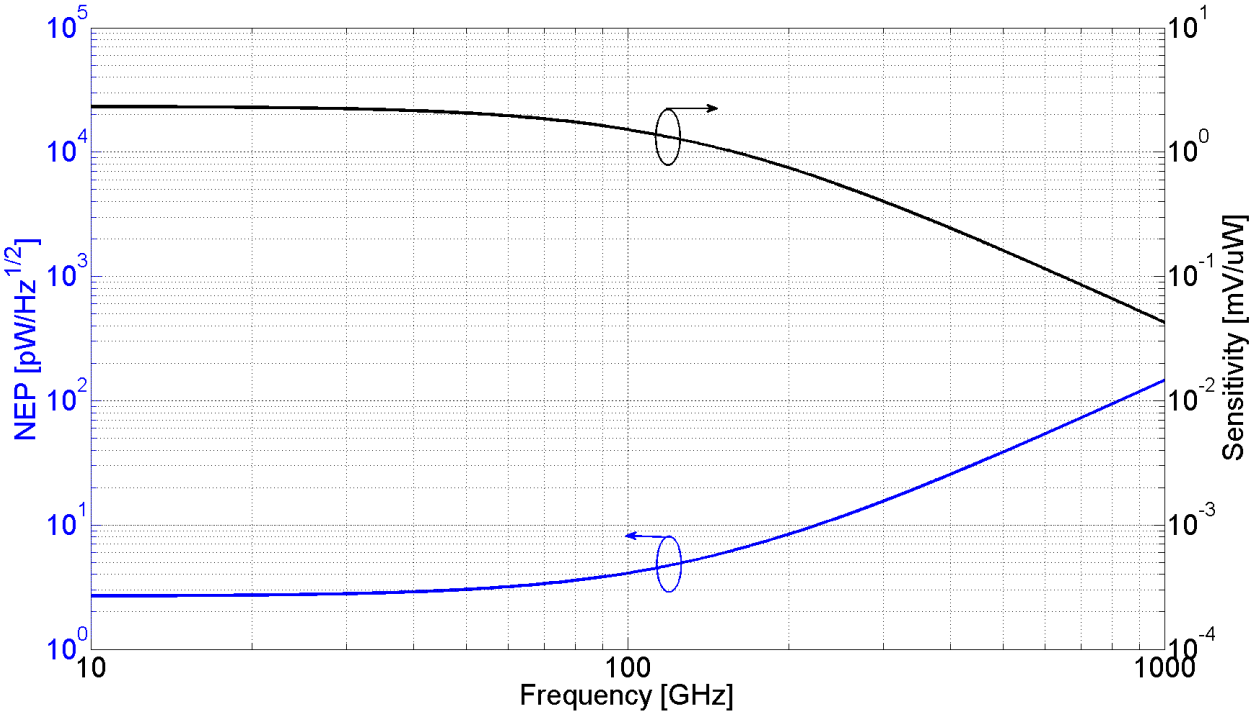

Figure 4.19 Optical NEP and voltage sensitivity under mismatched condition as a function of frequency.

4.1.3.4 Frequency Multiplier Measurements

Another application of the fabricated embedded diode structures is in frequency multiplication. The experimental setup is the same as used above for the voltage rectification experiments. The GS probe is used to both pump the diode with the fundamental frequency and also to pick up the harmonics generated by the nonlinear characteristics of the diode. Figure 4.20 shows the 3rd harmonics of the fundamental frequencies for 4GHz and 5GHz. The input power on x axis represents the power that is absorbed by the embedded diode, and it is swept by controlling the RF source power level. The bias is again fixed at 0.7V where the best nonlinear behavior is achieved from the diode.

Figure 4.21 shows the output power of the frequency multiplier at different fundamental frequencies, when the input power (absorbed by diode) is fixed at approximately -13dBm. The

output powers for both of the 2nd and 3rd harmonics decreases when the fundamental pump frequency increases. For higher frequency multiplication, more power needs to be fed into the device to achieve good conversion efficiency.

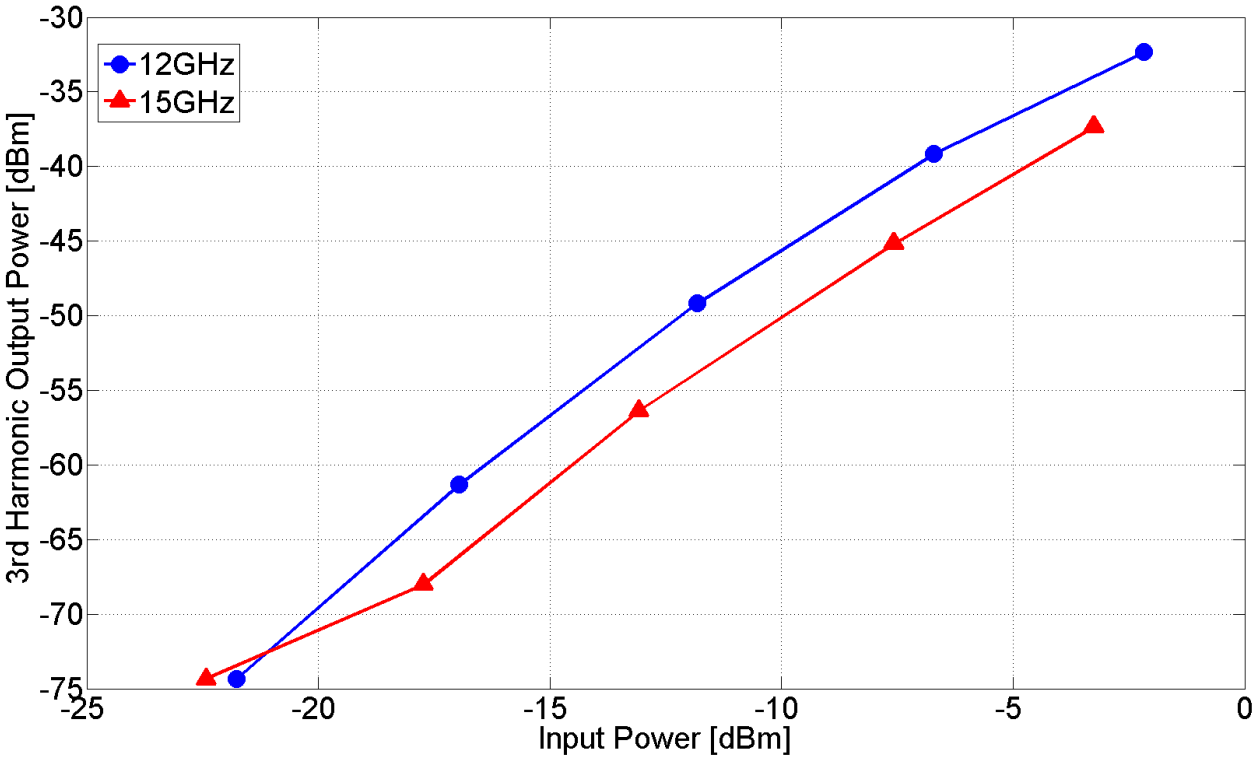

Figure 4.20 3rd harmonics output power of 4GHz and 5GHz fundamental input frequencies.

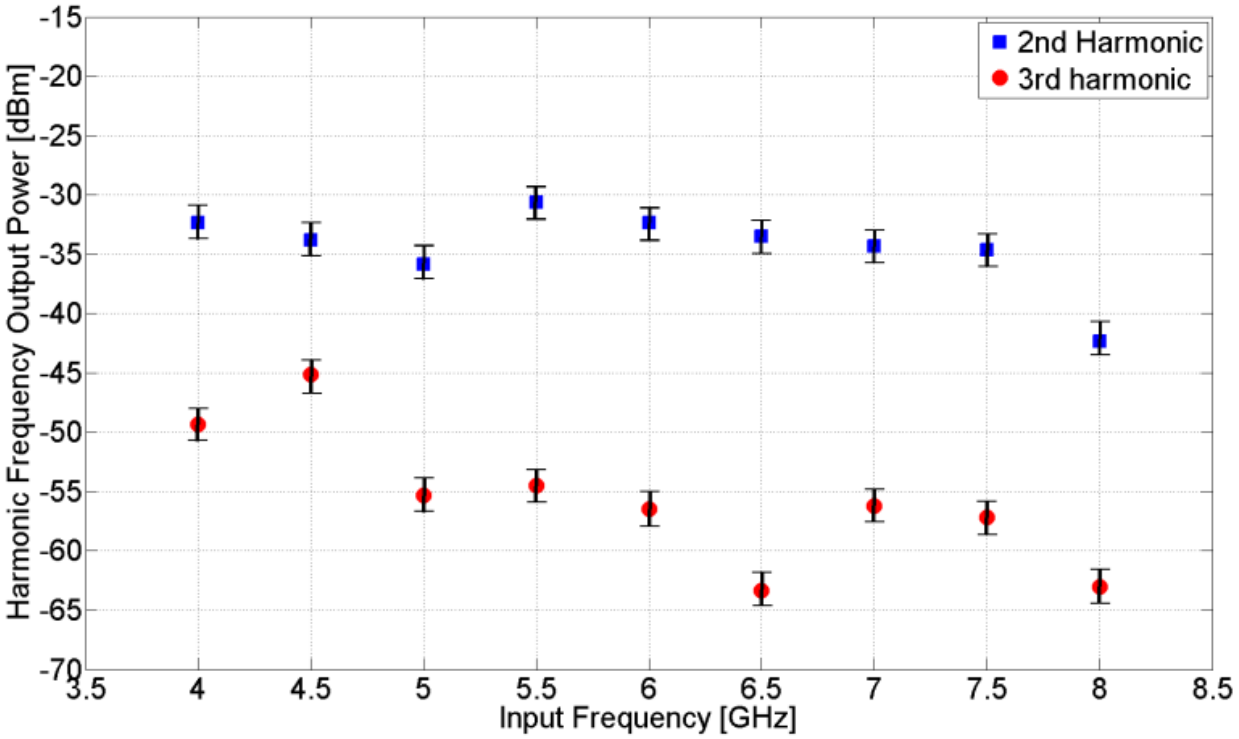

Figure 4.21 Output power of 2nd ($2f_o$) and 3rd ($3f_o$) harmonics at different fundamental frequencies. The input power at f_o is approximately -13dBm.

4.1.3.5 Frequency Mixer Measurements

Frequency mixing is also tested using this embedded diode structure. Again, the GS probe is used for feeding in the RF signal and also to measure the output signal. A separate RF source was used as a local oscillator (LO), whose frequency is fixed at 18GHz. The RF input frequency is fixed at 19GHz, and its power is being swept in order to see the variation of IF output power at 1GHz for different input power values. Figure 4.22 shows the results of output power for 1GHz at different LO power while sweeping the RF input power. Here again, the conversion efficiency improves with increase in the LO power.

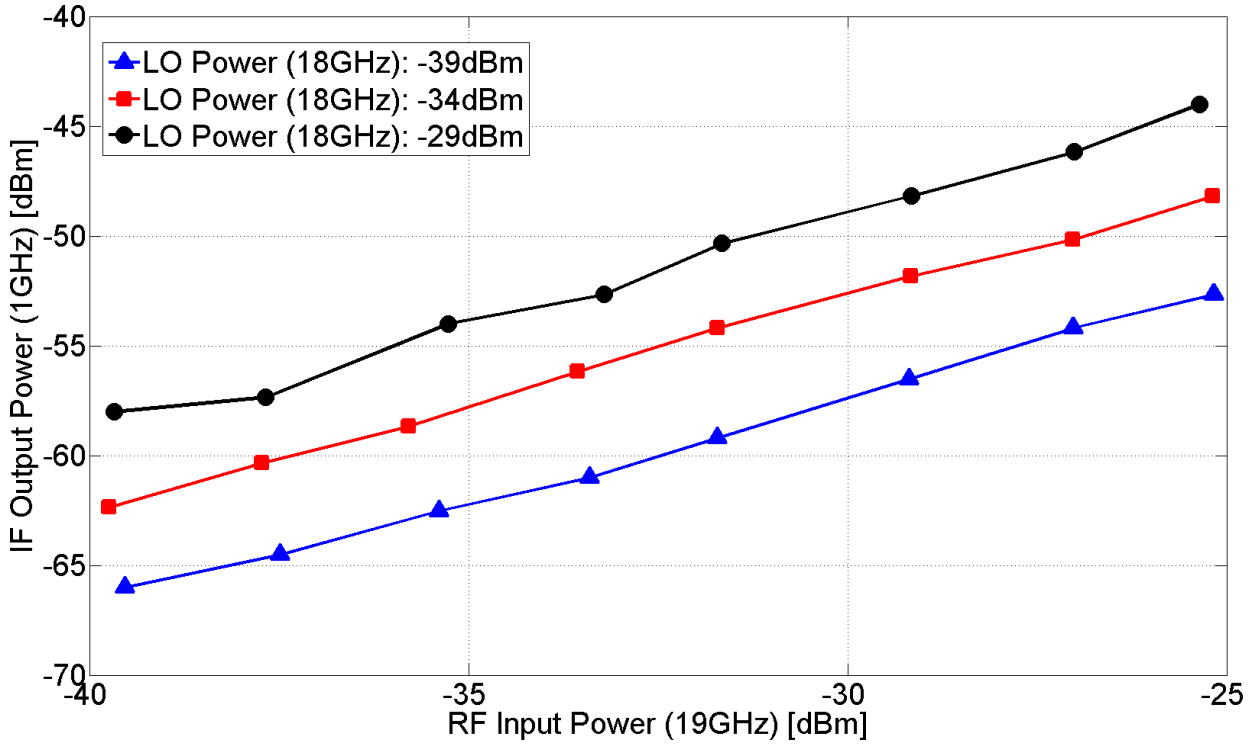

Figure 4.22 Output power of IF (1GHz) at different LO power and RF power.

In summary, similar DC characteristics of embedded diodes on the same substrate indicate that the embedded fabrication procedure is reliable for multiple diodes assembling on a single wafer. Strong RF responses of the embedded diodes allow designing large variety of MMW and THz integrated circuits based on the embedded integration.

Based on above results and analysis, embedded diode process has been proved to be an advanced, large area compatible, low cost and reliable method for DC especially for RF circuit applications. To maximize the advantages of this novel process, it is necessary to push this active device process to be applicable further into THz integrated circuits. The image sensor, as an example, operating at W-band will be demonstrated and well explained in the following sections.

4.2 THz Schottky Diode Image Sensor based on Embedded Diode Structure

4.2.1 Device Sensitivity and Equivalent Small Signal Model

The NEP of GaAs SBD has been demonstrated to be as low as 5pW/Hz$^{0.5}$ in the 100-120 GHz frequency range [97], and this value increases with frequency due to the parasitics associated with the diodes. This has been well explained based on the Schottky diode equivalent circuit and related equations 4.1-4.5 in the previous section. The small signal equivalent model for the SBD detector is shown in Figure 4.23.

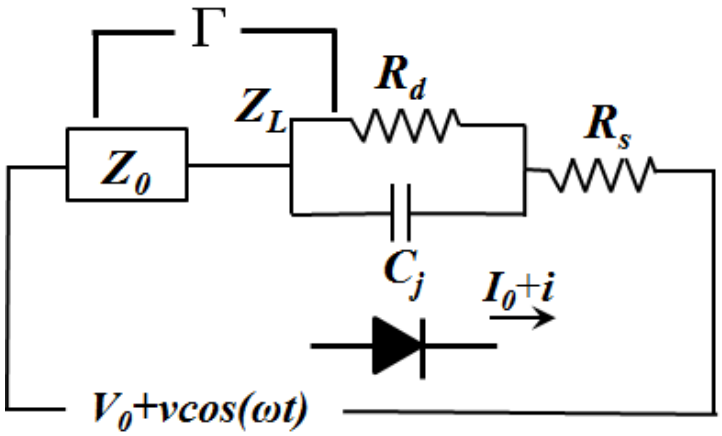

Figure 4.23 Small signal equivalent model for a SBD detector (Single pixel)

The junction resistance or the differential resistance R_d comes from the Schottky barrier, which is dependent upon applied bias voltage. If the THz signal is small, it is largely determined by the DC bias voltage. The series resistance R_s arises due to the Ohmic contact and pad contacts. The reflection coefficient Γ can be derived from Eq. 4.6, where Z_L is the impedance of the diode and Z_o is the characteristic impedance of the antenna element.

$$\Gamma = \frac{Z_L - Z_o}{Z_L + Z_o} \tag{4.6}$$

The mismatch loss (1-$|\Gamma|^2$) between antenna and the SBD should be minimized to achieve maximum power transfer.

4.2.2 Antenna Design and Device Selection

Two-terminal planar log-periodic antenna, shown in Figure 4.24, is designed and applied here for broadband detection. The antenna was optimized to cover a frequency range from approximately 30 GHz to 0.7 THz. The corresponding resonance frequency limits are determined by the lengths of longest and shortest teeth through equation 4.7 [104]

$$f_n = \frac{c}{\pi(R_n + r_n)/2} \tag{4.7}$$

in which, c is the speed of light in free space, R_n and r_n are outer and inner radius of the nth antenna tooth, which are shown in Figure 4.24. Moreover, two adjacent resonance frequencies follow the relation in equation (8) [105],

$$\ln(f_n) - \ln(f_{n+1}) = \ln(\tau) \tag{4.8}$$

where $\tau = R_{n+1}/R_n$ and $\sqrt{\tau} = r_n/R_n$. The log-periodic antenna follows the self-complementary principle, thus the input impedance through the entire frequency range agrees with Mushiake Principles [106], with a constant value of $120\pi/2=188.4\Omega$. The antenna impedance is another constraint when choosing diodes with proper series and junction resistance for a better impedance matching. In this design, τ is equal to 0.81 and the outer radius R_1 of the longest tooth is 3.7mm

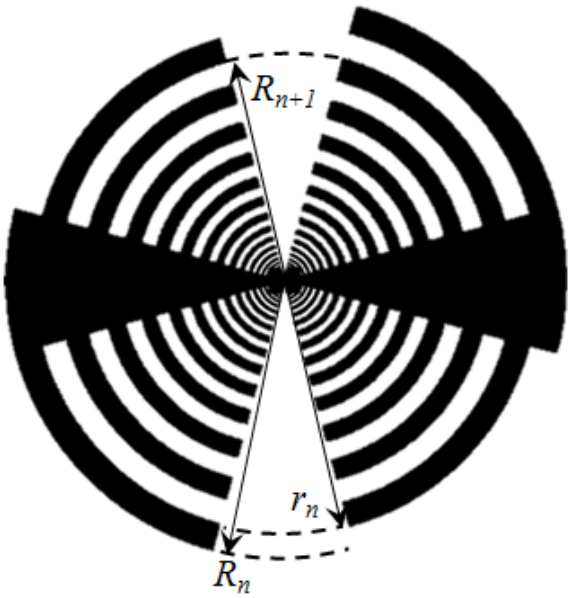

Figure 4.24 Schematic of Log-Periodic Antenna

The above analysis shows that small series parasitic resistance leads the improvement of NEP value, while low junction capacitance leads to higher cut off frequency. Based on these criteria, another commercially available Schottky diode (Agilent HSCH-9401) was selected. This diode chip has several advantages over the previous diodes: firstly, the contact pad is larger, which helps to improve the contact between via and reduce the resistance; secondly, polyimide is coated on the chip after it is fabricated, only leaving the contact pad open, and this can protect the diode core area during the fabrication process in any unexpected situation, and preserve the diode high frequency performance. The key parameters for this diode are shown in Table 4.3. The diode is available in a chip format having dimensions of approximately 610 μm x 255 μm and thickness of ~100 μm.

Table 4.3 Typical Specs of Agilent HSCH-9401 GaAs Schottky diode.

Cutoff-Frequency f_{ci} (GHz)	Series Resistance R_s (Ω)	Junction Capacitance C_j (fF)	Reverse Current I_R (nA)
>800	6	35fF	200nA

This diode has a high cut off frequency, low junction capacitance, and can be used in building up a THz imaging array. The chip is thin and thus a thin flex substrate can be used for embedding the diodes. The dimensions are small and thus it requires special handling. For the work carried out here, it was manually handled using vacuum tweezers.

4.2.3 Fabrication of THz Image Detector

The fabrication process follows the same procedures of the embedded diode structure discussed earlier. Figure 4.25a shows one opened cavity as well as the copper mask around it. The GaAs SBD is then placed into the opened cavity, which is shown in Figure 4.25b. A thin layer of SU-8 is spin coated and patterned to open via for the contact pads of the diode, and Figure 4.25c shows an example photomicrograph. Figure 4.26 shows a 2x2 fabricated imaging array on a Zeonor substrate and a close up view of the antenna structure.

The entire fabrication process of this embedded actives integration is low-cost and large-area compatible, and it is not only limited for imaging sensors. Varieties of other high frequency circuits are also achievable through this method to realize larger area with complicated designs. In addition, the low-temperature feature is friendly to the polymer based devices, which further widens its applicable range.

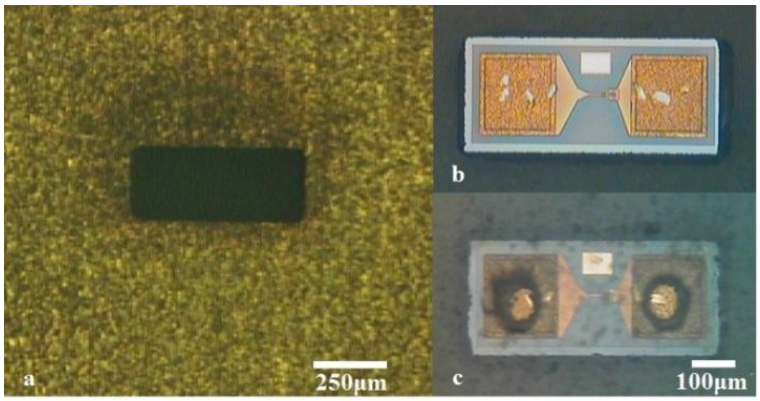

Figure 4.25 a) Roger thin sheet surface with laser cut cavity, b) after placement of diode in cavity and c) after spin coating SU-8 layer with vias opened directly on top of diode pads.

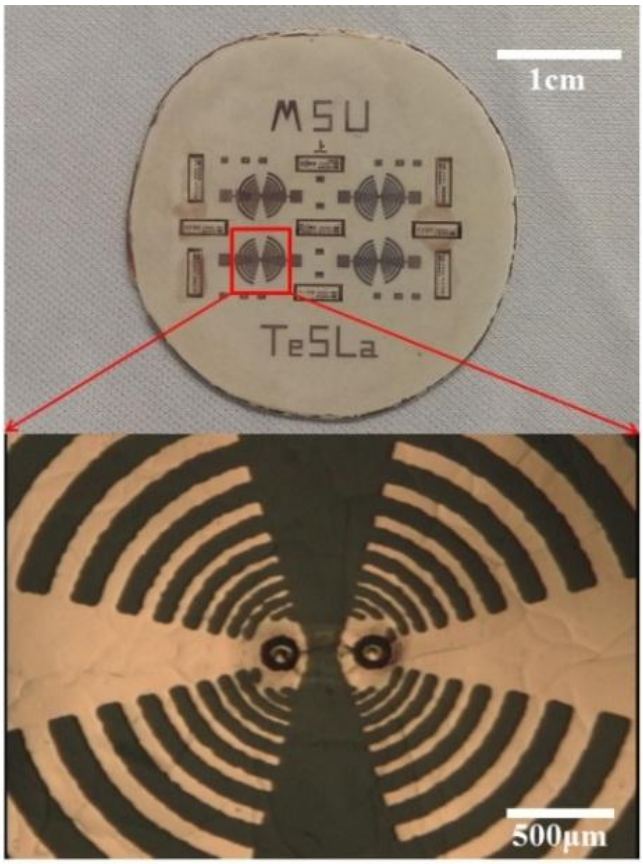

Figure 4.26 Fabricated imaging array and close up view of a single detector pixel element.

4.2.4 Measured Results

4.2.4.1 Detector Element Characteristics

The I-V characteristics of a fabricated single pixel detector element are measured on a wafer probe station using a semiconductor parameters analyzer, and the results are shown in Figure 4.27. The fabricated device has strong non-linear behavior in 0.65-0.75V forward bias region. Applying curve fitting with the ideal diode I-V equation, the best fit parameters extracted are: R_s=12Ω, I_s=7.88×10^{-14}A and n=1.187. These values are then used to calculate the NEP as well the voltage sensitivity. The total resistance (R_d+R_s) is also calculated based on the curve fitting and plotted as a function of applied bias. In order to verify that the diode's original performance is not degraded by the embedded fabrication process, I-V characteristics measured at step h and at step k in Figure 4.6 are shown in Figure 4.28. In the operation region of 0.4-0.8V forward bias, in which the strongest nonlinear region is included, two curves are overlapped, which indicates that this fabrication process is reliable and suitable for heterogeneous integration. The series resistance of the device was measured to be higher than the typical value listed in Table 3, which is possibly due to the variance of semiconductor fabrication of different GaAs SBDs.

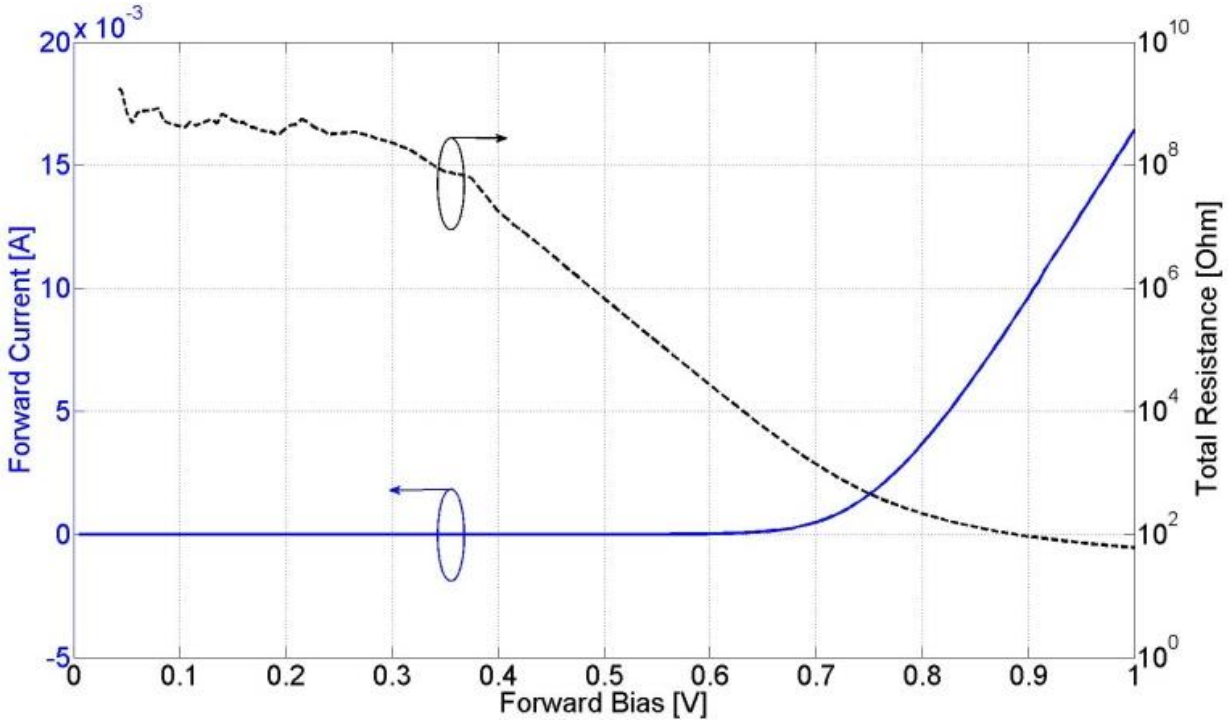

Figure 4.27 Measured I-V characteristics of a single pixel element and its calculated total resistance (R_d+R_s).

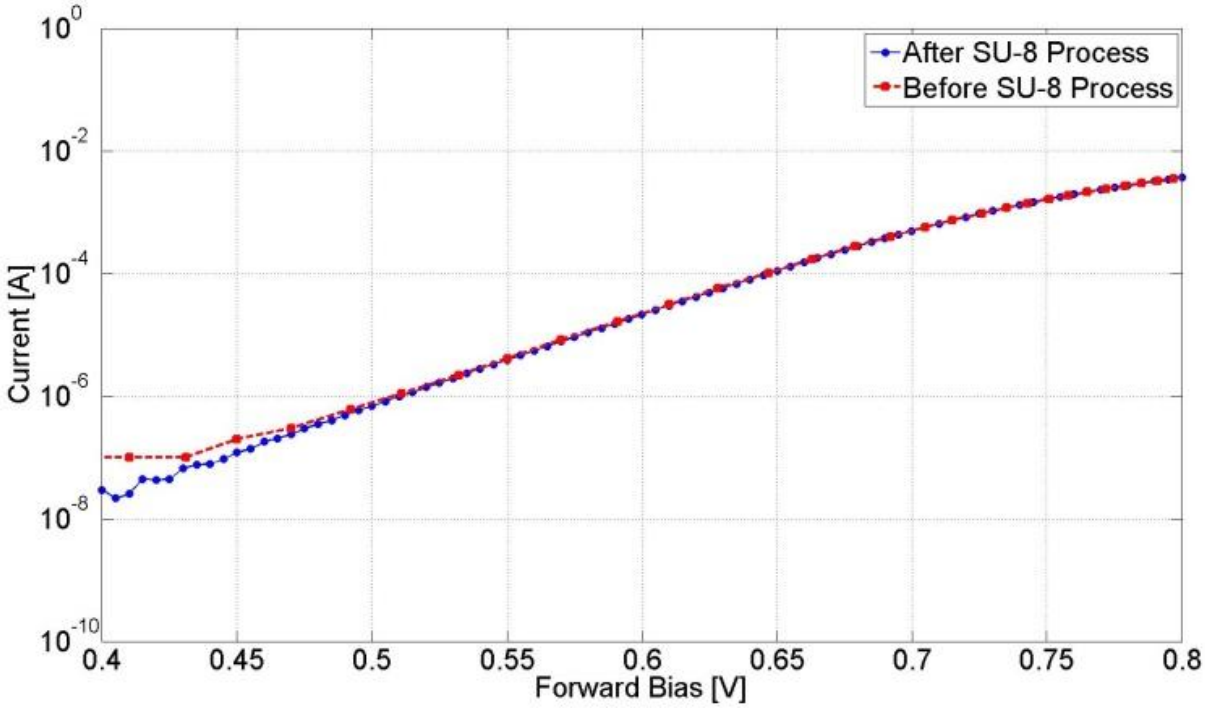

Figure 4.28 Comparison of Measured I-V Characteristics before and after SU-8 Process.

NEP and voltage sensitivity at 0.1THz was first calculated using Equations (1)-(6) with the parameters extracted from the curve fit and device datasheet. The differences between the antenna impedance and the diode junction resistance R_d is relatively large (approximately 200Ω to 1.5kΩ) at the strongest nonlinear region. The power loss (reflection) due to the impedance mismatch must be considered and included in the calculations. Meanwhile, the *1/f* noise power spectrum density in current form S_I has been taken as 10^{-21} A^2/Hz at the modulation frequency of approximately 1 KHz based on the report from refs. [107-109], which gives its value in voltage form around 9×10^{-16} V^2/Hz. Figure 4.29 shows the optical NEP (including power loss) and voltage sensitivity versus forward bias. The highest voltage sensitivity is about 7.7mV/μW at 0.68V, and the lowest NEP is 3.6pW/√Hz at 0.74V, which is in good match with other detectors [92].

Electrical NEPs (perfectly impedance matched and no power loss condition) were also calculated, and the lowest value is about 2.9 pW/√Hz at 0.74 V. The difference between optical and electrical NEP at this bias value is small because the diode junction resistance R_d has dropped to a proper value and improved the impedance matching to the antenna. When moving away from this bias position, the difference becomes larger, as shown in Figure 4.30. The two curves deviate from each other at the lower and higher bias regions other than 0.74V.

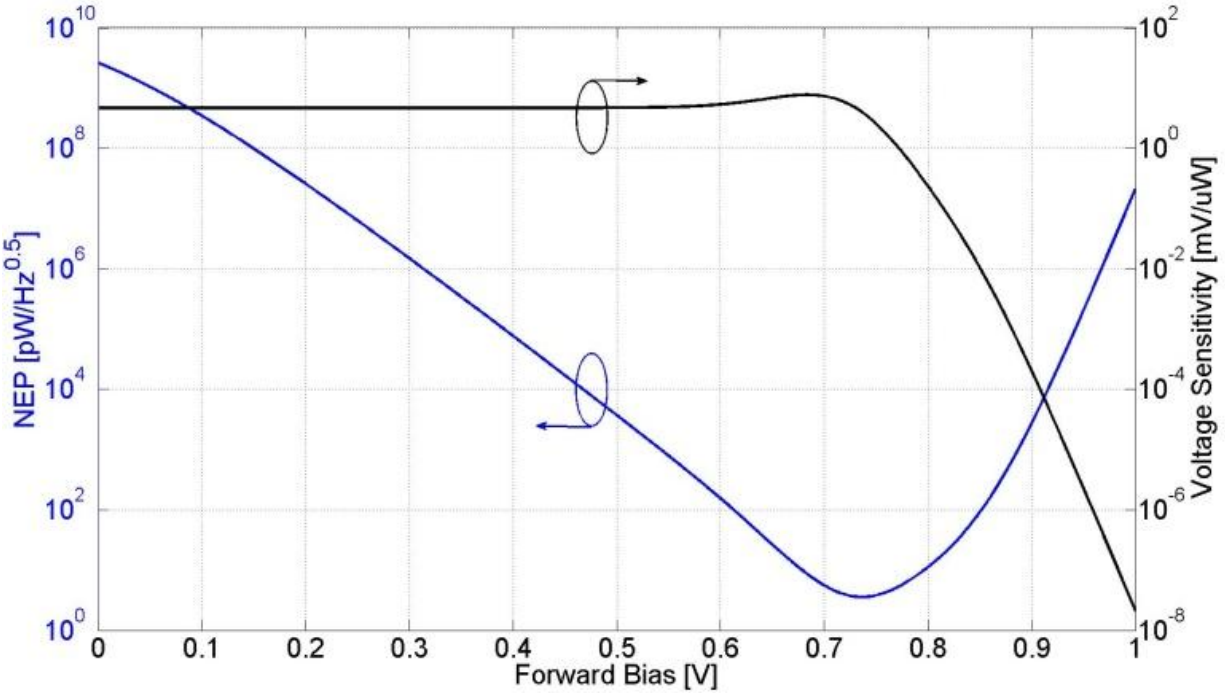

Figure 4.29 NEP and voltage sensitivity at 100GHz including the power loss condition (optical NEP).

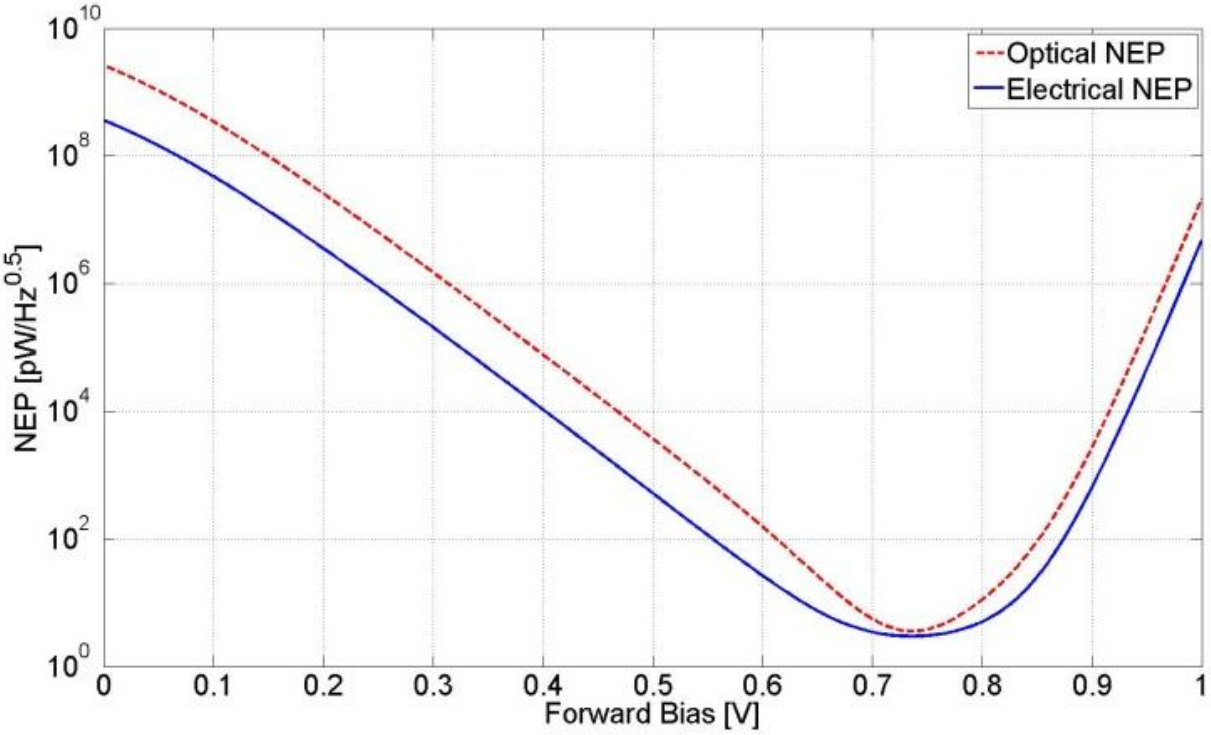

Figure 4.30 Optical and electrical NEP with respected to forward bias.

4.2.4.2 Detector RF Response

The measurement setup for characterizing the RF response of a single pixel SBD detector is shown in Figure 4.31. A W-band (75-110GHz) Backward Wave Oscillator (BWO) was used as the source. The power incident on the detector element was calibrated by using a harmonic mixer in combination with a spectrum analyzer. The DUT is placed between the transmitting and receiving horn antennas, but closer to the receiving antenna for more accurate power calibration. The rectified voltage generated from the detector was measured using a Keithley nano-voltmeter. Measurements were first carried out by fixing the wave frequency and power while changing the forward bias. The power received by the horn antenna without the detector in the path was measured first and fixed at around -35dBm (316nW), by calculating the area differences between horn antenna and device log-periodic antenna, the power incident on the detector element was characterized at approximately -45dBm (31.6nW). Figure 4.32 shows the measured rectified

output voltage at different DC forward bias points. The RF frequency and incident power on the detector are 104.6GHz and -45dBm. A maximum rectified voltage of 0.3mV is measured near a DC bias of 0.67V. The SBD detector has the strongest non-linearity, better impedance matching and thus higher sensitivity at this bias value. Measured average voltage sensitivity β_v of the detector through the whole W band is approximately 7500V/W.

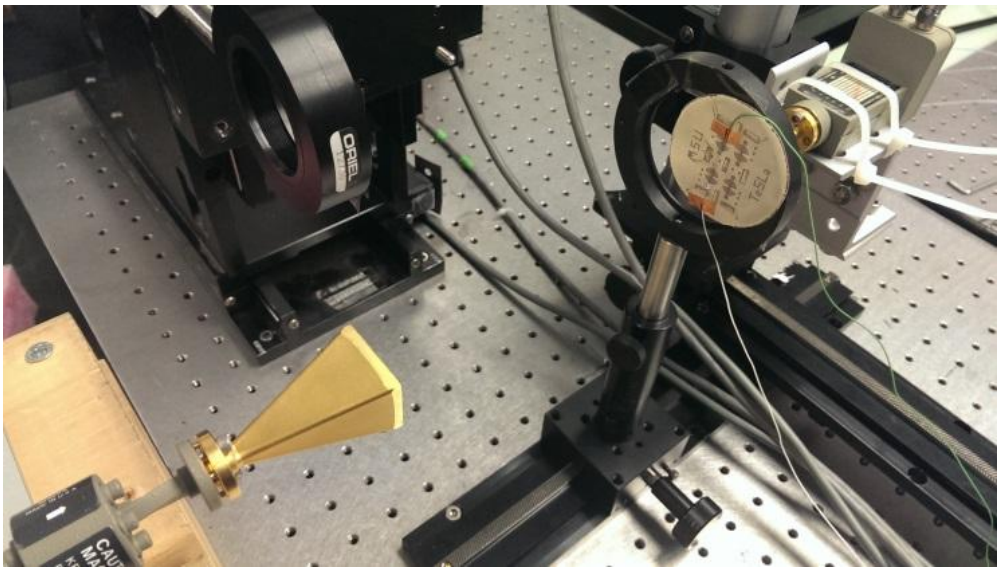

Figure 4.31 Measurement setup for one detector element at 100GHz.

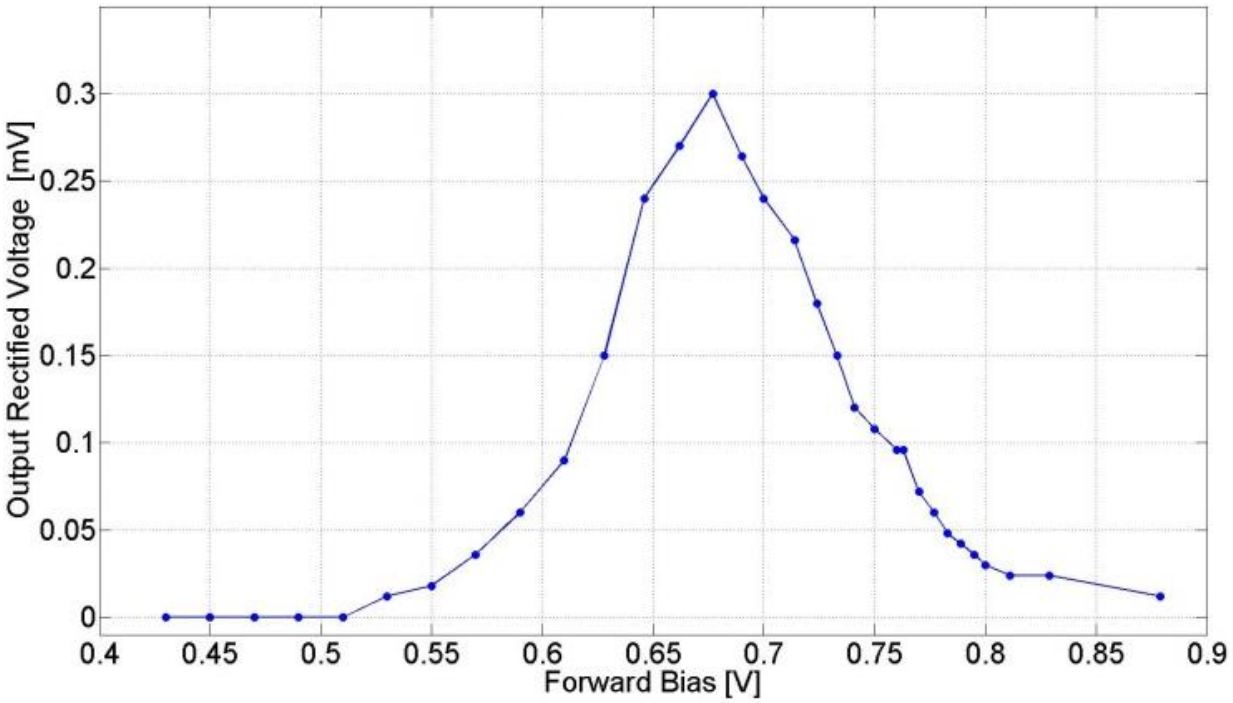

Figure 4.32 Output rectified voltage as a function of bias voltage at fixed RF frequency (104.6GHz) and power (-45dBm).

Output rectified voltage changing with respect to the incident power is also measured and plotted in Figure 4.33. The frequency was also fixed at 104.6GHz and the incident power was altered by adding attenuators in the wave path. The detector element was biased at 0.67V, which gives the strongest nonlinearity. From these results, it is clear that the rectified voltages increase when the incident power increase, and the trend follows the square law in the low power region.

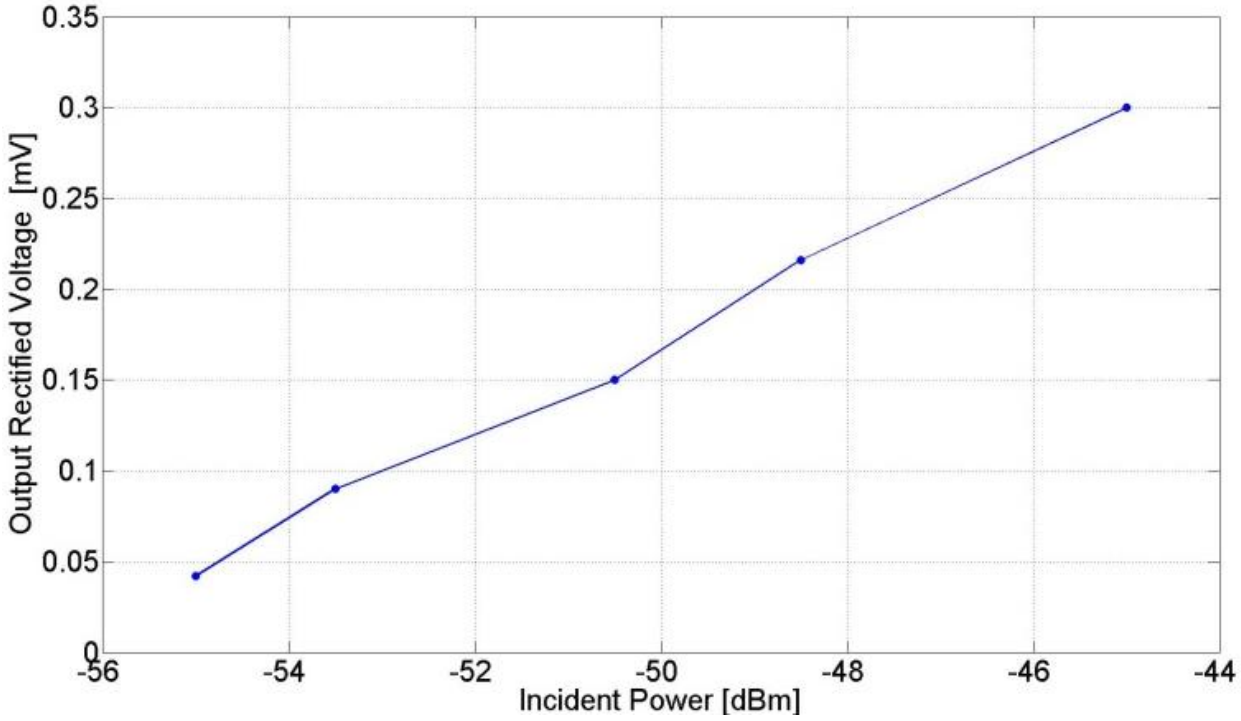

Figure 4.33 Output rectified voltage as a function of incident power at fixed bias voltage of 0.67V.

NEP values for frequencies higher than 0.1THz were also calculated. As the frequency goes higher, NEP increases due to the decreasing of the voltage sensitivity. For frequencies of 0.2THz, 0.5THz and 0.8THz, the lowest NEPs are 6.1 pW/√Hz, 17.3pW/√Hz and 33.5pW/√Hz. This is expected as the parasitics (junction capacitance C_j) associated with the diode begin to dominate and shunts the incident signal from the non-linear element (R_d).

4.2.4.3 Imaging Test based on Single Detector Element

One of the prominent applications of THz radiation is detecting concealed objects in an enclosure for security applications. THz waves can penetrate thin, low loss materials but are unable to penetrate lossy materials and metals. The imaging process setup in this work is depicted in Figure 4.34. The object for imaging was sealed in an envelope and vertically placed between the BWO continuous wave (CW) source and the detector element. A robotic arm

controlled by a micro-stepper motor holds the envelope. The stepper motor is programed to be able to move the object to be scanned along x (horizontal) and z (vertical) directions with a desired step size. After each step, the trigger signal voltage is brought down to low which enables the DAQ card to collect the DC rectified output voltage from the detector. This voltage is then sent to the computer, and then the trigger voltage goes back to high to disable the DAQ to finish acquiring the data in this cycle. The detector scans the envelope with the object inside line by line sequentially, and the data read into the computer will form a matrix for plotting out the final imaging result.

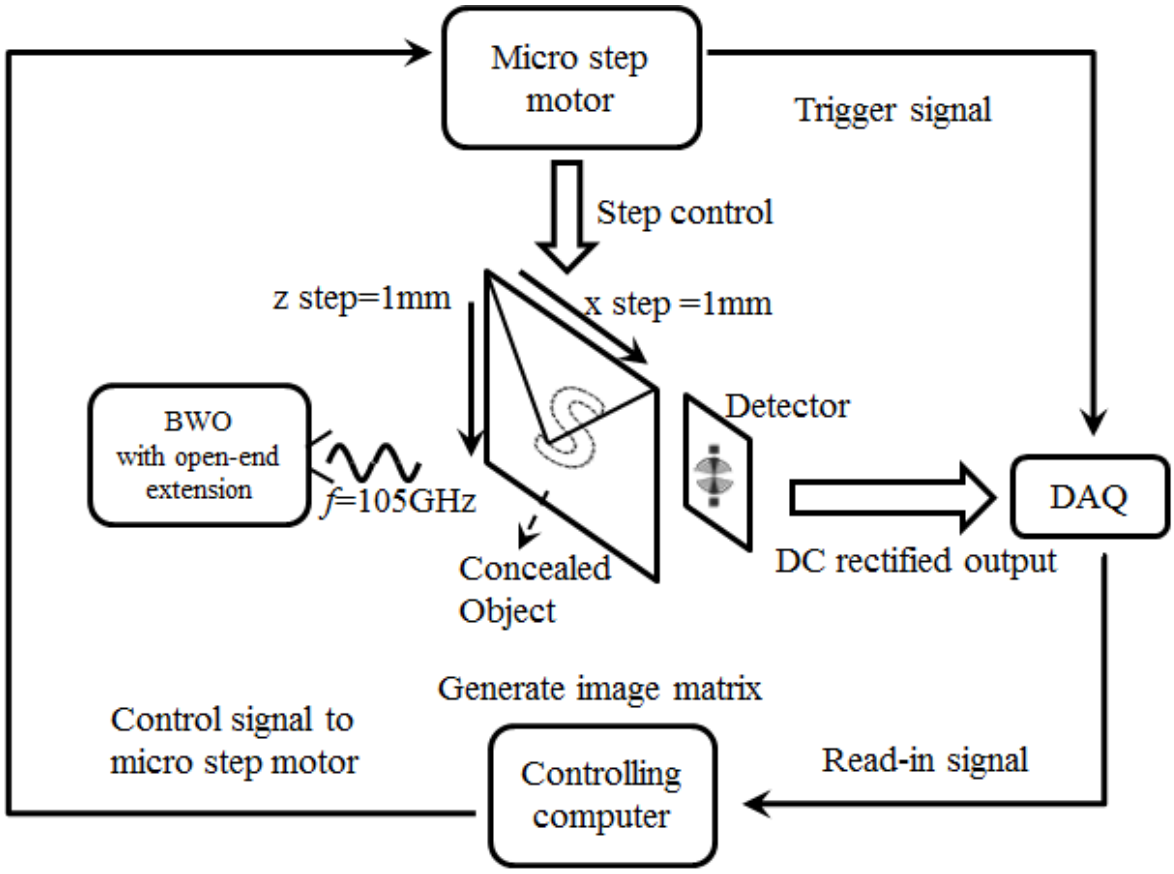

Figure 4.34 Schematic diagram of the imaging process setup

In this image scanning process, a 1.5mm thick metallized plastic "S", shown in Figure 4.35a, is enclosed in an optically opaque paper envelope. A 105 GHz CW signal (~ 25 μW) from the backward wave oscillator (BWO) impinges on the envelope. The BWO is only connected to an open-end extension waveguide instead of a horn antenna. This was done in order to eliminate the interference between the metallic S and the horn antenna and also to achieve a close to a plane-wave signal incident on the object. The distance from the waveguide aperture to the envelope and envelope to the detector is 50mm and 2mm, respectively. The scanning size is 40mm×40mm and scanned at 1mm increments in both x- and y-directions. Figure 4.35b shows the captured image result for the concealed object. The captured imaging resolution is 1mm × 1mm over an area of 40mm×40mm. From this scanned image, the object can clearly be identified.

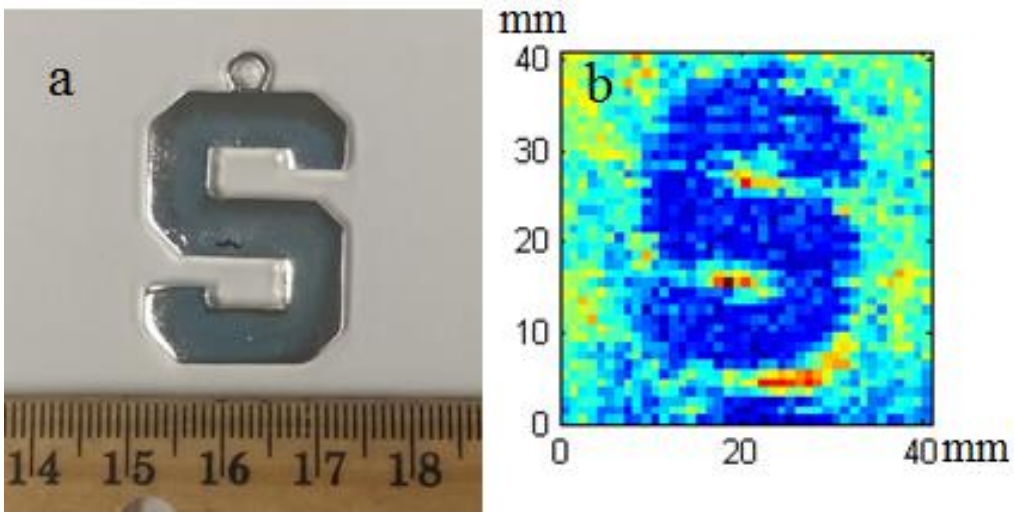

Figure 4.35 (a) Optical image of Metallic "S" sample to be tested before sealing in the envelope and (b) Detected image after scanning through the envelope with "S" inside (40x40 pixels).

The sharpness of the scanned image is determined by both the scan step size of the stepper motor and, more importantly, the spatial resolution of the detector itself. To estimate the resolution of the detector element, a sharp edge thin aluminum plate is mounted on the robotic arm and placed vertically between the open-end extension waveguide from the BWO and the

detector element. The transmitted signal (rectified output voltage) is then taken while moving the aluminum plate with 0.1mm steps by the micro stepper motor [110, 111]. The half power level (3dB or ~0.707 of the maximum value) of the gradient of the transmitted signal as a function of the moving distance is determined as the spatial resolution of the detector. Figure 4.36 shows both the normalized transmitted function with respect to the plate moving distance and the inverse value of the gradient function. At a frequency of 105GHz, a spatial resolution of 1.55mm is obtained.

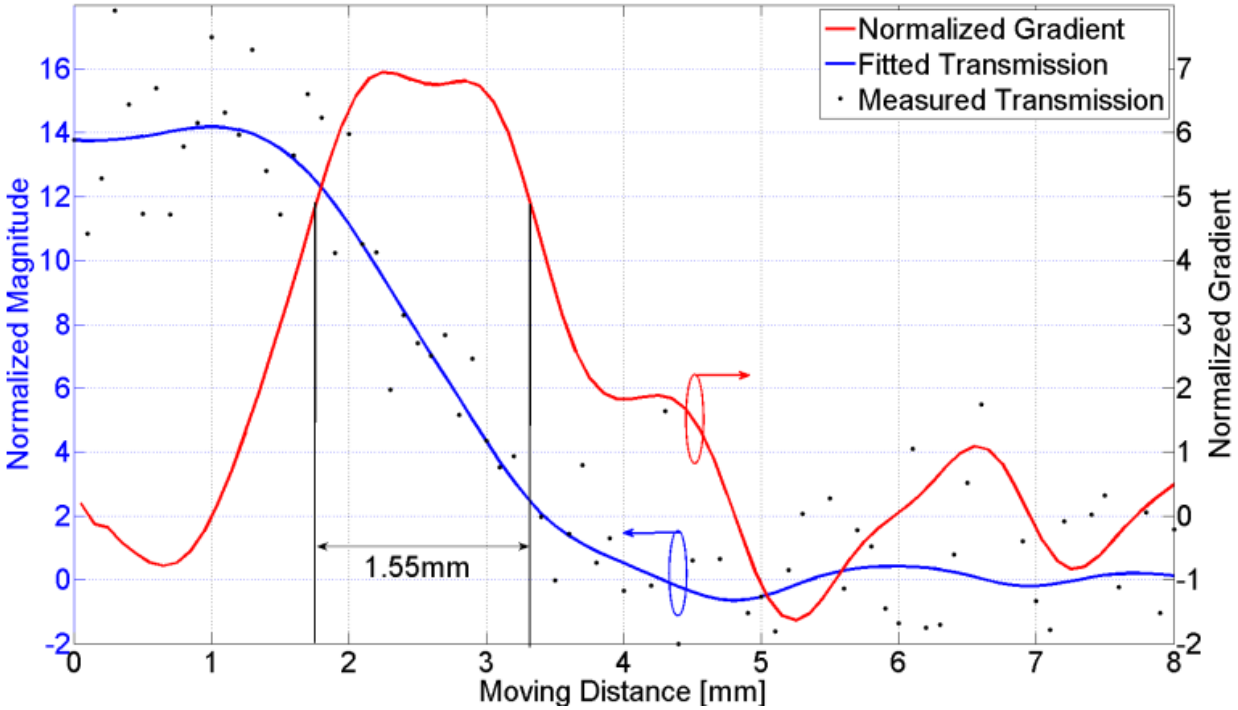

Figure 4.36 Normalized transmission function and its normalized gradient (inverse value). Half level (0.707 of max) gives approximately 1.55mm spatial resolution.

The wavelength at 105GHz in free space is around 2.9mm, so the 1.55mm spatial resolution in this work matches closely with the Rayleigh Criterion [112], which states that 2/λ is the minimum lateral distance to distinguish two separated individuals. According to this, the image

resolution can be improved by launching higher frequency wave to the detector system. The scanning time for one detector element to generate the image in Figure 4.35 is about 2 hours, mostly caused by the limitations of the stepper motor speed and period of the trigger signal. To exceed this instrumental limitation, a large area detector array is preferable, as the same image can be acquired by using fewer steps, leading to a faster image capturing time for the same area size.

Embedded active structure for THz integrated circuits has been presented and discussed. Simulations as well as preliminary measurement results at low frequency show that such process has potential and it is applicable for THz frequency region. To demonstrate an example of THz circuit with active device, a THz image detector based on novel embedded actives structure has been designed, fabricated, and measured. The newly developed embedded process is low-cost, large-area, and low-temperature compatible, which allows heterogeneous integration of THz devices on a large variety of substrates. GaAs Schottky diodes are embedded in a dielectric layer beneath the broadband log periodic antenna to reduce the influence of the connection parasitics. I-V characteristic measurements before and after the entire process show that the performance of the core element remains intact during the fabrication, which indicates THz devices and integrated circuits are realizable with this concept. The calculated NEP value at 0.1 THz of 3.6pW/√Hz as well as the voltage sensitivity of 7500mV/W is comparable with most of the detectors presented in open literature. Finally, a concealed metallic object has been successfully detected and imaged at 0.1THz by using a single detector element. The imaging detector can be potentially made larger using the fabrication in this work to achieve high density, large area FPAs.

Chapter 5 Summary and Conclusions

Starting from the introduction of THz gap and its unique properties for different applications, the thesis first introduced the existing THz technologies and current developing trends. Based on the discussion of different THz components, including THz source, waveguides and detectors, challenges to bring THz systems to wafer level integrated circuit form have been addressed. In order to achieve miniaturized integrated THz circuit (monolithic THz circuits), novel methods to integration are proposed: THz thin ribbon waveguide as the passive device, and GaAs nanowire Schottky diode and embedded diodes for active circuits.

THz thin ribbon waveguide has been systematically studied. Detailed theoretical calculations proved that the waveguide properties such as cutoff frequency are related to the waveguide geometry. Intensive simulations and numerical values also showed that such thin dielectric ribbon waveguide has the ability to confine the EM wave along the straight line with low power loss. With the high-*k* core assisted by low-*k* claddings, propagating wave can be confined in the cladding layer and reduce the radiation loss at the waveguide bends. Two alternate fabrication processes: photopatternable nanocomposites with tailorable dielectric constant, and laser cut Rogers dry thin films, which are also based on different polymer-ceramic nanocomposites, have been developed as the thin ribbon waveguide. The measurement of fabricated waveguides having straight and curved shapes showed promising results and indicated thin ribbon waveguide can provide a practical route for large area, low cost and low temperature compatible integrated THz passive circuits.

THz active devices integration is discussed using THz detectors as examples. First a GaAs nanowire based THz detector on flexible substrate is fabricated and demonstrated. Novel self-alignment process, which utilizes the undercut phenomena, has been developed in order to

achieve large area, low cost THz direct detectors on a host of flex substrates. Measured results of the fabricated sample showed that the NEP value of 11pW/Hz$^{0.5}$ at 26GHz at room temperature is achieved, and further calculations on NEP at higher frequencies proved that such devices can be used as THz detector. NEP of 44pW/Hz$^{0.5}$ at 0.5THz and 170pW/Hz$^{0.5}$ at 1THz is achievable with good impedance matching. This process realized the THz detector with high sensitivity; meanwhile, the novel process opens possible routes to fabricate large area, low cost and room temperature compatible THz active devices which require Schottky diodes as the nonlinear elements.

To further study the possibility of achieving the integration of THz active devices at wafer level, embedded active process has been demonstrated as a second approach. By embedding the active devices such as Schottky diodes underneath the dielectric layer, the parasitics can be reduced. Preliminary fabrication and measurements show that Schottky diodes preserve their original I-V characteristics after post processing. This proved that the proposed process does not degrade the characteristics of the embedded devices. This process can also be further advanced for heterogeneous integration for THz integrated circuits (i.e., mixing of different semiconductor technologies on a common substrate). Measured results at low frequency verified the reliability of the process. NEP value of 3.6pW/√Hz at 0.1THz can be achieved, which is comparable with most of other THz direct detectors. Using the embedded diode based detector array, a concealed object is imaged at 0.1 THz demonstrating the potential and applicability of embedded diode process. Based on the discussion of the design and fabrication process for passive and active devices in this research, conventional THz circuits can be miniaturized from a bulky system (e.g., brass based system) to wafer level integrated circuits. As mentioned in the introduction, components and elements such as rectangular metallic waveguides and surface mounted diodes

can be replaced by proposed thin ribbon waveguides and embedded active process, and the diode itself has the potential to be manufactured using the self-alignment undercut fabrication process. This research work successfully proposed and demonstrated novel processes that are compatible with wafer-level integration. Different types of THz integrated circuits that can be designed and fabricated using the proposed processes are presented under the future work section. Overall, the proposed processes holds significant potential in the design of THz integrated circuits that would be difficult to achieve using conventional approaches.

Chapter 6 Suggestions for Future Work

This research work proposed several approaches to realize the miniaturization of THz circuits form bulky systems to wafer-level integration circuit form. From passive device point of view, thin dielectric ribbon waveguides having lower radiation loss and simple, large area, wafer-level fabrication can replace conventional waveguides and interconnects. From active device point of view, GaAs nanowire based Schottky diodes with novel self-alignment undercut fabrication process can be applied to manufacture low cost, large area nonlinear device on a host of flex substrates. The embedded active process carried out a solution to realize the reduction of parasitics at THz frequency and achieved large area, low cost heterogeneous fabrication at wafer-level. These research and developments hold significant potential in the realization of complex THz integrated circuits. Up to this point, proposed novel passive and active devices and their fabrications are studied in isolation, and they hold strong potential on forming different types of integrated THz circuits when combined (e.g., mixers, multiplier, phaser shifters, etc.).

Future research work should conduct more studies on advancing the fabrication process of the thin dielectric waveguide to a higher degree of wafer-level integration, and focusing on the development of varieties of integrated THz circuits using the proposed ribbon waveguides and embedded active process. In the first chapter, it was proposed in general that a high frequency (114GHz) tripler can be realized using the techniques and process developed in this research work. Beyond this point, integrated THz circuits such as mixer, phase shifter, and oscillator also need to be realized by the integration of ribbon waveguides and embedded active process.

Several critical aspects require careful and delicate study for future research in this part:

1. Study the circuit structure and device characteristics

This can provide a general overview on the circuit structure and better understanding of the device functions and characteristics that construct complex circuits. This will also help to determine how the novel processes and devices can be applied and integrated for the proposed circuits. Also, it will help to determine the selections of active devices that will be embedded into the certain THz circuitry.

2. Transitions between novel and conventional devices.

   It is very possible that novel and conventional waveguides are both present in one THz circuit design. For this to be practical, transitions are required to connect the conventional waveguides to these newly developed waveguides. This may include studying the field distribution and power confinement in new and existing waveguides, and efficient waveguide transition structures need to be designed and fabricated.

3. Multi-layer integration

   To increase the circuit density with more functions, multi-layer stacking, or 3D packaging of different circuits will be an on-going trend. Thin ribbon waveguide has the potential to realize this, but it still require systematical study on how to integrate them in a proper manner that the performance of every functional circuit will not be degraded by the existence of other neighbor circuits. Also, waveguide transitions between different layers needs to be studied in detail.

The GaAs NW Schottky diode detector is an improvement from the previous carbon nanotube (CNT). From the device reliability point of view, NW based detector is more controllable on the properties of the GaAs NW over CNT. However, further study on how to optimize each process step to reach higher reliability is still necessary. Numbers of NWs in the gap could be more accurately controlled if DEP parameters are further optimized. By controlling

the number of nanowires in parallel, the impedance matching between antenna and the NWs can be further improved. Also, the properties of proposed Schottky diode need deeper study, since the nonlinearity greatly influences the sensitivity of the detector, better understanding and engineering of the formation of metal-semiconductor junction needs to be analyzed in detail and improved to reduce series resistance and increase nonlinearity.

In Chapter 4, a THz image sensor has been demonstrated based on embedded GaAs Schottky diode structure. Based on this process, parasitics at high frequency can be greatly reduced, which can help increase the THz detector sensitivity. As mentioned, only one GaAs Schottky diode has been embedded into the detector, this is acceptable if the image size is small and high resolution is not required. However, for imaging a large sample, imaging array is preferred, and the scan efficiency will be greatly improved comparing to single pixel detector. This work has shown that all 4 embedded diodes in one fabrication batch perform similar DC and RF characteristics. Future research can continue focusing on improving the process reliability of embedding large numbers of diodes to form a full-fledge THz imaging array. This includes optimizing the compatibility of different materials used in the process, effectively opening via on each of the diode pads to reduce the contact resistance, properly designing the antenna as well as the array structure so that maximum resolution can be achieved. Most importantly, CMOS based readout circuitry for both single pixel and array imager are required. In this work, the readout circuits are setup using conventional breadboard, long wires induce large noise over the measured signal. This reduces the signal to noise ratio of the detectors. Furthermore, there is great room to improve the scanning speed and mechanism, by applying high-end step motor with optimized coding and signal processing techniques, real-time imaging can be achieved, which make this image sensor to be applicable for a wide range of applications.

APPENDICES

Appendix A: Process for placing GaAs diodes into the cavities

1. Spin coat Su-8 10 on the 1mm thick Zeonor 1420R substrate (follow the SU-8 datasheet for the spinning speed), this will form a glue layer of approximately 10um thick.
2. Soft back Zeonor substrate with SU-8 10 glue on contact hotplate at 65 ℃ for 2minutes.
3. Then put on Rogers 3003 polymer-ceramic thin film on the glue surface, note that one needs to hold the edge of the thin film and gently drop it on the glue flatly, make sure there is no wrinkle on Rogers 3003 thin film.
4. Put on the Teflon thin film on top of the Rogers 3003, and then put on the weight. Raise the hotplate temperature up to 95 ℃. When reach the target temperature (95 ℃), hold for 2 minutes.
5. Remove the substrate from the hotplate and put it on a non-metal surface, let it cool down to room temperature.
6. Drop GaAs flip chip diodes into the premade cavities in the Rogers 3003 thin film.
7. After finish placing the diodes into the cavities, carefully put the substrate back onto hotplate and bake for another 3 minutes at 95 ℃.
8. Carefully put Teflon thin film on the substrate, always bring the Teflon thin film close to the substrate surface from the top and gently contact it, place the Teflon thin film on the substrate surface as stable as possible, this will prevent placed GaAs diodes becoming loose or even sticking onto the Teflon thin film.
9. Put on the weight metal carefully and gently, don’t drop it heavily on the Teflon surface.
10. Keep the substrate on the hotplate for 1 to 2 minutes at 95 ℃.
11. *Take the weight and the Teflon thin film down carefully and cool down the sample on a non-metal surface.

12. Check under the microscope and see if any diode is damaged.
13. **If everything is good, put the substrate into the vacuum bag, and then slide the Teflon thin film on top of the substrate in the vacuum bag. Note that the Teflon thin film should not scratch the substrate surface, or the diodes will come down.
14. Seal the vacuum bag, turn on the vacuum pump and put the bag with the sample on a hotplate at 65 ℃ for 5 minutes, use weight to make better contact.
15. Cool down the sample to room temperature. Planar expose the sample at 3 steps, each will last for 10 minutes. Check the back side of the substrate is facing towards the UV source, and when fixing the vacuum bag to the mask aligher, make sure the vacuum bag won't block the path of the moving UV lamp hose.
16. After expose, take down the vacuum bag, carefully and gently open the bag, take out the Teflon out first, and make sure it doesn't scratch the substrate surface. Take out the sample carefully and a sample with fixed diodes is finished. Check under the microscope to make sure diodes are not damaged.

*If diodes don't stick in the cavities, and they come up with Teflon, one needs to redo the placing work for the diodes. After re-putting the diodes in the cavities, let the sample sit on a contact hotplate for 3 minutes at 95 ℃.

**Vacuum bag needs to connect to the rubber pipe which the mask aligner used to suck the mask on the metal mask holder.

Appendix B: $BaTiO_3$ Nanocomposite Thin Dielectric Ribbon Waveguide Fabrication

1. Material Preparation

The nanocomposite material for fabricating thin dielectric ribbon waveguide is a mixture of $BaTiO_3$ power and SU-8 photosensitive epoxy, and its dielectric constant can be tuned by changing the volume loading of $BaTiO_3$ in the mixture, and this volume loading ratio is determined by the weight percentage (wt%) of two composites. In order to determine the wt% of each composite for a given volume loading ratio of the mixture, chemical ingredients in SU-8 epoxy is first studied and their wt% are listed in the Table below [SU-8 SDS sheet from MicroChem]:

Table A. 1 Wt% of Chemical Ingredient in SU-8 Epoxy

SU-8 Epoxy Chemical Compositions	wt%
Epoxy Resin	35-75
GBL (Gamma Butyrolactone)	22-60
Photo Initiator (Triarylsulfonium Hexafluoroantimonate Salt)	1.5-3.3
Propylene Carbonate	1-5

Epoxy resin serves as the effective solid content of the SU-8, and it is dissolved in the GBL solvent. These two compositions contribute more than 95% of weight of the SU-8. The photo initiator and propylene carbonate occupy the rest of the SU-8, which have approximately 5% of the total weight.

The GBL acts as the solvent and it evaporates during the soft bake on the hotplate after spin coat SU-8. Photo initiator only has about 3%, and propylene carbonate also evaporates during the soft back, thus the volume loading in the nanocomposite mixture is actually between epoxy resin

and $BaTiO_3$. The wt% of epoxy resin in SU-8 100 in this work is approximately 73.5%. In addition, the densities of epoxy resin (ρ=1.25g/cm^3) and $BaTiO_3$ (ρ=5.5g/cm^3) are also required to calculate the wt% of the two composites. For example, say 30% volume loading of $BaTiO_3$ is needed for a mixture, the calculation for wt% of SU-8 and $BaTiO_3$ is shown as:

$$\frac{M_{SU-8}}{M_{BT}} = \frac{\rho_{epoxy}}{\rho_{BT} \cdot 0.735} \cdot \frac{70\%}{30\%} \tag{A.1}$$

where M_{SU-8} and M_{BT} are the mass of SU-8 and $BaTiO_3$, and ρ_{epoxy} *and* ρ_{BT} are the densities of epoxy resin and $BaTiO_3$. For example, 20g $BaTiO_3$ needs 14.43g SU-8 100 to get 30% volume loading mixture. Furthermore, SU-8 developer or thinner is also added into the mixture, and this helps reduce the mixture viscosity and further reduce the time of ball milling, which is used to enhance the mixture uniformity. Usually 25% of SU-8 weight developer or thinner is sufficient to add into the mixture. The following describes the preparation procedures in detail.

(1) Measure 20g $BaTiO_3$ powder using weighing paper and pour into a pre-cleaned brown bottle.

(2) Put this brown bottle on hot plate for 10 minutes at 150 ℃ to remove the moisture.

(3) Take th brown bottle down and cool down to room temperature, drop 3-4 droplets of HDMS in the bottle, close cap and shake well. Open the cap and let HDMS vapor comes out for 10 minutes.

(4) Pour SU-8 100 14.43g into the brown bottle

(5) Pour 4.8g SU-8 developer or thinner into the brown bottle.

(6) Drop 6-7 big steel bags and 3-4 small steel balls into the bottle, close the cap, and seal it with black tape.

(7) Put the bottle into tumbler and start rotate for 3-4 days to mix the powder and the epoxy well.

2. Fabrication

(1) Tape Zeonor thin film on the supporting substrate (silicon), make sure there is no leakage at the taping.

(2) Pour the mixture on the substrate and cover the whole area.

(3) Spin coating requires 3 steps:

a. 500rpm for 5 seconds, at 83rpm/s acceleration

b. Hold 500rpm for 9 seconds

c. Ramp up to 700rpm at 83 rpm/s acceleration and hold for 20 seconds.

(4) Soft bake at 65℃ for 10 minutes, and then 95℃ for 30 minutes. Then ramp down temperature gradually about 15℃/s to room temperature.

(5) Tape double side tape to the mask aligner substrate holder to fix the substrate, and start expose 20minutes for 5 times, this applies to planar expose as well as expose with mask.

(6) Post bake requires 65℃ for 5 minutes and 95℃ for 10 minutes. Ramp down the temperature by 15℃/s to room temperature.

(7) Put into developer for 10 minutes or until the structure is released.

(8) Rinse the sample with IPA.

Appendix C: LabView programming of Data Acquisition Card (DAQ) for acquiring data for THz imaging sensor

The image matrix data of a concealed metallic or dielectric object detected by THz image sensor is acquired using a Data Acquisition Card (DAQ), and it is programmed and controlled through LabView from National Instruments. The block diagram schematic as well as the controlling code is shown in Figure A.1.

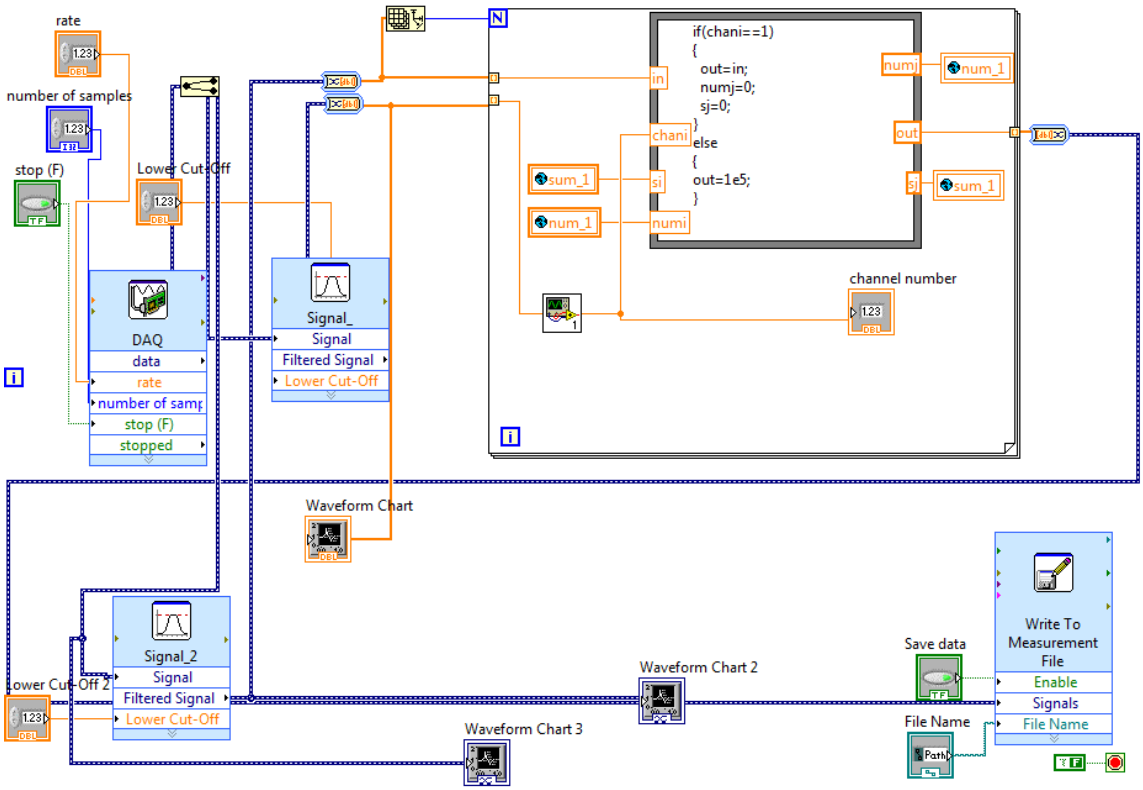

Figure A.1 LabView block diagram schematic for controlling the DAQ to fetch measured image matrix data

The operating process of the DAQ can be described as below:

(1) The indexer of the step motor first sends a trigger (low) signal to DAQ, telling it to start fetching the voltage signal from the detector.

(2) During the period of this low trigger signal, DAQ only reads in the voltage from detector once, and put it in a txt file, then write 0 in the file during the rest of the low trigger period.

(3) The indexer then sends high level trigger signal to DAQ and tell it to stop reading. During this high level trigger period, DAQ writes 100000 in the same file until the next low trigger comes.

(4) The indexer sends a signal to the step motor and moves it to the next adjacent position, then repeat the sequence from step (1) to (3).

Note that the txt file generated by the DAQ card only has one column of data, while the sensor attached to the step motor moves as a raster scanning line by line, thus the post signal processing is required, and Matlab is used then to process the txt file and generate the final image. The code in the M-file for reading and processing the data in the txt tile is shown below:

----------Code Start----------

```
clear, close all
% before using this code, you need to convert the file from DAQ to txt
% format, and delete several lines without any data values, and save as txt

step=1;    % horizontal and vertical step distance is 1mm

m = input('points per row:')       % input numbers of points in horizontal direction
n = input('number of columns:')    % input numbers of points in vertical direction

[filename, PathName,FilterIndex] = ...
   uigetfile('.txt','Please Select the File to Load','Four Point Probe Data');
```

```
Data = importdata(filename,'\t');  %tab delimited, 3 lines of header
A=Data(Data>0&Data<1)
%A=Data(Data>0&Data<5)              % select effective data value from DAQ and put into matrix
A
%A=smooth(smooth(smooth(smooth(smooth(A)))));       %smooth the data
Reshape_A=reshape(A,m,n)           % change A from one column to (m,n) matrix
Prime_Reshape_A=Reshape_A'         % take transpose of A
Prime_Reshape_A(2:2:end,:)=fliplr( Prime_Reshape_A(2:2:end,:)); %reverse every even row of
A transpose
B=Prime_Reshape_A                  % B is the final matrix data to create image
B=flipud(B);                       %flip up and down of the final B matrix
x=[step/2:step:(m*step-step/2)]    % define horizontal position respected to the matrix B
y=[step/2:step:(n*step-step/2)]    % define vertical position respected to the matrix B
%colormap(gray)                    % grayscale pics
imagesc(x,y,-B)                    % create the image data for the final matrix B
colorbar('location','eastoutside') % create colorbar on the right side (eastoutside)
```

----------Code End----------

The generated image could show random color anomalies due to the noise from the voltage source providing the bias to the detector, thus additional coding might be needed to correct the noise points and generate a clearer image.

BIBLIOGRAPHY

BIBLIOGRAPHY

[1] K. Humphreys, J.P. Loughran, M. Gradziel, W. Lanigan, T. Ward, J.A. Murphy, and C. O'Sullivan, "Medical applications of terahertz imaging: a review of current technology and potential applications in biomedical engineering," *In Proc. 26th Annual International Conference of Engineering in Medicine and Biology Society*, vol.1, pp. 1302-1305, Sep, 2004.

[2] Z.D. Taylor, R.S. Singh, D.B. Bennett, P. Tewari, C.P. Kealey, N. Bajwa, M.O. Culjat, A. Stojadinovic, H. Lee, J. Hubschman, E.R. Brown, and W.S. Grundfest, "THz Medical Imaging: in vivo Hydration Sensing," *Terahertz Science and Technology*, vol.1, no.1, pp. 201-219, Sep, 2011.

[3] K. Kawase, Y. Ogawa, Y. Watanabe, and H. Inoue," Non-destructive terahertz imaging of illicit drugs using spectral fingerprints," *Optics Express*, vol. 11, Issue 20, pp. 2549-2554, 2003.

[4] M. Tonouchi, "Cutting-edge terahertz technology," *Nature Photonics*, vol. 1, pp. 97–105, 2007.

[5] M. Hangyo, M. Tani, and T. Nagashima, "Terahertz Time-Domain Spectroscopy of Solids: A Review," *International Journal of Infrared and Millimeter Waves*, vol. 26, Issue 12, pp. 1661-1690, Dec, 2005.

[6] C. A. Schmuttenmaer, "Exploring Dynamics in the Far-Infrared with Terahertz Spectroscopy," *Chem. Rev.*, vol. 104, pp.1759-1779, 2004.

[7] E. Seok, D. Shim, C. Mao, R. Han, S. Sankaran, C. Cao, W. Knap, and Kenneth K. O, "Progress and Challenges Towards Terahertz CMOS Integrated Circuits," *Journal of Solid-State Circuits*, vol. 45, no. 8,pp.1554-1564, August 2010.

[8] J. Nah, H. Fang, C, Wang, K, Takei, M. H. Lee, E. Plis, S. Krishna, and A. Javey, "III−V Complementary Metal−Oxide−Semiconductor Electronics on Silicon Substrates," *Nano Lett.*, vol.12, no.7, pp.3592-3595, 2012.

[9] R. Han, Y. Zhang, Y. Kim, D. Y. Kim, H. Shichijo, E. Afshari , and Kenneth K. O, "Active Terahertz Imaging Using Schottky Diodes in CMOS: Array and 860-GHz Pixel," *Journal of Solid-State Circuits*, vol. 48, no. 10,pp.2296-2308, October 2013.

[10] W. Deal, X.B. Mei, K.M.K.H. Leong, V.Radisic, S.Sarkozy, and R. Lai, "THz Monolithic Integrated Circuits Using InP High Electron Mobility Transistors," *Terahertz Science and Technology, IEEE Transactions on*, vol.1, no.1, pp.25-32, Sept. 2011.

[11] K. Wang, and D.M. Mittleman "Metal Wires for Terahertz Wave Guiding", *Nature*, vol. 432, pp. 376-379, 2004.

[12] R. Mendis and D. Grischkowsky, "Undistorted guided-wavepropagation of subpicosecond terahertz pulses," *Opt. Lett.*, vol. 26, pp. 846-848, 2001.

[13] R. Mendis, D. M. Mittleman, "An investigation of the lowest-order transverse-electric (TE_1) mode of the parallel-plate waveguide for THz pulse propagation," *J. Opt. Soc. Am. B*, Vol.26, No. 9, Sept. 2009.

[14] M. Wächter, M. Nagel, and H. Kurz, "Metallic slit waveguide for dispersion-free low-loss terahertz signal transmission," *Applied Physics Letters*, vol. 90, pp. 061111-1 -3, 2007.

[15] G. Gallot, S. P. Jamison, R. W. McGowan, and D. Grischkowsky, "Terahertz Waveguides," *Opt. Soc. Am. B.*, Vol. 17, No. 5, pp. 851-863, May 2000.

[16] B. Bowden, J. A. Harrington, and O. Mitrofanov, "Low-loss modes in hollow metallic terahertz waveguides with dielectric coatings," *Applied Physics Letters*, vol. 93, pp. 181104-1 -3, 2008.

[17] C. R. Williams, S. R. Andrews, S. A. Maier, A. I. Ferna ́ndez-domi ́nguez, L. Marti ́n-moreno, and F. J. Garci ́a-vidal," Highly confined guiding of terahertz surface plasmon polaritons on structured metal surfaces," *Nature Photonics*, vol. 2, pp. 175 – 179, 2008.

[18] W. Zhu, A. Agrawal, and A. Nahata, "Planar plasmonic terahertz guided-wave devices," *Optics Express*, Vol. 16, Issue 9, pp. 6216-6226, 2008.

[19] S. Pandey, B. Gupta, and A Nahata, "Terahertz plasmonic waveguides created via 3D printing," *Optics Express*, Vol. 21, Issue 21, pp. 24422-24430, 2013.

[20] G. Kumar, S. Li, M. M. Jadidi, and T. E. Murphy, "Terahertz surface plasmon waveguide based on a one-dimensional array of silicon pillars," *New Journal of Physics*, vol.15, pp. 805031, 2013.

[21] Kumar, K. Thyagarajan, and A. K. Ghatak, "Analysis of rectangular-core dielectric waveguides: an accurate perturbation approach,", *Optics Letters*, Vol. 8, No. 1, pp. 63-65, Jan. 1983.

[22] E. Snitzer, "Cylindrical dielectric waveguide modes," *J. Opt. Soc. Am.*, vol. 51, 491, 1961.

[23] K. D. Laakmann, and W. H. Steier, "Waveguides: characteristic modes of hollow rectangular dielectric waveguides," *Applied Optics*, Vol. 15, Issue 5, pp. 1334-1340, 1976.

[24] L. Chen, H. Chen, T. Kao, J. Lu, and C. Sun, "Low-loss subwavelength plastic fiber for terahertz waveguiding," *Optics Letters*, Vol. 31, No. 3, pp.308-310, Feb. 2006.

[25] C. Lai, Y. Hsueh, H. Chen, Y. Huang, H. Chang, and C. Sun," Low-index terahertz pipe waveguides," *Optics Letters*, Vol. 34, No. 21, pp. 3457-3459, Nov. 2009.

[26] D. Chen and H. Chen, "A novel low-loss Terahertz waveguide: Polymer tube," *Opt. Exp.*, vol. 18, pp. 3762–3767, 2010.

[27] Y. Matsuura, R. Kasahara, T. Katagiri, and M. Miyagi, “Hollow infrared fibers fabricated by glass-drawing technique,” *Opt. Express*, vol. 10, no.12, pp. 488-492, 2002.

[28] C. Yeh, F. I. Shimabukuro, and J. Chu, “Ultralow loss dielectric ribbon waveguide for millimeter/submillimeter waves,” *Applied Physics Letters*, vol.54, pp. 1183-1185, 1989.

[29] R. Mendis, and D. Grischkowsky, "Plastic Ribbon THz Waveguides," Journal of Applied Physic, vol. 88, no. 7, pp. 4449-4451, 2000.

[30] C. Yeh, F. Shimabukuro, and P. H. Siegel, “Low-loss terahertz ribbon waveguides,” Applied Optics, vol. 44, no. 28, pp. 5937- 5946, 2005.

[31] X. Yang, and P. Chahal, "THz ribbon waveguides using polymer-ceramic nanocomposites," In Proc. 62nd Electronic Components and Technology Conference (ECTC), pp.225-230, May 29 -June 1, 2012.

[32] G.P. Gallerano, S. Biedron, “Overview of Terahertz radiation Sources,” Proceedings of the 2004 FEL Conference, pp.216-221, Aug 29-Sep 3, Trieste, Italy, 2004

[33] P. Shumyatsky and R. R. Alfano, “Terahertz Sources,” *Journal of Biomedical Optics, Vol.* 16, No.3, pp.033001-9, March, 2011.

[34] J. Faist, F. Capasso, D. L. Sivco, C. Sirtori, A. L. Hutchinson, and A. Y. Cho, “Quantum Cascade Laser,” *Science,* Vol.264 (5158), pp.553-55622, April 1994.

[35] B. S. Williams, “Terahertz Quantum-cascade Lasers,” *Nature Photonics,* Vol.1,pp. 517 – 525, Sep. 2007.

[36] Q. Y. Lu, N. Bandyopadhyay, S. Slivken, Y. Bai, and M. Razeghi, “Continuous operation of a monolithic semiconductor terahertz source at room temperature,” *Appl. Phys. Lett., Vol.* 104, pp. 221105, 2014.

[37] M. C. Wanke, E.W. Young, C. D. Nordquist, M. J. Cich, A. D. Grine, C. T. Fuller, J. L. Reno and M. Lee, “Monolithically integrated solid-state terahertz transceivers,” Nature Photonics, Vol. 4, pp.565-569, August, 2010.

[38] B. Zhang, Y. Fan, F.Q. Zhong, X.F. Yang, K.J. Song, and X.Q. Lin, "A 225GHz four-anode frequency tripler for wireless application," *IET International Communication Conference on Wireless Mobile and Computing (CCWMC 2009)*, pp.626-628, Shanghai, China, 7-9 Dec. 2009.

[39] S. Zhang, B. Zhang, Y. Fan, “Design of a 114GHz-135GHz Passive Tripler, ” *In Proc. Signals Systems and Electronics (ISSSE), 2010 International Symposium on*, vol.2, pp.1-3, 17-20 Sept. 2010, Nanjing, China.

[40] N. Erickson, G. Narayanan, R. Grosslein, G. Chattopadhyay, A. Maestrini, E. Schlecht,” 1500 GHz Tunable Source Using Cascaded Planar Frequency Doublers,” *In Proc. 13th*

International Symposium on Space Terahertz Technology, pp.177-186, Harvard University, March 2002.

[41] C.Ko, S. Chen, C. Chiang, T. Kuo, Y.C. Shih, T.H. Chen, "Embedded active device packaging technology for next-generation chip-in-substrate package, CiSP," Proc. on 56th *Electronic Components and Technology Conference*,pp. 322-329.8 May 30th –June 2nd, 2006, San Diego, CA.

[42] Y.P. Hung, T.C. Chang, C.K. Lee, Y.C. Lee, J.Y. Chang, S.Y. Huang, C.K. Hsu, S.M. Li, J.H. Huang, F.J. Leu, R.S. Cheng, Y.W. Huang, and T.H. Chen, "Processing characteristics and reliability of embedded DDR2 memory chips," *5th International Microsystems Packaging Assembly and Circuits Technology Conference (IMPACT), 2010*, pp.1,4, 20-22 Oct. 2010.

[43] L. Boettcher, D. Manessis, A. Ostmann, S. Karaszkiewicz, H. Reichl, "Embedding of Chips for System in Package realization - Technology and Applications," *3rd International Microsystems, Packaging, Assembly & Circuits Technology Conference, 2008. IMPACT 2008.*,pp.383-386, 22-24 Oct. 2008.

[44] M. Wojnowski, M. Engl, B. Dehlink, G. Sommer, M. Brunnbauer, K. Pressel, R. Weigel, "A 77 GHz SiGe mixer in an embedded wafer level BGA package," Proc. on *58th Electronic Components and Technology Conference. ECTC 2008*, pp. 290-296, 27-30 May 2008, Lake Buena Vista, FL.

[45] M. Itoh, S. Hoshi and H. Linaga, "Technology of Embedded Ultra-High Frequency Power Amplifier ICs in the Print Circuit Boards", *Oki Technical Review*, Issue 216 Vol.77, No.1, April 2010.

[46] F. Sizov, "THz radiation sensors." *Opto−Electronics Review*, Vol. 18,No.1, pp.10–36,2010

[47] Colin Baker, "Homeland Security, Medical, Phamaceutical and Non-destructive Testing Applications for THz Radiation," *Applications of THz Radiation, APS march Meeting*, March, 2005

[48] F. Sizov, A.Rogalski, "Review: THz detectors," *Progress in Quantum Electronics*, Vol. 34, pp278–347, 2010

[49] John Byrd, "THz Detectors, Accelerator-Based Sources of Coherent Terahertz Radiation," *UCSC*, Santa Rosa CA, January 21-25, 2008

[50] Paul Muralt, "Micromachined infrared detectors based on pyroelectric thin films," *Rep. Prog. Phys.*,Vol. 64, pp1339–1388, 2001

[51] H. M. Manohara, E. W. Wong , E. Schlecht , B. D. Hunt , and P. H. Siegel, "Carbon Nanotube Schottky Diodes Using Ti-Schottky and Pt-Ohmic Contacts for High Frequency Applications," *Nano Letters*, Vol. 5, No. 7 pp1469-1474 2005.

[52] N. P. Dasgupta , J.Sun , C. Liu , S. Brittman , S. C. Andrews ,J. Lim , H. Gao , R. Yan , and P. Yang, "25th Anniversary Article: Semiconductor Nanowires –Synthesis, Characterization, and Applications," *Adv. Mater.*,Vol. 26, pp. 2137–2184, 2014.

[53] W. Lu, and C. M Lieber, "TOPICAL REVIEW: Semiconductor nanowires," *J. Phys. D: Appl. Phys.*, Vol. 39, pp. R387–R406, 2006.

[54] X. Duan and C. M. Lieber, "General Synthesis of Compound Semiconductor Nanowires," *Adv. Mater.*, Vol. 12, No. 4, pp. 298-302, 2000.

[55] M. DeJarld, J. C. Shin, W. Chern, D. Chanda, K. Balasundaram, J. A. Rogers, and X. Li, "Formation of High Aspect Ratio GaAs Nanostructures with Metal-Assisted Chemical Etching," *Nano Lett.*, Vol.11, pp. 5259–5263, 2011.

[56] http://www.cytodiagnostics.com/, Product has been discontinued.

[57] L. Romeo, D. Coquillat, M. Pea, D. Ercolani, F. Beltram, L. Sorba, W. Knap, A. Tredicucci, and M. S. Vitiello, "Nanowire-based field effect transistors for terahertz detection and imaging systems," *Nanotechnology*, Vol.24, no. 21, pp.4005, April, 2013.

[58] D. Schneiderbanger, C. Kneuer, M. Sterns, R. Rehner, S. Martius, L.Schmidt, "A 75–110 GHz seventh-harmonic balanced diode mixer in a novel circuit configuration," *Wireless Technology, 2008. EuWiT 2008. European Conference on*, pp.158-161, Amsterdam, 27-28 Oct. 2008.

[59] B. Zhang, Y. Fan, S. X. Zhang, X.F Yang, F.Q. Zhong, Z. Chen, "110 GHz High Performanced Varistor Tripler," *Microwave and Millimeter Wave Circuits and System Technology (MMWCST), 2012 International Workshop on*, pp.1-2, Chengdu, China 19-20 April, 2012.

[60] A. Karpov, D. Miller, F. Rice, J. A. Stern, B. Bumble, H. G. LeDuc, and J. Zmuidzinas, "Low Noise 1 THz–1.4 THz Mixers Using Nb/Al-AlN/NbTiN SIS Junctions," *IEEE Transactions On Applied Superconductivity*, vol.17, no.2, pp343-346, June 2007.

[61] D. Pukala, and I. Mehdi, "THz frequency multiplier chains based on planar Schottky diodes," *Proc. SPIE 4855, Millimeter and Submillimeter Detectors for Astronomy*, no. 447, Feb 1, 2003.

[62] C. Yeh and F. Shimabukuro. *The Essence of Dielectric Waveguides*. Springer, 2008.

[63] X. Yang, and P. Chahal, "THz ribbon waveguides using polymer-ceramic nanocomposites," *In Proc. 62nd Electronic Components and Technology Conference (ECTC)*, pp.225-230, May 29 -June 1, 2012.

[64] D.M. Pozar, *Microwave Engineering*, 4th Edition, John Wiley & Sons, Inc., 2011.

[65] C. Yeh, F. Shimabukuro, and P. H. Siegel, "Low-loss terahertz ribbon waveguides," Applied Optics, vol. 44, no. 28, pp. 5937- 5946, 2005.

[66] S. S. Ray and M. Bousmina, Polymer nanocomposites and their applications: *American Scientific* Stevenson Ranch, CA, 2006.

[67] P. Chahal, A. Haridass, A. Pham, R. Tummala, M. Allen, M. Swaminathan and J Laskar, "Integration of thin film passive circuits using high/low dielectric constant materials," *In Proc. 47th Electronic Components and Technology Conference (ECTC)*, pp.225-230, May 18-21,1997.

[68] P. Chahal, R. R. Tummala, M. G. Allen, and M. Swaminathan, "A Novel Integrated Decoupling Capacitor for MCM-L Technology," *Components, Packaging, and Manufacturing Technology, Part B: Advanced Packaging, IEEE Transactions on*, vol.21, no.2, pp.184-193, May, 1998.

[69] V Agarwal, P. Chahal, R.R. Tummala, and M.G Allen, "Improvements and recent advances in nanocomposite capacitors using a colloidal technique," *48th IEEE Electronic Components Technology Conference*, pp. 165-170, 25-28 May, 1998.

[70] J.A. Hejase, P.R. Paladhi, P. Chahal, "Terahertz Characterization of Dielectric Substrates for Component Design and Nondestructive Evaluation of Packages," *IEEE Tran On Components, Packaging And Manufacturing Technology*, vol. 1, no. 11, pp.1685-1694, Nov.2011.

[71] Arup Choudhury, "Dielectric and Piezoelectric Properties of Polyetherimide/$BaTiO_3$ Nanocomposites," *Materials Chemistry and Physics*, vol. 121, no. 1–2, pp. 280-285, 2010.

[72] S. Arscott, F. Garet, P. Mounaix, L. Duvillaret, J.-L. Coutaz, D. Lippens, "Terahertz Time-domain Spectroscopy of Films Fabricated from SU-8," *Electron. Lett.*,vol. 35, no.3, pp. ,243-244, 2005.

[73] T. Hoshina, K. Takizawa, J. Li, T Kasama, H. Kakemoto, T. Tsurumi, "Domain Size Effect on Dielectric Properties of Barium Titanate Ceramics", *Japanese Journal of Applied Physics*, vol. 47, no. 9, pp. 7607~7611, 2008

[74] X. Yang, J. Hejase, P. Paladhi, P. Chahal, "Planar Terahertz Circuits Using Thin Dielectric Waveguides", *Proc 36th Infrared, Millimeter and Terahertz Waves (IRMMW-THz) conf*, pp. 1-2, Houston, TX, Oct. 2011.

[75] J.A. Hejase, B. Schulte, and P. Chahal, "Design and test of wide-band terahertz dielectric sub-wavelength focusing probes," *Proc. 61st Electronic Components and Technology Conference (ECTC)*, pp.1035-1040, May 31 2011-June 3, 2011.

[76] H. J. Fan, P. Werner, and M. Zacharias, "Semiconductor Nanowires: From Self-Organization to Patterned Growth," *Small*, vol. 2, pp. 700-717, 2006.

[77] Y Cui, X Duan, J Hu, and C. M. Lieber, "Doping and Electrical Transport in Silicon Nanowires," J. Phys. Chem. B, , vol.104, no. 22, pp 5213–5216, 2000.

[78] M. S. Gudiksen, L. J. Lauhon, J. Wang, D. C. Smith, and C. M. Lieber, "Growth of

nanowire superlattice structures for nanoscale photonics and electronics," *Nature*, no. 415, pp. 617-620 7 February 2002.

[79] N. Han, F. Wang, S. Yip, J. J. Hou, F. Xiu, X. Shi, *et al.*, "GaAs nanowire Schottky barrier photovoltaics utilizing Au–Ga alloy catalytic tips," *Applied Physics Letters,* vol. 101, pp. 013105-013105, 2012.

[80] C. Gutsche, A. Lysov, I. Regolin, A. Brodt, L. Liborius, J. Frohleiks, *et al.*, "Ohmic contacts to n-GaAs nanowires," *Journal of Applied Physics,* vol. 110, pp. 014305-014305, 2011.

[81] X. Yang and P. Chahal, "Large-area low-cost substrate compatible CNT Schottky diode for THz detection," *Electronic Components and Technology Conference (ECTC), 2011 IEEE 61st*, pp. 2158-2164, May 31-June 3.

[82] S. A. Fortuna and X. Li, "GaAs MESFET with a high-mobility self-assembled planar nanowire channel," *Electron Device Letters, IEEE,* vol. 30, pp. 593-595, 2009.

[83] X. Yang and P. Chahal, "Embedded actives for terahertz circuit applications: Imaging array," *Electronic Components and Technology Conference (ECTC), 2012 IEEE 62nd*, pp. 2082-2086. May 29 -June 1

[84] P. Chahal, F. Morris, and G. Frazier, "Zero bias resonant tunnel Schottky contact diode for wide-band direct detection," *Electron Device Letters, IEEE,* vol. 26, pp. 894-896, 2005

[85] A. Bid, A. Bora, and A. K. Raychaudhuri, "1/f noise in nanowires," *Nanotechnology,* vol. 17, p. 152, 2005.

[86] S. Ju, P. Chen, C. Zhou, Y.-g. Ha, A. Facchetti, T. J. Marks, *et al.*, "1/f noise of SnO2 nanowire transistors," *Birck and NCN Publications,* p. 153, 2008.

[87] C. A. Richter, H. D. Xiong, X. Zhu, W. Wang, V. M. Stanford, W. K. Hong, *et al.*, "Metrology for the electrical characterization of semiconductor nanowires," *Electron Devices, IEEE Transactions on,* vol. 55, pp. 3086-3095, 2008.

[88] C.-J. Chiang, T. M. Wallis, D. Gu, A. Imtiaz, P. Kabos, P. T. Blanchard, *et al.*, "High frequency characterization of a Schottky contact to a GaN nanowire bundle," *Journal of Applied Physics,* vol. 107, pp. 124301-124301, 2010.

[89] M. M. Gitin, F. W. Wise, G.Arjavalingam, Y. Pastol and R. C. Compton, "Broad-Band Characterization of Millimeter-Wave Log-Periodic Antennas by Photoconductive Sampling", Transactions on Antennas and Propagation, vol. 42, no. 3, Mar. 1994.

[90] M. S. Vitiello, D. Coquillat, L. Viti, D. Ercolani, F. Teppe, A. Pitanti, *et al.*, "Room-temperature terahertz detectors based on semiconductor nanowire field-effect transistors," *Nano letters,* vol. 12, pp. 96-101, 2011.

[91] Öjefors, U. R. Pfeiffer, A. Lisauskas, and H. G. Roskos, "A 0.65 THz Focal-Plane Array in a Quarter-Micron CMOS Process Technology," *Journal of Solid-State Circuits,* vol. 44, no.

7,pp. 1968-1976, Jul., 2009.

[92] F. Sizov, and A.Rogalski, “Review, THz Detector”, *Progress in Quantum Electronics*, vol. 34, pp. 278–347, 2010.

[93] H. M. Manohara, E. W. Wong, E. Schlecht, B. D. Hunt, and P. H. Siegel, “Carbon Nanotube Schottky Diodes Using Ti-Schottky and Pt-Ohmic Contacts for High Frequency Applications,” *Nano Letters*, vol. 5. no. 7, pp. 1469-1474, 2005

[94] X. Yang, and P. Chahal, “Large-area Low-cost Substrate Compatible CNT Schottky Diode For Thz Detection”, *Proc 61st Electronic Components and Technology Conference (ECTC)*, Lake Buena Vista, FL, May 31st-June 1st, pp. 2158-2164, 2011.

[95] P. Chahal, F. Morris, and G. Frazier, "Zero Bias Resonant Tunnel Schottky Contact Diode for Wide-Band Direct Detection," *Electron Device Letters*. vol. 26, no. 12, pp. 894-896, 2005

[96] M. Sakhno, F. Sizov, and A. Golenkov, “Uncooled THz/sub-THz Rectifying Detectors: FET vs. SBD”, *Journal of Infrared, Millimeter, and Terahertz Waves*, Springer, Sep. 2013, DOI: 10.1007/s10762-013-0023-2.

[97] V. V. Parshin, “The Precise Microwave Resonator Spectroscopy of Gases and Condensed Media,”In proc. 6th *International Symposium on Physics and Engineering of Millimeter and Sub Millimeter Waves*, Kharkov, pp. 30–35, 2007

[98] W. Knap, M. Dyakonov, D. Coquillat, F. Teppe, N. Dyakonova, J. Łusakowski, K. Karpierz, M. Sakowicz, G. Valusis, D. Seliuta, I. Kasalynas, A.E. Fatimy, Y. M. Meziani, T. Otsuji, “Field Effect Transistors for Terahertz Detection: Physics and First Imaging Applications”, *Journal of Infrared, Millimeter, and Terahertz Waves*, Vol. 30, Issue 12, pp. 1319-1337, December 2009.

[99] B. Zhang;, Y. Fan, Zhang, S. X., X. Yang, F. Zhong and Z. Chen, "110GHz high performanced varistor tripler," *2012 International Workshop Microwave and Millimeter Wave Circuits and System Technology (MMWCST)* , pp. 19-20 April 2012.

[100] D. Schneiderbanger, C. Kneuer, M. Sterns, R. Rehner, S. Martius, L. Schmidt, "A 75–110 GHz seventh-harmonic balanced diode mixer in a novel circuit configuration," *European Conference of Wireless Technology, EuWiT 2008.,* pp.158,161, 27-28 Oct. 2008.

[101] D. Schneiderbanger, A. Cichy, R. Rehner, M. Sterns, S. Martius, L. Schmidt, "A hybrid broadband millimeter-wave diode ring mixer with advanced IF extraction technique," *European Microwave Conference, 2007.*,pp.656,659, 9-12 Oct. 2007.

[102] Xianbo Yang; Chahal, P., "Embedded actives for terahertz circuit applications: Imaging array," *Proc. 62nd Electronic Components and Technology Conference (ECTC),* pp.2082-2086, May 29 2012-June 1 2012.

[103] J. A. Hejase, P. R. Paladhi, and P. Chahal, "Terahertz Characterization of Dielectric Substrates for Component Design and Nondestructive Evaluation of Packages", *Tran on Components, Packaging And Manufacturing Technology*, Vol. 1, No. 11, pp. 1685-1694, 2011

[104] M. M. Gitin, F. W. Wise, G.Arjavalingam, Y. Pastol and R. C. Compton, "Broad-Band Characterization of Millimeter-Wave Log-Periodic Antennas by Photoconductive Sampling", *Transactions on Antennas and Propagation*, vol. 42, no. 3, Mar. 1994.

[105] A. Scheuring, A. Stockhausen, S. Wuensch, K. Ilin, and M. Siegel, "A new analytical Model for log-periodic Terahertz Antennas, " *In Proc. of 4th European Conference on Antennas and Propagation (EuCAP),*April, 12-16th, 2010, Barcelona, Spain.

[106] Y. Mushiake, "Self-complementary antennas," *Antennas and Propagation Magazine*, vol. 34, Issue 6, pp. 23-29, Dec. 1992

[107] A. C. Young, J. D. Zimmerman, E. R. Brown, and A. C. Gossard, "1/f noise in all-epitaxial metal-semiconductor diodes," *Applied Physics Letters*, vol. 88, pp.073518-1-3, 2006.

[108] J. D. Song, W. J. Choi, I. K. Han, and J. I. Lee, "Characteristics of 1/f Noise in Au/GaAs Schottky Diode Embedded with Self-Assembled InAs Quantum Dots," *Journal of the Korean Physical Society*, Vol. 45, pp. S542-S546, Dec. 2004.

[109] R. Singha, and D. Kanjilal, "Temperature Dependence of 1/f Noise in Pd/n-GaAs Schottky Barrier Diode," Journal of Applied Physics, Vol. 91, No. 1, pp. 411-413, Jan. 2002

[110] J. A. Hejase, B. Schulte, and P. Chahal, "Design and test of wide-band terahertz dielectric sub-wavelength focusing probes," Proc. 61st Electronic Components and Technology Conference (ECTC), Lake Buena Vista, FL, May 31st-June 1st, pp. 1035-1040, 2011

[111] U. Schade, K.Holldack, M. C. Martin, and D. Fried, "THz near-field imaging of biological tissues employing synchrotron radiation," Proc. SPIE., vol. 5725, pp. 46-52, 2005.

[112] M. Born and E. Wolf, Principles of Optics: Electromagnetic Theory of Propagation, *Interference and Diffraction of Light*, Cambridge.